From the Plateau to the Bog: How Environmental Variables Control Permafrost Progression and Methane Emissions

Joel Frederick Eklof

A dissertation

submitted in partial fulfillment of the

requirements for the degree of

Doctor of Philosophy

University of Washington

2024

Reading Committee:

Rebecca Neumann, Chair

Jessica Lundquist

Ben Jones

Bernard Hallet

Program Authorized to Offer Degree:

Civil and Environmental Engineering

University of Washington

Abstract

From the Plateau to the Bog: How Environmental Variables Control Permafrost Progression and Methane Emissions

Joel Frederick Eklof

Chair of the Supervisory Committee:

Rebecca B. Neumann

Department of Civil and Environmental Engineering

Permafrost, or ground at or below 0 °C for two or more years, covers approximately 24% of the northern hemisphere and contains around two times the amount of carbon currently in Earth's atmosphere. Atmospheric temperatures in the Northern Hemisphere have warmed faster than the global average, causing widespread warming and thawing of permafrost. As permafrost thaws, carbon that was once relatively inaccessible becomes available for microbes to process and release as greenhouse gases. When this process occurs in an oxygen-poor wetland, methane, a greenhouse gas with 28-35 times the global warming potential of carbon dioxide, is released.

Permafrost thaw and methane emissions vary significantly across the permafrost zone. Environmental factors other than air temperature, such as ecologic, hydrologic, and topographic conditions, also regulate permafrost temperature, progression, and stability. Methane emissions have spatial and temporal variability caused by complex interactions of environmental factors, including soil moisture, soil temperature, vegetation, and nutrient access. To better understand the environmental factors that cause this variability, we instrumented Alaskan permafrost sites that experience varying climate conditions.

In Chapter 2, we investigate environmental controls on permafrost thaw at a warm and wet site at the southern fringe of the permafrost zone. Our study (2020-2022) captured three of the snowiest years and three of the four wettest years since site monitoring began in 2015. Average thaw rates along an across-site transect increased nine-fold from 6 ± 5 cm/year (2015-2020) to 56 ±12 cm/year (2020-2022). This thaw was not uniform. Hummock locations, residing on topographic high points with relatively dense canopy, experienced only 8 ± 9 cm/year of thaw, on average. Hollows, topographic low points with low canopy cover, and transition locations, which had canopy cover and elevation between hummocks

and hollows, thawed 44 ± 6 cm/year and 39 ± 13 cm/year, respectively. Mechanisms of thaw differed between these locations. Hollows had high warm-season soil moisture, which increased thermal conductivity, and deep cold-season snow coverage, which insulated the soil. Transition locations thawed primarily due to thermal energy transported through subsurface taliks during individual rain events. Most increases in depth to permafrost occurred below the ~45 cm thick seasonally frozen layer and expanded site taliks. This chapter highlights the importance of canopy cover and microtopography in controlling soil thermal inputs, the ability of subsurface runoff from individual rain events to trigger warming and thaw, and the acceleration of thaw caused by consecutive wet and snowy years. As northern high-latitudes become warmer and wetter and precipitation events become more extreme, the importance of these controls on soil warming and thaw is likely to increase.

In Chapter 3, we investigate how environmental variables affected the spatial and temporal variability of depth to permafrost at our colder, drier, and more stable permafrost site. To better understand the impacts of these variables, we installed 25 high-resolution soil temperatures along a transect into permafrost at a discontinuous permafrost site in Interior, Alaska, with broad variation in environmental variables. Local slope and wetland proximity of transect locations caused variations in thermal regime and depth to permafrost. Locations on mild slopes had high near-surface soil moisture entering the cold season, increasing thermal conductivity and making them colder than drier locations. The bog complex, which remains unfrozen all year, acted as a thermal buffer for nearby permafrost locations, keeping them warmer than comparable locations. Warm season meteorological forcing controlled year-to-year variation in depth to permafrost at locations with consistent amounts of seasonal ground ice from year to year. Cold-season meteorological forcing was the primary control on locations with variable year-to-year ground ice content. Two locations that only overcame the zero curtain in 2023 experienced 15 cm and 58 cm shallowing of the permafrost table, respectively, while all other locations experienced permafrost thaw. This result shows the relative sensitivity of permafrost locations at a thermal tipping point compared to locations that are either warmer or colder.

Chapter 4 investigates the impact of advectively transported nutrient inputs from the permafrost plateau on methane emissions from a downgradient bog complex. We found that the advection of nitrogen from the surrounding permafrost plateau and warm soil temperatures significantly enhanced methane emissions. Root damage sustained from rapid soil freezing inhibited nutrient use from plateau vegetation during the early growing season, doubling nitrogen availability in the plateau. Early season June rain flowed through the top ~40 cm of plateau soils, picking up excess nitrogen and transporting it into the wetland complex. This flux of nutrients fueled a 65% increase in methane emissions and a 30% increase in gross primary productivity. Our study identifies rain's important and unconsidered role in governing the nutrient balance of thawing permafrost landscapes.

Table of Contents

List of Figures

List of Tables

Acknowledgements:

In writing this dissertation and conducting this research, I have lived and worked on the unceded ancestral lands of the Coast Salish people, including the tribes and bands of the Duwamish, Puyallup, Cayuse, Umatilla Tulalip, and Walla Walla nations. During fieldwork and outreach activities, I have lived and worked on the unceded ancestral lands of the Tanana, Koyukon, and Dena'ina Elnena nations and had the opportunity to work with Elder Kenneth, an Athabaskan Elder, to teach science through multiple ways of knowing. Indigenous peoples have been in relationship with the boreal landscapes of Alaska for thousands of years. We recognize the deep, reciprocal knowledge these peoples have cultivated with this environment, sustaining themselves and the ecosystems around them through generations of observation, resilience, and respect. Their understanding of place transcends time. As this research contributes to the academic pursuit of knowledge, I strive to honor and amplify Indigenous voices, remaining mindful of the responsibilities of working on these lands.

The United States Department of Energy and the National Science Foundation funded the work presented in this dissertation.

I am profoundly lucky to have had many support systems throughout this graduate research journey. To my University of Washington community, my Fairbanks community, my Tacoma community, and my supportive friends sprinkled across the country and world. Thank you. None of this would have been possible without your support and kindness.

I could not possibly thank my advisor, Becca Neumann, sufficiently for her endless patience, commitment, and mentorship during these last six years. She has shown over and over an inspiring commitment to support me as a researcher, professional, and individual. You taught me to be a scientist in service of humanity, and you treated me as your scientific peer. Thanks to Becca, I am a better educator, a better scientist, and a better person. Plus, I am never without an ample amount of Sharpies.

I want to extend my gratitude to the extraordinary community of graduate students who played an integral role in making this experience enjoyable and fulfilling. The UW Hydro-Biogeochem Research Group has been a tremendous support during my time in graduate school. From writing group to lunchtime swim workouts to morning climbs to becoming a UW sailing speed record holder despite not knowing how to sail, this group has added immensely to my graduate experience. Yasmine Farhat, Sam Fung, Robin Ruhm, Rachel Strickman, and Nick Waldo: Thank you for the laughter, camaraderie, and friendship. To my original UW Master's in Hydrology and Hydrodynamics cohort, thank you for the late nights studying and the joyous mediocrity of our intramural teams. Thank you to the UW Environmental Fluid Mechanics Group for exceptional support and community over the years, especially before I had my lab group to call home. Thank you to the Fishbowl and

Treehouse communities, whose daily conversations and grounding presence significantly impacted my personal and professional life during this journey.

I worked with extraordinary individuals in the field. To Marie English, Greg Vandas, Katie Ring, and Katherine LeBlanc, thank you for your dedication to this project. Thank you to Colin Edgar and Ben Jones for field support when personal travel was impossible. To my Dad, Bill Eklof, thank you for joining me in the field at -25 °C to make Chapter 2 possible.

To the Bonanza Creek LTER community, graduate students, USGS researchers, faculty members, and staff, thank you for the resources, support, and friendship. To my fellow graduate students with whom I spent endless hours in the field, Jessie Rush, Hailey Webb, Evan Schijns, Will Cox, Nor Serocki, Kristen Bill, Barrett Sullivan, Tessa Meyer, and Leah Reese, your expertise and friendship made the science and long periods away from loved ones possible. Thank you to the exceptional Bonanza Creek staff, especially Jamie Hollingsworth and Colin Edgar. To Catherine Dielman and Evan Kane, thank you for your time, wisdom, and mentorship. You had no obligation, and I am exceptionally grateful.

To my Bonanza Creek Fostering Science community, thank you for trusting me to participate in this exceptional program. To Christa Mulder and Katie Spellman, you inspire me daily and have fundamentally changed my goals as a scientist, educator, and professional. Your skills, expertise, and passion have helped me recalibrate what is most important in this profession. To my fellow instructors, Theresa Villano, Natalie Schuldt, Kara Kornhauser, and Chloé Eklof, you inspire me and make me a more effective educator.

To my Tacoma community, you have rallied to support Chloé and me countless times. Leaving for four-month field campaigns was always immensely difficult, but your support of Chloé and me made being gone to pursue this dream possible. I especially want to thank Michelle Wrigley, Micah Haven, Justin and Laura Ehli, and Dan Goodrich.

To my friends across the country, thank you for the long phone conversations and always being there to support me. I thank Becca Ebert, Jensen Handwork, Eric Schnell, Kericho Corry, Aaron Altabet, Robin VanHouten, and Ian Latimer. Always supporting me and always ready to pick up the phone.

I want to thank my family. For the 100s of walks you gave Murray when I was in the field, for all the field snacks and rides to the airport, and always being willing to help. To Murray, my work-from-home partner-in-crime, I will always spend my Pomodoro productivity breaks wrestling with you on the carpet.

Finally, and most importantly, Chloé. You are the most supportive partner in the world. I have collectively spent over two years away from you to do the work described in this document. We got married, bought a house, got a dog, and built a life together during my time in this position. Thank you for supporting me in pursuing my dream, and I look forward to a lifetime of supporting yours. I love you.

1 Chapter 1: Introduction

1.1 Motivation and Background

Permafrost, or ground that has been at or below 0 °C for two or more years[1], covers approximately 24% of the terrestrial landscape of the Northern Hemisphere[2]. Atmospheric temperatures in the Northern Hemisphere have warmed faster than the global average, and this amplified warming will strengthen in the future[3]. Permafrost trends are consistent with atmospheric temperature trends, with widespread warming and thaw observed since 1980[4]. When ice-rich permafrost thaws, the ground subsides. This subsidence creates thermokarst features like thaw wetlands[5]. This process causes immediate loss of previously frozen soil organic carbon[6,7]. While emissions of this landscape transition are eventually offset by carbon sequestration as wetland biomass, on the shorter time scale of decades to centuries, which is the most relevant timescale for climate policy and modeling, this process often has a positive warming potential due to emissions of methane[8,9]. In addition to greenhouse gas emissions, permafrost degradation impacts ecosystem function[10], changes geomorphological characteristics[11], and poses a threat to society through significant impacts on the infrastructure and economy of cold regions[12–15].

Permafrost thaw and methane emissions vary significantly across the permafrost zone. Environmental factors other than the air temperature, such as ecologic, hydrologic, and topographic conditions, also regulate permafrost temperature, progression, and stability[16]. Permafrost can degrade at mean annual air temperatures (MAATs) as low as -20 °C and persist at MAATs as high as +2 °C[17]. Methane emissions also have large-scale spatial and temporal variability caused by complex interactions of environmental factors[18–21]. Some of these factors include soil moisture[19,21], soil temperature[19,22], vegetation[23,24], and nutrient access[25,26]. Hydrologic inputs from permafrost landscapes into wetland areas can affect these variables and alter methane emissions [18].

To explore these processes' variability and better understand the environmental factors that cause this variability, we instrumented two Alaskan permafrost sites that experience varying climate conditions. The first site, called Brown's Lake Bog, is a permafrost site located at the southern fringe of the permafrost zone in Kenai Wildlife Refuge outside of Soldotna, AK. This site is in the isolated permafrost zone, meaning permafrost underlays less than 10% of the landscape[2]. The MAAT of this region is consistently above 0 °C, making the local climate no longer conducive to permafrost formation[16,27]. The permafrost at this site is thawing rapidly. Our second site is 400 km further within the Bonanza Creek Long Term Ecological Research Forest outside Fairbanks, AK. This site is in the discontinuous permafrost zone, meaning that permafrost underlies 50-90% of the landscape. The MAAT of this region is consistently below 0 °C[2] and has colder and more stable permafrost than Brown's Lake Bog.

1.2 Dissertation Overview

Using high-resolution soil temperature profilers and various environmental observations, **Chapter 2** explores the environmental controls on permafrost thaw at a site at the southern fringe of the permafrost zone. This study aims to understand better the impact of rain and other factors, such as snow depth, canopy cover, and microtopography on permafrost thaw. The site contains ecosystem-protected permafrost, which persists in unfavorable climates due to favorable ecologic conditions. The state of ecosystem-protected permafrost acts as a forecaster of future permafrost dynamics at more northern sites as the permafrost zone continues to become warmer and wetter. This study highlights the importance of microtopography, canopy cover, and advective heat transport by rain on permafrost thaw in the ecosystem-protected permafrost zone. This chapter has been previously published as:

Eklof J F, Jones B M, Dafflon B, Devoie É G, Ring K M, English M E, Waldrop M P and Neumann R B 2024 Canopy cover and microtopography control precipitation-enhanced thaw of ecosystem-protected permafrost Environ. Res. Lett. 19 044055 https://doi.org/10.1088/1748-9326/ad31d7

The data supporting this study's findings are openly available at the following URL/DOI: https://doi.org/10.15485/2204548.

Chapter 3 explores the environmental controls on permafrost spatial and temporal variability at a well-studied discontinuous permafrost site in the Interior of Alaska. While many environmental variables controlling soil thermal regimes and permafrost progression are well understood individually, interactions between these variables and how these interactions control permafrost and soil thermal metrics are less understood. We installed high-resolution temperature profilers and collected environmental along a 210-meter transect to investigate these interactions. This transect spans diverse environmental conditions and captures a range of thermal regimes. This transect spanned the distance between a wetland complex and the upland mixed-forest plateau terminus. This study highlights the importance of wetland proximity, slope-induced changes to soil moisture and thermal conductivity, and the complexities of meteorological forcing on soil thermal regimes.

Chapter 4 uses a wide range of environmental instrumentation and observations, in combination with on-site eddy covariance tower data, to understand the impact of the surrounding permafrost underlain watershed on methane emissions from a bog complex in the Interior of Alaska. A prior study by Neumann et al. highlighted the ability of hydrologic inputs of the permafrost plateau to enhance methane emissions. However, there was insufficient data to mechanistically understand the processes involved. To fill this gap in understanding, we explicitly tracked water, energy, and nutrient movement across the permafrost plateau and into the bog complex. This study highlights the critical and

unconsidered role of advectively transported nutrients from the surrounding watershed in governing bog methane emissions.

Chapter 5 summarizes the dissertation and discusses the implications of research findings for the future of the permafrost zone. Additionally, I provide final thoughts on the role of permafrost systems in the greater narrative of climate change and global warming.

2 Chapter 2: Canopy Cover and Microtopography Control Precipitation-Enhanced Thaw of Ecosystem-Protected Permafrost

2.1 Introduction

Permafrost covers approximately 24% of the terrestrial landscape of the Northern Hemisphere[2]. Atmospheric temperatures in the Northern Hemisphere have warmed faster than the global average, and this amplified warming is expected to strengthen in the future[28]. Permafrost trends are consistent with atmospheric temperature trends, with widespread warming observed since 1980[4]. However, other environmental factors, such as vegetation, soil properties, hydrology, topography, local climate, and snow, also regulate permafrost temperature and thaw progression[4,16,29–33].

Rainfall is one such environmental factor that contributes to permafrost dynamics. Rainfall can accelerate permafrost thaw through advective heat transport[34–40] and by increasing soil thermal conductivity[41–43], but rain can also slow thaw since wetter soils require more energy to warm due to greater heat capacity[41,43–45] and experience increased evaporative cooling [46]. Northern high-latitude precipitation is expected to increase[47,48], which may enhance the role of rain in permafrost progression.

We hypothesize that ecosystem-protected permafrost, the warmest and most vulnerable of the permafrost classes, will be most sensitive to these changes. Ecosystem-protected permafrost is located in regions with a mean annual air temperature (MAAT) above 0 °C, where permafrost persists in unfavorable climates due to favorable ecologic conditions[16]. Understanding how ecosystem-protected permafrost degrades is crucial because ecosystem-protected permafrost acts as a forecaster and predictor of future thaw in increasingly climatically similar, more northern latitudes[49]. Degradational features such as taliks are common in these warm permafrost systems[35,36,50]. Taliks are layers of year-round unfrozen ground that have been shown to enhance permafrost thaw. One potential mechanism is the enhancement of advective heat transport with rain by providing subsurface lateral flow paths for runoff[35,36,38].

To better understand the impact of rain, as well as other environmental factors affecting permafrost in the ecosystem-protected zone, we instrumented a rapidly degrading permafrost plateau in south-central Alaska with high-resolution soil temperature sensors and measured environmental variables, including canopy cover, snow, and microtopography. Our study occurred from 2019 to 2022 and contained the wettest and snowiest years since 2015.

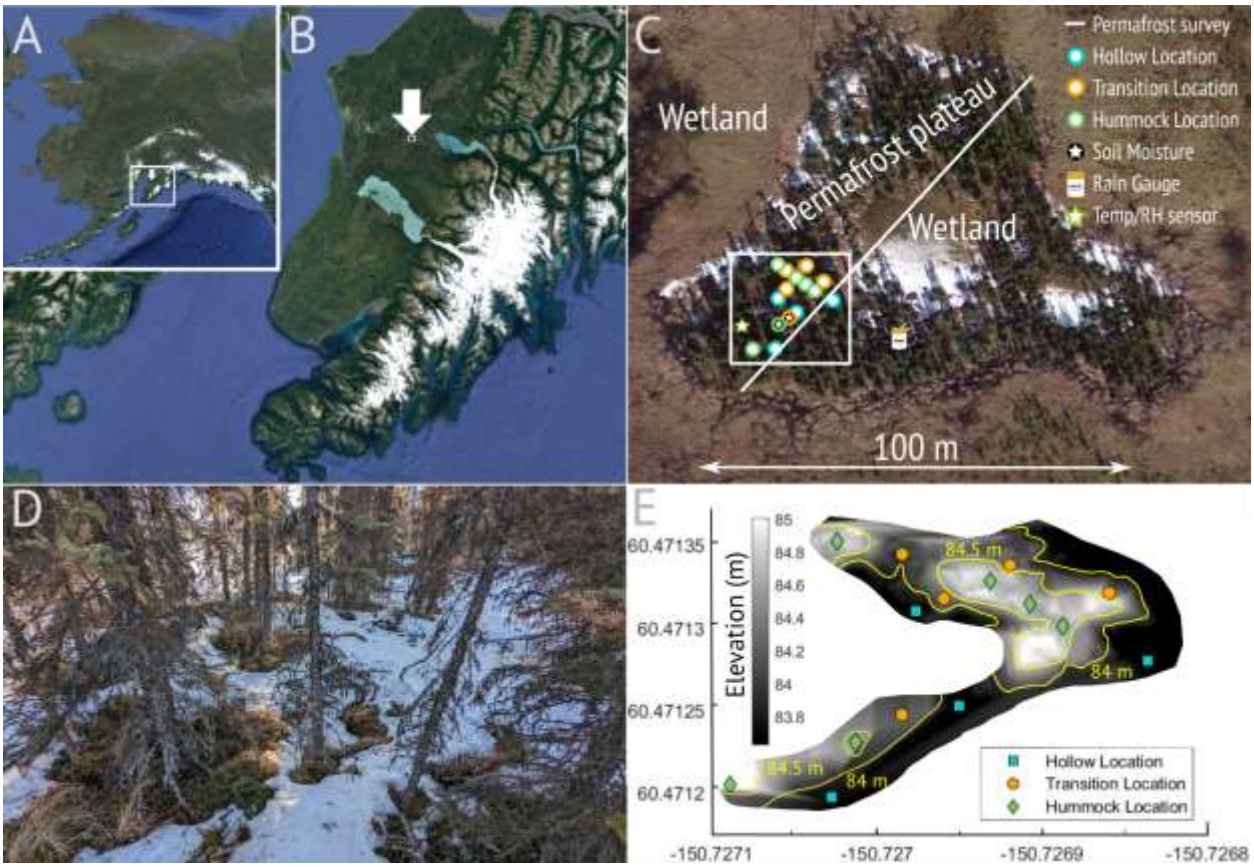

Figure 2.1 Site Overview. *(A) Alaska map with an inset of the Kenai Peninsula shown in panel B. (B) Kenai Peninsula map with an arrow indicating an inset of the site location shown in panel C. (C) A Google Earth image of site with an inset of our core instrumentation area shown in panel E. Instrumented high-elevation (hummock) locations are green, mid-elevation (transition) locations are orange, and low-elevation (hollow) locations are light blue. Wetland and permafrost areas, along with rain gauge, temperature/RH sensor, and two soil moisture sensor locations, are labeled. The across-site permafrost transect is shown as a white line. (D) A field photo of plateau topography and snow cover heterogeneity. (E) A digital elevation model of our core instrumentation area. Shapes denote the instrumented locations shown in the inset of panel C. Names, and locations of individual DTPs are shown in Figure 0.4.*

2.2 Methods

2.2.1 Site Description

The site is located in the western Kenai Peninsula lowlands (60.47 °N, -150.73 °W) (**Error! Reference source not found.**A, B) within the Kenai National Wildlife Refuge (permit: 2018-Res-RBNeumann-6276). Fieldwork took place from May 2019 to September 2022. The plateau is surrounded by and contains wetland features (**Error! Reference source not found.**C) and experiences a semi-continental climate due to Cook Inlet to the northwest, Kachemak Bay to the south, and its location within the rain shadow of the Kenai mountains to the east. Plateau and wetland soil is peat-dominated to 3-meter depth[27]. In 2015, the average seasonally frozen ground thickness was 45 cm, which overlayed continuous

taliks[27]. The average depth of permafrost measured in 2015 was 1.37 cm, with an average permafrost thickness of 5.61 m[27]. Black spruce trees (*Picea mariana*) grow on the most elevated sections (hummocks) of the permafrost plateau (**Error! Reference source not found.**D). Plateau lowland areas (hollows) contain no live trees.

2.2.2 Soil Temperature Measurements

Soil temperatures were measured using 160 cm long Distributed Temperature Profilers (DTPs) with sensors every 10 cm[51] installed in August 2020. DTPs have an accuracy of ± 0.05 °C and a 15-minute measurement interval. Data were depth-corrected annually for frost heave and subsidence and linearly interpolated for location-to-location consistency.

2.2.3 Geospatial Measurements and Relative-Elevations

A digital elevation model was created in MATLAB (R2022b) using 1620 real-time kinematic points recorded using Emlid Reach RS2 units in November 2020 (**Error! Reference source not found.**E). Relative-elevations were determined by comparing DTP elevations to the average elevation of the surrounding 5-meter radius area. Relative-elevations were used to define locations as a hummock, transition, or hollow (**Error! Reference source not found.**C, E). Hummock locations were > 0.2 m above, transition locations were between 0.2 m above and 0.1 m below, and hollow locations were > 0.1 m below their surroundings (**Error! Reference source not found.**E).

2.2.4 Meteorological Measurements and Data

Precipitation was measured with an annually calibrated HOBO Rain Gauge installed in April 2019 in a 5-meter clearing. Air temperature was recorded with a HOBO Temperature/RH Logger installed in April 2019 using dense black spruce as a radiation shield[52]. Data were gap-filled using two National Weather Service stations, COCOAKKP7 and COOPKEYA2, located within 6 km[53]. Air temperature and precipitation data from 2015 to 2019 were sourced from interagency weather station SDFA2, located 16 km west. Trends in SDFA2 data were consistent with in situ meteorological measurements recorded during the study period. Snow depth was measured with an avalanche probe in March 2022. Snow water equivalent data were sourced from the Moose Pen SNOTEL site 32 km northeast[54]. Cumulative shortwave radiation was calculated using HPEval, a MATLAB-based software tool that uses high-resolution hemispherical photos to estimate shortwave radiation below the forest canopy[55].

2.2.5 Hydrologic Measurements

In-Situ pressure transducers and barometer were deployed in fully-screened PVC wells annually from May to September (2019-2022). Sensor data were verified with manual groundwater measurements taken 2-3 times annually between May and September with a Solinst Water Level Meter. Soil moisture was measured continuously from the surface to

the permafrost table at one hummock (90 cm length sensor) and one transition (120 cm length sensor) location (**Figure 2.1**C) using GroPoint Multi-Depth Soil Moisture Sensors attached to GroPoint Data Loggers installed in August 2020. Profilers measured a composite value of percent water every 15 cm along the length of the sensor at a 30-minute interval. Outputs were calibrated for peat soils[56], and a manufacturer-provided dielectric correction (1.019) was applied for ≤0°C soils.

2.2.6 Thermal Conductivity Modeling

Soil thermal conductivity was estimated using a physically-based model[57] that used the degree of saturation, dry thermal conductivity, and wet thermal conductivity as inputs. The degree of saturation was calculated by normalizing the measured water content by the highest observed water content, 96.7%. Dry and wet thermal conductivities were estimated through weighted averages of the thermal conductivities of air (0.025 W/m·K), water (0.579 W/m·K at 10 °C), and organic matter (~0.074 W/m·K). Dry thermal conductivity (0.027 W/m·K) assumed 96.7% air and 3.3% organic matter. Wet thermal conductivity (0.562 W/m·K) assumed 96.7% water and 3.3% organic matter. We calculated thermal conductivities for ≤0°C soils, assuming no ice content and maximum possible ice content. Maximum ice content was estimated as the difference between the measurement location's current and the highest observed water content. The thermal conductivity of 0 °C ice is 2.22 W/m·K.

2.2.7 Canopy Measurements

The canopy cover percentage was determined through image analysis of upward-facing smartphone photos taken with a Moment 14 mm fisheye lens one meter above the soil surface in July 2022. Photos were analyzed in ImageJ by cropping the photo into a circle, splitting the photo into color panes, thresholding the blue pane into sky and vegetation pixels, and calculating percent cover from the relative proportion of pixels[58].

2.2.8 Depth to Frost Table Measurements

Permafrost table depth was estimated annually through manual probing. Probe length was 2.2 m from 2019-2021 and extended to 3.1 m in 2022. Measurements took place annually in mid-September. DTP location probing included four replicates within a 30 cm radius. Across-site transect (**Error! Reference source not found.**C) probing included three r eplicates, mimicking the methods and locations of Jones et al.[27].

2.2.9 Statistical Methods

Environmental variables and thermal response metrics were compared for hummock, transition, and hollow locations using one-way ANOVA followed by Tukey HSD post-hoc using $\alpha = 0.05$. Data were $\log_{10}$ transformed to increase normality and reduce skew before ANOVA analysis. Data presented in the figures are shown in non-transformed space for

visual clarity. Correlations were determined by fitting data with a linear regression model and using two-sided hypothesis testing with α = 0.05.

2.3 Results

2.3.1 Site Meteorological Conditions

From 2015 to 2022, MAAT was +3.3 °C with a mean annual precipitation of 480 mm [53]. From 2020 to 2022, the site experienced the three snowiest years (A) and the second, third, and fourth wettest years (**Figure 2.2**B) since 2015. Average air temperature did not vary significantly (**Figure 0.1**). Three large warm-season rain events, defined as events with > 50 mm of rain over two weeks, took place during our study in July 2020 (58 mm), July 2021 (54 mm), and July 2022 (77 mm) (**Figure 2.2**B i, ii). The July 2020 event occurred before site DTPs and soil moisture profilers were installed. Therefore, it is not included in further analyses.

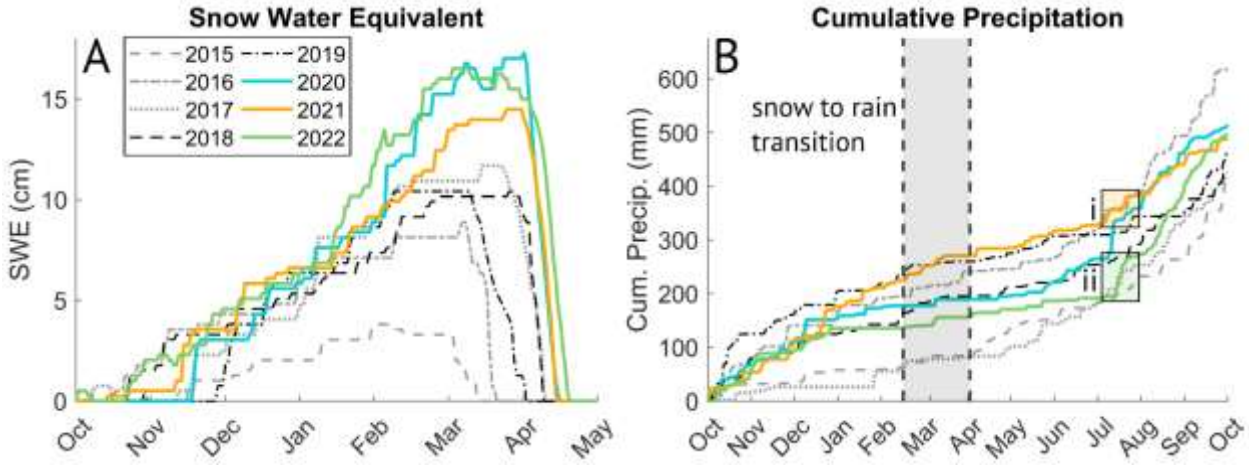

Figure 2.2 Meteorological forcing from 2015 to 2022*. Line graphs show stacked annual time series of (A) snow water equivalent and (B) cumulative precipitation. Data for 2020 is blue, 2021 is orange, and 2022 is green. Data from 2015-2019 are gray or black with varied line styles. The snow-to-rain transition period is shown as a gray box in Panel B. Black-bordered orange (i) and green (ii) boxes in Panel B show periods of intense rain during July 2021 and 2022, respectively.*

2.3.2 Permafrost Degradation Along the Across-Site Transect

Permafrost thaw rates accelerated during the study period (2020-2022) relative to preceding years (2015-2020). In the time between depth to permafrost measurements by Jones et al.[27] in 2015 and our measurements in 2020, the permafrost table along the across-site transect (**Figure 2.1**C) deepened 32 ± 25 cm, or 6 ± 5 cm/year, on average (**Figure 2.3**). Between 2020 and 2022, the permafrost table deepened 112 ± 37 cm or 56 ± 18 cm/year (**Figure 2.3**), a nine-fold increase in annual thaw rate compared to 2015-2020. Documented thaw occurred below the base of the seasonally frozen layer, expanding existing taliks.

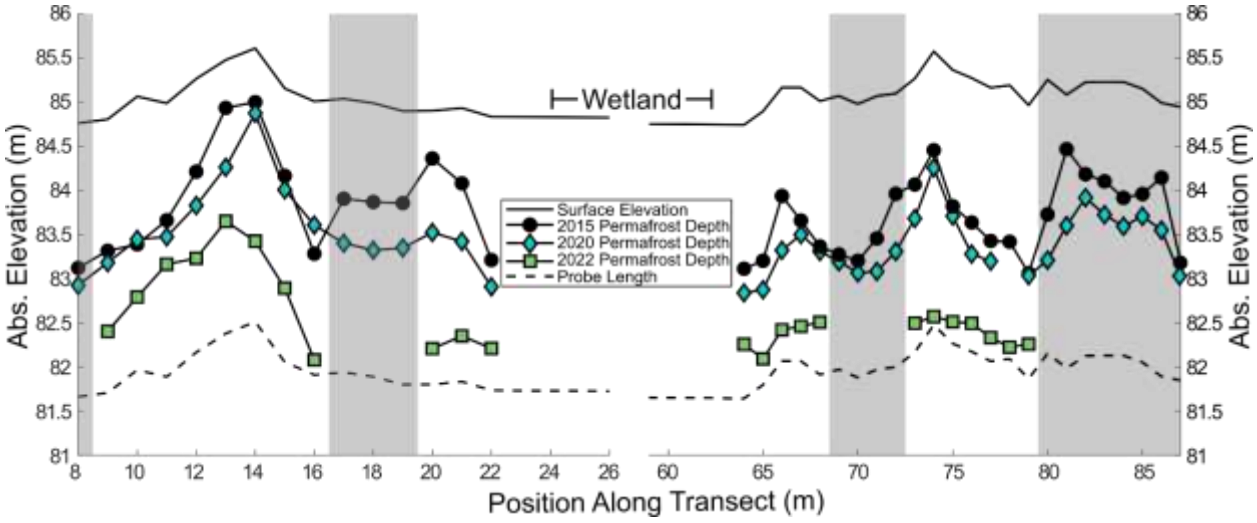

Figure 2.3 Permafrost thaw along the across-site transect shown in Figure 2.1C. *Depths to the permafrost table measured in 2015 by Jones et al.[27] are shown as black circles. Our measurements from September 2020 and September 2022 are blue diamonds and green squares, respectively. Surface elevation is marked with a thin, solid black line based on data from Jones et al.[27]. Maximum probe depth is marked with a dashed black line. Gray vertical bars label locations with permafrost deeper than our 3.1 m probe in 2022. Wetland locations are labeled.*

2.3.3 Environmental Variables Within Microtopographic Groups

Five were categorized as hummock, four as hollow, and six as transition locations among fourteen instrumented locations. The three groups had significantly different relative-elevations (**Figure 2.4**A, $p < 0.001$). The average canopy cover of hummock, transition, and hollow locations was 77 ± 7%, 65 ± 14%, and 58 ± 7%, respectively. Percent coverage statistically differed between hummock and hollow locations (**Figure 2.4**B, $p < 0.05$). The average snow depth of hummock, transition, and hollow locations was 8 ±10 cm, 18 ±13 cm, and 35 ±12 cm, respectively. Snow depth was only statistically different between hummock and hollow locations (**Figure 2.4**C, $p < 0.05$). Shortwave radiation and moss depth did not significantly differ among groups (SI Fig. S2). Snow depth had significant negative correlations with relative-elevation (**Figure 2.4**D, $p < 0.05$) and canopy cover

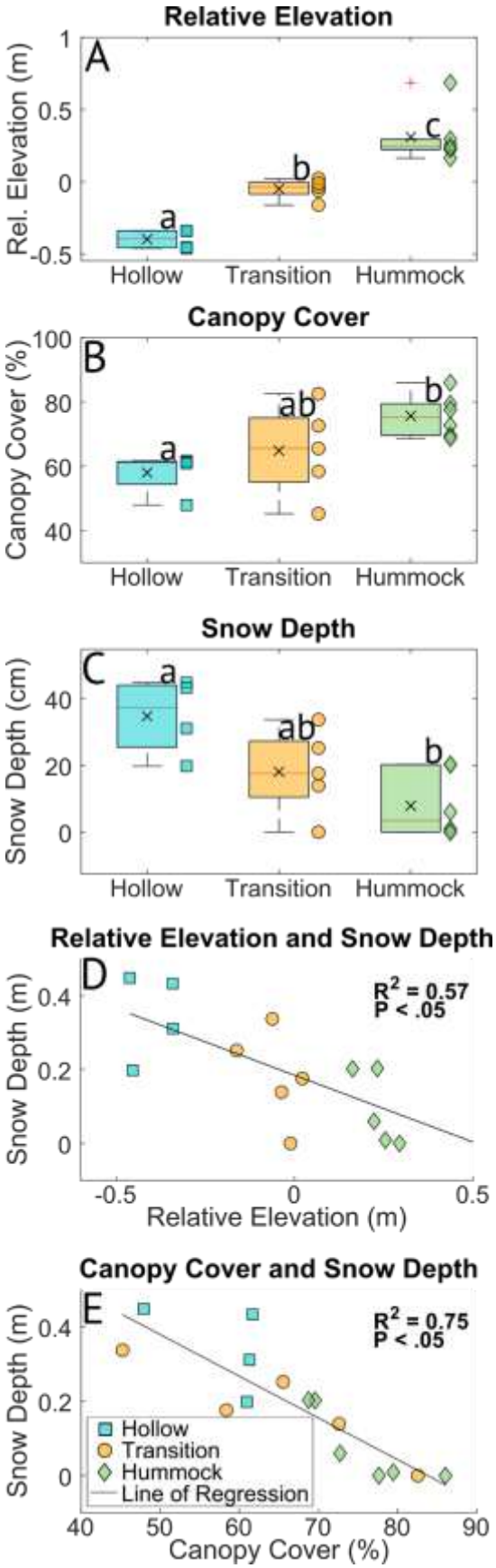

(**Figure 2.4**E, $p < 0.05$). Canopy cover and relative-elevation were significantly correlated (**Figure 0.2**).

Figure 2.4 Environmental variables across the site. *(A-C) Box and whisker plots showing: (A) relative-elevation of sensor locations, (B) canopy percentage, and (C) snow depth. On each box plot, the central line indicates the median, "x" marks the mean, edges of the box indicate the 25th and 75th percentiles, whiskers indicate the most extreme non-outlier data points, and a red plus marker indicates an outlier greater than 2.7 standard deviations from the mean. Letters on top of boxes indicate data sets with statistically significant differences in mean as determined through one-way ANOVA. (D-E) Scatter plots showing: (D) snow depth versus relative-elevation and (E) snow depth versus canopy cover.*

2.3.4 Permafrost and Subsurface Temperature Regimes within Microtopographic Groups

Hummock locations had significantly shallower depths to the permafrost table (**Figure 2.5**A, $p < 0.001$) and significantly slower rates of annual permafrost thaw (**Figure 2.5**B, $p < 0.05$) than transition and hollow locations. In 2022, the average depth to permafrost at hummock locations was 97± 39 cm compared to 252 ± 53 cm and 288 ±15 cm at transition and hollow locations, respectively. Average annual thaw rates between 2020 and 2022 at hummock locations were 8±9 cm/year compared to 39 ±13 cm/year and 44 ± 6 cm/year at transition and hollow locations, respectively.

At a depth of 10 cm, cold-season soil temperatures of hummock locations were significantly colder (-3.5±1.7°C) than hollow locations (-0.6 ± 0.4 °C), while transition locations (-1.7 ± 1.1 °C) were statistically indistinguishable from either group (**Figure 2.5**C, $p < 0.05$). A comparison depth of 10 cm was chosen to

maximize sensitivity to surface-atmosphere interactions while avoiding diel temperature oscillations. In hummock and transition locations, freezing temperatures (-0.05°C) reached significantly deeper depths of 28±11 cm and 20±11 cm, respectively, than in hollow locations where -0.05°C reached a depth of 3±6 cm (Fig. 5E, $p<0.001$). A threshold of -0.05 °C was used to track the extent of freezing since DTPs have a confidence interval of ±0.05 °C.

Hummock locations were significantly cooler (5.2 ± 1.7 °C) than hollows (9.1 ± 0.7 °C) during the warm-season at 10 cm depth, while temperatures at transition locations (7.9 ± 0.4 °C) were statistically indistinguishable from either group (**Figure 2.5**D, $p<0.05$). In hummock locations, warm temperatures (+3 °C) only reached a depth of 20 ± 17 cm, while in transition and hollow locations, warm temperatures reached depths of 69 ± 33 cm and 101±9 cm, respectively. The warming depth in hummock locations was significantly shallower than in transition and hollow locations (**Figure 2.5**F, $p < 0.05$). A threshold of +3 °C was the warmest temperature that did not penetrate beyond the 160 cm sensor length.

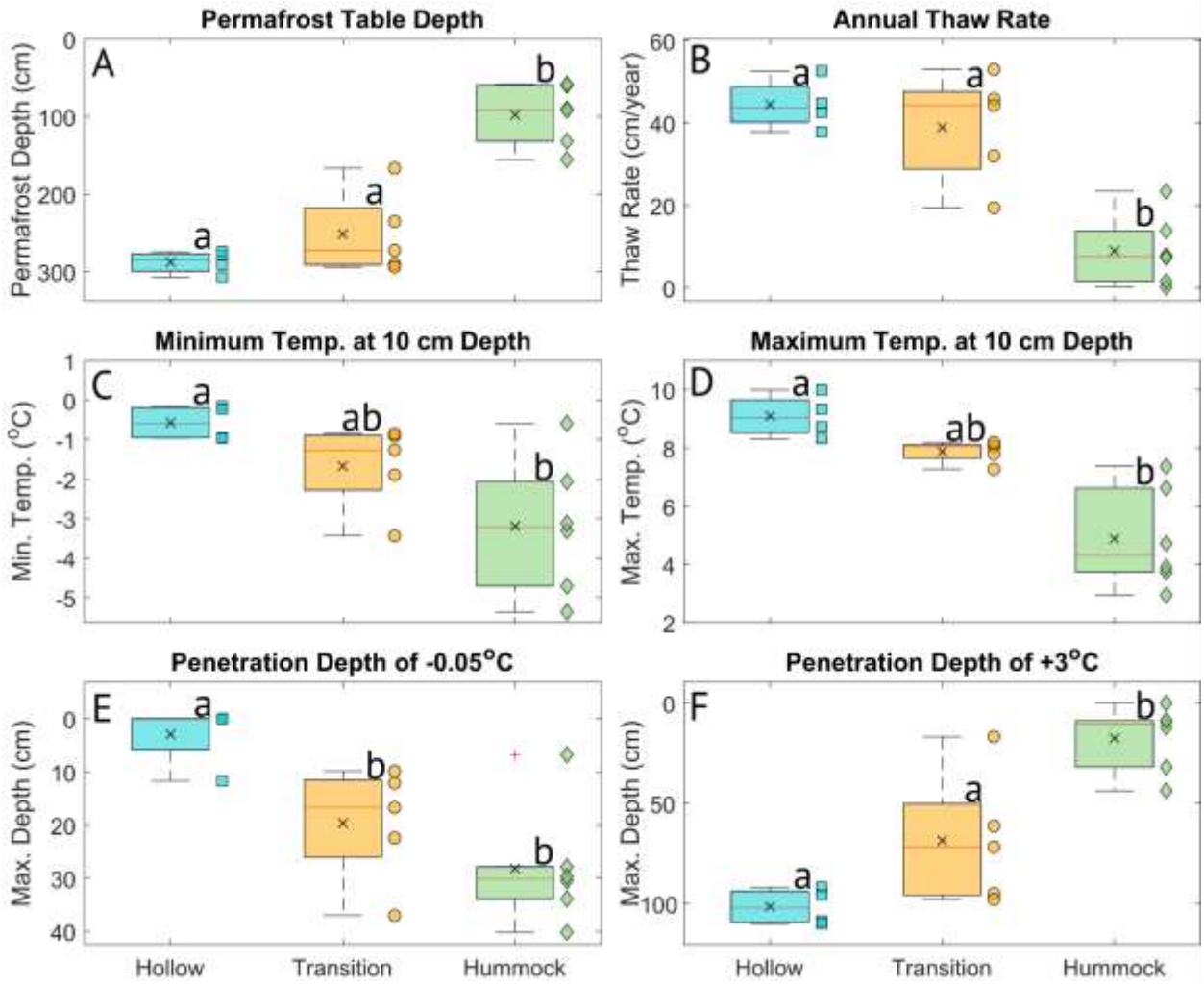

Figure 2.5 Permafrost progression and thermal metrics among relative-elevation groups. *Box and whisker plots showing: (A) Depth to the permafrost table measured on September 9, 2022, (B) average annual deepening of the permafrost table between 2020 and 2022, (C) minimum and (D) maximum temperature reached at a depth of 10 cm between 2020 to 2022, (E, F) maximum penetration of (E) -0.5 °C and (F) +3 °C. Boxplot statistics are described in Figure 2.4.*

2.3.5 Thermal and Hydrologic Responses to Large Rain Events

Large rain events (> 50 mm) occurred in July 2021 and 2022 (**Figure 2.2**B). During these events, a greater thickness of the soil column at transition locations warmed from ≤ 0 °C to above-freezing temperatures than at hummock or hollow locations in both 2021 (**Figure 2.6**A, $p < 0.01$) and 2022 (**Figure 2.6**B, $p < 0.01$). During the 2021 rain event, an average of 107 ± 20 cm of soil within transition locations warmed from ≤ 0 °C to > 0 °C compared to 31 ± 42 cm and 6 ± 4 cm of soil in hollow and hummock locations, respectively (**Figure 2.6**A). A similar thickness of transition soil warmed from ≤ 0 °C to > 0 °C during the 2022 rain event, 106 ± 14 cm, compared to < 1 cm and 10 ± 1 cm of soil in hollow and hummock locations, respectively (**Figure 2.6**B). The observed thickness of transition-location warming and thaw that occurred during both rain events (106 cm,107 cm) included over 40% of total above-permafrost soil during both years (252 ± 53 cm) (Fig. **Figure 2.5**A, **Figure 2.6**). Smaller warm-season rain events did not cause notable warming.

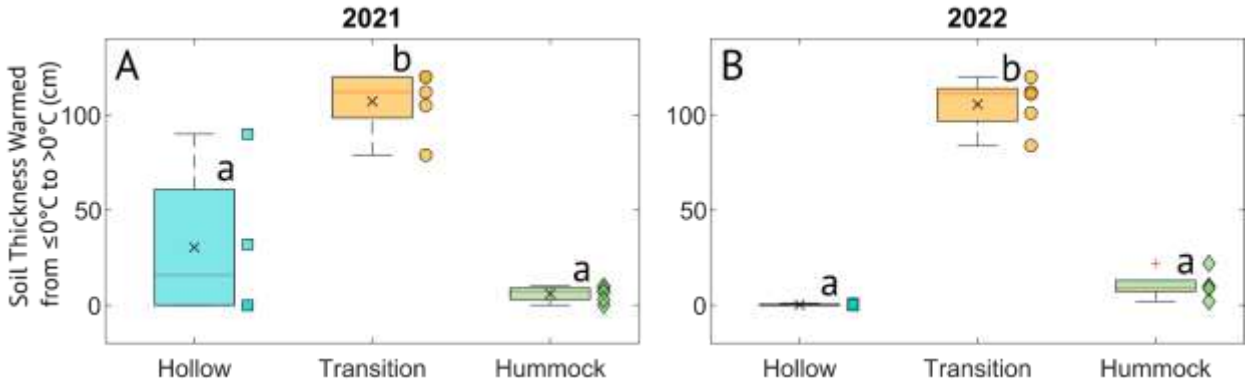

Figure 2.6 Thermal response to rain among microtopographic groups. *Box and whisker plots showing: (A, B) soil profile thickness of hollow, transition, and hummock locations that warmed from ≤ 0 °C to above-freezing temperatures from one week before the largest rain event of the year to one week after the conclusion of the rain event in (A) 2021 and (B) 2022. Boxplot statistics are described in Figure 2.4.*

Figure 7 shows the soil thermal impact of the 2021 rain event on example locations from each microtopographic group. Hummock and hollow locations experienced short-term perturbations in soil temperature, where temperatures briefly warmed and then returned to near-linear rates of seasonal warming (**Figure 2.7**B, E). At transition location #1, soil temperatures between 40-140 cm increased from 0 °C to < 1 °C positive temperatures while soils at 20-30 cm depths remained ≤ 0 °C (**Figure 2.7**C). Transition location #2 had a greater response than transition location #1. Soils between 20-120 cm depth at transition location #2 warmed from ≤ 0 °C to 1-4 °C (**Figure 2.7**D). Transition location #2 had a greater

proportion of higher elevation area surrounding it than transition location #1. In the context of hydrologic flow, the proportion of surrounding higher elevation area can be thought of as the ratio of the area contributing recharge to lower elevations ($Area_C$) to the area receiving recharge ($Area_R$). Transition location #1 had 2 m^2 of contributing area per 1 m^2 of receiving area, leading to an $Area_C$: $Area_R$ ratio of 2:1, while transition location #2 had 6 m^2 of contributing area per 1 m^2 of receiving area, leading to an $Area_C$: $Area_R$ ratio of 6:1. Observed responses were similar in 2022 (**Figure 0.3**).

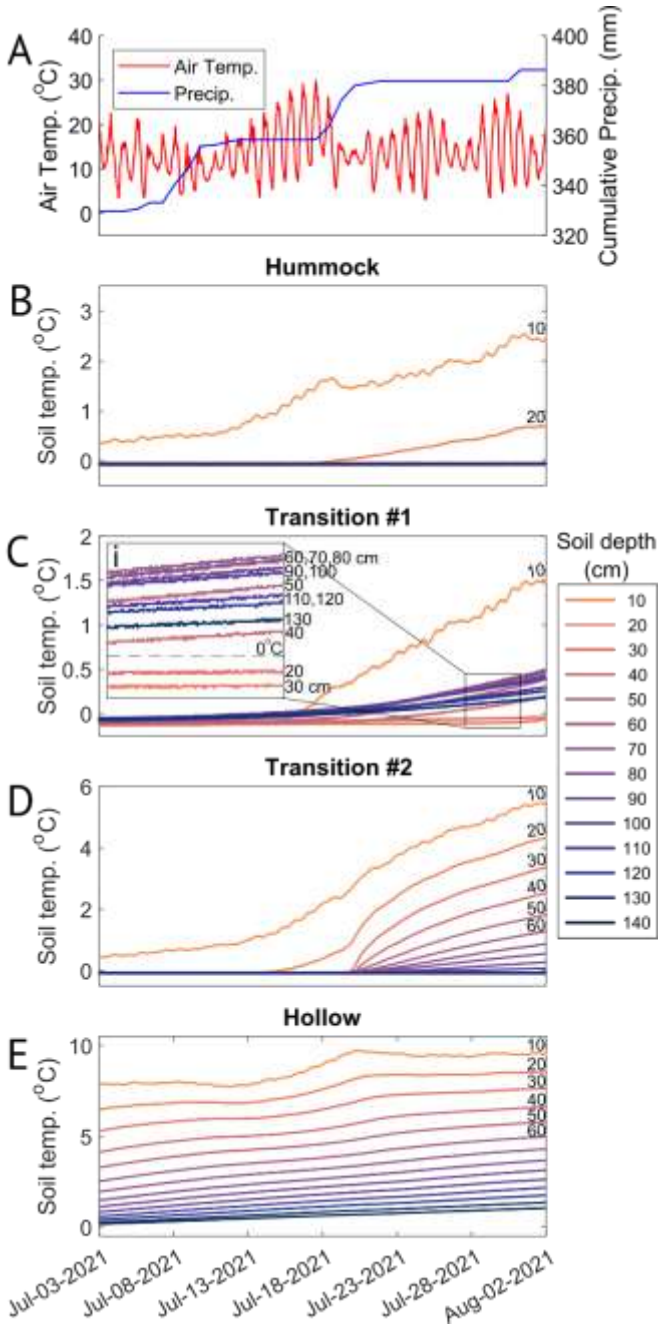

Figure 2.7 Soil temperature responses to the rain event in July 2021. *(A) Air temperature (red, left axis) and cumulative precipitation (blue, right axis). (B-E) Soil temperature at depths from 10 to 140 cm below the soil surface (depths are labeled on the figure and colored according to the legend) for (B) hummock location, (C) transition location #1 with zoomed inset (i), (D) transition location #2, and (E) hollow location. The hummock location and transition location #1 were instrumented with soil moisture sensors, see Figure 2.8. Y-axis scales vary by location.*

Near-surface (top 10 cm) soil water content of the instrumented hummock location decreased by 0.1 ± 5.0% (< 1% change) during the 5.4 cm rain event in 2021 and increased by 9.1 ± 5.5% (29% change) during the 7.7 cm rain event in 2022 (**Figure 2.8**A, **Table 2.1**). The near-surface water content of the instrumented transition location increased by 0.7 ± 5.8% (2% change) and 3.5 ± 4.4% (9% change) during the 2021 and 2022 rain events, respectively (**Figure 2.8**B, **Table 2.1**). In the hollow locations, the water table moved closer to the land surface by 12.6 ± 3.2 cm (60% change) and 12.8±2.1 cm (62% change) on average during the two rain events (**Figure 2.8**C, **Table 2.1**).

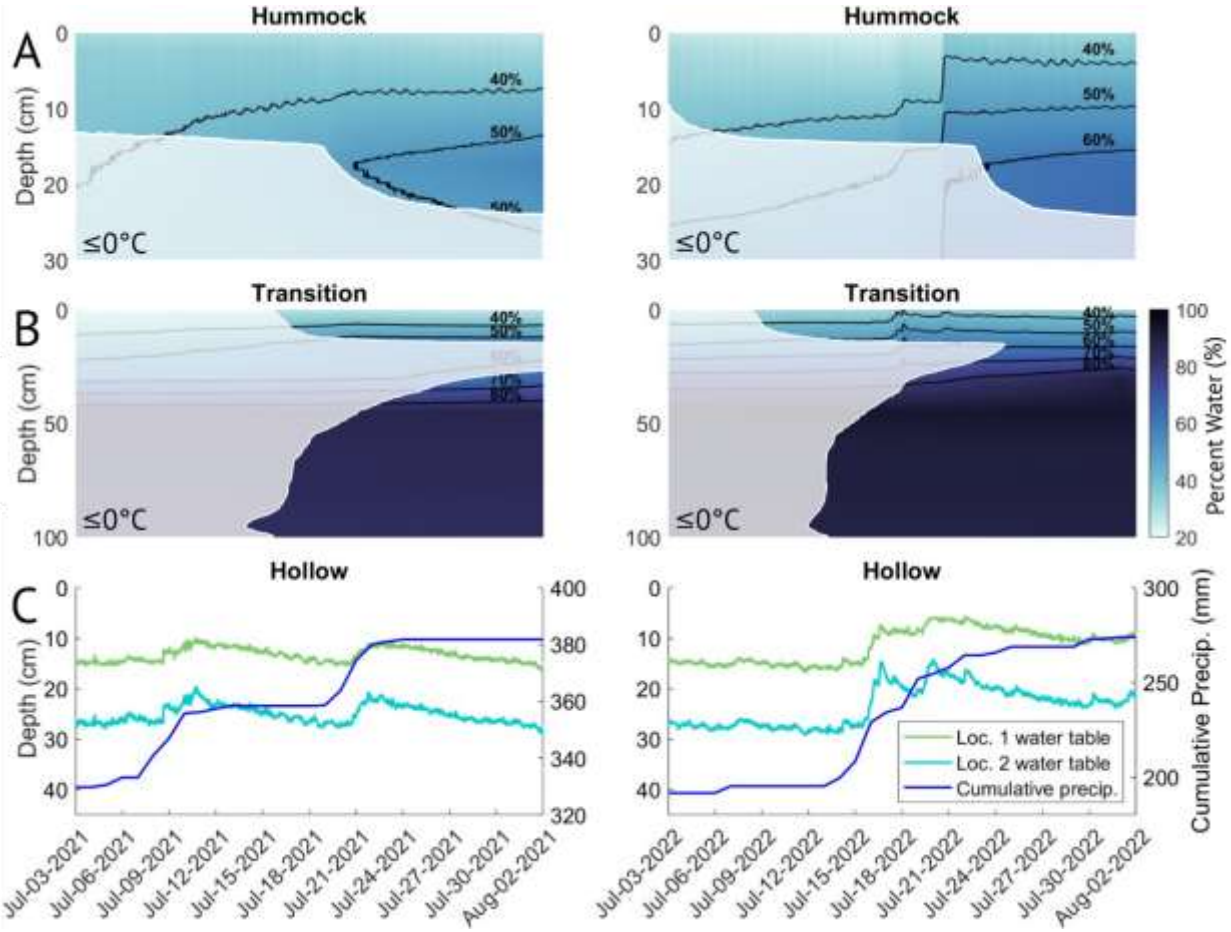

Figure 2.8 Hydrologic response to rain events in July 2021 (left column) and July 2022 (right column). *Colormap plots show soil moisture as percent water for: (A) hummock location and (B) transition location, which are the hummock and Transition #1 locations in Figure 2.7B, C. Areas with a transparent white mask have a soil temperature of ≤ 0 °C. (C) Water table depth of two hollow locations (green and light blue, left axis) and cumulative precipitation (dark blue, right axis). Y-axis scales vary by location.*

Before the rain events, the hummock location had an estimated thermal conductivity of 0.265 ± 0.044 W/m·K in 2021 and 0.244 ± 0.053 W/m·K in 2022 (**Table 2.1**). Estimated pre-event thermal conductivity for the transition location ranged from 0.263 to 0.627 W/m·K and 0.287 to 0.556 W/m·K in 2021 and 2022, respectively (**Table 2.1**). This range was due to uncertainty associated with ice content (see **2.2.6**). Soil moisture was not logged at hollows, so thermal conductivity could not be calculated. Due to presumably high soil moisture, hollow locations likely had greater near-surface thermal conductivity than transition or hummock locations.

Event Timing	Hollow WT Depth (cm)	Transition θ (% water)	Hummock θ (% water)	Transition λ (W/m·K)	Hummock λ (W/m·K)
Pre-2021 Event	21.1 ± 8.8	34.6 ± 3.1	35.0 ± 2.2	0.263 to 0.627	0.265 ± 0.044
Post-2021 Event	14.6 ± 6.8	35.3 ± 5.8	34.9 ± 5.0	0.267 ± 0.071	0.265 ± 0.065
2021 Event Change	12.6 ± 3.2 (60% shallower)	0.7 (2%)	-0.1 (0%)	-0.360 (-57%) to 0.004 (1%)	-0.001 (0%)
Pre-2022 Event	20.6 ± 8.7	38.7 ± 3.6	31.4 ± 3.4	0.287 to 0.556	0.244 ± 0.053
Post-2022 Event	9.8 ± 5.9	42.3 ± 4.4	40.5 ± 5.5	0.307 ± 0.061	0.297 ± 0.069
2022 Event Change	12.8 ± 2.1 (62% shallower)	3.5 (9%)	9.1 (+29%)	-0.249 (-45%) to 0.020 (7%)	0.053 (+22%)

Table 2.1 Average depth to water table (WT), near-surface water content (θ), and near-surface thermal conductivity (λ) in response to July 2021 and 2022 rain events. *Change in depth to the water table is averaged for two hollow locations (see Figure 2.7C). Soil moisture and thermal conductivity values are average values for soil between 0-10 cm from one transition and one hummock location before (July 3) and after (August 2) the rain events in 2021 and 2022 (see Figure 2.7A, B). Thermal conductivity values of soils at ≤ 0 °C are given as a range corresponding to maximum and minimum potential ice content (see 2.2.6). Standard deviations are given for average values.*

2.4 Discussion

2.4.1 Accelerated Thaw Due to Consecutive Rainy and Snowy Years

As noted in the results, our study captured notably wet and snowy years (**Figure 2.2**), accompanied by a nine-fold increase in thaw rates along the across-site transect (**Figure 2.3**), expanding existing taliks. These taliks begin isolated, progress to connected taliks, and mature into flow-through taliks[38]. Flow-through taliks that are hydrologically connected to wetlands often experience enhanced thaw that is nearly irreversible[36,59]. This process could partially explain the thaw observed at the wetland-plateau interface (**Figure 2.3**).

Hummock locations thawed slowly (**Figure 2.5**B) during the study period, while all other locations, including the across-site transect, which contained no hummock locations, thawed rapidly (**Figure 2.3**, **Figure 2.5**B). This outcome emphasizes the stability of hummock locations and the susceptibility of transition and hollow locations to rain and snow (**Figure 2.5**B). Increased thickness of taliks, which likely accompanied permafrost thaw at most site locations, has biogeochemical consequences such as increased methane emissions[60,61], thermal consequences such as greater thaw rates[35,36], and hydrologic consequences including increased connectivity[35,36,38].

It is known that rain and snow accelerate thaw. During three rainy and snowy years like our site experienced, Iijima et al.[34] observed a transition from permafrost stability to thaw (~5 cm/year) at a colder (-8 °C MAAT) discontinuous site. Especially rainy years accelerated observed thaw rates in Interior, AK[37], and rain from a single wet summer increased thaw for multiple years at a Siberian tundra site[62]. Seasonally frozen layer thickness has increased with snow depth in both field[63,64] and modeling[65,66] studies. At our site, locations with greater snow depth (Fig. 4C) thawed more rapidly (Fig. 5B), supporting the notion that snowy conditions between 2020 and 2022 exacerbated permafrost degradation. Composite effects of consecutive wet and snowy years likely contributed to the observed increase in thaw.

2.4.2 Transition Locations Thawed Rapidly Due to Advective Heat Transport by Rain

Over 100 cm of above-permafrost transition soil warmed from ≤ 0 °C to > 0 °C during individual rain events in 2021 and 2022 (**Figure 2.1**, **Figure 2.1**C, D). Two potential mechanisms of rain-induced energy transport could have caused this warming: increased soil thermal conductivity due to increased soil moisture [41–43] and advective heat transport[18,34,37,39,40].

Increased thermal conductivity due to increased soil moisture is not the dominant mechanism. Soil-atmospheric thermal interactions are controlled by near-surface thermal conductivity[67]. Transition-location thermal conductivity likely decreased during the rain

events. Depending on pre-event ice content, the instrumented transition location experienced between a ~57% decrease and ~7% increase in near-surface thermal conductivity (**Table 2.1**). Regardless, there was no evidence of increased top-down warming or thaw during the rain events (**Figure 2.7**C, **Figure 2.8**B). After the 2021 event, near-surface soils at transition location #1 remained ≤ 0 °C while soils from 40-140 cm warmed (**Figure 2.7**C, **Figure 2.8**B). Thus, our data indicates that another mechanism is responsible for the observed warming and thaw at transition locations.

The pattern of warming and thaw indicates advective heat transport as the primary mechanism. Rain temperature, to a first approximation, is the same as air temperature[68]. When rain temperature exceeds soil temperature, rain events can add thermal energy to the soil through thermal conduction, rapidly warming soils[18]. During the large July rain events, the air temperature was substantially warmer than soil temperature at hummock and transition locations and slightly warmer than hollow-location soil (**Figure 2.7**). Transition locations presumably received runoff from surrounding higher-elevation hummocks and released water into lower-elevation hollows. Subsurface runoff increases the energy available for warming and thaw, explaining why transition locations warmed during rain events, but hummocks, which did not receive runoff, did not experience enhanced warming. Once flow-limiting soil ice melted within transition locations, subsurface runoff flowed into taliks, warming deeper soil layers. Hollow locations received runoff, but had warm soils before rain, which minimized the soil-runoff thermal gradient.

Energy contributed by advective heat transport depends on runoff water temperature and volume, while energy needed to warm and thaw soils depends on pre-event soil temperature, water content, and ice content. A key relationship that connects energy contributed to the energy needed in this context is the ratio between the land area contributing runoff (AreaC) and the land area receiving runoff ($Area_R$). The contributing area influences the volume of runoff generated, while the receiving area influences the volume of water and ice that must be warmed and thawed. Transition location #1, which had an $Area_R$: $Area_C$ ratio of 1:2, had a smaller magnitude thermal response to rain (**Figure 2.7**C) than transition location #2 (**Figure 2.7**D), which had a ratio of 1:6. The larger $Area_R$: $Area_C$ ratio of Transition location #2 presumably corresponded with relatively greater runoff volume, and therefore, more energy for warming and thaw.

Figure 2.9 explores the ability of various combinations of these factors to cause the observed warming and thaw, which involved warming 100 cm of soil with 86% water content (**Figure 2.8**B) from 0 °C to 1 °C and melting of an unknown amount of ground ice (SI1.1 Advective Heat Transport Calculation for Figure 2.9, **Figure 2.7**C, D). Since runoff temperature and ice content were unknown quantities, ranges of these values were used as figure axes (**Figure 2.9**). The runoff temperature was constrained between 0 °C and the average air temperature during the event, 15 °C. At the site, $Area_R$: $Area_C$ varied from 1:2 to 1:6, depending on the transition location. The average $Area_R$: $Area_C$ scenario (1:4) is

presented as a solid line in **Figure 2.9**, with the maximum and minimum scenarios, 1:6 and 1:2, respectively, represented by dashed lines. Along each scenario line, energy in subsurface runoff equals energy required for the observed warming and thaw. Above each line, there is a surplus of runoff energy. Below each line, there is insufficient energy to cause the observed warming and thaw. In the orange figure section, all $Area_R$: $Area_C$ scenarios had excess energy. In the blue section, some scenarios had excess energy while others had insufficient energy. In the green section, all scenarios had insufficient energy. See SI1.1 Advective Heat Transport Calculation for Figure 2.9 for a full calculation description.

Figure areas along and above each scenario line in **Figure 2.9** confirm that energy in rain-induced subsurface runoff was sufficient to cause the observed warming and thaw, but only if the average ground ice content was low. Using an average $Area_R$: $Area_C$ ratio of 1:4 and an estimated runoff temperature of 7.5 °C, our analysis suggests sufficient energy to warm 100 cm of soil from 0 °C to 1 °C and melt 1.5% of average ground ice. Since all above-permafrost soil except the ~45 cm seasonally frozen layer is ice-free talik [27], ice content is not homogenously distributed but concentrated in the top 45 cm of the soil profile. With this ice distribution, energy from the 1:4 scenario and 7.5 °C runoff temperature was sufficient to melt 3.3% of seasonally frozen layer ice content. The highest observed $Area_R$: $Area_C$ ratio, 1:6, had sufficient energy to melt up to 6% of seasonally frozen layer ice content. Runoff temperature was estimated as 7.5 ± 5 °C by mass averaging 1 °C hummock soil water and 15 °C rainwater. Since rain-enhanced thaw depends on runoff, small rain events are not expected to cause notable warming and thaw. To create large-scale advective heat transport, rain events must be sufficiently large to offset losses from evapotranspiration and add sufficient moisture to reach the point of free drainage.

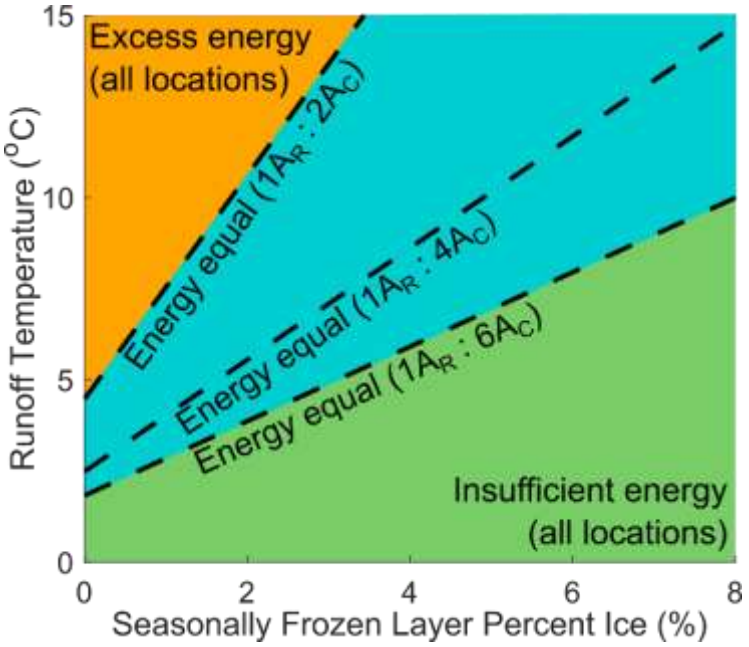

Figure 2.9 Energy analysis of rain-induced warming and thaw. *Dashed black lines mark where the energy stored in runoff is equal to the energy needed to warm and thaw transition-location soil to 1 °C for ratios of soil area receiving runoff ($Area_R$) to soil area contributing runoff ($Area_C$) of 1:2, 1:4, and 1:6. Below each line, the observed amount of warming is not possible with energy solely from runoff. Above each line, there is a surplus of energy. In the orange region, all scenarios have excess runoff energy. In the green region, there is insufficient energy to cause the observed warming and thaw. In the blue region, some scenarios have sufficient energy while others have insufficient energy based on ratios of soil area receiving runoff ($Area_R$) to soil area contributing runoff ($Area_C$). The x-axis is the percent ice contained in the seasonally frozen layer of transition-location soil. The y-axis is the temperature of runoff as it reaches the transition location. This analysis assumes a homogeneous soil profile. The full analysis is shown in SI1.1 Advective Heat Transport Calculation for Figure 2.9.*

Multiple field and modeling studies have highlighted the ability of rain to enhance warming and thaw[34–39,62], while others have reported a minimal (or cooling) impact[46,69]. The ability of a single rain event to cause soil warming through advective heat transport has been shown in a wetland environment[18]. Our study highlights the impact of a single rain event on the warming and thaw of a warm permafrost plateau containing taliks. Transition locations, which our results indicate are vulnerable to the thermal inputs from rain, are highlighted in deep red and labeled as "Rain Enhanced Thaw" in **Figure 2.10**, which presents a conceptual overview of factors affecting permafrost thaw at our site.

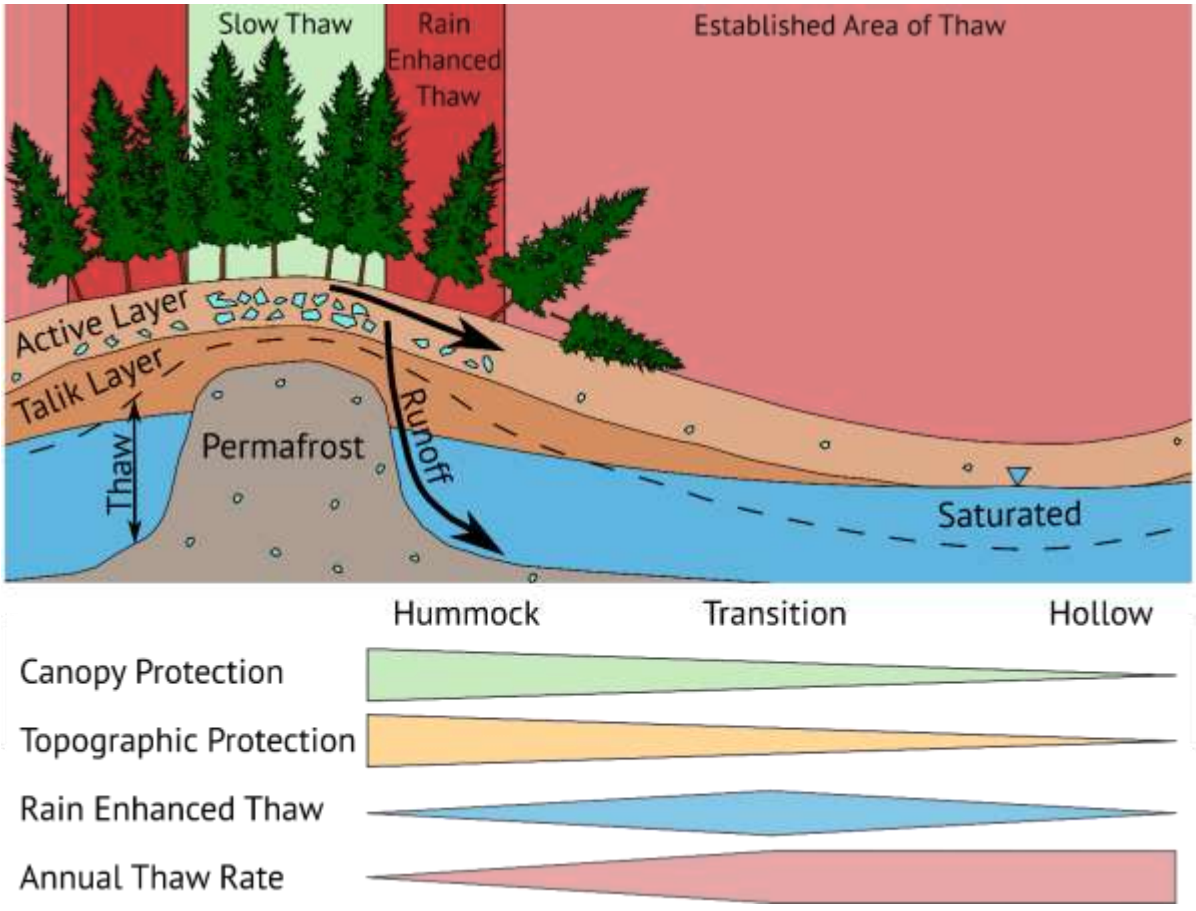

Figure 2.10 Conceptual overview. The top section shows a permafrost plateau cross-section. Light red represents areas expected to thaw rapidly with or without large rain events, and dark red represents areas only expected to thaw rapidly in the presence of large rain events. Light blue geometric shapes represent soil ice content. A blue triangle marks the top of the water table. Thick arrows show subsurface flow paths of rain-induced runoff that can warm soil through advective heat transport. A thin arrow shows the thaw that took place between 2020 and 2022. A dashed black line represents the depth of permafrost before 2020. The seasonally frozen layer is shown in light tan, the talik layer in dark tan, and the permafrost in gray. The bottom section shows the relative magnitude of canopy protection, topographic protection, rain-enhanced thaw, and annual thaw rates among hummock, transition, and hollow locations. Canopy protection and topographic protection refer to the slowing of permafrost thaw caused by dense canopy cover and high relative-elevation, both of which reduce snow depth and soil moisture, which are known to accelerate permafrost thaw (Discussion Section 2.4.3).

2.4.3 Hummock and Hollow Location Thaw was Controlled by Canopy Cover and Microtopography

During our study, hummock locations thawed gradually (8 ± 9 cm/year), while hollow locations thawed rapidly (44 ± 6 cm/year) (**Figure 2.5**). Observed hummock soil temperatures were always colder than hollow temperatures (**Figure 2.5**C, D), with cold temperatures reaching deeper depths at hummock locations during the cold season (**Figure 2.5**E) and warm temperatures unable to deeply penetrate during the warm-season (**Figure 2.5**F). These temperature regimes were expected since hollow locations had deeper snow (**Figure 2.4**C) and wetter soils (**Table 2.1**) than hummock locations, both known causes of warming and thaw[37,39,40,63–66]. Thus, in **Figure 2.10**, hummock locations are represented as "Slow Thaw," while hollow location areas are labeled "Established Area of Thaw."

Our data indicate that canopy cover and relative-elevation controlled snow depth and soil moisture, which varied significantly between hummock and hollow locations (**Figure 2.4**A, B). Canopy can reduce snow depth through interception of snowfall and the contribution of melt-inducing longwave radiation to snowpack[70–72]. Microtopography can affect snow depth through accumulation in microtopographic depressions during wind-driven snow transport[73]. These relationships are reflected in our data, establishing correlations between both canopy and relative-elevation with snow depth (**Figure 2.4**D, E). Black spruce can reduce soil moisture through transpiration and direct interception of precipitation[74], and higher relative-elevation locations have reduced soil moisture due to exiting runoff[29,75]. In this way, dense canopy and high relative-elevation keep hummock locations drier (**Table 2.1**) and cooler during the warm-season (**Figure 2.5**D, F). This is referred to as "Canopy Protection" and "Topographic Protection" in **Figure 2.10**.

Without topographic variation, canopy cover would theoretically be the primary control of soil moisture and snow depth. In this scenario, areas with dense canopy would thaw slowly due to lower soil moisture and shallower snow depth, while areas with minimal canopy cover would thaw more rapidly. Low canopy areas would, in turn, subside over time, becoming localized low points that accumulate moisture. These wet depressions would continue to thaw and become wetter until a lack of oxygen due to soil saturation would cause back spruce death[76], leading to less canopy at topographic low points and perpetuating the feedback loop[77,78]. The eventual result of this theoretical model for landscape progression is a positive correlation between relative-elevation and canopy cover, as we have at our site (**Figure 0.2**). Without the ecosystem protection supplied by black spruce, this scenario would advance more rapidly and uniformly.

2.4.4 Implications for a Warmer and Wetter Future

Observed warming and thaw at this ecosystem-protected site provides a preview of expected future permafrost progression regimes in more northern latitudes. Rain-induced energy transport to transition locations provided sufficient energy to cause warming and thaw of low ice-content soil due partly to hydrologically connected taliks (**Figure 2.9**, **Figure 2.10**). In the absence of taliks, this mechanism could, over time, cause enhanced thaw and the development of taliks. As larger rain events become more common in northern high-latitudes[79–83], and air temperatures continue to rise[28], the energy contribution from this mechanism is expected to increase. This increase, however, is not expected across the entire permafrost zone. Precipitation changes vary highly across northern high latitudes[48]. In addition, permafrost sites located in continental climates, such as the semi-continental climate of our site, have been shown to experience the greatest rain-induced warming through enhanced summer precipitation and warmer summer air temperatures. In contrast, maritime climates tend to experience a slight cooling effect from heavy rainfall[84].

Our analyses indicate that the nine-fold increase in thaw rates observed between 2020 and 2022 (Figure 2.3) was facilitated by low ice content and taliks within the permafrost plateau. Decades of exposure to a MAAT above 0 °C presumably caused permafrost soils to warm, taliks to form, and soil to lose ice content. This prior slow warming allowed energy inputs from three snowy and wet years and two large warm-season rain events to overcome the low resistance to thaw. As temperatures in northern high-latitudes continue to warm more quickly than the global average[28], causing more of the permafrost zone to experience mean annual temperatures above 0 °C, more permafrost will likely slowly degrade and become vulnerable to similar rapid thaw events. For example, in response to increased winter precipitation and snow at a colder and more stable site in northern Sweden, Sannel et al.[59] observed permafrost soils warm while the late-season thaw depth remained relatively stable. This site is now more vulnerable to the type of future thaw observed at our site.

2.4.5 Conclusion

Based on high-resolution soil temperature data, repeat permafrost surveys, and measurements of environmental variables; we determined that the thaw of our ecosystem-protected permafrost site and expansion of taliks accelerated during three consecutive wet and snowy years. Neither thaw rates nor thaw mechanisms were uniform across the site. Hummock locations experienced only 8 ± 9 cm/year of thaw, while hollow and transition locations thawed 44 ± 6 cm/year and 39 ± 13 cm/year, respectively (**Figure 2.5**B). Mechanisms of thaw between hollow and transition locations differed. Hollow locations had high thermal conductivity due to high soil moisture (**Table 2.1**) and ample cold-season insulation from deep snow (**Figure 2.3**C). In contrast, transition locations experienced substantial warming and thaw from thermal energy transported through subsurface taliks by runoff during individual rain events (**Figure 2.6**, **Figure 2.7**C, D, **Figure 2.9**). As northern high-latitudes continue to become warmer and wetter and rain events become more extreme, these observed mechanisms of warming and thaw are expected to increase.

3 Chapter 3: Local Slope, Wetland Proximity, and Meteorological Conditions Control the Spatial and Temporal Variation of Permafrost and Thermal Regimes in Interior, Alaska

3.1 Introduction

Permafrost, or soil that remains at or below 0 °C for two or more years[1], covers 12.9-17.8 km^2 or 9-14% of Earth's exposed land surface area[2,85]. Over the last several decades, northern high latitudes have experienced more significant warming than lower latitudes, and this trend of amplified warming is expected to strengthen in the future[3,28]. Permafrost trends are consistent with atmospheric temperature trends, with widespread warming and thaw observed since 1980[4]. In addition to trends in atmospheric temperature, other environmental variables, such as hydrology, topography, local climate, and landscape features, also regulate permafrost temperature and progression[4,16,29–33]. Permafrost can degrade at mean annual air temperatures (MAATs) as low as -20 °C and persist at MAATs as high as +2 °C[17].

While many environmental variables controlling soil thermal regimes and permafrost progression are well understood individually, interactions between these variables and how these interactions control permafrost and soil thermal metrics are less understood. To better understand the impacts of these complex interactions, we installed a transect of 25 high-resolution soil temperatures on a discontinuous permafrost plateau in Interior, Alaska. This 210 m transect began at a collapse scar bog feature and ended at the upgradient permafrost plateau terminus. We chose this transect because of the significant variation in environmental variables shown to influence permafrost, such as elevation[33], slope[86–88], soil moisture[42,89], canopy cover[33,90,91], organic layer thickness[30,31,33,92,93], and snow depth[63–66]. Our study took place between 2019 and 2022.

3.2 Methods

3.2.1 Site Description

The site is in Interior, Alaska (64.70 °N, −148.3 °W) within the Bonanza Creek Long Term Ecological Research Forest and is part of the Alaska Peatland Experiment. Fieldwork took place from June 2019 through October 2023. The site is in the discontinuous permafrost zone. From 2011 to 2020, the mean annual air temperature (MAAT) was -0.7 ± 1.5 °C, and the mean annual precipitation was 294 ± 106 mm[94]. The site consists of a wetland bog complex surrounded by a higher-elevation permafrost plateau. Permafrost plateau soil comprised 20-50 cm of peat underlain by mineral soil. Plateau peat soils had a low bulk density (0.27 ± 0.16 g/cm^3) and high field water content (74 ± 16 vol.%)[95]. Plateau vegetation changed with elevation. As elevation increased, sphagnum moss gave way to feather moss,

and black spruce progressed from small and sparse to dense and large with a nearly closed canopy. Understory vegetation includes cotton-grass (*Eriophorum chamissonis*), cloudberry (*Rubus chamaemorus*), labrador tea (*Ledum groenlandicum*), lowbush cranberry (*Vaccinium vitis-idaea*), and blueberry (*Vaccinium uliginosum*). Permafrost thaw commenced at the site between 50 and 400 years ago[96,97].

3.2.2 Field Measurements

Soil temperatures were measured using 120 cm and 160 cm length Distributed Temperature Profilers (DTPs) with sensors every 10 cm[51] installed in August 2020. DTPs have a 15-minute measurement interval and an accuracy of ± 0.05 °C. Data were linearly interpolated for location-to-location consistency and depth-corrected annually to account for frost heave and subsidence. HOBO TidbiT v2 temperature data loggers were used to capture soil temperature at wetland locations beneath DTPs. TidbiTs were deployed every 10 cm at a 15 minute-measurement interval with an accuracy of ± 0.2 °C. Permafrost table depth was estimated annually through manual probing in early-September with three replicate measurements per location. The probe length was 2.2 m.

Soil moisture was measured at seven locations using GroPoint Multi-Depth Soil Moisture Sensors attached to GroPoint Data Loggers. We installed four sensors in August 2020 and added three more in October 2022. Profilers took spatially continuous soil moisture readings from the surface to the permafrost table. Profilers measured a composite value of percent water every 15 cm at a 30-minute measurement interval. Outputs were calibrated for peat and mineral soils[56]. We applied a manufacturer-provided dielectric correction (1.019) for ≤ 0 °C soils. Soil moisture was used to model thermal conductivity, following the methods described by Eklof et al.[88].

The canopy cover percentage was determined through image analysis of upward-facing smartphone photos taken with a Moment 14 mm fisheye lens one meter above the soil surface. Photos were taken annually during peak vegetation. Photos were analyzed in ImageJ by cropping the photo into a circle, splitting the photo into color panes, thresholding the blue pane into sky and vegetation pixels, and calculating percent cover from the relative proportion of pixels[58]. Cumulative shortwave radiation at each location was calculated using HPEval, a MATLAB-based software tool that uses high-resolution hemispherical photos to estimate shortwave radiation below the forest canopy[55].

Relative elevation of instrumentation was determined through a combination of manual level surveys and real-time kinematic (RTK) GPS data points multiple times per year. Instrumentation locations were also determined through RTK GPS. Points were recorded using Emlid Reach RS2 units. Control points located at higher elevation non-permafrost locations were used to compare RTK GPS surveys across time.

Daily cold season snow depth measurements at 30 locations were calculated from timelapse camera photos (6080x3420p) taken three times per day by Wingscapes TimelapseCam Pro cameras. Cameras captured multiple orange 1-meter PVC stakes partially buried by the snow. Snow depth values were determined by multiplying the fraction of above-snow PVC by the 1-meter total length in ImageJ[98,99].

3.2.3 Flux Tower Measurements

Fluxes of water and energy were collected with two on-site eddy covariance towers. One tower is on the permafrost plateau, and one is on the wetland complex. Each tower recorded microclimate and eddy covariance data. Tower data utilized in these analyses include precipitation, soil moisture, air temperature, evapotranspiration, snow depth, and ground heat flux. Data information is detailed in Euskirchen et al.[96].

3.2.4 Statistical Methods

Environmental variables and thermal response metrics were compared for hummock, transition, and hollow locations using one-way ANOVA followed by Tukey HSD post-hoc using $\alpha = 0.05$. Data were log10 transformed to increase normality and reduce skew before ANOVA analysis. Data presented in the figures are shown in non-transformed space for visual clarity. Correlations were determined by fitting data with linear and exponential regression models and using two-sided hypothesis testing with $\alpha = 0.05$.

3.3 Results

3.3.1 Meteorological Conditions During Study Period

From 2010 to 2020, the mean annual air temperature (MAAT) was -0.72 ± 1.54 °C with a mean annual precipitation of 294 ± 106 mm and peak snow depth of 0.50 ± 0.12 m[94]. From 2021 to 2023, the site experienced conditions that were colder (**Figure 3.1**A, D), drier (**Figure 3.1**B, E), and snowier (**Figure 3.1**F) than the preceding period. MAAT in 2021, 2022, and 2023 were -1.56 °C, -1.43 °C, and -1.08 °C, respectively. Total precipitation values were 196 mm, 207 mm, and 222 mm, respectively (**Figure 3.1**E). Peak snow depths were 0.78 m, 0.86 m, and 0.62 m, respectively (**Figure 3.1**F). On December 26, 2022, the site experienced a rain-on-snow event that dropped 42 mm of rain in less than 24 hours.

Colder than average mean annual air temperatures were driven by the cold season atmospheric temperatures, with 2021, 2022, and 2023 experiencing freezing degree day (FDD) values of -2676 deg-days, -2616 deg-days, and -2507 deg-days, respectively (**Figure 3.1**G). FDD values from each study year exceeded the 2010-2020 average of -2359 ± 491 deg-days (**Figure 3.1**G). Cold season ground heat flux in 2021, 2022, and 2023 were -52814 W/m^2, -35646 W/m^2, and -35212 W/m^2, respectively (**Figure 3.1**). Growing degree day (GDD) values of 2107 deg-days in 2021, 2094 deg-days in 2022, and 2114 deg-days in 2023 were comparable to the 2010-2020 average of 2098 ± 108 deg-days (**Figure 3.1**I). Relative

values in warm season ground heat flux followed the same pattern, with 2023 being the highest, followed by 2021, then 2022 (**Figure 3.1**K). However, variation in warm season ground heat flux was greater than GDD, potentially due to variation in average warm season soil water content (**Figure 3.1**L). Warm season ground heat flux in 2021, 2022, and 2023 were 69633 W/m^2, 57834 W/m^2, and 79299 W/m^2, respectively (**Figure 3.1**K). Average warm-season soil water content was 55%, 51%, and 60%, respectively.

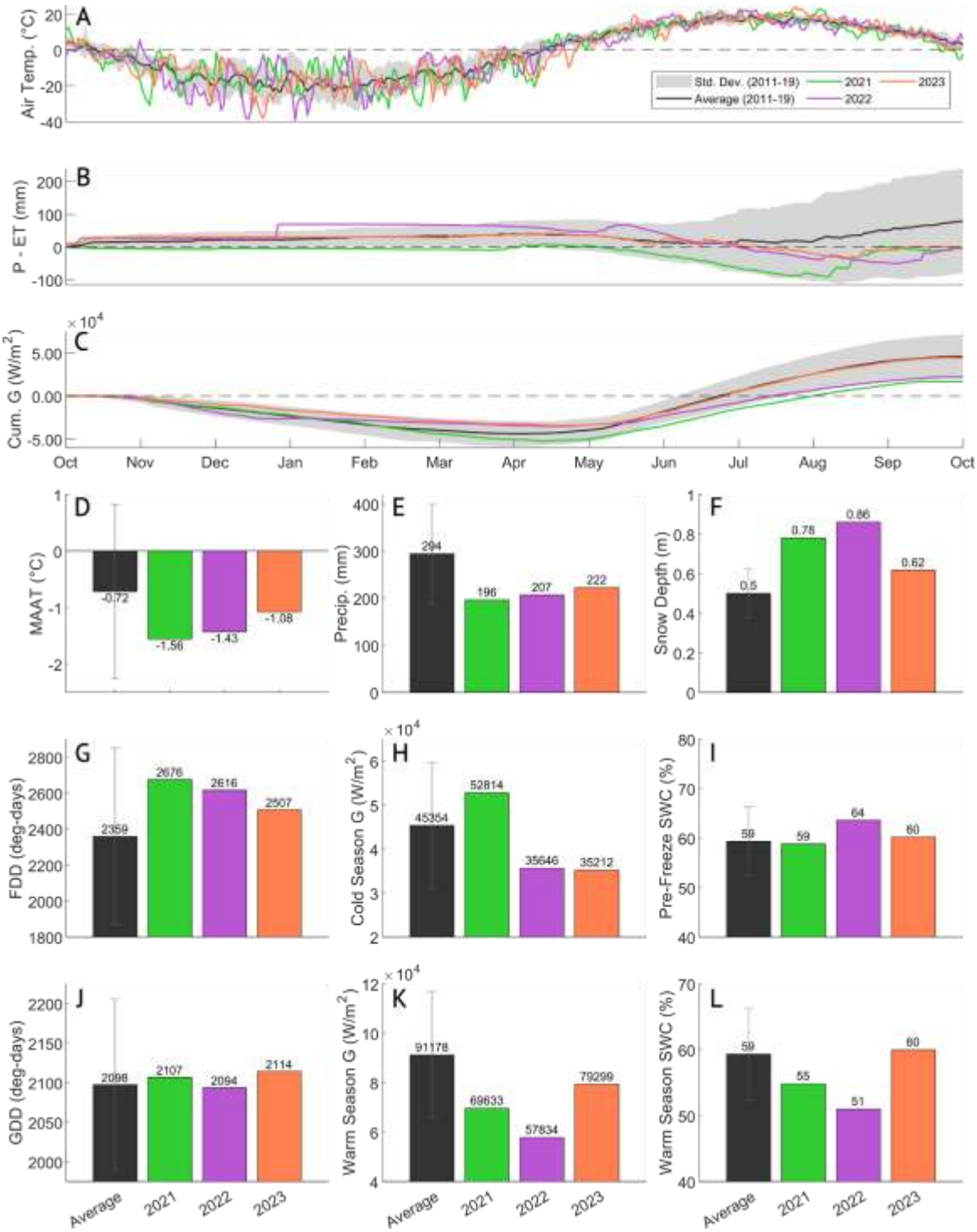

Figure 3.1 Meteorological forcing during the study period. *Line graphs show annual time series of (A) average daily air temperature, (B) cumulative evapotranspiration subtracted from cumulative precipitation and (C) cumulative ground heat flux. Data for 2021 is green, 2022 is purple, and 2023 is orange. Average values are shown as a black line surrounded by a gray band that indicates one standard deviation above and below. (D)-(L) Bar charts showing: (D) annual air temperature (MAAT), (E) maximum snow depth, (F) Duration of snowy conditions, (G) freezing degree days from atmospheric temperature, (H) cold season cumulative ground heat flux, (I) soil water content two weeks before soil began freezing (mid-September), (J) air temperature growing degree days, (K) warm season cumulative ground heat flux, and (L) average warm season soil water content. Years and data colors correspond to the line graphs (A-C). All data was sourced from the on-site black spruce flux tower. All average values (black) contain data from 2010-2020.*

3.3.2 Across-Transect Thermal and Environmental Variables

Figure 3.2 shows variations in depth to permafrost, thermal metrics, and environmental variables along the permafrost plateau transect. Along the transect (left to right in **Figure 3.2**), absolute elevation increased (**Figure 3.2**A), organic thickness decreased (**Figure 3.2**A, G), the thickness of above-permafrost mineral soil increased (**Figure 3.2**A), and canopy cover density increased (**Figure 3.2**A, F). Depth to permafrost was shallowest in Zone 3 and became deeper both toward the wetland complex in Zone 1 and 2 and deeper into the black spruce forest in Zones 4 and 5 (**Figure 3.2**A, B). Maximum warm season temperature measured at a depth of 10 cm did not vary notably along the transect except for higher values at the plateau-bog boundary in Zone 1 and the plateau terminus at the upgradient (right) edge of Zone 5 (**Figure 3.2**C). Zone 3 experienced the coldest winter temperatures at a depth of 10 cm, with warmer minimum temperatures along the transect in both directions (**Figure 3.2**C). The zones, delineated by vertical lines through the figure, are based on zero curtain behavior shown in **Figure 3.2**D. The zero-curtain is a sustained period when soil temperature remains nearly constant at 0 °C as phase change occurs [100]. Zones 1 and 5 never overcome the zero curtain, Zones 2 and 4 overcome the zero curtain during only some years, and Zone 3 overcomes the zero curtain during all observed cold seasons. Soil moisture peaks in Zone 3 and decreases in both directions along the plateau transect except for high soil moisture at the plateau-bog interface in Zone 1 (**Figure 3.2**E). An aerial photo showing the zone locations on the landscape, soil temperature data from each zone, and accompanying environmental variables (elevation, soil moisture, and canopy cover) are shown in **Figure 3.3**.

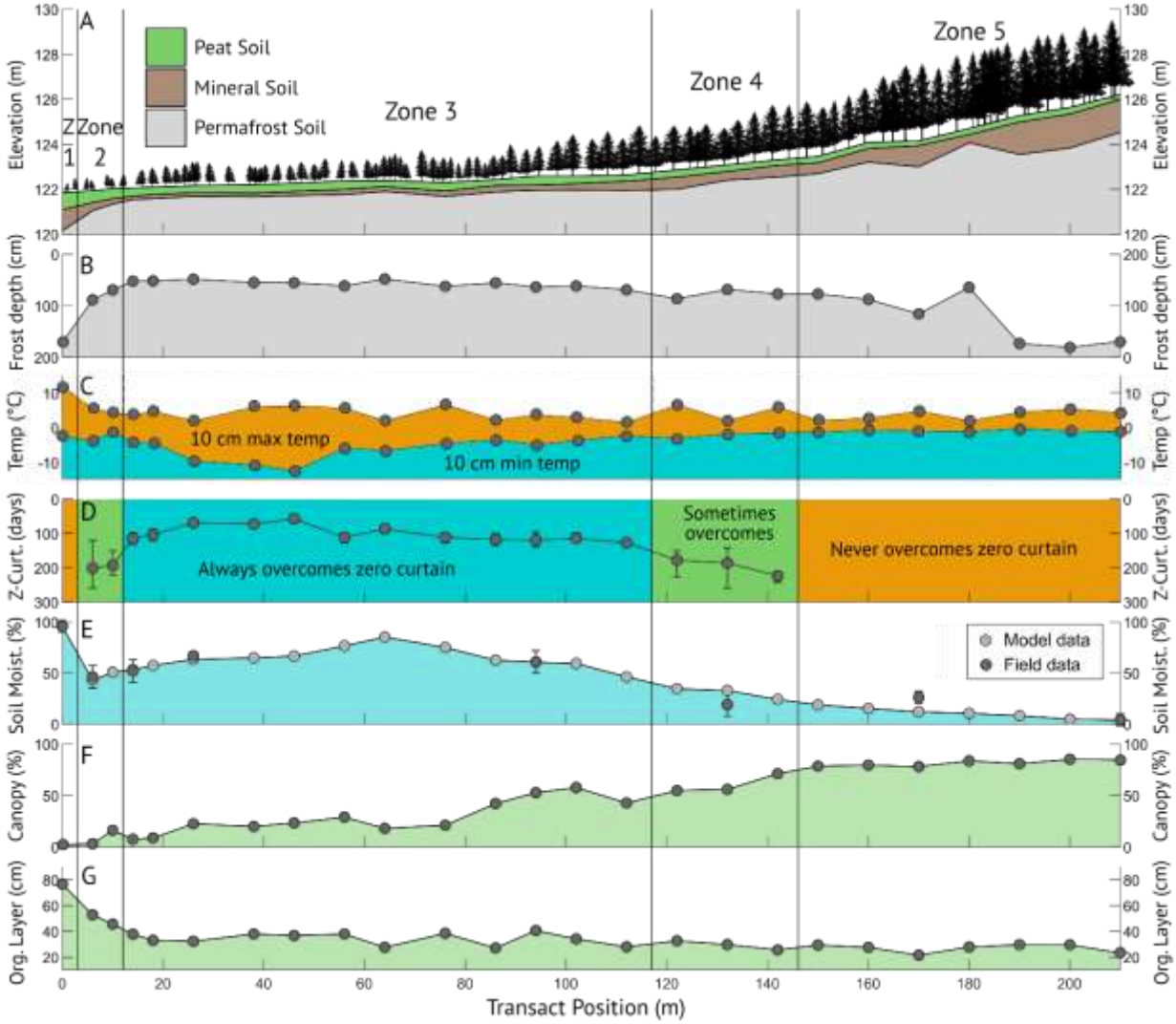

Figure 3.2 Variables along permafrost transect. *Line graphs with data markers show: (A) absolute elevation, permafrost depth, relative tree height, and soil profile composition with relative tree height is based on backpack LiDAR data recorded in July 2022, (B) permafrost table depth (gray) relative to the surface, (C) maximum (orange) and minimum (blue) soil temperatures experienced at a depth of 10 cm, (D) zero curtain duration (time in days for all soil to reach < 0 °C temperatures) locations with an orange background never overcome the zero curtain, locations with a green background sometimes overcome the zero curtain, and locations with a blue background overcame the zero curtain during all study years, (E) average soil moisture (blue) in the top 30 cm of the soil profile in mid-September before atmospheric temperatures dropped below freezing with dark gray data points indicating field data and light gray data points indicating modeled values based on surrounding measurements and local slope (**Figure 0.20**), (F) canopy cover percentage (green) calculated through processing hemispherical photos, (G) organic layer thickness which is made up of both surface mosses and peat (green). Vertical lines separate thermal regime zones defined by zero curtain behavior.*

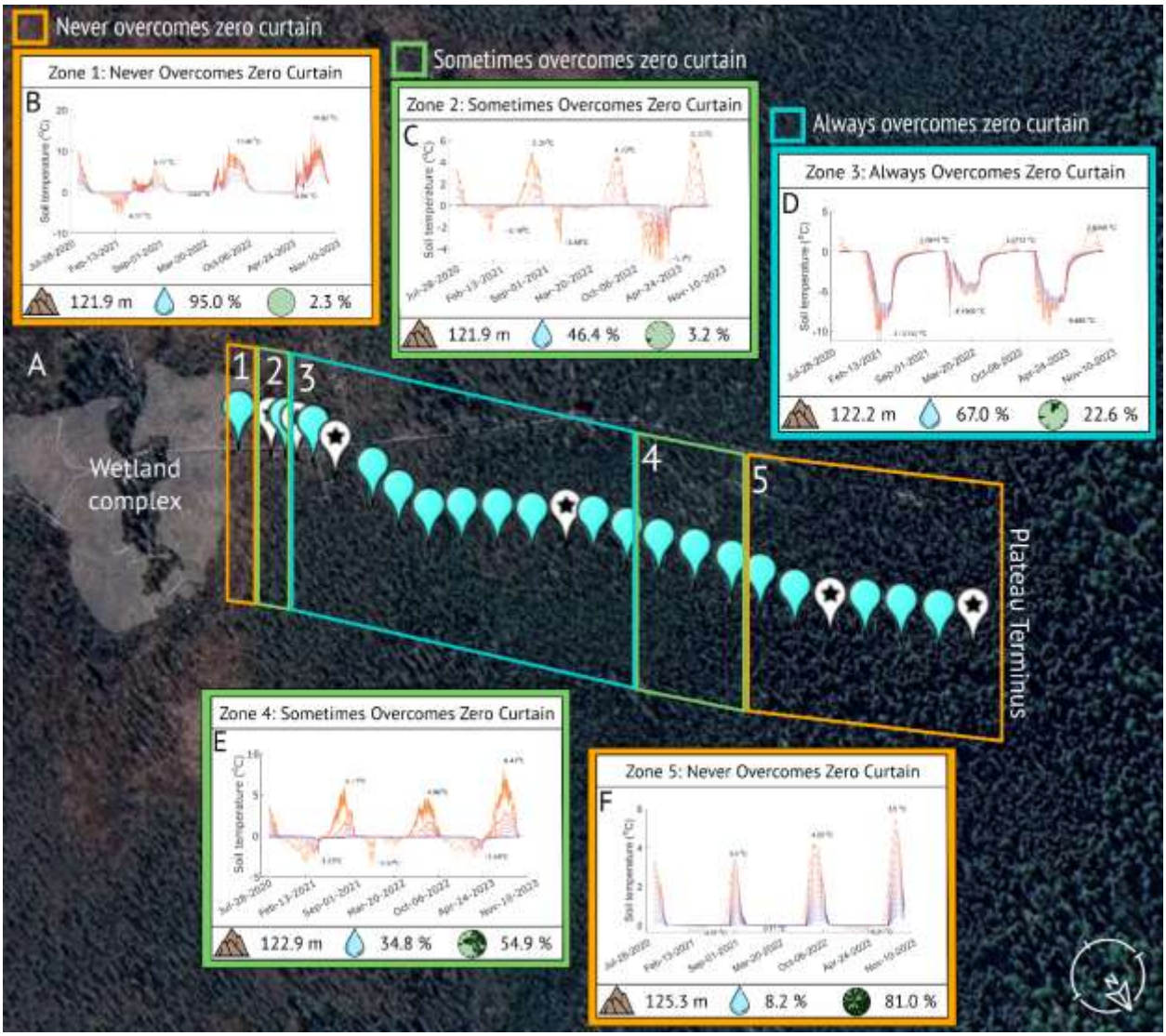

Figure 3.3 Aerial photo and example data from zero curtain based thermal regimes. *(A) Aerial photo from Google Maps with markers indicating study locations. Locations marked in white with a star indicate DTP locations with additional field data, including soil moisture and snow depth, while locations in blue contain only DTP sensors. Locations are categorized based on zero curtain behavior, with locations that never overcame the zero curtain in orange, those that overcame the zero curtain during some years in green, and those that never overcame the zero curtain in blue. The name of each regime group, the downgradient wetland complex, and the upgradient permafrost terminus are labeled on the image. A compass at the top left corner shows direction. (B-F) Soil temperatures at depths from 10 to 140 cm below the soil surface (depths are labeled on the figure and colored according to the legend), absolute elevation, pre-cold season soil moisture in the top 30 cm of the soil profile, and canopy closure for example locations from thermal regime group: (B) Zone 1 (C) Zone 2, (D) Zone 3, (E) Zone 4, and (F) Zone 5. Soil temperature data is from DTPs. These data have been interpolated and georeferenced. Absolute elevation was determined from output from a 2017 airborne LiDAR survey. Canopy cover data was calculated from upward-facing fisheye photos. Soil moisture data was determined through soil moisture profiler data or slope-based modeling* ***Figure 0.20***.

3.3.3 Thermal and Environmental Variables within Thermal Regimes

Among our 25 transect locations, one was categorized as Zone 1, two as Zone 2, 12 as Zone 3, three as Zone 4, and seven as Zone 5. Zone 3 locations had statistically shallower depths to the permafrost table (**Figure 3.4**A, $p < 0.001$) than Zone 1 and Zone 5 locations and statistically shorter zero curtain durations than all other locations (**Figure 3.4**B, $p < 0.001$). Average depths to permafrost in Zone 1, Zone 2, Zone 3, Zone 4, and Zone 5 were 170 cm, 79 ± 14 cm, 57 ± 7 cm, 77 ± 9 cm, and 124 ± 50 cm, respectively. The average zero curtain duration in Zone 3 was 100 ± 23 days compared to 170 ± 6 days and 196 ± 24 in Zone 2 and Zone 4. Zone 1 and Zone 5 never overcame the zero curtain. Zone 3 reached statistically colder minimum temperatures at a depth of 10 cm than Zone 5 (**Figure 3.4**C, $p < 0.05$). Average minimum temperatures in Zone 1, Zone 2, Zone 3, Zone 4, and Zone 5 were -1.3 °C, -3.1 ± 1.0 °C, -6.0 ± 3.3 °C, -2.4 ± 0.7 °C, and -1.0 ± 0.4 °C, respectively. Average maximum temperatures reached at a depth of 10 cm did not vary significantly among thermal groups (figure 4D).

Zone 1 and Zone 3 had statistically higher near-surface (top 30 cm) pre-cold season thermal conductivities than Zone 4 and Zone 5, with Zone 5 having statistically lower thermal conductivity than all other zones (**Figure 3.4**E, $p < 0.001$). Thermal conductivity values were timed to coincide with average daily atmospheric temperatures dropping below 0 °C. Average thermal conductivity values within the top 30 cm of the soil profile in Zone 1, Zone 2, Zone 3, Zone 4, and Zone 5 were 0.56 W/m·K, 0.33 ± 0.03 W/m·K, 0.42 ± 0.05 W/m·K, 0.24 ± 0.03 W/m·K, and 0.11 ± 0.04 W/m·K, respectively. Zone 1 had a statistically higher ratio of near-surface thermal conductivity to total energy required to freeze soil water in the seasonally frozen layer than Zone 1 and Zone 5, with Zone 2 and Zone 4 being statistically indistinguishable from both groups (**Figure 3.4**F, $p < 0.001$). Average ratios of near-surface thermal conductivity to total energy required to freeze soils in Zone 1, Zone 2, Zone 3, Zone 4, and Zone 5 were 0.009 $m^{-1}K^{-1}day^{-1}$, 0.022 ± 0.004 $m^{-1}K^{-1}day^{-1}$, 0.032 ± 0.004 $m^{-1}K^{-1}day^{-1}$, 0.022 ± 0.003 $m^{-1}K^{-1}day^{-1}$, and 0.014 ± 0.006 $m^{-1}K^{-1}day^{-1}$, respectively. The organic layer thickness was statistically greater in Zone 1 than in Zone 3, Zone 4, and Zone 5, with Zone 2 being statistically indistinguishable from either group (**Figure 3.4**G, $p < 0.001$). Organic layer thickness values in Zone 1, Zone 2, Zone 3, Zone 4, and Zone 5 were 77 cm, 49 ± 5 cm, 34 ± 5 cm, 29 ± 4 cm, and 27 ± 3 cm, respectively. The canopy cover percentages of Zone 1 and Zone 2 were statically lower than those of all other zones. The canopy cover percentage of Zone 3 was statistically lower than in Zone 5, with Zone 4 being statistically indistinguishable from Zone 3 and Zone 5 (**Figure 3.4**H, $p < 0.001$). Canopy cover percentages in Zone 1, Zone 2, Zone 3, Zone 4, and Zone 5 were 2%, 10 ± 9%, 29 ± 16%, 61 ± 9%, and 82 ± 3%, respectively. Elevation of Zone 5 is statistically greater than that of all other groups (**Figure 3.4**I, $p < 0.001$). Elevations in Zone 1, Zone 2, Zone 3, Zone 4, and Zone 5 were 121.9 m, 122.0 ± 0.1 m, 122.3 ± 0.2 m, 123.1 ± 0.2 m, and 124.8 ± 1.0 m, respectively. The number of freezing days experienced before soil was insulated by snow was statistically greater in Zone 5 than Zone 1, with all other zones being statistically

indistinguishable from either group (**Figure 3.4**J, $p < 0.05$). We used a snow depth of 25 cm to indicate insulation based on time series air and soil temperature correlations. Freezing days prior to insulation by snow for Zone 1, Zone 2, Zone 3, Zone 4, and Zone 5 were 38 ± 6 days, 51 ± 16 days, 49 ± 14 days, 66 ± 6 days, and 93 ± 42 days, respectively.

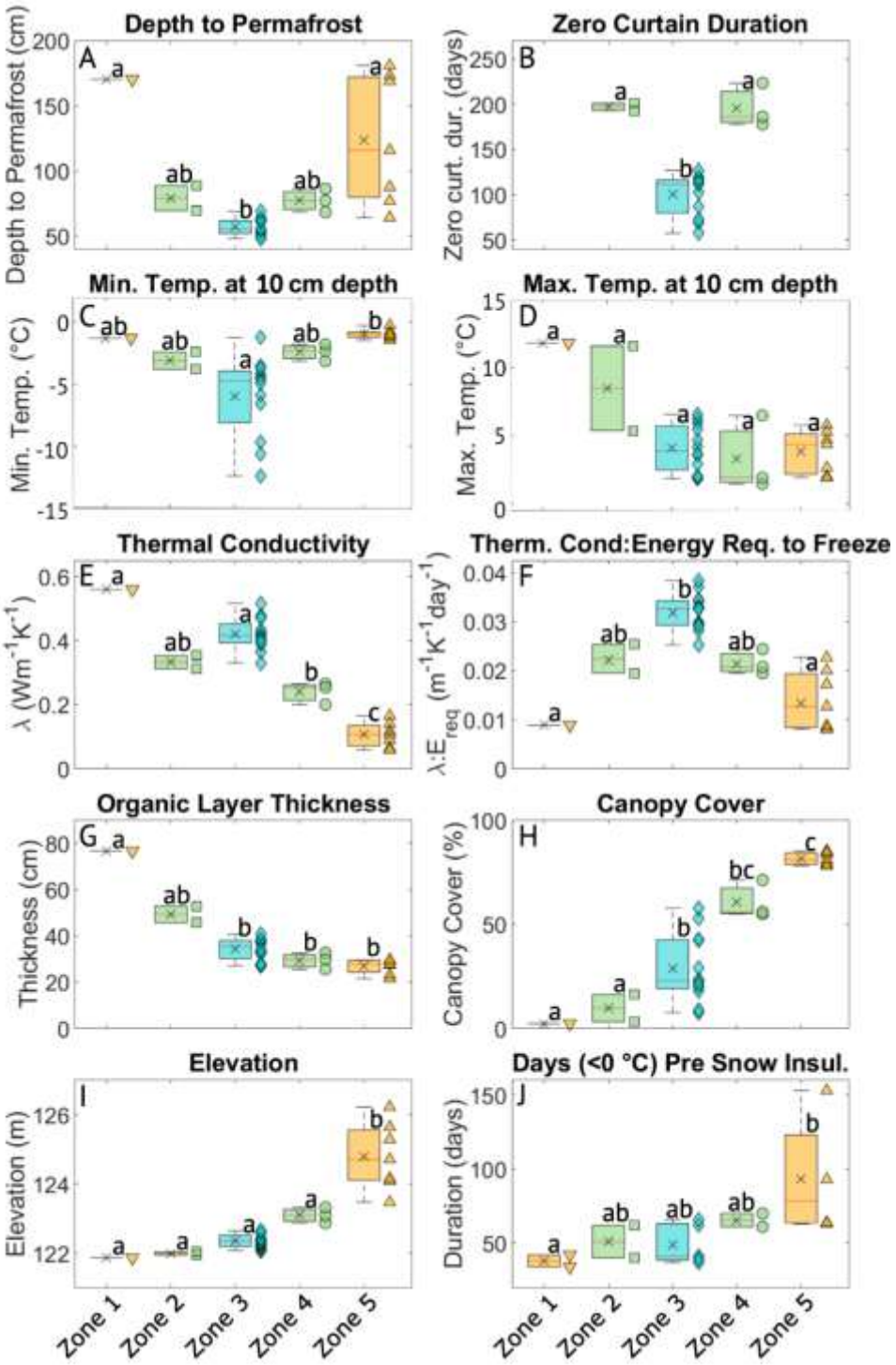

Figure 3.4 Permafrost, thermal, and environmental metrics among zero curtain thermal regime groups. *Box and whisker plots showing: (A) Average depth to permafrost table, (B) average zero curtain duration, average (C) minimum and (D) maximum soil temperature reached at a soil depth of 30 cm, (E) soil moisture in the top 30 cm of the soil profile two weeks before freezing of soil ice, (F) the ratio of soil moisture values in the top 30 cm, (G) organic layer thickness including peat and moss thicknesses, (H) canopy cover percentage calculated from upward-facing hemispherical photos, (I) elevation, and (J) days with below freezing atmospheric temperatures before snow depth reached a depth of 25 cm. Symbols indicate which zero curtain thermal regime. Data from Zone 1 are shown as orange downward-facing triangles. Data from Zone 2 are shown as green squares. Data from Zone 3 are shown as blue diamonds. Data from Zone 4 are shown as green circles. Data from Zone 5 are shown as orange upward-facing triangles. On each box plot, the central line indicates the median, 'x' marks the mean, edges of the box indicate the 25th and 75th percentiles, whiskers indicate the most extreme non-outlier data points, and a red plus marker indicates an outlier greater than 2.7 standard deviations from the mean. Letters on top of boxes indicate data sets with statistically significant differences in mean as determined through one-way ANOVA.*

3.3.4 Depth to Permafrost Correlation to Thermal and Environmental Metrics

Depth to permafrost had a significant exponential correlation with near-surface thermal conductivity (**Figure 3.5**A, $R^2 = 0.70$, $p < 0.001$). The single Zone 1 location is a clear outlier with the highest thermal conductivity, 0.56 W/m·K, and one of the highest depths to permafrost, 170 cm. Depth to permafrost had a significant linear correlation with zero curtain duration (**Figure 3.5**B, $R^2 = 0.71$, $p < 0.001$). Zero curtain duration of these locations (Zone 2, Zone 3, and Zone 4) had a significant linear correlation with the ratio of average pre-cold season thermal conductivity in the top 30 cm and total energy required to freeze all active layer soil water (**Figure 3.5**C, $R^2 = 0.76$, $p < 0.001$). Zone 5 locations, which never overcame the zero curtain, had a significant linear correlation between depth to permafrost and near-surface thermal conductivity (**Figure 3.5**D, $R^2 = 0.66$, $p < 0.05$). Depth to permafrost did not correlate with elevation, organic layer thickness, canopy cover, snow depth, or days with below-freezing atmospheric temperatures prior to insulation from snow. Scatter Plots for each variable are included in the SI (**Figure 0.21**).

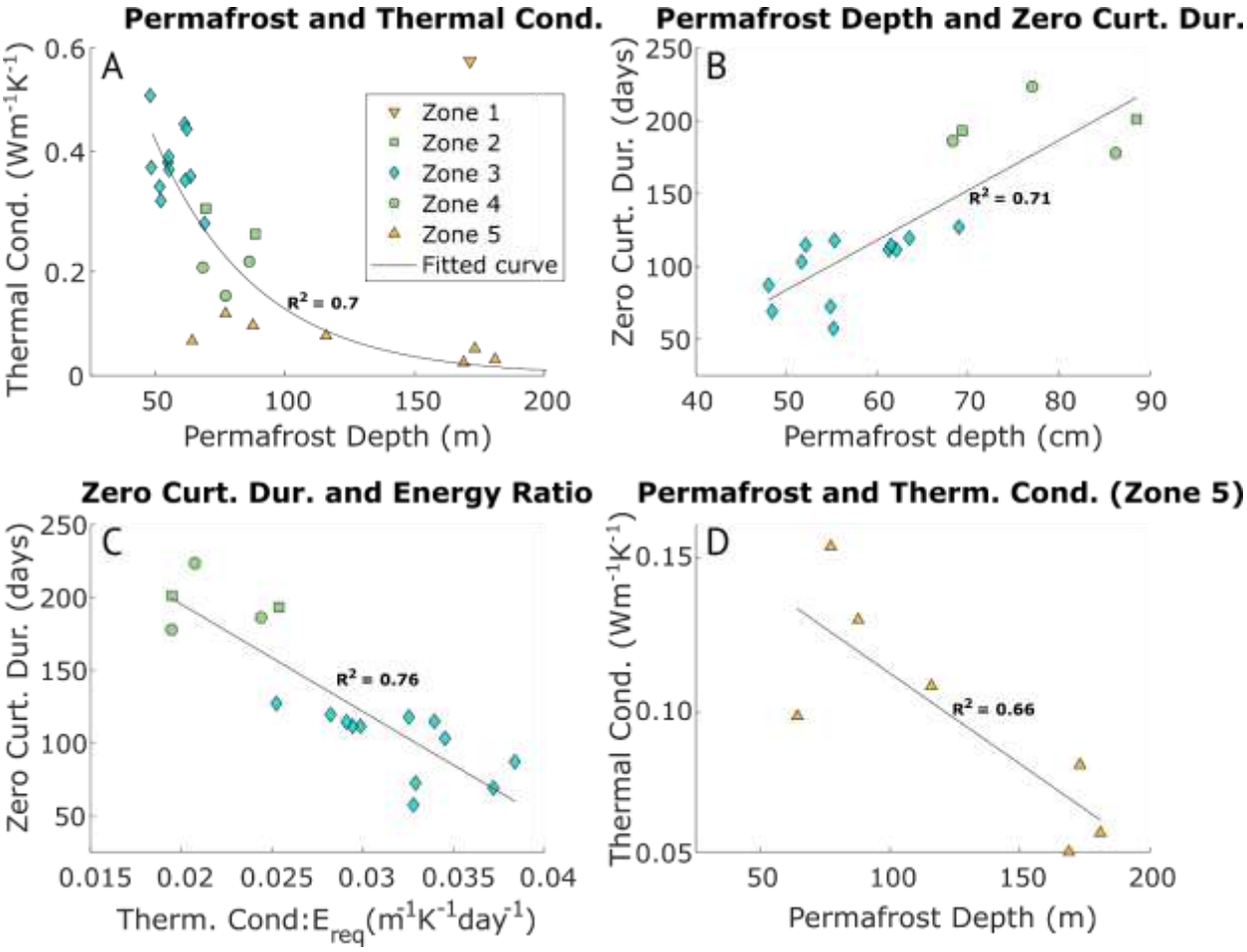

Figure 3.5 Correlations between depth to permafrost and thermal and environmental metrics. *Scatter plots showing (A) depth to permafrost and soil moisture at all locations, (B) zero curtain duration and the ratio of near-surface soil moisture to total active layer water of locations from Zones 2, 3, and 4, (C) permafrost depth and zero curtain duration of locations from Zones 2, 3, and 4, and (D) depth to permafrost and soil moisture for locations in Zone 5.*

Depth to permafrost had a significant exponential correlation with bog proximity for the four closest locations (***Figure 3.6***B, $R^2 = 0.99$, $p < 0.05$). Depth to permafrost was deepest at the edge of the bog complex and shallowed as the distance from the bog complex increased (***Figure 3.6***B). A non-statistically significant exponential correlation in energy gradient between bog and plateau soils followed the same trend as depth to permafrost (***Figure 3.6***C, $R^2 = 0.79$). The energy gradient between bog and individual permafrost plateau locations was calculated by dividing the difference in cold season average soil temperature in the top 30 cm of the soil profile by the distance between these locations.

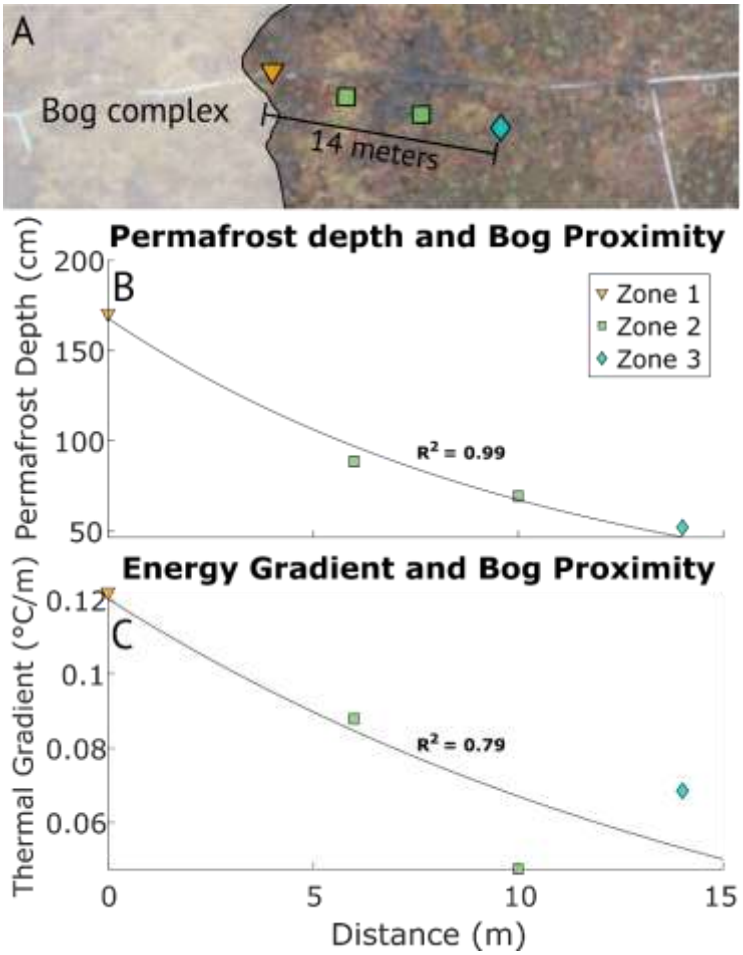

Figure 3.6 Correlations between depth to permafrost and proximity to the bog complex. *(A) An aerial Google Earth photo showing the proximity of site locations relative to the wetland complex edge. Scatter plots showing (B) permafrost depth and spatial distance to the bog edge and (C) the thermal gradient between soils in the center of the bog with permafrost-underlain site locations.*

3.3.5 Annual Variation in Permafrost Depth and Thermal Metrics

When considering all locations, there was no statistically significant year-to-year difference in mean depth to permafrost, zero curtain duration, and minimum or maximum soil temperature (**Figure 3.7**A, C, E, and G). Spatial differences in permafrost and thermal behavior across all years were greater than temporal variation (**Figure 3.2**, **Figure 3.3**, and **Figure 3.4**). However, when comparing the year-to-year differences in the behavior of each location to itself, we see significant variation. Relative to the median, 2022 had significantly shallower depth to permafrost, while 2023 had significantly deeper permafrost (**Figure 3.7**B, $p < 0.001$). Depths to permafrost relative to the median in 2021, 2022, and 2023 were +0.3 ± 2.1 cm, -3.6 ± 3.8 cm, and +2.8 ± 5.4 cm, respectively. Depth to permafrost in 2023 had two clear outliers from Zone 2, which experienced shallower depths to permafrost in 2023. These locations had depths to permafrost that were 13.7 cm and 56.4 cm shallower

than the three-year median, respectively. Relative to the median, 2022 had a significantly longer zero curtain duration, while 2023 had a significantly shorter zero curtain duration (**Figure 3.7**D, $p < 0.001$). Average zero curtain durations relative to the median in 2021, 2022, and 2023 were +2 ± 7 days, +22 ± 28 days, and -19 ± 25 days, respectively. Relative to the median, 2022 had a significantly warmer minimum cold-season temperature at a depth of 30 cm, while 2023 had a significantly colder minimum temperature (**Figure 3.7**F, $p < 0.001$). Average minimum soil temperatures relative to the median in 2021, 2022, and 2023 were -0.6 ± 0.9 °C, +1.1 ± 0.9 °C, and -0.3 ± 0.6 °C, respectively. Relative to the median, 2021 had a significantly cooler maximum warm-season temperature at a depth of 30 cm, while 2023 had a significantly warmer maximum temperature (**Figure 3.7**H, $p < 0.001$). Average maximum soil temperatures relative to the median in 2021, 2022, and 2023 were -0.5 ± 1.1 °C, -0.1 ± 0.2 °C, and +0.9 ± 1.1 °C, respectively.

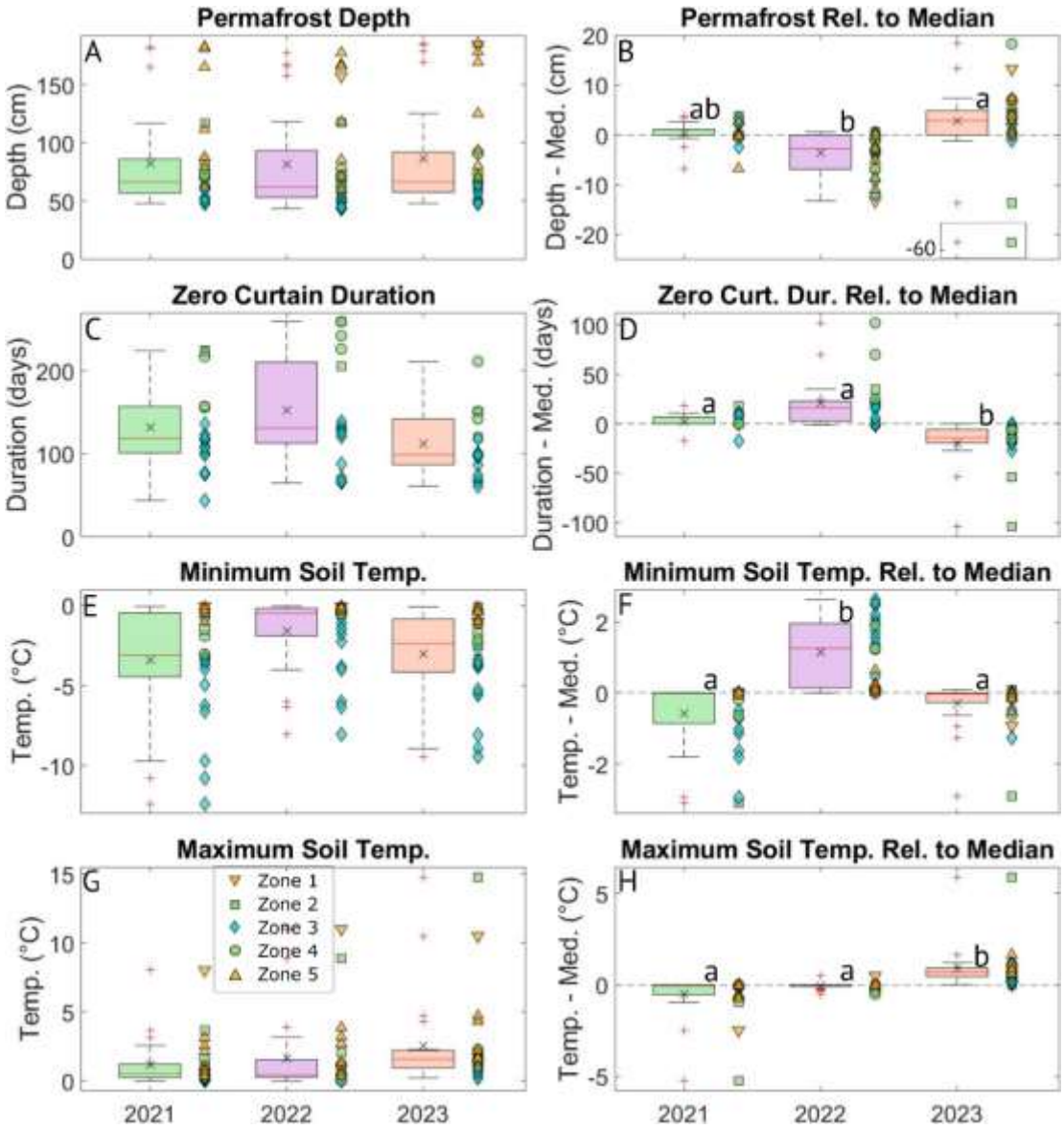

Figure 3.7 Year-to-year change in permafrost and thermal metrics. *Box and whisker plots showing: (A) depth to permafrost, (B) annual depth to permafrost relative to median values, (C) zero curtain duration, (D) zero curtain duration relative to median values, (E) minimum soil temperature measured at a depth of 30 cm, (F) minimum soil temperatures relative to median values, (G) maximum soil temperature measured at a depth of 30 cm, (H) maximum soil temperatures relative to median values. Median values include data from 2021 to 2023. Each marker shows data from a single field location. Symbols indicate the zero curtain thermal regime of that location. Data from Zone 1 are shown as orange downward-facing triangles. Data from Zone 2 are shown as green squares. Data from Zone 3 are shown as blue diamonds. Data from Zone 4 are shown as green circles. Data from Zone 5 are shown as orange upward-facing triangles. Years are indicated by boxplot color, with 2021, 2022, and 2023 shown in green, purple, and orange, respectively. Boxplot statistics are described in Figure 3.4.*

3.4 Discussion

3.4.1 Local Slope controlled Spatial Variation in Permafrost Depth and Thermal Behavior

As noted in our results, depth to permafrost was significantly correlated to near-surface thermal conductivity going into the cold season (**Figure 3.5**A). The only zone that did not follow this trend was Zone 1, whose behavior was affected by bog proximity (**Figure 3.5**A, ***Figure 3.6***). Thermal conductivity is affected by soil type, moisture, and ice content [41–43]. Since near-surface soil for all locations consisted entirely of peat, and all near-surface soils were unfrozen before the cold season, thermal conductivity was controlled primarily by near-surface soil moisture. Soil moisture was, in turn, controlled by local slopes, with transect areas on mild slopes being wetter than locations on steep slopes (**Figure 0.20**). The probable cause for these differences in soil moisture is flow rate. The water output rate of sloped locations was greater than that of less sloped locations, with comparably minimal variation in hydrologic input, leading to drier conditions.

The impact of slope on soil moisture diminishes when there is insufficient water to reach the point of free drainage and flow. During most warm-season periods in each study year, warm-season soil moisture was below the point of free drainage, forest wells remained dry, and flow was not observed. Lack of subsurface flow caused the near-surface soil moisture during the warm season to vary minimally between plateau locations. The sole exception was Zone 1, which remained saturated all year due to proximity to the wetland complex. The lack of variation in soil moisture, leading to a lack of variation in warm season thermal conductivity, contributes to the lack of variation in maximum temperatures reached at a depth of 10 cm across the transect (**Figure 3.4**D).

Among Zone 2, Zone 3, and Zone 4 locations that overcame the zero curtain, depth to permafrost was correlated to zero curtain duration. Zero curtain duration is the time required after soils reach 0 °C and to freeze fully, indicated by temperatures less than 0 °C at all soil depths. Locations that froze more quickly tended to have shallower permafrost. Zero curtain duration depends on the total amount of energy that must be released to freeze all soil water and the rate at which that energy can escape. Intuitively, zero curtain

duration was highly correlated to the ratio of near-surface thermal conductivity, a measure of the rate at which energy moves through the soil, and the total amount of energy that must be released to freeze all water in the seasonally unfrozen layer. This relationship acts as a feedback loop. Locations with shallow permafrost require less released energy to freeze because they contain less total water due to lower water-containing volume. When permafrost deepens, however, increased total water due to increased thawed pore space can rapidly increase the energy required to overcome the zero curtain.

3.4.2 Proximity to the Bog Complex Controlled Permafrost Depth and Thermal Behavior of Nearby Locations

At the edge of the wetland complex, correlations between slope, soil moisture, thermal conductivity, and depth to permafrost break down. Thermal variables, environmental variables, and depth to permafrost at these locations were controlled by bog proximity (***Figure 3.6***A, B), presumably due to energy from the wetland (***Figure 3.6***C). The bog complex never overcomes the zero curtain (**Figure 0.62**-**Figure 0.67**), has deep soils that remain above 0 °C, and has a large thermal capacity due to year-round saturation. These characteristics cause the wetland complex to act as a thermal buffer, keeping nearby permafrost locations warmer than they might otherwise be.

For example, the lone Zone 1 location, which was located at the plateau-bog interface and never overcame the zero curtain, was saturated despite resting on a steep slope that would coincide with dry conditions elsewhere on the transect (**Figure 0.20**). The wetness of this location caused it to have the highest cold-season thermal conductivity and the greatest necessary energy release to overcome the zero curtain. Due to the thermal buffer of the wetland complex and the high energy requirement to freeze soil water, this location never overcame the zero curtain and experienced the warmest soil temperatures of all permafrost locations. Moving upgradient away from Zone 1, wetland influence, quantified by the cold-season thermal gradient, diminished (***Figure 3.6***).

The warming and wetting effects of wetland proximity are independent of meteorological forcing. Regardless of annual precipitation and temperatures, Zone 1 is expected to remain saturated and never overcome the zero curtain. Moving further upgradient, the relative impact of wetland proximity diminished and became more comparable to that of meteorological forcing. Zone 2 locations overcame the zero curtain in 2023 but not 2022. In 2023, the cooling effects of cold atmospheric temperatures and high thermal conductivity overcame the warming effects of thermal buffering from the wetland complex.

3.4.3 Year-to-year Variation in Permafrost Depth was Controlled by Warm Season Meteorological Forcing Unless Cold Season Forcing Changed Soil Ice Content

For most transect locations, depth to permafrost was greater in 2023 than in 2022 (**Figure 3.7**B). This result was initially unexpected because soils in 2023 had significantly colder

minimum temperatures (**Figure 3.7**F) and rapidly overcame the zero curtain (**Figure 3.7**D). Warmer soil temperatures and longer zero curtains in 2022 were presumably due to a rain-on-snow event that dropped 42 mm of rain in less than 24 hours on December 26, 2022 (**Figure 3.1**B) and warmed below-freezing soil temperatures at most locations to 0 °C (**Figure 3.3**). Despite the anomalous cold-season warming event and the significantly warmer soil temperatures exiting the cold season, depth to permafrost counterintuitively shallowed in 2022. This evidence led us to conclude that winter meteorological conditions are not the primary control on year-to-year permafrost depth at most locations.

Instead of cold-season conditions, year-to-year variation in depth to permafrost correlated with warm-season conditions. The combination of higher warm-season growing degree days (**Figure 3.1**A, J) and higher warm-season thermal conductivity due to higher average warm-season soil moisture (**Figure 3.1**L) led to higher warm-season ground heat flux in 2023 than in 2022 (**Figure 3.1**K). The magnitude of warm-season ground heat flux in 2021 was between those of 2022 and 2023. Depths to permafrost in 2021 followed a similar pattern as ground heat flux, with median values between those of 2022 and 2023 statistically indistinguishable from either group.

The key reason warm-season behavior dominated year-to-year variation at most locations while cold-season behavior did not is that there was little variation in total energy required to warm and thaw soils among locations that always overcame the zero curtain or never overcame the zero curtain. The energy required to induce phase change, in this case, freezing or melting soil water, requires considerably more energy than warming or cooling soils. For locations that overcame the zero curtain in all study years, colder minimum temperatures experienced in 2023 coincided with a < 4% increase in energy requirement compared to 2022 soils. Among locations that never overcame the zero curtain, the increase in energy requirement was ~50% greater in 2023 than in 2022. However, the magnitude of this increase was small, < 4% of the total energy requirement of Zone 3 locations. Warm-season ground heat flux was 37% greater in 2023 than in 2022, sufficient to overcome cold-season energy differences for Zone 1, Zone 3, and Zone 5 locations. Thus, warm-season meteorological forcing dominated the impacts of cold-season meteorological forcing.

Warm-season conditions did not determine permafrost behavior for all locations. In 2023, two Zone 2 locations experienced shallowing in depth to permafrost (**Figure 3.7**B) of 14 cm and 56 cm, respectively. This difference is an order of magnitude greater than year-to-year differences experienced across the rest of the transect (~5 cm). These two locations overcame the zero curtain in 2023 but not in 2021 or 2022. Due primarily to increased soil ice content in 2023, these Zone 2 locations experienced 40% and 125% increases in energy requirements to thaw compared to 2022. The change in required thaw energy was greater than the increase in ground heat flux experienced in 2023, resulting in the observed difference in depth to permafrost. Calculation specifics are included in

SI2.2 Energy Required for Thaw Calculations for Figure 3.2 and Figure 3.5

3.4.4 Impacts of Changing Meteorological Forcing on Long-Term Permafrost Progression

Northern high latitudes are projected to get warmer and wetter[28,79–83]. As displayed in our study, the impact of these changes on year-to-year permafrost depth depends on various factors. Locations that always or never overcame the zero curtain resisted changes in cold-season meteorological forcing. These locations experienced relatively small changes in depth to permafrost driven by warm-season temperature and thermal conductivity. These trends mirror continuous and ecosystem-protected permafrost, which experiences relatively slow change. Continuous permafrost areas are thermally similar to Zone 3 locations, while ecosystem-protected permafrost is similar to Zone 5. Ecosystem-protected permafrost can remain for decades despite never overcoming the zero curtain[16,33]. Permafrost sites in currently cold and stable permafrost regions may experience slow warming over time, making site permafrost more susceptible to variations in cold-season behavior.

Once locations reach a thermal tipping point, meaning they only overcome the zero curtain during some years, they become more sensitive to changing cold-season conditions. At our site, two locations overcame the zero curtain in 2023 that could not in 2021 and 2022. This change in cold-season thermal behavior resulted in an over 50 cm change in measured depth to the frost table at one location. At discontinuous permafrost sites like ours, we expect locations at this thermal tipping point to be common where colder permafrost locations spatially transition to warmer ones. At our site, permafrost shallowed due to especially cold cold-season conditions. A thermal trend opposite to that observed at our site is expected to be equally common. Suppose a location that normally overcomes the zero curtain cannot fully freeze during a particularly snowy or warm cold season. In that case, this location would leave the cold season with substantially lower energy required to thaw soils due to low ice content and be at risk for thaw. This case is likely to result in the formation of taliks, locations underlain by permafrost containing a layer of soil that remains unfrozen year-round, which have been shown to lead to future thaw[35,36,61,88].

Extrapolating to the greater permafrost zone, regions containing permafrost that always or never overcomes the zero curtain are expected to experience relatively small year-to-year changes in depth to permafrost due to warm season meteorological forcing. Though this same variation in warm-season forcing is expected to impact locations on the thermal tipping point, our study demonstrates that changes in ground ice content due to variations in cold-season conditions cause larger-scale changes and, therefore, dictate the behavior of soil thermal regimes and permafrost progression.

3.4.5 Conclusion

Using high-resolution soil temperature data, repeat permafrost surveys, and measurements of environmental variables, we determined that spatial variation in thermal regime and depth to permafrost was controlled by local slope and wetland proximity. Locations on mild slopes had higher near-surface soil moisture going into the cold season, allowing them to release more energy, freeze more quickly, and become colder than drier locations on steeper slopes. Locations near the wetland complex were warmer and had deeper depths to permafrost than locations with similar environmental metrics across the site due to the wetland acting as a thermal buffer. The spatial variation in permafrost depth across our measurement transect was over 100 cm.

By comparing year-to-year variation in depth to permafrost and thermal variables, we determined that among locations that either overcame the zero curtain during all years (Zone 3) or never overcame the zero curtain (Zone 1 and Zone 5), year-to-year differences in depth to permafrost were due to differences in warm-season ground heat flux, driven by warm season atmospheric temperatures and differences in thermal conductivity caused by soil moisture. These observed variations in permafrost depth were ~5 cm and showed little to no dependence on cold-season conditions. In contrast, locations that overcame the zero curtain during only some years were highly sensitive to cold-season meteorological forcing. Locations that overcame the zero curtain in 2023 experienced 14 cm and 56 cm shallowing of the permafrost table, respectively. This result shows the relative sensitivity of permafrost locations at a thermal tipping point compared to significantly warmer or colder locations.

4 Chapter 4: The Watershed-Bog Connection: How Permafrost Plateau Nutrient Inputs Affect Methane Emissions

4.1 Introduction

As permafrost thaws, previously frozen carbon is processed and rapidly lost to the atmosphere[6]. Thaw of ice-rich permafrost causes subsidence, resulting in thermokarst features such as wetlands. Formation of wetlands, such as bogs, generates methane, a greenhouse gas 28-34 times greater global warming potential over a 100-year timescale than carbon dioxide[101,102]. Methane emissions regulate the near-term global warming potential of permafrost thaw[8]. Though initial greenhouse gas emissions from permafrost thaw can be offset over decades of carbon accumulation in biomass of bog plants, methane emissions are often sufficient to offset this long-term carbon uptake[6,8,9]. Warming atmospheric temperatures in northern high latitudes have and will continue to increase wetland methane emissions through continued permafrost thaw and the formation of new wetland areas[103,104]. Despite the importance of understanding these processes, our estimates of methane emissions and how emissions will respond to long-term environmental changes remain highly uncertain. Estimates of Boreal-Arctic wetland CH_4 emissions have ranged from 9 to 53 Tg CH_4/yr[105–115].

Saturated wetland soil is anoxic (i.e., without oxygen). Anoxic environments allow certain microorganisms to thrive, such as methanogens, which break down organic carbon and produce methane (CH4). Methane production and transport rates are sensitive to environmental conditions, including temperature[115–118] and gross primary productivity[115,119]. Warmer temperatures enhance methane emissions by increasing rates of microbial processing[116,120], while increased vegetation growth provides recently fixed carbon as substrate[23,119,121–123] and aids methane transport through increased rates of diffusive and convective transport[119,124–127]. Increased rates of microbial activity and plant growth require increased consumption rates of nutrients such as nitrogen[128–133].

Nitrogen is often a limiting nutrient for plant and microbial processes in bog systems[134]. Bog systems are hydrologically disconnected from the surrounding landscape and only receive nutrients from rain, snow, and runoff from immediately surrounding areas. Studies have shown methane emissions increase when nitrogen is added to wetland systems[135–137]. This increase is due primarily to a relief of nitrogen limitation to plant growth[138–140]. Methane-producing microbes have also been shown to become nitrogen-limited[141], and microbes associated with our wetland complex were shown to process nitrogen-containing carbon compounds preferentially[142].

Data collected by Neumann et al. demonstrated that spring rainfall facilitated a ~30% increase in bog complex methane emissions[18]. During Neumann's study, spring rain caused subsurface runoff to flow from the permafrost plateau into the bog complex. This

hydrologic input rapidly warmed bog soils and enhanced methane emissions, likely through the support of vegetation growth and microbial processing rates. This study highlighted the watershed-bog connection and demonstrated how small hydrologic and biogeochemical changes in the plateau can propagate and become amplified in the bog. The bog methane response observed by Neumann et al. was complex[18]. Of two of the rainiest years on record, bog methane emissions only increased in the year with spring rain. Reasons for this are hypothesized, but additional data is needed to gain a mechanistic understanding because the study did not explicitly track water or nutrient inputs, and bog soil temperature data was limited.

To better understand the impact of the watershed-bog connection on methane emissions, we filled prior knowledge gaps by explicitly tracking energy, water, and nutrients across the permafrost plateau into the bog complex. We utilize high-resolution soil temperature data, nutrient data from ion exchange resins, and various hydrologic tools to understand this landscape-scale movement. On-site covariance tower data allowed us to track methane emissions and, combined with our environmental variables, identify the mechanisms responsible for enhanced methane emissions.

4.2 Methods

4.2.1 Site Description

The site is in Interior, Alaska (64.70 °N, −148.3 °W) within the Bonanza Creek Long Term Ecological Research Forest, part of the Alaska Peatland Experiment. Fieldwork took place from June 2019 through October 2023. The site is in the discontinuous permafrost zone. From 2011 to 2020, the mean annual air temperature (MAAT) was -0.7 ± 1.5 °C, and the mean annual precipitation was 294 ± 106 mm[94].

The bogs are composed of ~70 cm thick peat mats (bulk density, 0.06 g/cm^3 ± 0.03 g/cm^3; field water content, 86 ± 10 vol.%) that float on top of a ~70 cm thick watery peat layer (bulk density, 0.21 ± 0.20 g/cm^3; field water content, 89 ± 11 vol.%), that is underlain by mineral soil[95]. The bog complex is dominated by *Sphagnum* mosses and vascular plants such as water sedge (*Carex* spp.), bog rosemary (*Andromeda polifolia*), cotton grass (*Eriophorum* spp.), and leather leaf (*Chamaedaphne calyculata*). Drier and higher elevation bog areas called hummocks additionally support dwarf birch (*Betula nana*), bog birch (*Betula glandulosa*), and larch (*Larix laricina*).

Permafrost plateau soil consists of 20-50 cm of peat underlain by mineral soil. Plateau peat soils have a low bulk density (0.27 ± 0.16 g/cm^3) and high field water content (74 ± 16 vol.%)[95]. Plateau vegetation changes with elevation. As elevation increases, sphagnum moss gives way to feather moss and black spruce progress from small and sparse to dense and large with a nearly closed canopy. Understory vegetation includes cotton-grass (*Eriophorum chamissonis*), cloudberry (*Rubus chamaemorus*), labrador tea

(*Ledum groenlandicum*), lowbush cranberry (*Vaccinium vitis-idaea*), and blueberry (*Vaccinium uliginosum*). Permafrost thaw commenced at the site between 50 and 400 years ago[96,97].

4.2.2 Field Measurements

Soil temperatures were measured using 120 cm and 160 cm long Distributed Temperature Profilers (DTPs) with sensors every 10 cm[51] installed in August 2020. DTPs have a 15-minute measurement interval and an accuracy of ± 0.05°C. Data were linearly interpolated for location-to-location consistency and depth-corrected annually to account for frost heave and subsidence. HOBO TidbiT v2 temperature data loggers were used to capture wetland soil temperatures beneath DTPs. The shallowest TidbiT sensors were installed to overlap with the deepest DTP sensors (~140 cm depth) and extended every 10 cm to the peat-mineral soil interface. TidbiTs had a 15-minute measurement interval with an accuracy of ± 0.2 °C. Permafrost table depth was estimated annually through manual probing in early September with three replicate measurements per location. The probe length was 2.2 m. Additional depth to frost table measurements were taken via manual probing weekly in the bog complex and bi-weekly in the permafrost plateau.

In-Situ pressure transducers were deployed in piezometers screened at 25 cm, 50 cm, and 100 cm in the bog complex and fully screened PVC wells at seven locations in the permafrost plateau from May to September (2019–2023). Barometers were installed underground in dry, fully screened wells during parallel periods. Sensor data were verified with manual groundwater measurements taken weekly in the bog complex and bi-weekly in the permafrost plateau with a Solinst Water Level Meter. Soil moisture was measured at seven locations using GroPoint Multi-Depth Soil Moisture Sensors attached to GroPoint Data Loggers. Four sensors were installed in August 2020, and three additional sensors were installed in October 2022. Profilers took spatially continuous soil moisture readings from the surface to the permafrost table. Profilers measured a composite value of percent water every 15 cm at a 30-minute measurement interval. Outputs were calibrated for peat and mineral soils[56], and a manufacturer-provided dielectric correction (1.019) was applied for ≤0 °C soils. Bog complex water storage and saturated thickness were calculated by combining averaged piezometer-derived water level data at each bog location with manual measurements of water levels to mineral soil. These values were verified by tracking the floating bog surface relative to mineral soil[143]. Since the bog consists of a peat mass floating on a watery peat layer, the bog surface rises when the thickness of the watery peat layer increases.

Soil nutrient and metal availability were measured using UNIBEST Ion-Exchange Resin Capsules[144]. Resins were deployed and retrieved monthly in 2021, 2022, and 2023 during the growing season, June through October. Resins continuously absorb both cations and anions. Quantities of elements and molecules accumulated in the capsule during deployment relate to bioavailability. Resins frozen into the soil while deployed remained

until the next deployment/retrieval date. Resins were installed at 13 locations across the site. Three to five resins were simultaneously installed at each location to capture multiple depths. In the permafrost plateau, resins were installed into the soil at depths of 15, 30, and 45 cm using a spring-loaded PVC design by WECSA, LLC, and into plateau wells beneath pressure transducers to measure nutrient availability in the subsurface aquifer. Resins with coated 10 g tungsten fishing weights were installed inside the wells to move downward with the thawing frost table. In the bog complex, resins were hung in piezometers screened at 25 cm, 50 cm, and 100 cm at a depth of 50 cm. Resins were extracted with 2M HCl and analyzed for total N, NO_3-N, NH_4-N, Al, B, Ca, Cu, Fe, K, Mg, Mn, Na, P, S, and Zn by the UNIBEST lab facility.

Plant species heights and abundance were measured annually using the "point bar" method. This method measures the frequency and height of vegetation in meter-squared plots by recording all vegetation encounters with light emitted from a downward-facing laser along an "X" pattern. The metal frame used in this method was placed into permanently installed PVC pipes to ensure repeat surveys captured common locations. We additionally estimated the percentage cover of all vascular and bryophyte species in the same one-meter by one-meter plots. Moss growth was measured bi-weekly with three cranked wire installations at seven plateau locations[145–147].

Relative elevation of instrumentation was determined through a combination of manual level surveys and real-time kinematic (RTK) GPS. Surveys were conducted roughly monthly. GPS data were recorded using Emlid Reach RS2 units. Control points, higher elevation non-permafrost locations, were used to compare RTK GPS surveys across time.

4.2.3 Flux Tower Measurements

Fluxes of water, energy, and gases were collected with two on-site eddy covariance towers. One flux tower is on the permafrost plateau, and the other is on the bog complex. Tower data utilized in these analyses include precipitation, air temperature, evapotranspiration, snow depth, methane emissions, gross primary productivity (GPP), and ground heat flux. Eddy covariance measurements are detailed in Euskirchen et al.[96].

4.2.4 Statistical Methods

Environmental variables and thermal response metrics were compared using one-way ANOVA followed by Tukey HSD post-hoc using $\alpha = 0.05$. Data were $\log_{10}$ transformed to increase normality and reduce skew before ANOVA analysis. Data presented in the figures are shown in non-transformed space for visual clarity. Correlations were determined by fitting data with linear or exponential regression models and using two-sided hypothesis testing with $\alpha = 0.05$.

4.3 Results

4.3.1 Bog Methane Fluxes During Study Period

The cumulative methane flux observed by the bog complex covariance tower was highest in 2023, followed by 2022 and 2021. Cumulative methane fluxes were 429 mg/m^2, 584 mg/m^2, and 806 mg/m^2 in 2021, 2022, and 2023, respectively (**Figure 4.1**).

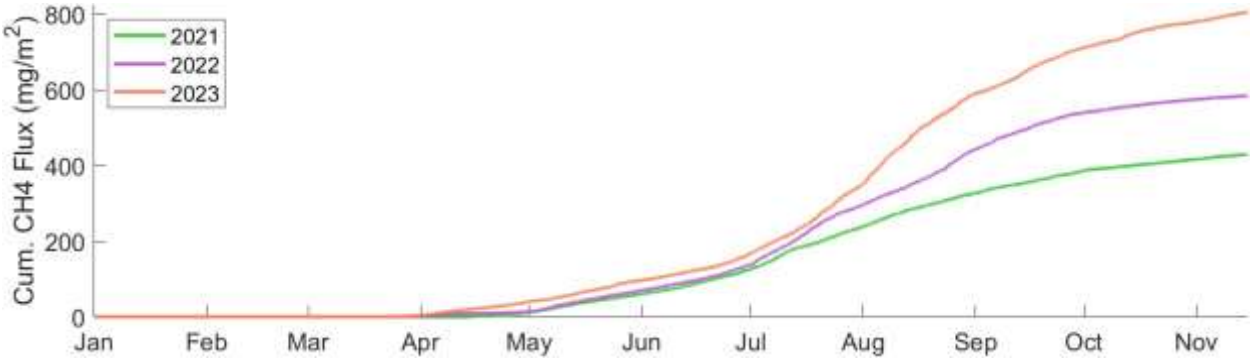

Figure 4.1 Bog complex methane emissions from 2021 to 2023. *Line graphs show stacked annual time series of bog methane flux. Data for 2021 is green, 2022 is purple, and 2023 is orange.*

4.3.2 Permafrost Plateau Thermal, Hydrologic, and Environmental Behavior

The wettest study year was 2021, followed by 2023 and 2022 (**Figure 4.2**A). Total water balance values, calculated by subtracting cumulative evapotranspiration from cumulative precipitation and snow water equivalent, were 46 cm, -18 cm, and 3 cm in 2021, 2022, and 2023, respectively (**Figure 4.2**A). The timing of precipitation varied from year to year. During the 2021 growing season, most precipitation fell during August and September. In 2022, the most precipitation fell from September to early October. In 2023, precipitation events spread throughout the growing season, with the largest occurring in June and August. Periods of saturated conditions on the permafrost plateau, which coincided with flow from the plateau into the bog complex, occurred primarily during periods of heavy precipitation (**Figure 4.2**A, B). In 2021, saturated conditions in the permafrost plateau did not occur until August, but that event resulted in the greatest observed average saturated thickness, 45 cm (**Figure 4.2**B). Saturated conditions in 2022 were present during most of July and October (**Figure 4.2**B). There was likely flow in May 2022 prior to seasonal measurements. Intermittent saturated conditions in June, July, August, and September 2023 coincided with wet and dry periods (**Figure 4.2**A, B).

Cumulative ground heat flux was greatest in 2023, followed by 2022 and 2021 (**Figure 4.2**C). These net cumulative values were 29606 W/m^2, 42451 W/m^2, and 58633 W/m^2 in 2021, 2022, and 2023, respectively. Seasonal ground heat flux varied substantially between years. The negative ground heat flux experienced during the 2021 cold season was greater than those experienced in 2023 and 2022. Cold-season ground heat flux values in 2021,

2022, and 2023 were -30231 W/m^2, -8888 W/m^2, and -17663 W/m^2, respectively. Warm-season ground heat flux was greatest in 2023, followed by 2021 and 2022. Warm-season ground heat flux in 2021, 2022, and 2023 were 68955 W/m^2, 56993 W/m^2, and 78281 W/m^2, respectively. Seasonal thaw in the permafrost plateau progressed similarly during all study years (**Figure 4.2**D). Seasonal thaw progressed more quickly in 2021 and 2023 than in 2022 (**Figure 4.2**D). As shown in the example soil temperature data (**Figure 4.2**E), soils froze more quickly in 2023 than in 2021 or 2022. The average zero curtain duration, or time required after reaching a soil temperature of 0 °C for all soil water to freeze, in 2023 was 20 and 40 days shorter than in 2021 and 2022, respectively. Gross primary productivity was 8% greater in 2023 than in 2021 and 2022 (**Figure 4.2**F). On September 3, 2021, 2022, and 2023, gross primary productivity values were 29794 µmol/m^{2}s, 28539 µmol/m^{2}s, and 32254 µmol/m^{2}s, respectively.

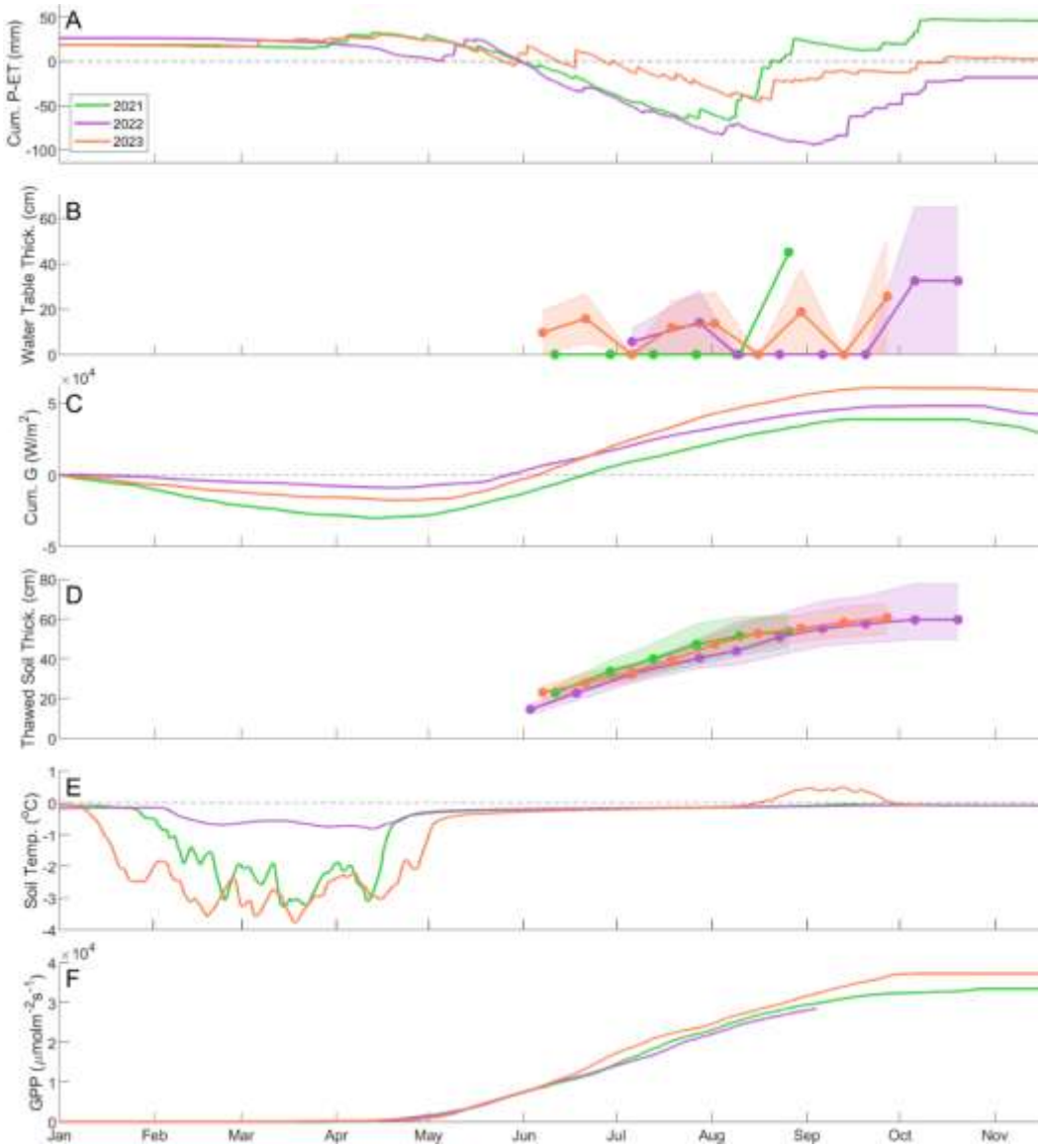

Figure 4.2 Permafrost plateau hydrologic, thermal, and environmental variables. *Line graphs show stacked annual time series of (A) cumulative total water consisting of maximum snow water equivalent and cumulative precipitation minus cumulative evapotranspiration, (B) median water table thickness, (C) cumulative ground heat flux, (D) median depth of thawed soil, (E) soil temperature at a depth of 30 cm, and (F) gross primary productivity (GPP). Data for 2021 is green, 2022 is purple, and 2023 is orange. Shaded areas define the first and third quartiles from the median with color according to the year.*

Availability of ammonium (NH_4) was greater in 2023 than in 2021 or 2022 at all observed soil depths (**Figure 4.3**A, B, C). Across all years, availability values show seasonal trends, peaking in August and declining in September. In 2023, available NH_4 began high, especially at a depth of 30 cm, and maintained heightened values until September. Values at 15 cm depth tend to be lower than those measured at 30 cm and 50 cm during the same measurement periods.

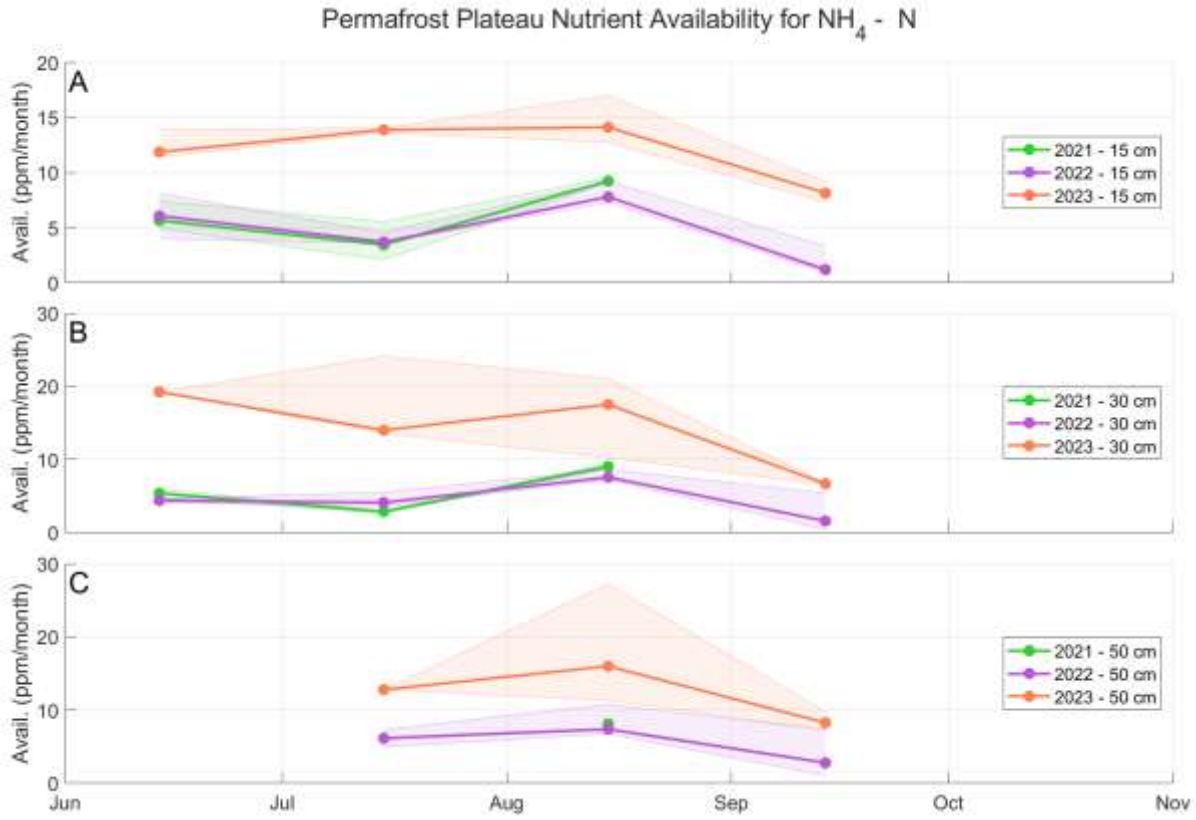

Figure 4.3 Plateau NH_4-N availability time series plots. *Line graphs show a stacked time series of availability of NH_4-N at depths of (A) 15 cm, (B) 30 cm, and (C) 50 cm. Data for 2021 is green, 2022 is purple, and 2023 is orange. Shaded areas define the first and third quartiles from the median with color according to the year.*

4.3.3 Bog Complex Thermal, Hydrologic, and Environmental Behavior

Bog tower data confirmed the results from the permafrost plateau tower that 2021 was the wettest study year, followed by 2023 and 2022 (**Figure 4.2**A, **Figure 4.4**A). Total water balance values from the bog tower were lower than those measured by the forest tower,

with less variation between years. These values were -43 cm, -89 cm, and -56 cm in 2021, 2022, and 2023, respectively (**Figure 4.4**A). The timing of spikes in total water caused by precipitation events was identical between the forest and bog towers (**Figure 4.2**A, **Figure 4.4**A). During all years, bog saturated thickness, a measurement of bog water storage, decreased during June and July and increased due to precipitation in August and September. During June 2023, there are clear spikes in bog saturated thickness (**Figure 4.4**B) that coincide with June rain events (**Figure 4.4**A) and the presence of groundwater flow from the permafrost plateau (**Figure 4.2**B).

Cumulative ground heat flux was greatest in 2022 (**Figure 4.2**C). Net cumulative heat flux values were 34801 W/m^2, 58511 W/m^2, and 35264 W/m^2 in 2021, 2022, and 2023, respectively. Seasonal ground heat flux varied substantially between years. The negative ground heat flux experienced during the 2021 cold season was greater than in 2023 and 2022. The cumulative values in 2022 begin a week after a large rain-on-snow event during a cold-season heat wave, which likely caused ground heat flux values to be minimized. Cold season ground heat flux in 2021, 2022, and 2023 were -45972 W/m^2, -179 W/m^2, and -27089 W/m^2, respectively. Warm season ground heat flux was greatest in 2021, followed by 2023 and 2022. Warm season ground heat flux in 2021, 2022, and 2023 were 97905 W/m^2, 70611 W/m^2, and 75969 W/m^2, respectively. Gross primary productivity was 30% greater in 2023 than in 2021 and 2022 (**Figure 4.4**H). In 2021, 2022, and 2023, gross primary productivity values were 17899 µmol/m^{2}s, 18034 µmol/m^{2}s, and 23447 µmol/m^{2}s, respectively.

During the cold season of 2021, with the highest magnitude negative ground heat flux, bog edge locations reached negative soil temperatures, indicating the formation of ground ice (**Figure 4.4**D). Shallow soil temperatures from both the bog edge and bog center reached above-zero temperatures in 2022, then in 2023 and 2021 (**Figure 4.4**D, F). Shallow soils during years with lower magnitude negative ground heat flux during the cold season (**Figure 4.4**C) warmed faster during the following warm season (**Figure 4.4**D, F). Deep soil temperatures experienced early-season spikes in soil temperatures during late April or early May, coinciding with the melting of the snowpack. Compiled soil temperature metrics from six locations indicated no statistical significance in the minimum soil temperature reached during the cold season of 2021, 2022, or 2023 at shallow or deep soil depths (**Figure 4.5**A, B). Location-to-location variation in shallow soil temperatures was higher in 2021 than in other years, with minimum temperatures observed from -3.3 °C to 0.0 °C (**Figure 4.5**A). Maximum temperatures in 2023 were significantly above the median, and those in 2021 were significantly below the median (**Figure 4.5**C, D, $p < 0.05$), with temperatures observed in 2022 being statistically indistinguishable from median temperature values. Maximum shallow soil temperatures in 2021, 2022, and 2023 were 7.8 ± 2.5 °C, 9.5 ± 1.5 °C, and 10.9 ± 2.3 °C, respectively (**Figure 4.5**C). Maximum deep soil temperatures in 2021, 2022, and 2023 were 7.2 ± 3.1 °C, 8.7 ± 2.8 °C, and 10.2 ± 3.6 °C, respectively (**Figure 4.5**D).

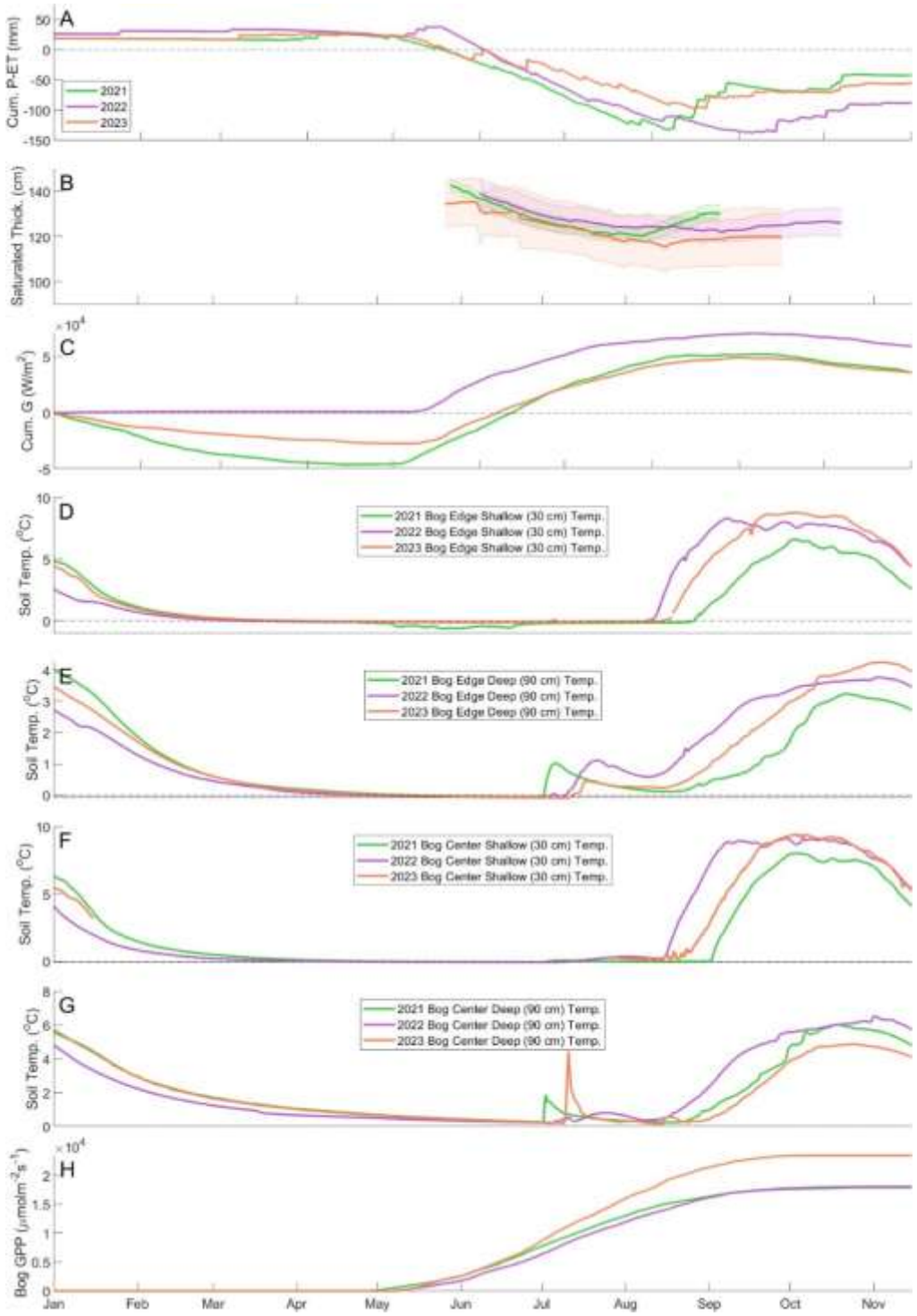

Figure 4.4 Bog complex hydrologic, thermal, and environmental variables. *Line graphs show stacked time series of (A) bog saturated thickness, (B) cumulative ground heat flux, (C) near-surface (10 cm) soil temperature at bog edge locations, (D) deep (90 cm) bog temperature at bog edge locations, (E) near-surface (10 cm) soil temperature at bog center locations, (F) deep (90 cm) soil temperature at bog center locations, and (G) gross primary productivity (GPP). Data for 2021 is green, 2022 is purple, and 2023 is orange. Shaded areas define the first and third quartiles from the median with color according to the year.*

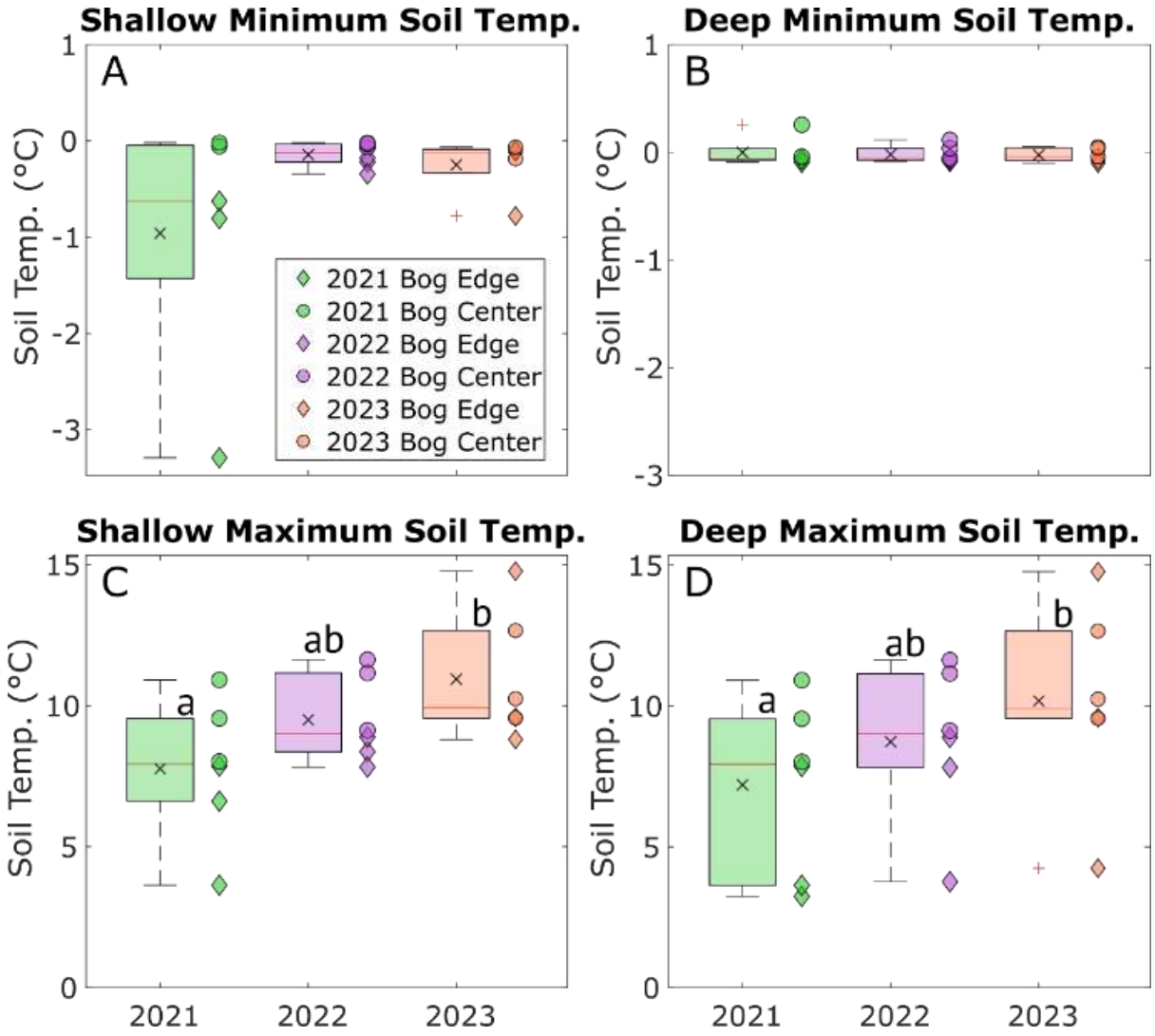

Figure 4.5 Year-to-year bog soil temperature. *Box and whisker plots showing: (A, B) Minimum soil temperatures reached in (A) shallow and (B) deep soil depths in 2021, 2022, and 2023. (C, D) Maximum soil temperatures reached in (C) shallow and (D) deep soil depths in 2021, 2022, and 2023. Shallow and deep soil temperature measurements were observed at 30 cm and 90 cm, respectively. Data for 2021 is green, 2022 is purple, and 2023 is orange. Data from bog edge locations are shown as diamonds. Data from bog center locations are shown as circles. On each box plot, the central line indicates the median, 'x' marks the mean, edges of the box indicate the 25th and 75th percentiles, whiskers indicate the most extreme non-outlier data points, and a red plus marker indicates an outlier greater than 2.7 standard deviations from the mean. Letters on top of boxes indicate data sets with statistically significant differences in mean as determined through one-way ANOVA.*

Ammonium (NH_4) availability in the bog complex was comparable each year at all observed depths (**Figure 4.6**A, B, C). Over all years, availability values declined in September. In 2023, available NH_4 began below 2022 values, then increased sharply in July and maintained high values in August. Values at 100 cm depth tended to be lower than those measured at 25 cm and 50 cm.

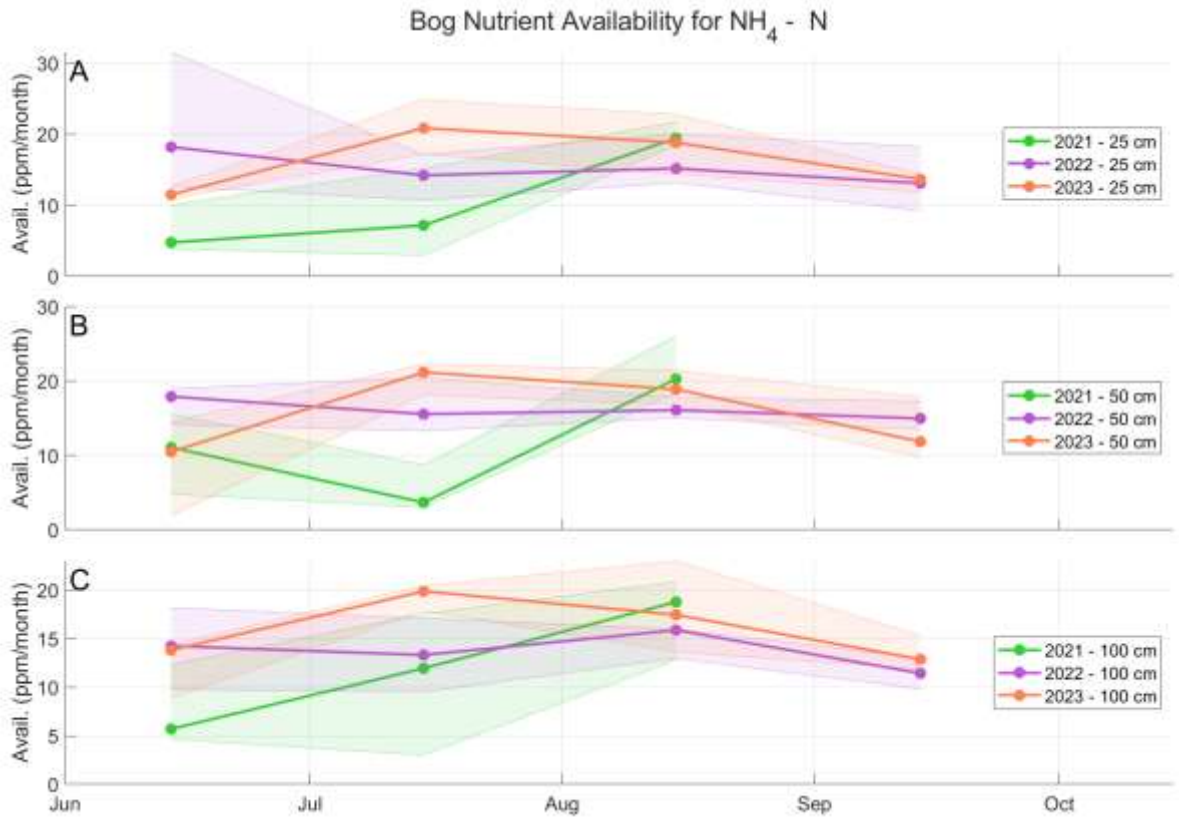

Figure 4.6 Bog NH_4-N availability time series plots. *Line graphs show a stacked time series of availability of NH_4- N in piezometers screened at depths of (A) 25 cm, (B) 50 cm, and (C) 100 cm. Data for 2021 is green, 2022 is purple, and 2023 is orange. Shaded areas define the first and third quartiles from the median with color according to the year.*

4.4 Discussion

4.4.1 Root Damage Due to Rapid Freezing of Plateau Soils Caused Increased Nutrient Availability

Ammonium (NH_4) availability in plateau soils was twice as high in 2023 than in 2021 or 2022 (**Figure 4.3**). This increase was likely due to decreased plateau nitrogen consumption due to root damage caused by the rate at which soils froze during the 2023 cold season. Nitrogen in permafrost plateau soils depends on the balance of nutrient consumption by plateau vegetation and the nutrient supply created by microbes as they convert soil organic nitrogen into bioavailable forms such as NH_4^+ and NO_3^-. When supply exceeds demand, excess nitrogen leaches into plateau soil. Excess nitrogen can be advectively transported in groundwater when plateau soils are saturated.

During the cold season, microbial activities continue, albeit at slower rates[148–150]. This microbial processing results in standing pools of bioavailable nitrogen that peak in the early spring as soils thaw[151,152]. Once soil thaws, plateau vegetation can utilize this

standing nitrogen pool. However, plants with damaged roots cannot efficiently use nitrogen during the early growing season[153,154].

The zero curtain duration was the shortest in 2023 (**Figure 3.7**). Although boreal trees and vascular vegetation can tolerate cold stress experienced annually during the cold season, sudden and rapid temperature drops such as this can result in freezing-induced injuries[153,154], hindering growth and productivity. Damage to cell membranes is attributed to ice formation and cellular dehydration during chilling and freezing[155,156]. Root damage in 2023 presumably reduced the ability of plateau vegetation to grow and take up nitrogen, leading to the high values of nitrogen availability observed in 2023 (**Figure 4.3**).

4.4.2 The Amount and Timing of Rain-Induced Nutrient Transport Controlled Bog Biogeochemical Response

Saturated conditions were observed in the permafrost plateau during some periods of the growing season in 2021, 2022, and 2023 (**Figure 4.2**B). Driven by variation in elevation head between plateau and bog locations, these periods presumably caused nutrient-carrying subsurface flow from the permafrost plateau into the wetland complex. The magnitude of the nutrient flux depends primarily on the flow rate from the plateau and soil nutrient availability. During 2023, plateau ammonia availability was the highest (**Figure 4.3**), and maximum hydrologic flow rates were the lowest. The highest flow rates, indicated by the thickest saturated layer, occurred in 2021 and 2022 (Figure 2B).

In August 2021, average ammonium availability was around half of that observed in 2023, but saturated thickness was roughly double. These two factors caused the 2021 August nitrogen flux to be similar in scale to that of June 2023. The probable reason nutrient fluxes in 2023 increased methane emissions (**Figure 4.1**) and bog vegetation growth (**Figure 4.4**H), while a similar magnitude flux in 2021 did not, is timing. Rates of vegetation growth, as shown through the slope of the bog gross primary productivity plot in **Figure 4.4**H, peaked annually in June and July and then slowed in August. The June 2023 nitrogen flux occurred when nutrient needs and consumption were highest, allowing vegetation and microbial communities that may have been nutrient-limited otherwise to continue at uninhibited rates. Since the nitrogen flux in 2021 occurred after vegetation growth and nutrient consumption had slowed, the impact on methane-affecting processes was reduced.

In addition to the timing of nutrient fluxes affecting the impact on biogeochemical processes, timing also affected the nutrient flux magnitude. During May 2022, the site experienced large amounts of early-season precipitation (**Figure 4.2**A). A nitrogen flux into the bog complex during this period would have likely increased plant growth and microbial processing rates. However, because most permafrost plateau soils were still frozen (**Figure 4.2**D), flow entered the bog complex as either surface runoff or shallow subsurface flow (<

10 cm). This thin hydrologically active layer limited the available substrate for nutrient accumulation, presumably causing the nutrient flux to be relatively small.

The impacts of seasonal timing on biogeochemical processes and nutrient concentrations made the June 2023 flux ideal for maximizing the nutrient flux magnitude and impact on biogeochemical processes. Fluxes of water took place in June after surface soils had thawed to between 20 cm and 40 cm (**Figure 4.2**D), and plateau nitrogen availability in this layer was high (**Figure 4.3**A, B), leading to a high magnitude nitrogen flux. This nitrogen flux occurred during peak bog complex nutrient consumption rates, maximizing the impact on vegetation growth and microbial processing rates. These factors, in concert, aided the increase in methane emissions observed in 2023.

4.4.3 Methane Emissions Scaled with Bog Complex Soil Temperatures and Vegetation Activity

Wetland methane emissions are closely linked to temperature[115–118] and gross primary productivity[115,119]. These variables tend to scale together due to warmer temperatures increasing rates of microbial processing[116,120], increased vegetation growth which provides recently fixed carbon as additional substrate for microbes[23,119,121–123], and aiding methane transport through increased rates of diffusive and convective flow[119,124–127].

The expected behavior of these variables mirrors our observed relationships. Methane emissions were highest in 2023, with emissions in 2022 and 2021 being 38% and 88% lower, respectively (**Figure 4.1**). Following a similar trend, maximum bog complex soil temperatures were highest in 2023, with temperatures that were 28% and 40% lower in 2022 and 2021 (**Figure 4.4**D-G, **Figure 4.5**), and gross primary productivity was highest in 2023 with values that were 30% and 31% lower in 2022 and 2021 **Figure 4.4**H). The impact of these interconnected values was presumably amplified by observed nitrogen fluxes from the plateau into the wetland complex in 2023, reducing nitrogen-limitation of vegetation growth and microbial processing rates.

In 2021, elevated negative ground heat flux caused some bog edge locations, the highest emitting sections of the bog, to freeze. The additional energy needed to thaw these frozen soils caused these locations to warm more slowly during the following growing season (**Figure 0.62-0.64**). This delayed warming slowed biogeochemical processes such as plant growth and microbial processing, likely contributing to lower methane emissions observed in 2021.

4.4.4 Biogeochemical Responses to Climate in a Warmer and Wetter Future

Prior studies have demonstrated that the amount and timing of rain can regulate soil temperatures within permafrost thaw bogs, affecting vegetation growth and methane emissions[18]. In addition to energy fluxes, our study demonstrates that the amount and timing of rain can regulate the nutrient availability of bog soils through rain-induced

nutrient fluxes from the permafrost-underlain watershed into the wetland complex. As boreal regions experience continued permafrost thaw and formation of new wetland areas[104,157] and northern high latitudes continue to experience increased precipitation, especially in the early warm season[47,158], our data indicate that methane emissions will increase and accelerate short-term global warming.

Our study demonstrates the complex interactions between cold-season conditions and methane emissions. In 2023, cold-season conditions caused roots to rapidly freeze and become damaged, which reduced spring nitrogen uptake by plateau vegetation, increasing nitrogen availability in the plateau. Advective transport of this excess nitrogen supported biogeochemical processes and enhanced methane emissions. In 2021, however, freezing of bog soils reduced methane emissions. Cold-season conditions were sufficient to freeze some bog-complex soils, delaying soil warming and reducing vegetation growth and methane emissions. Soil ground heat flux is controlled by atmospheric temperature, soil thermal conductivity, and insulation from snow. As northern high-latitude cold seasons continue to become warmer and wetter, thermally-driven controls on methane emissions are likely to increase in importance.

4.4.5 Conclusion

During our study period at a permafrost thaw bog complex in Interior, Alaska, we observed methane emissions in 2023 that were 38% and 88% greater than the previous two years, respectively. Based on high-resolution soil temperature data, nutrient availability data, flux tower data, and hydrologic data, we determined that this increase in methane emissions was due to a combination of nitrogen transport from the permafrost plateau watershed and warm bog soil temperatures. Warm soil temperatures increased microbial activity and vegetation growth rates, while nitrogen fluxes from the plateau watershed allowed these processes to continue at high rates without becoming nitrogen-limited. Nitrogen availability in the permafrost plateau was around two times greater in 2023 than in the preceding years due to root damage that occurred because of a shortened period of soil freezing.

5 Conclusions

5.1 Summary of Key Findings

Chapter 2:

- There was a nine-fold increase in permafrost thaw rates due to three consecutive wet and snowy years and a history of above 0 °C mean annual air temperatures.
- Microtopographic high points stayed cold and experienced minimal thaw due to shallow cold-season snow and low warm-season soil moisture.
- Microtopographic low points thawed rapidly due to deep insulating cold-season snow and high warm-season soil moisture.
- Locations on slopes thawed due to advective heat transport by rain-induced subsurface runoff.
- Identified mechanisms of thaw are expected to increase in importance, frequency, and magnitude in a warmer and wetter future with more extreme weather events.

Chapter 3:

- Locations on shallow slopes reached colder temperatures with a shallower depth to permafrost due to high cold-season thermal conductivity caused by higher soil moisture.
- Near-wetland locations were warmer and had a deeper depth to permafrost than locations with similar environmental metrics due to the wetland acting as a thermal buffer.
- Warm-season meteorological conditions controlled the year-to-year variation in depth to permafrost among locations that always or never overcame the zero curtain.
- Year-to-year variations in depth to permafrost among locations that sometimes overcame the zero curtain were controlled by cold-season meteorological conditions if conditions resulted in a difference in soil ice content.

Chapter 4:

- Advection of nitrogen from the permafrost underlain plateau watershed, in combination with warm temperatures, increased methane emissions by 65%.
- Root damage from rapid soil freezing inhibited plateau vegetation nitrogen consumption, doubling nitrogen availability.
- The timing of runoff from the permafrost plateau controlled the effects of bog complex biogeochemistry.

5.2 Research Implications and Closing Remarks

A main takeaway of Chapter 2 is that changing precipitation will cause permafrost to thaw more quickly than we predicted. A main takeaway of Chapter 4 is that nutrient-carrying plateau hydrologic inputs will enhance methane emissions beyond expected levels. Key findings across these studies add greater nuance to our understanding of what is well known: atmospheric greenhouse gas concentrations continue to increase, greater greenhouse gas concentrations are causing northern high-latitudes to warm at increasing rates, this warming is causing permafrost to thaw, and the process of thaw is in turn fueling climate change. Current best estimates consider emissions from permafrost thaw on the order of magnitude of a top-emitting country such as the United States or China, a fraction of total anthropomorphic emissions.

I believe continuing to further our understanding of the changing permafrost zone is crucial for two primary reasons: 1) Harsh consequences for the 35 million people living in permafrost landscapes, especially in Indigenous Communities, and 2) when humanity finally reduces our own carbon emissions, emissions from northern high-latitudes will persist.

The consequences of permafrost thaw are harsh, including acceleration of climate change, infrastructure damage, ecosystem degradation, and the displacement and disruption of Indigenous Communities. In this region, it is crucial to understand what controls thaw rates and the impact that thaw has on local and global communities, as well as to engage and support local peoples disproportionately impacted by the consequences of thaw. To this end, not only are continued scientific efforts necessary, but so are efforts to involve and support those most affected in co-producing research and making STEM (Science, Technology, Engineering, and Math) careers attainable for those most affected. We require broad perspectives in this herculean effort, especially from those with long histories in these changing landscapes who have wisdom from multiple frameworks of knowing.

During my Ph.D. I co-coordinated, co-instructed, and am now Associate Director of a youth education program called Fostering Science. This program provides free science experiences to Alaskan foster youth. Most of these youth are Alaska Native. Our instructor team consists of Alaska Native Elders, artists, and scientists. I co-created and co-ran a leadership program called Bonanza Creek Leaders-in-Training. During this program, our paid participants write a cover letter and resume, receive science and science communication training, co-create and teach science curriculum for our youth camp, and assist in running the camp as junior counselors. I plan to continue this work as a key part of my professional efforts and identity.

The other reason understanding the northern high-latitude warming-thaw-emission feedback loop is essential is that even if humanity were to become carbon neutral tomorrow, emissions from the north would continue. If atmospheric concentrations of

greenhouse gas emissions are considered credit card debt, emissions from permafrost thaw are interest payments. As we make purchases and increase our debt, the interest payments will continue to increase. Emissions from permafrost are so exceptionally tricky because when humanity stops making new purchases on our planet's credit card, we will still have interest payments due to emissions from thaw. For this reason, to cool our climate, we not only need to become carbon neutral but sufficiently carbon negative to offset emissions from permafrost in what will surely be a warmer and wetter Arctic.

There is a positive impact to be made in this world. Through understanding these natural systems, through educating the next generation of scientists, and through choosing to do work that makes a positive difference, this work matters.

References

1. Everdingen, R. O. V. Multi-Language Glossary of Permafrost and Related Ground-Ice Terms in Chinese, English, French, German, Icelandic, Italian, Norwegian, Polish, Romanian, Russian, Spanish, and Swedish. (International Permafrost Association, Terminology Working Group, 1998).
2. Brown, J., Sidlauskas, F. J. & Delinski, G. Circum-Arctic map of permafrost and ground ice conditions. (1997).
3. Serreze, M. C. & Barry, R. G. Processes and impacts of Arctic amplification: A research synthesis. Glob. Planet. Change **77**, 85–96 (2011).
4. Smith, S. L., O'Neill, H. B., Isaksen, K., Noetzli, J. & Romanovsky, V. E. The changing thermal state of permafrost. Nat. Rev. Earth Environ. **3**, 10–23 (2022).
5. Kokelj, S. V. & Jorgenson, M. T. Advances in Thermokarst Research. Permafr. Periglac. Process. **24**, 108–119 (2013).
6. Jones, M. C. et al. Rapid carbon loss and slow recovery following permafrost thaw in boreal peatlands. Glob. Change Biol. **23**, 1109–1127 (2017).
7. Frolking, S., Roulet, N. & Fuglestvedt, J. How northern peatlands influence the Earth's radiative budget: Sustained methane emission versus sustained carbon sequestration. J. Geophys. Res. Biogeosciences **111**, (2006).
8. Turetsky, M. R., Wieder, R. K., Vitt, D. H., Evans, R. J. & Scott, K. D. The disappearance of relict permafrost in boreal north America: Effects on peatland carbon storage and fluxes. Glob. Change Biol. **13**, 1922–1934 (2007).

9. Johansson, T. et al. Decadal vegetation changes in a northern peatland, greenhouse gas fluxes and net radiative forcing. Glob. Change Biol. **12**, 2352–2369 (2006).
10. Heijmans, M. M. P. D. et al. Tundra vegetation change and impacts on permafrost. Nat. Rev. Earth Environ. **3**, 68–84 (2022).
11. Jones, B. M. et al. Lake and drained lake basin systems in lowland permafrost regions. Nat. Rev. Earth Environ. **3**, 85–98 (2022).
12. Hjort, J. et al. Impacts of permafrost degradation on infrastructure. Nat. Rev. Earth Environ. **3**, 24–38 (2022).
13. Whiteman, G., Hope, C. & Wadhams, P. Vast costs of Arctic change. Nature **499**, 401–403 (2013).
14. Melvin, A. M. et al. Climate change damages to Alaska public infrastructure and the economics of proactive adaptation. Proc. Natl. Acad. Sci. **114**, E122–E131 (2017).
15. Alvarez, J., Yumashev, D. & Whiteman, G. A framework for assessing the economic impacts of Arctic change. Ambio **49**, 407–418 (2020).
16. Shur, Y. L. & Jorgenson, M. T. Patterns of permafrost formation and degradation in relation to climate and ecosystems. Permafr. Periglac. Process. **18**, 7–19 (2007).
17. Jorgenson, M. T. et al. Resilience and vulnerability of permafrost to climate change. Can. J. For. Res. **40**, 1219–1236 (2010).
18. Neumann, R. B. et al. Warming Effects of Spring Rainfall Increase Methane Emissions From Thawing Permafrost. Geophys. Res. Lett. **46**, 1393–1401 (2019).

19. Bubier, J. L., Moore, T. R., Bellisario, L., Comer, N. T. & Crill, P. M. Ecological controls on methane emissions from a Northern Peatland Complex in the zone of discontinuous permafrost, Manitoba, Canada. Glob. Biogeochem. Cycles **9**, 455–470 (1995).
20. Oberle, F. K. J. et al. Towards determining spatial methane distribution on Arctic permafrost bluffs with an unmanned aerial system. SN Appl. Sci. **1**, 236 (2019).
21. von Fischer, J. C., Rhew, R. C., Ames, G. M., Fosdick, B. K. & von Fischer, P. E. Vegetation height and other controls of spatial variability in methane emissions from the Arctic coastal tundra at Barrow, Alaska. J. Geophys. Res. Biogeosciences **115**, (2010).
22. Christensen, T. R., Jonasson, S., Callaghan, T. V. & Havström, M. Spatial variation in high-latitude methane flux along a transect across Siberian and European tundra environments. J. Geophys. Res. Atmospheres **100**, 21035–21045 (1995).
23. Ström, L., Mastepanov, M. & Christensen, T. R. Species-specific Effects of Vascular Plants on Carbon Turnover and Methane Emissions from Wetlands. Biogeochemistry **75**, 65–82 (2005).
24. Keuschnig, C. et al. Reduced methane emissions in former permafrost soils driven by vegetation and microbial changes following drainage. Glob. Change Biol. **28**, 3411–3425 (2022).
25. Kashi, N. N. et al. Nutrients Alter Methane Production and Oxidation in a Thawing Permafrost Mire. Ecosystems **26**, 302–317 (2023).

26. Lara, M. J., Lin, D. H., Andresen, C., Lougheed, V. L. & Tweedie, C. E. Nutrient Release From Permafrost Thaw Enhances CH4 Emissions From Arctic Tundra Wetlands. J. Geophys. Res. Biogeosciences **124**, 1560–1573 (2019).
27. Jones, B. M. et al. Presence of rapidly degrading permafrost plateaus in south-central Alaska. The Cryosphere **10**, 2673–2692 (2016).
28. Rantanen, M. et al. The Arctic has warmed nearly four times faster than the globe since 1979. Commun. Earth Environ. **3**, 1–10 (2022).
29. Engstrom, R., Hope, A., Kwon, H., Stow, D. & Zamolodchikov, D. Spatial distribution of near surface soil moisture and its relationship to microtopography in the Alaskan Arctic coastal plain. Hydrol. Res. **36**, 219–234 (2005).
30. O'Donnell, J. A., Romanovsky, V. E., Harden, J. W. & McGuire, A. D. The Effect of Moisture Content on the Thermal Conductivity of Moss and Organic Soil Horizons From Black Spruce Ecosystems in Interior Alaska: Soil Sci. **174**, 646–651 (2009).
31. Blok, D. et al. The Cooling Capacity of Mosses: Controls on Water and Energy Fluxes in a Siberian Tundra Site. Ecosystems **14**, 1055–1065 (2011).
32. Juszak, I., Erb, A. M., Maximov, T. C. & Schaepman-Strub, G. Arctic shrub effects on NDVI, summer albedo and soil shading. Remote Sens. Environ. **153**, 79–89 (2014).
33. Loranty, M. M. et al. Reviews and syntheses: Changing ecosystem influences on soil thermal regimes in northern high-latitude permafrost regions. Biogeosciences **15**, 5287–5313 (2018).

34. Iijima, Y. et al. Abrupt increases in soil temperatures following increased precipitation in a permafrost region, central Lena River basin, Russia. Permafr. Periglac. Process. **21**, 30–41 (2010).

35. Connon, R., Devoie, É., Hayashi, M., Veness, T. & Quinton, W. The Influence of Shallow Taliks on Permafrost Thaw and Active Layer Dynamics in Subarctic Canada. J. Geophys. Res. Earth Surf. **123**, 281–297 (2018).

36. Devoie, É. G., Craig, J. R., Connon, R. F. & Quinton, W. L. Taliks: A Tipping Point in Discontinuous Permafrost Degradation in Peatlands. Water Resour. Res. **55**, 9838–9857 (2019).

37. Douglas, T. A., Turetsky, M. R. & Koven, C. D. Increased rainfall stimulates permafrost thaw across a variety of Interior Alaskan boreal ecosystems. Npj Clim. Atmospheric Sci. **3**, 1–7 (2020).

38. Devoie, É. G. et al. Mechanisms of Discontinuous Permafrost Thaw in Peatlands. J. Geophys. Res. Earth Surf. **126**, e2021JF006204 (2021).

39. Mekonnen, Z. A., Riley, W. J., Grant, R. F. & Romanovsky, V. E. Changes in precipitation and air temperature contribute comparably to permafrost degradation in a warmer climate. Environ. Res. Lett. **16**, 024008 (2021).

40. Magnússon, R. Í. et al. Extremely wet summer events enhance permafrost thaw for multiple years in Siberian tundra. Nat. Commun. **13**, 1556 (2022).

41. Farouki, O. T. Thermal Properties of Soils. in (Defense Technical Information Center, Fort Belvoir, VA, 1981). doi:10.21236/ADA111734.

42. Hinkel, K. M. & Nelson, F. E. Spatial and temporal patterns of active layer thickness at Circumpolar Active Layer Monitoring (CALM) sites in northern Alaska, 1995–2000. J. Geophys. Res. Atmospheres **108**, (2003).
43. Subin, Z. M. et al. Effects of Soil Moisture on the Responses of Soil Temperatures to Climate Change in Cold Regions. J. Clim. **26**, 3139–3158 (2013).
44. Hinkel, K. M., Paetzold, F., Nelson, F. E. & Bockheim, J. G. Patterns of soil temperature and moisture in the active layer and upper permafrost at Barrow, Alaska: 1993–1999. Glob. Planet. Change **29**, 293–309 (2001).
45. Clayton, L. K. et al. Active layer thickness as a function of soil water content. Environ. Res. Lett. **16**, 055028 (2021).
46. Hamm, A. & Frampton, A. Impact of lateral groundwater flow on hydrothermal conditions of the active layer in a high-Arctic hillslope setting. The Cryosphere **15**, 4853–4871 (2021).
47. Bintanja, R. & Selten, F. M. Future increases in Arctic precipitation linked to local evaporation and sea-ice retreat. Nature **509**, 479–482 (2014).
48. Bintanja, R. et al. Strong future increases in Arctic precipitation variability linked to poleward moisture transport. Sci. Adv. **6**, eaax6869 (2020).
49. Beilman, D. W., Vitt, D. H. & Halsey, L. A. Localized Permafrost Peatlands in Western Canada: Definition, Distributions, and Degradation. Arct. Antarct. Alp. Res. **33**, 70–77 (2001).
50. Glossary of Permafrost and Related Ground-Ice Terms. (Ottawa,Ontario,Canada, 1988).

51. Dafflon, B. et al. A distributed temperature profiling system for vertically and laterally dense acquisition of soil and snow temperature. The Cryosphere **16**, 719–736 (2022).
52. Lundquist, J. D. & Huggett, B. Evergreen trees as inexpensive radiation shields for temperature sensors: TREES AND TEMPERATURE SENSORS. Water Resour. Res. **44**, (2008).
53. NOAA. National Maps - Alaska - NOAA's National Weather Service. https://www.nws.noaa.gov/outlook_ak_tab.php (2023).
54. USDA. Kenai Moose Pens (966) - Site Information and Reports. USDA https://wcc.sc.egov.usda.gov/nwcc/site?sitenum=966 (2023).
55. Jonas, T., Webster, C., Mazzotti, G. & Malle, J. HPEval: A canopy shortwave radiation transmission model using high-resolution hemispherical images. Agric. For. Meteorol. **284**, 107903 (2020).
56. Yoshikawa, K., Overduin, P. P. & Harden, J. W. Moisture content measurements of moss (Sphagnum spp.) using commercial sensors. Permafr. Periglac. Process. **15**, 309–318 (2004).
57. Zhao, Y. et al. A new thermal conductivity model for sandy and peat soils. Agric. For. Meteorol. **274**, 95–105 (2019).
58. Beckschäfer, P. Hemispherical_2.0 – Batch Processing Hemispherical and Canopy Photographs with ImageJ – User Manual. (2015). doi:10.13140/RG.2.1.3059.4088.
59. Sjöberg, Y. et al. Thermal effects of groundwater flow through subarctic fens: A case study based on field observations and numerical modeling. Water Resour. Res. **52**, 1591–1606 (2016).

60. Heslop, J. K. et al. Thermokarst lake methanogenesis along a complete talik profile. Biogeosciences **12**, 4317–4331 (2015).

61. O'Neill, H. B., Roy-Leveillee, P., Lebedeva, L. & Ling, F. Recent advances (2010–2019) in the study of taliks. Permafr. Periglac. Process. **31**, 346–357 (2020).

62. Magnússon, R. Í. et al. Extremely wet summer events enhance permafrost thaw for multiple years in Siberian tundra. Nat. Commun. **13**, 1556 (2022).

63. Johansson, M. et al. Rapid responses of permafrost and vegetation to experimentally increased snow cover in sub-arctic Sweden. Environ. Res. Lett. **8**, 035025 (2013).

64. O'Neill, H. B. & Burn, C. R. Talik Formation at a Snow Fence in Continuous Permafrost, Western Arctic Canada. Permafr. Periglac. Process. **28**, 558–565 (2017).

65. Zhou, J. et al. Monitoring and modeling the influence of snow pack and organic soil on a permafrost active layer, Qinghai–Tibetan Plateau of China. Cold Reg. Sci. Technol. **90–91**, 38–52 (2013).

66. Park, H., Fedorov, A. N., Zheleznyak, M. N., Konstantinov, P. Y. & Walsh, J. E. Effect of snow cover on pan-Arctic permafrost thermal regimes. Clim. Dyn. **44**, 2873–2895 (2015).

67. El-Din, M. M. S. On the heat flow into the ground. Renew. Energy **18**, 473–490 (1999).

68. Byers, H. R., Moses, H. & Harney, P. J. Measurement of rain temperature. J. Meteorol. **6**, 51–55 (1949).

69. Gao, B. & Coon, E. T. Evaluating simplifications of subsurface process representations for field-scale permafrost hydrology models. The Cryosphere **16**, 4141–4162 (2022).

70. Woo, M. & Giesbrecht, M. A. Simulation of snowmelt in a subarctic spruce woodland: 1. Tree model. Water Resour. Res. **36**, 2275–2285 (2000).

71. Lundquist, J. D., Dickerson-Lange, S. E., Lutz, J. A. & Cristea, N. C. Lower forest density enhances snow retention in regions with warmer winters: A global framework developed from plot-scale observations and modeling. Water Resour. Res. **49**, 6356–6370 (2013).

72. Webster, C., Rutter, N., Zahner, F. & Jonas, T. Measurement of Incoming Radiation below Forest Canopies: A Comparison of Different Radiometer Configurations. J. Hydrometeorol. **17**, 853–864 (2016).

73. Clark, M. P. et al. Representing spatial variability of snow water equivalent in hydrologic and land-surface models: A review. Water Resour. Res. **47**, (2011).

74. Perron, N., Baltzer, J. L. & Sonnentag, O. Spatial and temporal variation in forest transpiration across a forested boreal peatland complex. Hydrol. Process. **37**, e14815 (2023).

75. Graham, J. D., Ricciuto, D. M., Glenn, N. F. & Hanson, P. J. Incorporating Microtopography in a Land Surface Model and Quantifying the Effect on the Carbon Cycle. J. Adv. Model. Earth Syst. **14**, e2021MS002721 (2022).

76. Krause, C. & Lemay, A. Root adaptations of black spruce growing in water-saturated soil. Can. J. For. Res. **52**, 653–661 (2022).

77. Haynes, K. M., Smart, J., Disher, B., Carpino, O. & Quinton, W. L. The role of hummocks in re-establishing black spruce forest following permafrost thaw. Ecohydrology **14**, e2273 (2021).

78. Dearborn, K. D., Wallace, C. A., Patankar, R. & Baltzer, J. L. Permafrost thaw in boreal peatlands is rapidly altering forest community composition. J. Ecol. **109**, 1452–1467 (2021).

79. Cohen, J. et al. Recent Arctic amplification and extreme mid-latitude weather. Nat. Geosci. **7**, 627–637 (2014).

80. Kusunoki, S., Mizuta, R. & Hosaka, M. Future changes in precipitation intensity over the Arctic projected by a global atmospheric model with a 60-km grid size. Polar Sci. **9**, 277–292 (2015).

81. Liu, J. et al. Projection of extreme precipitation induced by Arctic amplification over the Northern Hemisphere. Environ. Res. Lett. **16**, 074012 (2021).

82. Wang, P. et al. Increasing annual and extreme precipitation in permafrost-dominated Siberia during 1959–2018. J. Hydrol. **603**, 126865 (2021).

83. Thackeray, C. W., Hall, A., Norris, J. & Chen, D. Constraining the increased frequency of global precipitation extremes under warming. Nat. Clim. Change **12**, 441–448 (2022).

84. Hamm, A., Magnússon, R. Í., Khattak, A. J. & Frampton, A. Continentality determines warming or cooling impact of heavy rainfall events on permafrost. Nat. Commun. **14**, 3578 (2023).

85. Gruber, S. Derivation and analysis of a high-resolution estimate of global permafrost zonation. The Cryosphere **6**, 221–233 (2012).

86. Defersha, M. B., Quraishi, S. & Melesse, A. The effect of slope steepness and antecedent moisture content on interrill erosion, runoff and sediment size distribution in the highlands of Ethiopia. Hydrol. Earth Syst. Sci. **15**, 2367–2375 (2011).
87. Magnin, F. et al. Permafrost distribution in steep rock slopes in Norway: measurements, statistical modelling and implications for geomorphological processes. Earth Surf. Dyn. **7**, 1019–1040 (2019).
88. Eklof, J. F. et al. Canopy cover and microtopography control precipitation-enhanced thaw of ecosystem-protected permafrost. Environ. Res. Lett. **19**, 044055 (2024).
89. Shiklomanov, N. I. et al. Decadal variations of active-layer thickness in moisture-controlled landscapes, Barrow, Alaska. J. Geophys. Res. Biogeosciences **115**, (2010).
90. Blok, D. et al. Shrub expansion may reduce summer permafrost thaw in Siberian tundra. Glob. Change Biol. **16**, 1296–1305 (2010).
91. Myers-Smith, I. H. & Hik, D. S. Shrub canopies influence soil temperatures but not nutrient dynamics: An experimental test of tundra snow–shrub interactions. Ecol. Evol. **3**, 3683–3700 (2013).
92. Woo, M., Mollinga, M. & Smith, S. L. Climate warming and active layer thaw in the boreal and tundra environments of the Mackenzie Valley1. Can. J. Earth Sci. **44**, 733–743 (2007).
93. Fisher, J. P. et al. The influence of vegetation and soil characteristics on active-layer thickness of permafrost soils in boreal forest. Glob. Change Biol. **22**, 3127–3140 (2016).

94. Euskirchen, E. AmeriFlux AmeriFlux US-BZS Bonanza Creek Black Spruce. AmeriFlux; University of Alaska Fairbanks, Institute of Arctic Biology https://doi.org/10.17190/AMF/1756434 (2023).

95. Manies, K. L., Fuller, C. C., Jones, M. C., Waldrop, M. P. & McGeehin, J. P. Soil Data for a Thermokarst Bog and the Surrounding Permafrost Plateau Forest, Located at Bonanza Creek Long Term Ecological Research Site, Interior Alaska. Soil data for a thermokarst bog and the surrounding permafrost plateau forest, located at Bonanza Creek Long Term Ecological Research Site, Interior Alaska vols 2016–1173 16 http://pubs.er.usgs.gov/publication/ofr20161173 (2017).

96. Euskirchen, E. S., Edgar, C. W., Turetsky, M. R., Waldrop, M. P. & Harden, J. W. Differential response of carbon fluxes to climate in three peatland ecosystems that vary in the presence and stability of permafrost. J. Geophys. Res. Biogeosciences **119**, 1576–1595 (2014).

97. Klapstein, S. J. et al. Controls on methane released through ebullition in peatlands affected by permafrost degradation. J. Geophys. Res. Biogeosciences **119**, 418–431 (2014).

98. Parajka, J., Haas, P., Kirnbauer, R., Jansa, J. & Blöschl, G. Potential of time-lapse photography of snow for hydrological purposes at the small catchment scale. Hydrol. Process. **26**, 3327–3337 (2012).

99. Bongio, M., Arslan, A. N., Tanis, C. M. & De Michele, C. Snow depth time series retrieval by time-lapse photography: Finnish and Italian case studies. The Cryosphere **15**, 369–387 (2021).

100. Outcalt, S. I., Nelson, F. E. & Hinkel, K. M. The zero-curtain effect: Heat and mass transfer across an isothermal region in freezing soil. Water Resour. Res. **26**, 1509–1516 (1990).

101. Bergamaschi, P. et al. Atmospheric CH4 in the first decade of the 21st century: Inverse modeling analysis using SCIAMACHY satellite retrievals and NOAA surface measurements. J. Geophys. Res. Atmospheres **118**, 7350–7369 (2013).

102. Neubauer, S. C. & Megonigal, J. P. Moving Beyond Global Warming Potentials to Quantify the Climatic Role of Ecosystems. Ecosystems **18**, 1000–1013 (2015).

103. Poulter, B. et al. Global wetland contribution to 2000–2012 atmospheric methane growth rate dynamics. Environ. Res. Lett. **12**, 094013 (2017).

104. Zhang, Z. et al. Emerging role of wetland methane emissions in driving 21st century climate change. Proc. Natl. Acad. Sci. **114**, 9647–9652 (2017).

105. Spahni, R. et al. Constraining global methane emissions and uptake by ecosystems. Biogeosciences **8**, 1643–1665 (2011).

106. McGuire, A. D. et al. An assessment of the carbon balance of Arctic tundra: comparisons among observations, process models, and atmospheric inversions. Biogeosciences **9**, 3185–3204 (2012).

107. Zhu, X., Zhuang, Q., Qin, Z., Glagolev, M. & Song, L. Estimating wetland methane emissions from the northern high latitudes from 1990 to 2009 using artificial neural networks. Glob. Biogeochem. Cycles **27**, 592–604 (2013).

108. Bruhwiler, L. et al. CarbonTracker-CH_4: an assimilation system for estimating emissions of atmospheric methane. Atmospheric Chem. Phys. **14**, 8269–8293 (2014).

109. Watts, J. D., Kimball, J. S., Bartsch, A. & McDonald, K. C. Surface water inundation in the boreal-Arctic: potential impacts on regional methane emissions. Environ. Res. Lett. **9**, 075001 (2014).

110. Treat, C. C., Bloom, A. A. & Marushchak, M. E. Nongrowing season methane emissions–a significant component of annual emissions across northern ecosystems. Glob. Change Biol. **24**, 3331–3343 (2018).

111. Thompson, R. L. et al. Variability in Atmospheric Methane From Fossil Fuel and Microbial Sources Over the Last Three Decades. Geophys. Res. Lett. **45**, 11,499-11,508 (2018).

112. Peltola, O. et al. Monthly gridded data product of northern wetland methane emissions based on upscaling eddy covariance observations. Earth Syst. Sci. Data **11**, 1263–1289 (2019).

113. Saunois, M. et al. The Global Methane Budget 2000–2017. Earth Syst. Sci. Data **12**, 1561–1623 (2020).

114. Kuhn, M. A. et al. BAWLD-CH_4: a comprehensive dataset of methane fluxes from boreal and arctic ecosystems. Earth Syst. Sci. Data **13**, 5151–5189 (2021).

115. Yuan, K. et al. Boreal–Arctic wetland methane emissions modulated by warming and vegetation activity. Nat. Clim. Change **14**, 282–288 (2024).

116. Yvon-Durocher, G. et al. Methane fluxes show consistent temperature dependence across microbial to ecosystem scales. Nature **507**, 488–491 (2014).

117. Knox, S. H. et al. Identifying dominant environmental predictors of freshwater wetland methane fluxes across diurnal to seasonal time scales. Glob. Change Biol. **27**, 3582–3604 (2021).

118. Yuan, K. et al. Causality guided machine learning model on wetland CH4 emissions across global wetlands. Agric. For. Meteorol. **324**, 109115 (2022).

119. Chen, W. et al. Hysteretic relationship between plant productivity and methane uptake in an alpine meadow. Agric. For. Meteorol. **288–289**, 107982 (2020).

120. Zinder, S. H., Anguish, T. & Cardwell, S. C. Effects of Temperature on Methanogenesis in a Thermophilic (58°C) Anaerobic Digestor. Appl. Environ. Microbiol. **47**, 808–813 (1984).

121. Chanton, J. P. et al. Radiocarbon evidence for the substrates supporting methane formation within northern Minnesota peatlands. Geochim. Cosmochim. Acta **59**, 3663–3668 (1995).

122. Joabsson, null, Christensen, null & Wallén, null. Vascular plant controls on methane emissions from northern peatforming wetlands. Trends Ecol. Evol. **14**, 385–388 (1999).

123. van der Wal, R. & Stien, A. High-arctic plants like it hot: a long-term investigation of between-year variability in plant biomass. Ecology **95**, 3414–3427 (2014).

124. Chanton, J. P., Martens, C. S., Kelley, C. A., Crill, P. M. & Showers, W. J. Methane transport mechanisms and isotopic fractionation in emergent macrophytes of an Alaskan tundra lake. J. Geophys. Res. Atmospheres **97**, 16681–16688 (1992).

125. Thomas, K. L., Benstead, J., Davies, K. L. & Lloyd, D. Role of wetland plants in the diurnal control of CH4 and CO2 fluxes in peat. Soil Biol. Biochem. **28**, 17–23 (1996).

126. Kim, J., Verma, S. B., Billesbach, D. P. & Clement, R. J. Diel variation in methane emission from a midlatitude prairie wetland: Significance of convective throughflow in Phragmites australis. J. Geophys. Res. Atmospheres **103**, 28029–28039 (1998).

127. Käki, T., Ojala, A. & Kankaala, P. Diel variation in methane emissions from stands of Phragmites australis (Cav.) Trin. ex Steud. and Typha latifolia L. in a boreal lake. Aquat. Bot. **71**, 259–271 (2001).

128. Kadlec, R. H. Pond and wetland treatment. Water Sci. Technol. **48**, 1–8 (2003).

129. Ouellet-Plamondon, C., Chazarenc, F., Comeau, Y. & Brisson, J. Artificial aeration to increase pollutant removal efficiency of constructed wetlands in cold climate. Ecol. Eng. **27**, 258–264 (2006).

130. Paredes, D. et al. New Aspects of Microbial Nitrogen Transformations in the Context of Wastewater Treatment – A Review. Eng. Life Sci. **7**, 13–25 (2007).

131. Zhou, Q. et al. Effects of Vegetation and Temperature on Nutrient Removal and Microbiology in Horizontal Subsurface Flow Constructed Wetlands for Treatment of Domestic Sewage. Water. Air. Soil Pollut. **228**, 95 (2017).

132. Kelvin, K. & Tole, M. The Efficacy of a Tropical Constructed Wetland for Treating Wastewater During the Dry Season: The Kenyan Experience. Water. Air. Soil Pollut. **215**, 137–143 (2011).

133. Salimi, S. & Scholz, M. Impact of future climate scenarios on peatland and constructed wetland water quality: A mesocosm experiment within climate chambers. J. Environ. Manage. **289**, 112459 (2021).

134. Aerts, R., Wallen, B. & Malmer, N. Growth-Limiting Nutrients in Sphagnum-Dominated Bogs Subject to Low and High Atmospheric Nitrogen Supply. J. Ecol. **80**, 131–140 (1992).

135. Liu, L. & Greaver, T. L. A review of nitrogen enrichment effects on three biogenic GHGs: the CO2 sink may be largely offset by stimulated N2O and CH4 emission. Ecol. Lett. **12**, 1103–1117 (2009).

136. Bodelier, P. L. & Steenbergh, A. K. Interactions between methane and the nitrogen cycle in light of climate change. Curr. Opin. Environ. Sustain. **9–10**, 26–36 (2014).

137. Xu, X. & Tian, H. Methane exchange between marshland and the atmosphere over China during 1949–2008. Glob. Biogeochem. Cycles **26**, (2012).

138. Chapin, F. S. Direct and indirect effects of temperature on arctic plants. Polar Biol. **2**, 47–52 (1983).

139. Chapin III, F. S. & Shaver, G. R. Physiological and Growth Responses of Arctic Plants to a Field Experiment Simulating Climatic Change. Ecology **77**, 822–840 (1996).

140. Liu, X.-Y. et al. Nitrate is an important nitrogen source for Arctic tundra plants. Proc. Natl. Acad. Sci. **115**, 3398–3403 (2018).

141. Liu, D. Y., Ding, W. X., Jia, Z. J. & Cai, Z. C. Relation between methanogenic archaea and methane production potential in selected natural wetland ecosystems across China. Biogeosciences **8**, 329–338 (2011).

142. Waldo, N. B., Tfaily, M. M., Anderton, C. & Neumann, R. B. The importance of nutrients for microbial priming in a bog rhizosphere. Biogeochemistry **152**, 271–290 (2021).

143. Kettridge, N., Kellner, E., Price, J. S. & Waddington, J. M. Peat deformation and biogenic gas bubbles control seasonal variations in peat hydraulic conductivity. Hydrol. Process. **27**, 3208–3216 (2013).

144. Skogley, E. O. The universal bioavailability environment/soil test unibest. Commun. Soil Sci. Plant Anal. **23**, 2225–2246 (1992).

145. Clymo, R. S. The Growth of Sphagnum: Methods of Measurement. J. Ecol. **58**, 13–49 (1970).

146. Gunnarsson, U. & Rydin, H. Nitrogen fertilization reduces Sphagnum production in bog communities. New Phytol. **147**, 527–537 (2000).

147. Gunnarsson, U., Granberg, G. & Nilsson, M. Growth, production and interspecific competition in Sphagnum: effects of temperature, nitrogen and sulphur treatments on a boreal mire. New Phytol. **163**, 349–359 (2004).

148. Mikan, C. J., Schimel, J. P. & Doyle, A. P. Temperature controls of microbial respiration in arctic tundra soils above and below freezing. Soil Biol. Biochem. **34**, 1785–1795 (2002).

149. Elberling, B. & Brandt, K. K. Uncoupling of microbial CO2 production and release in frozen soil and its implications for field studies of arctic C cycling. Soil Biol. Biochem. **35**, 263–272 (2003).

150. Panikov, N. S., Flanagan, P. W., Oechel, W. C., Mastepanov, M. A. & Christensen, T. R. Microbial activity in soils frozen to below −39 °C. Soil Biol. Biochem. **38**, 785–794 (2006).

151. Miller, A. E. et al. Seasonal variation in nitrogen uptake and turnover in two high-elevation soils: mineralization responses are site-dependent. Biogeochemistry **93**, 253–270 (2009).

152. Jefferies, R. L., Walker, N. A., Edwards, K. A. & Dainty, J. Is the decline of soil microbial biomass in late winter coupled to changes in the physical state of cold soils? Soil Biol. Biochem. **42**, 129–135 (2010).

153. Zhang, H., Zhu, J., Gong, Z. & Zhu, J.-K. Abiotic stress responses in plants. Nat. Rev. Genet. **23**, 104–119 (2022).

154. Song, X., Gao, T., Ai, M. & Gao, S. Experimental investigation of freeze injury temperatures in trees and their contributing factors based on electrical impedance spectroscopy. Front. Plant Sci. **15**, (2024).

155. Shammi, S. et al. Machine learning-based detection of freezing events using infrared thermography. Comput. Electron. Agric. **198**, 107013 (2022).

156. Tian, S., Wang, S. & Xu, H. Early detection of freezing damage in oranges by online Vis/NIR transmission coupled with diameter correction method and deep 1D-CNN. Comput. Electron. Agric. **193**, 106638 (2022).

157. Jorgenson, M. T., Shur, Y. L. & Pullman, E. R. Abrupt increase in permafrost degradation in Arctic Alaska. Geophys. Res. Lett. **33**, (2006).

158. Euskirchen, E. S. et al. Consequences of changes in vegetation and snow cover for climate feedbacks in Alaska and northwest Canada. Environ. Res. Lett. **11**, 105003 (2016).

Supplemental

SI1. Chapter 2 Supplemental

SI1.1 Advective Heat Transport Calculation for Figure 2.9

In the main manuscript we state, "Energy from advective heat transport depends on water temperature and volume, while energy needed to warm and thaw soils depends on pre-event soil temperature, water content, and ice content. **Figure 2.9** explores viability of various variable combinations to cause the observed warming and thaw, which includes warming of 100 cm of 86% water content soil (**Figure 2.8**) from 0 °C to 1 °C, and melt of an unknown amount of ground ice (***Figure 2.7***C,D)."

Calculation of heat contribution from runoff:

$q_{runoff} = m_{runoff} * C_{water} * (T_{final_{runoff}} - T_{initial_{runoff}})$

q_{runoff} = heat energy from runoff (Joules)

m_{runoff} = mass of runoff (grams)

$C_{water} = 4.18\, J/g°C =$ specific heat of water

$T_{initial_{runoff}}$ = initial runoff temperature; varied from 0°C (frost table temp.) to 15°C (average air temperature and thus estimate for rain temperature), y-axis for Figure 9.

$T_{final_{runoff}} = 1°C =$ final runoff temp. equaling transition location post-event average soil temperature, 1°C

$q_{runoff} = \rho_{water}(R * A_C) * C_{water} * (T_{final_{runoff}} - T_{initial_{runoff}})$

$\rho_{water} = 0.99975\ g/cm^3 =$ density of water at 10°C

$R = 5.4\ cm =$ rainfall (cm)

$A_C =$ contributing surface area (cm^2)

Calculation of heat required for observed warming and thaw:

$q_{required} = m_{soil\ water} * C_{water} * (T_{final_{soil}} - T_{initial_{soil}}) + m_{ice\ content} * \Delta H_{ice}$

$q_{required}$ = heat energy required to cause warming of soils and melting of ground ice

$m_{soil\ water}$ = mass of pre-event water content at (86.05%) plus water resulting from melt of ground ice

$T_{initial} = 0°C =$ initial pre-event soil temperature at transition location

$T_{final} = 1°C =$ final post-event soil temperature at transition location

$m_{ice\ content}$ = mass of ice in 100 cm of transition soil (pre-event); x-axis for Figure 9.

ΔH_{ice} = heat of fusion, 333.55 J/g

$$q_{required} = (\rho_{water} * f_{water} * D * A_R + \rho_{ice} * f_{ice} * D * A_R) * C_{water} * (T_{final_{soil}} - T_{initial_{soil}}) + \rho_{ice} * f_{ice} * D * A_R * \Delta H_{ice}$$

$f_{water} = 0.8605 = 86.05\%/100 =$ soil fraction of water

$D = 100\ cm =$ soil warming depth

$A_R =$ receiving surface area (cm^2)

$\rho_{ice} = 0.9162\ g/cm^3 =$ density of ice at 0°C

$f_{ice} =$ soil fraction of ice; determined to be between 0.0 and 0.065 based on techniques described in Thermal Conductivity Modeling

Setting energy from runoff equal to energy required for warming and thaw ($q_{runoff} = q_{required}$)

$$\rho_{water}(R * Ac) * C_{water} * (T_{final_{runoff}} - T_{initial_{runoff}}) = (\rho_{water} * f_{water} * D * Ar + \rho_{ice} * f_{ice} * D * Ar) * C_{water} * (T_{final_{soil}} - T_{initial_{soil}}) + \rho_{ice} * f_{ice} * D * Ar * \Delta H_{ice}$$

Solving for initial runoff temperature, the y-axis in Figure 9

$$\boldsymbol{T_{initial_{runoff}}} = -\left(f_{water} * \frac{D}{R} * \frac{\boldsymbol{A_R}}{\boldsymbol{A_C}} + \frac{\rho_{ice}}{\rho_{water}} * \boldsymbol{f_{ice}} * \frac{D}{R} * \frac{\boldsymbol{A_R}}{\boldsymbol{A_C}}\right)(T_{final_{soil}} - T_{initial_{soil}}) - \frac{\rho_{ice}}{\rho_{water}} * \boldsymbol{f_{ice}} * \frac{D}{R} * \frac{\boldsymbol{A_R}}{\boldsymbol{A_C}} * \frac{\Delta H_{ice}}{C_{water}} + T_{final_{runoff}}$$

The equation above was used to create the colored scenario lines in **Figure 2.9**, designating when energy from runoff equals energy required for warming and thaw. The bolded variables — initial runoff temperature ($\boldsymbol{T_{initial_{runoff}}}$), the ratio of receiving soil area to runoff contributing area ($\boldsymbol{A_R/A_C}$), and ice fraction ($\boldsymbol{f_{ice}}$) — were varied to explore the plausibility of various scenarios. Initial runoff temperature ($\boldsymbol{T_{initial_{runoff}}}$) is the y-axis in Figure 9. Ice percentage, which is ice fraction ($\boldsymbol{f_{ice}}$) multiplied by 100, is the x-axis. The three scenario lines show the impact of the ratio between the receiving soil area and the contributing soil area ($\boldsymbol{A_R/A_C}$).

SI1.2 Chapter 2 Supplementary Figures

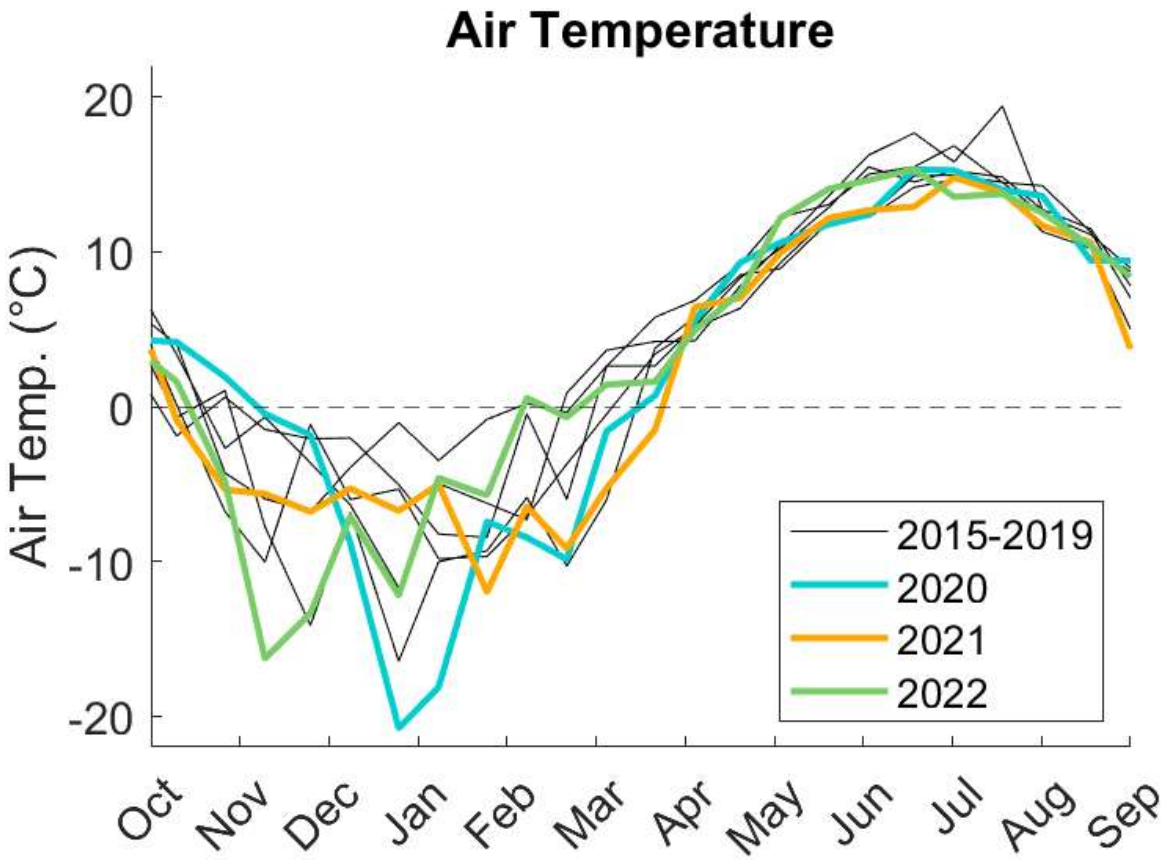

Figure 0.1 Line graph showing stacked annual time series of air temperature from 2015 to 2022. Data for 2020 are blue, 2021 are orange, and 2022 are green. Data from all other years are black.

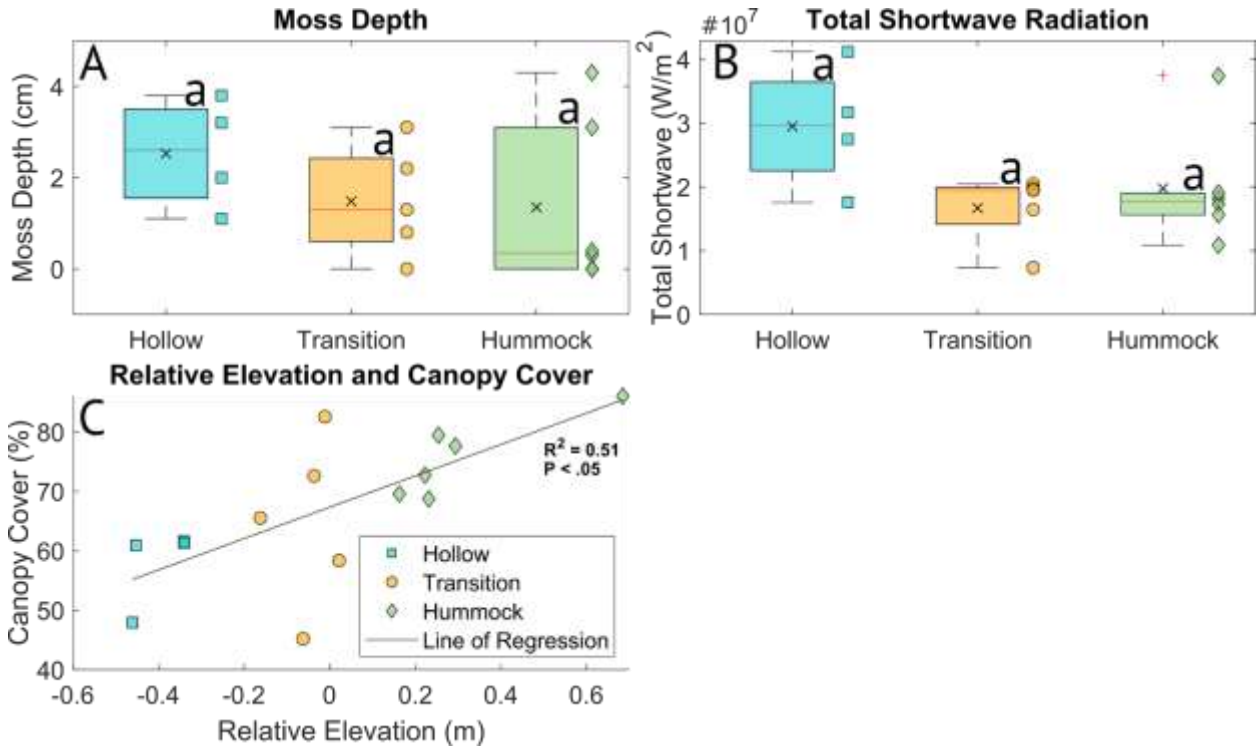

Figure 0.2 Additional environmental variables. Box and whisker plots showing: (A) moss depth, and (B) total shortwave radiation. Shortwave radiation was modeled using HPEval, a MATLAB-based software tool that uses high-resolution hemispherical photos to estimate shortwave radiation below the forest canopy [55]. Cumulative shortwave radiation was calculated using the model output during the growing season, March through October, for all locations. On each box plot, the central line indicates the median, "x" marks the mean, edges of the box indicate the 25th and 75th percentiles, whiskers indicate the most extreme non-outlier data points, and a red plus marker indicates an outlier greater than 2.7 standard deviations from the mean. Differing letters on top of boxes indicate data sets with statistically different distributions. (C) Scatter plot showing relative elevation versus canopy cover.

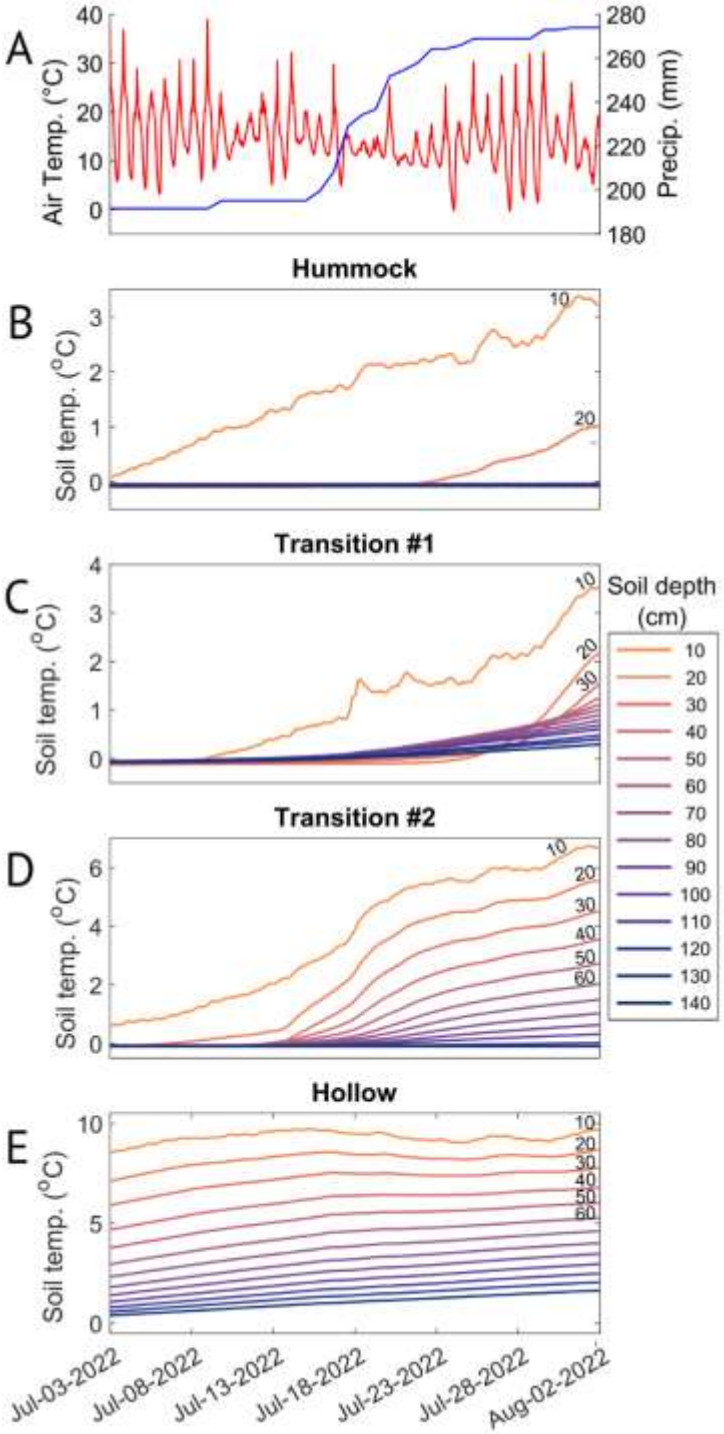

Figure 0.3 Soil temperature responses to rain events in July 2022. (A) Air temperature (red, left axis) and cumulative precipitation (blue, right axis). (B-E) Soil temperature at depths from 10 to 140 cm below the soil surface (depths labeled on the figure) according to colors in the legend for a (B) hummock location, (C) transition location #1 also shown in soil moisture Figure 2.8B), (D) transition location #2, and (E) hollow location. Y-axis scales vary by location.

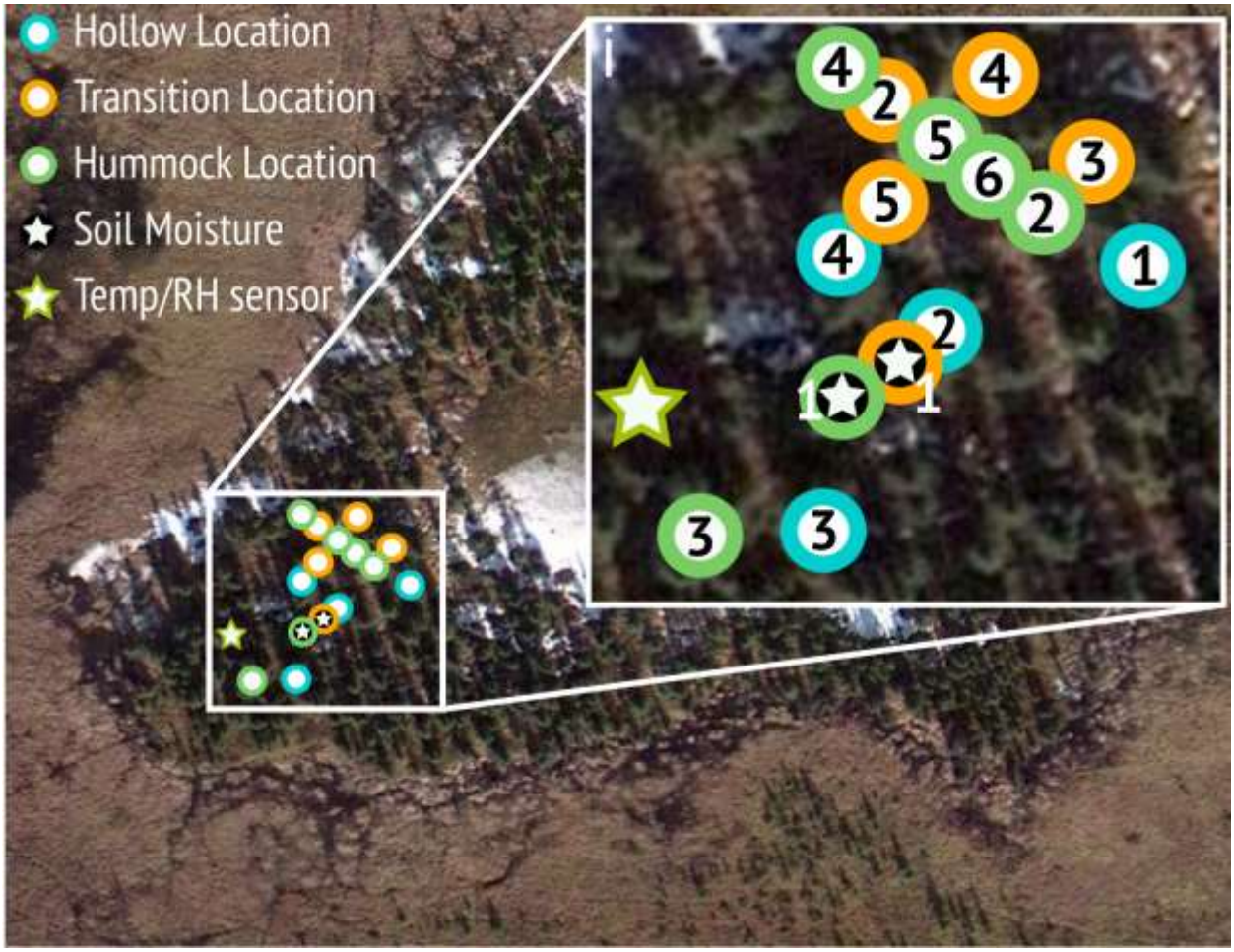

Figure 0.4 Site Locations. A Google Earth image of the site with an inset (i) showing a zoomed view of the core instrumentation area. Location identifiers (hollow 1-4, transition 1-5, hummock 1-6) are shown as numbers on colored circles that show the location relative-elevation category: hollow (light blue), transition (orange), and hummock (green). Locations with black inner circle and white star (transition #1 and hummock #1) have soil moisture profilers installed. Location identifiers match those shown in Figure S5-19.

Hollow #1

Environmental Variables:
Location Group: Hollow
Rel. Elevation (5 m): -0.46 m
Canopy Cover: 48%
Snow depth: 44.8 cm
Moss Thickness: 2.0 cm
Model SW Rad.: 3.16×10^7 W/m^2

Permafrost and Thermal Metrics
Permafrost Table Depth: 279.1 cm
Annual Thaw Rate: 37.8 cm/year
Min. 10 cm Temperature: -0.15°C
Max. 10 cm Temperature: +9.99°C
Penetration Depth of -0.05°C: 0 cm
Penetration Depth of +3°C: 109 cm

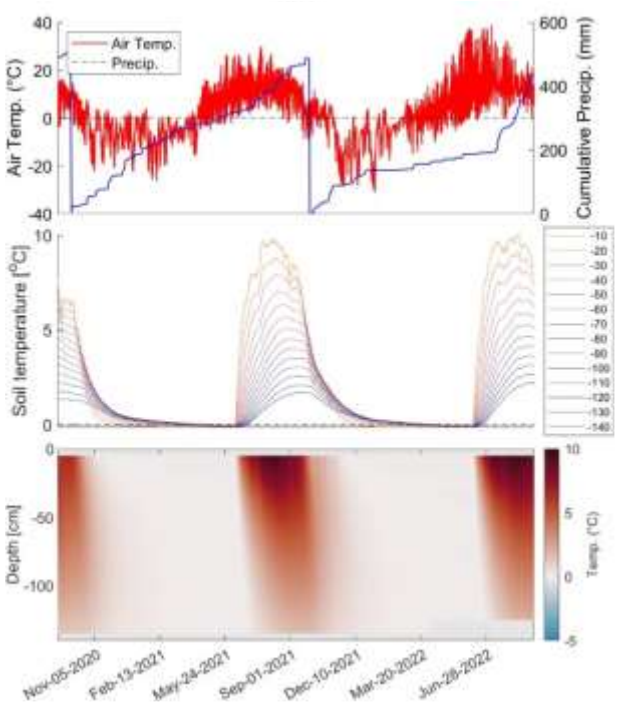

Figure 0.5 Full time series temperature plots and environmental variables for hollow #1 (Left column) Environmental variables including: microtopographic group, relative-elevation, canopy cover, snow depth, moss thickness, and modeled shortwave radiation. (Right Column) Air temperature (red, left axis) and cumulative precipitation (blue, right axis). Soil temperature at depths from 10 to 140 cm below the soil surface according to colors in the legend. Colormap plot of soil temperature according to color in the legend.

Hollow #2

Environmental Variables:
Location Group: Hollow
Rel. Elevation (5 m): -0.34 m
Canopy Cover: 62%
Snow depth: 43.3 cm
Moss Thickness: 1.1 cm
Model SW Rad.: 1.76 x 10^7 W/m^2

Permafrost and Thermal Metrics
Permafrost Table Depth: 307.6 cm
Annual Thaw Rate: 52.6 cm/year
Min. 10 cm Temperature: -0.95°C
Max. 10 cm Temperature: +9.34°C
Penetration Depth of -0.05°C: 0 cm
Penetration Depth of +3°C: 110 cm

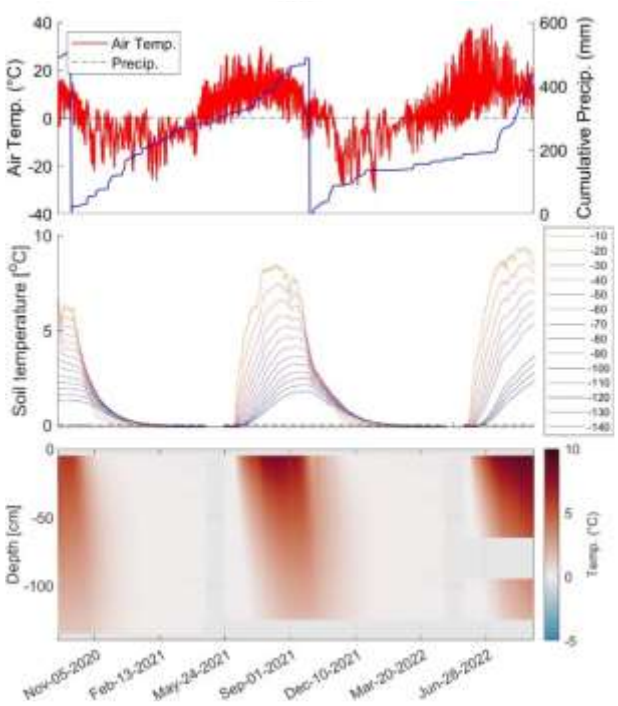

Figure 0.6 Full time series temperature plots and environmental variables for hollow #2 (Left column) Environmental variables including: microtopographic group, relative-elevation, canopy cover, snow depth, moss thickness, and modeled shortwave radiation. (Right Column) Air temperature (red, left axis) and cumulative precipitation (blue, right axis). Soil temperature at depths from 10 to 140 cm below the soil surface according to colors in the legend. Colormap plot of soil temperature according to color in the legend.

Hollow #3

Environmental Variables:
Location Group: Hollow
Rel. Elevation (5 m): -0.34 m
Canopy Cover: 61%
Snow depth: 31.1 cm
Moss Thickness: 3.8 cm
Model SW Rad.: 2.75 x 10^7 W/m^2

Permafrost and Thermal Metrics
Permafrost Table Depth: 274.3 cm
Annual Thaw Rate: 42.6 cm/year
Min. 10 cm Temperature: -0.96°C
Max. 10 cm Temperature: +8.32°C
Penetration Depth of -0.05°C: 12 cm
Penetration Depth of +3°C: 92 cm

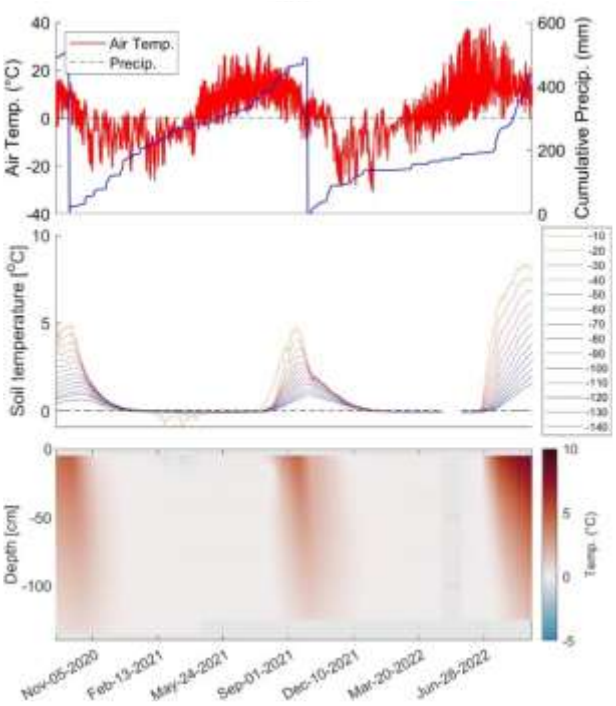

Figure 0.7 Full time series temperature plots and environmental variables for hollow #3. (Left column) Environmental variables including: microtopographic group, relative-elevation, canopy cover, snow depth, moss thickness, and modeled shortwave radiation. (Right Column) Air temperature (red, left axis) and cumulative precipitation (blue, right axis). Soil temperature at depths from 10 to 140 cm below the soil surface according to colors in the legend. Colormap plot of soil temperature according to color in the legend.

Hollow #4

Environmental Variables:
Location Group: Hollow
Rel. Elevation (5 m): -0.45 m
Canopy Cover: 61%
Snow depth: 19.8 cm
Moss Thickness: 3.2 cm
Model SW Rad.: 4.12 x 10^7 W/m^2

Permafrost and Thermal Metrics
Permafrost Table Depth: 291.1 cm
Annual Thaw Rate: 44.8 cm/year
Min. 10 cm Temperature: -0.23°C
Max. 10 cm Temperature: +8.73°C
Penetration Depth of -0.05°C: 0 cm
Penetration Depth of +3°C: 96 cm

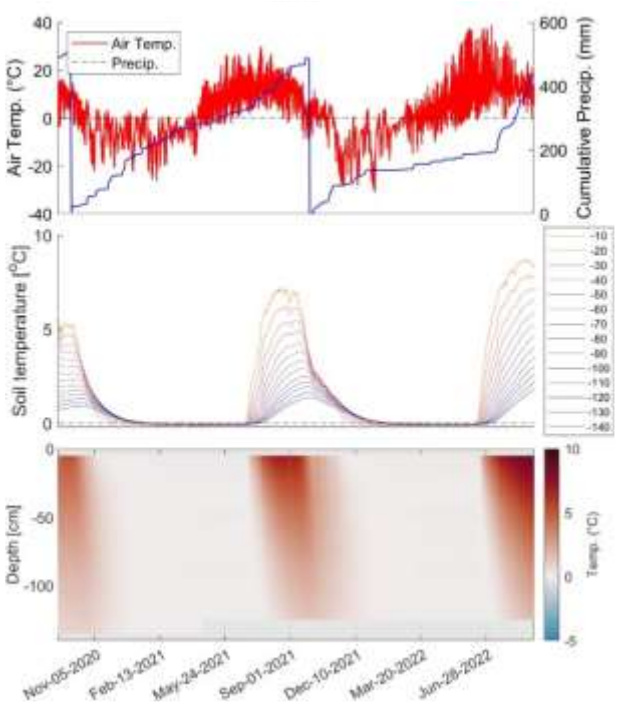

Figure 0.8 Full time series temperature plots and environmental variables for hollow #4. (Left column) Environmental variables including: microtopographic group, relative-elevation, canopy cover, snow depth, moss thickness, and modeled shortwave radiation. (Right Column) Air temperature (red, left axis) and cumulative precipitation (blue, right axis). Soil temperature at depths from 10 to 140 cm below the soil surface according to colors in the legend. Colormap plot of soil temperature according to color in the legend.

Transition #1

Environmental Variables:
Location Group: Hollow
Rel. Elevation (5 m): -0.04 m
Canopy Cover: 73%
Snow depth: 13.9 cm
Moss Thickness: 1.3 cm
Model SW Rad.: 1.98 x 10^7 W/m^2

Permafrost and Thermal Metrics
Permafrost Table Depth: 294.0 cm
Annual Thaw Rate: 53.0 cm/year
Min. 10 cm Temperature: -1.26°C
Max. 10 cm Temperature: +8.06°C
Penetration Depth of -0.05°C: 17 cm
Penetration Depth of +3°C: 17 cm

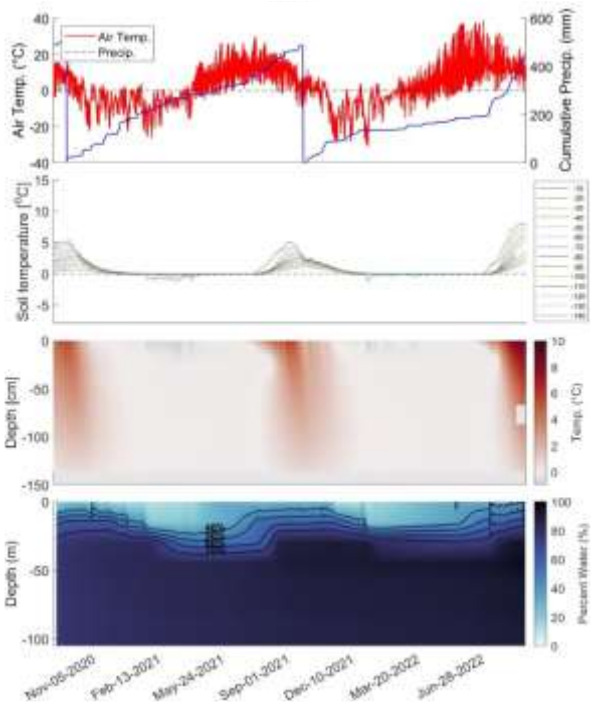

Figure 0.9 Full time series temperature plots and environmental variables for Transition #1. (Left column) Environmental variables including: microtopographic group, relative-elevation, canopy cover, snow depth, moss thickness, and modeled shortwave radiation. (Right Column) Air temperature (red, left axis) and cumulative precipitation (blue, right axis). Soil temperature at depths from 10 to 140 cm below the soil surface according to colors in the legend. Colormap plot of soil temperature according to color in the legend.

Transition #2

Environmental Variables:
Location Group: Hollow
Rel. Elevation (5 m): -0.16 m
Canopy Cover: 66%
Snow depth: 25.2 cm
Moss Thickness: 3.1 cm
Model SW Rad.: 1.94 x 10^7 W/m^2

Permafrost and Thermal Metrics
Permafrost Table Depth: 166.6 cm
Annual Thaw Rate: 19.4 cm/year
Min. 10 cm Temperature: -0.91°C
Max. 10 cm Temperature: +7.80°C
Penetration Depth of -0.05°C: 10 cm
Penetration Depth of +3°C: 61 cm

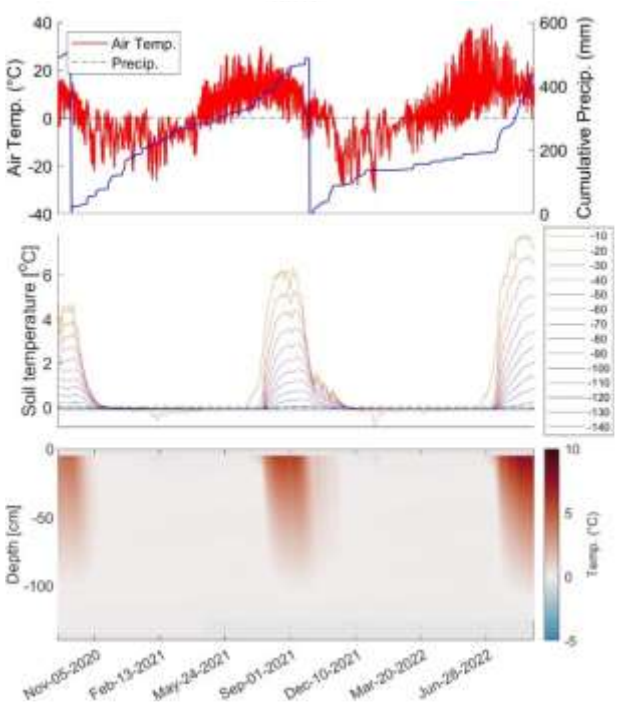

Figure 0.10 Full time series temperature plots and environmental variables for Transition #2. (Left column) Environmental variables including: microtopographic group, relative-elevation, canopy cover, snow depth, moss thickness, and modeled shortwave radiation. (Right Column) Air temperature (red, left axis) and cumulative precipitation (blue, right axis). Soil temperature at depths from 10 to 140 cm below the soil surface according to colors in the legend. Colormap plot of soil temperature according to color in the legend.

Transition #3

Environmental Variables:
Location Group: Hollow
Rel. Elevation (5 m): -0.06 m
Canopy Cover: 45%
Snow depth: 33.7 cm
Moss Thickness: 0.8 cm
Model SW Rad.: 2.04 x 10^7 W/m^2

Permafrost and Thermal Metrics
Permafrost Table Depth: 290.5 cm
Annual Thaw Rate: 45.8 cm/year
Min. 10 cm Temperature: -1.89 °C
Max. 10 cm Temperature: +8.07°C
Penetration Depth of -0.05°C: 22 cm
Penetration Depth of +3°C: 95 cm

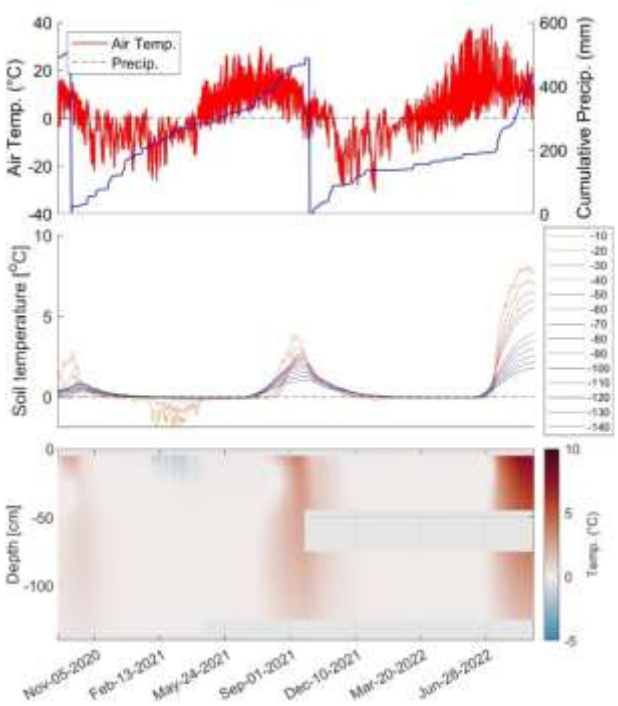

Figure 0.11 Full time series temperature plots and environmental variables for Transition #3. (Left column) Environmental variables including: microtopographic group, relative-elevation, canopy cover, snow depth, moss thickness, and modeled shortwave radiation. (Right Column) Air temperature (red, left axis) and cumulative precipitation (blue, right axis). Soil temperature at depths from 10 to 140 cm below the soil surface according to colors in the legend. Colormap plot of soil temperature according to color in the legend.

Transition #4

Environmental Variables:
Location Group: Hollow
Rel. Elevation (5 m): +0.02 m
Canopy Cover: 58%
Snow depth: 17.6 cm
Moss Thickness: 2.2 cm
Model SW Rad.: 1.64 x 10^7 W/m^2

Permafrost and Thermal Metrics
Permafrost Table Depth: 235.3 cm
Annual Thaw Rate: 44.3 cm/year
Min. 10 cm Temperature: -0.85°C
Max. 10 cm Temperature: +7.27°C
Penetration Depth of -0.05°C: 12 cm
Penetration Depth of +3°C: 72 cm

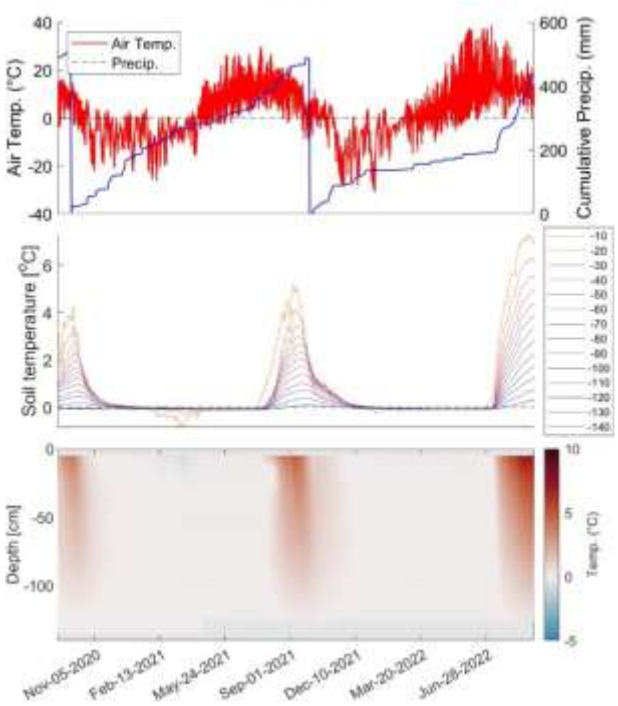

Figure 0.12 Full time series temperature plots and environmental variables for Transition #4. *(Left column) Environmental variables including: microtopographic group, relative-elevation, canopy cover, snow depth, moss thickness, and modeled shortwave radiation. (Right Column) Air temperature (red, left axis) and cumulative precipitation (blue, right axis). Soil temperature at depths from 10 to 140 cm below the soil surface according to colors in the legend. Colormap plot of soil temperature according to color in the legend.*

Transition #5

Environmental Variables:
Location Group: Hollow
Rel. Elevation (5 m): +0.02 m
Canopy Cover: 58%
Snow depth: 17.6 cm
Moss Thickness: 2.2 cm
Model SW Rad.: 7.34 x 10^6 W/m^2

Permafrost and Thermal Metrics
Permafrost Table Depth: 272.6 cm
Annual Thaw Rate: 32.0 cm/year
Min. 10 cm Temperature: -3.43°C
Max. 10 cm Temperature: +8.19°C
Penetration Depth of -0.05°C: 37 cm
Penetration Depth of +3°C: 98 cm

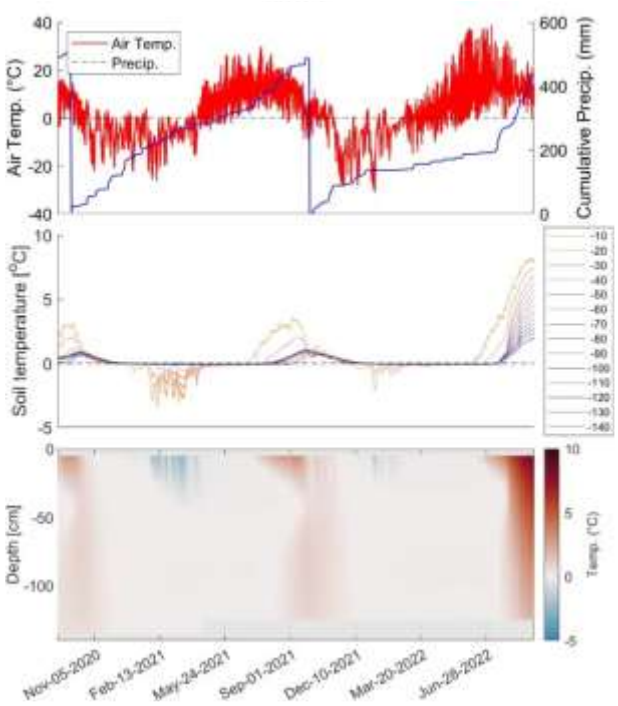

Figure 0.13 Full time series temperature plots and environmental variables for Transition #5. (Left column) Environmental variables including: microtopographic group, relative-elevation, canopy cover, snow depth, moss thickness, and modeled shortwave radiation. (Right Column) Air temperature (red, left axis) and cumulative precipitation (blue, right axis). Soil temperature at depths from 10 to 140 cm below the soil surface according to colors in the legend. Colormap plot of soil temperature according to color in the legend.

Hummock #1

Environmental Variables:
Location Group: Hollow
Rel. Elevation (5 m): +0.25 m
Canopy Cover: 79%
Snow depth: 0.9 cm
Moss Thickness: 0.4 cm
Model SW Rad.: 1.73 x 10^7 W/m^2

Permafrost and Thermal Metrics
Permafrost Table Depth: 155.6 cm
Annual Thaw Rate: 23.4 cm/year
Min. 10 cm Temperature: -4.71°C
Max. 10 cm Temperature: +6.63°C
Penetration Depth of -0.05°C: 34 cm
Penetration Depth of +3°C: 44 cm

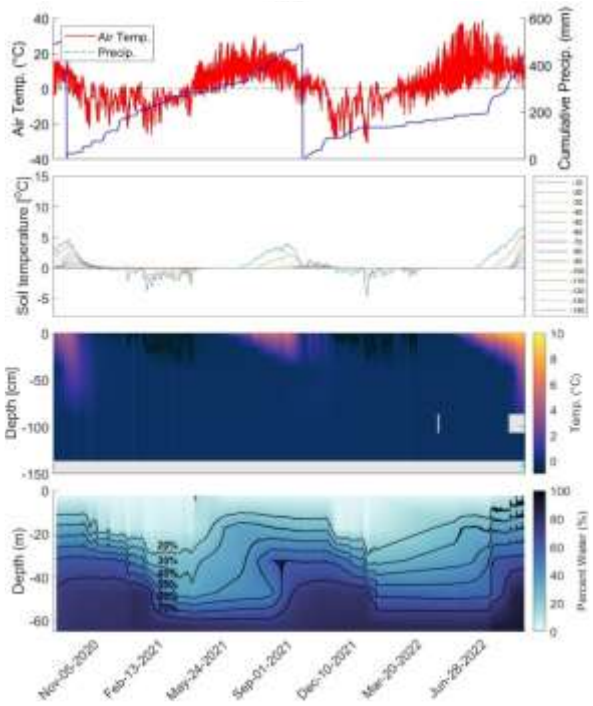

Figure 0.14 Full time series temperature plots and environmental variables for Hummock #1. (Left column) Environmental variables including: microtopographic group, relative-elevation, canopy cover, snow depth, moss thickness, and modeled shortwave radiation. (Right Column) Air temperature (red, left axis) and cumulative precipitation (blue, right axis). Soil temperature at depths from 10 to 140 cm below the soil surface according to colors in the legend. Colormap plot of soil temperature according to color in the legend.

Hummock #2

Environmental Variables:
Location Group: Hollow
Rel. Elevation (5 m): +0.22 m
Canopy Cover: 73%
Snow depth: 6.0 cm
Moss Thickness: 0.3 cm
Model SW Rad.: 1.82 x 10^7 W/m^2

Permafrost and Thermal Metrics
Permafrost Table Depth: 90.5 cm
Annual Thaw Rate: 0.1 cm/year
Min. 10 cm Temperature: -3.31°C
Max. 10 cm Temperature: +4.72°C
Penetration Depth of -0.05°C: 40 cm
Penetration Depth of +3°C: 12 cm

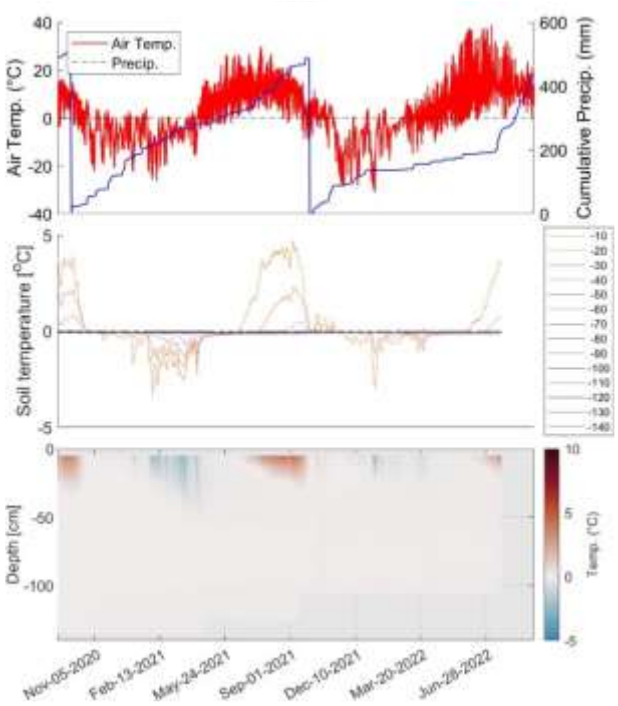

Figure 0.15 Full time series temperature plots and environmental variables for Hummock #2. (Left column) Environmental variables including: microtopographic group, relative-elevation, canopy cover, snow depth, moss thickness, and modeled shortwave radiation. (Right Column) Air temperature (red, left axis) and cumulative precipitation (blue, right axis). Soil temperature at depths from 10 to 140 cm below the soil surface according to colors in the legend. Colormap plot of soil temperature according to color in the legend.

Hummock #3

Environmental Variables:
Location Group: Hollow
Rel. Elevation (5 m): +0.69 m
Canopy Cover: 86%
Snow depth: 0.0 cm
Moss Thickness: 0.0 cm
Model SW Rad.: 1.09 x 10^7 W/m^2

Permafrost and Thermal Metrics
Permafrost Table Depth: 91.5cm
Annual Thaw Rate: 1.5 cm/year
Min. 10 cm Temperature: -5.36°C
Max. 10 cm Temperature: +7.37°C
Penetration Depth of -0.05°C: 28 cm
Penetration Depth of +3°C: 32 cm

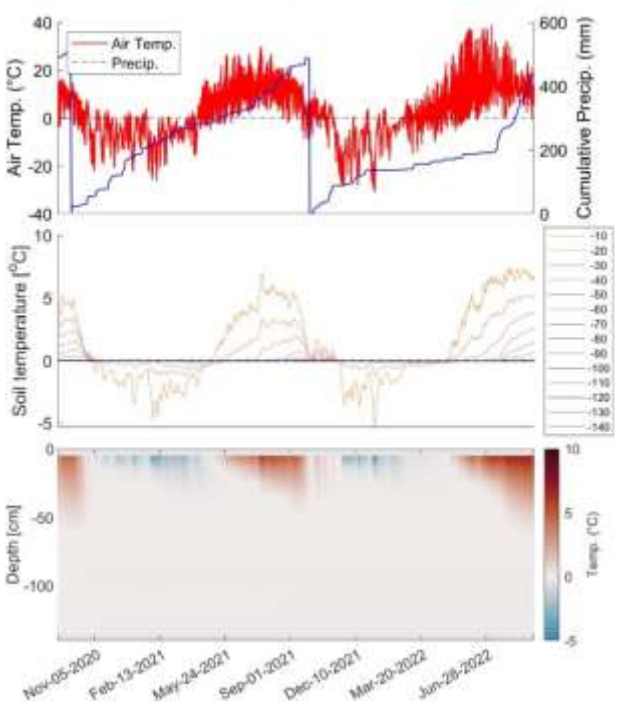

Figure 0.16 Full time series temperature plots and environmental variables for Hummock #3. (Left column) Environmental variables including: microtopographic group, relative-elevation, canopy cover, snow depth, moss thickness, and modeled shortwave radiation. (Right Column) Air temperature (red, left axis) and cumulative precipitation (blue, right axis). Soil temperature at depths from 10 to 140 cm below the soil surface according to colors in the legend. Colormap plot of soil temperature according to color in the legend.

Hummock #4

Environmental Variables:
Location Group: Hollow
Rel. Elevation (5 m): +0.16 m
Canopy Cover: 70%
Snow depth: 20.2 cm
Moss Thickness: 4.3 cm
Model SW Rad.: 1.91 x 10^7 W/m^2

Permafrost and Thermal Metrics
Permafrost Table Depth: 59.6 cm
Annual Thaw Rate: 7.8 cm/year
Min. 10 cm Temperature: -0.59°C
Max. 10 cm Temperature: +2.95°C
Penetration Depth of -0.05°C: 7 cm
Penetration Depth of +3°C: 0 cm

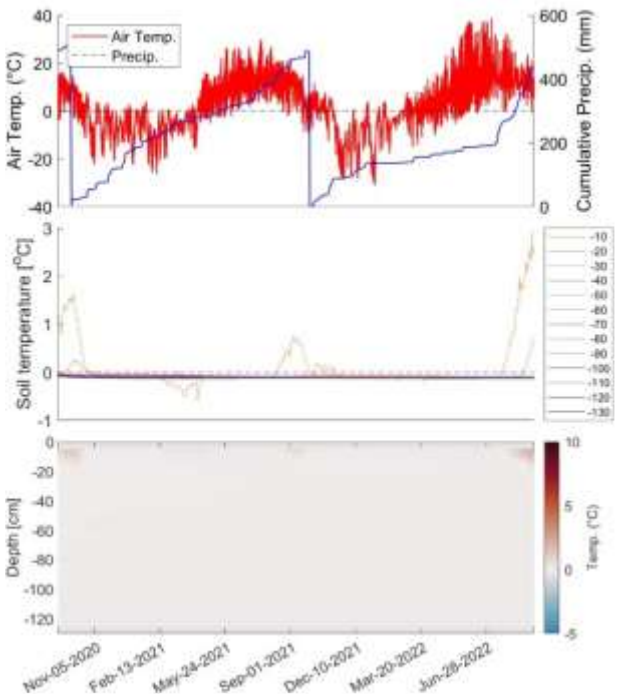

Figure 0.17 Full time series temperature plots and environmental variables for Hummock #4. (Left column) Environmental variables including: microtopographic group, relative-elevation, canopy cover, snow depth, moss thickness, and modeled shortwave radiation. (Right Column) Air temperature (red, left axis) and cumulative precipitation (blue, right axis). Soil temperature at depths from 10 to 140 cm below the soil surface according to colors in the legend. Colormap plot of soil temperature according to color in the legend.

Hummock #5

Environmental Variables:
Location Group: Hollow
Rel. Elevation (5 m): +0.29m
Canopy Cover: 78%
Snow depth: 0.0 cm
Moss Thickness: 0.0 cm
Model SW Rad.: 1.56 x 10^7 W/m^2

Permafrost and Thermal Metrics
Permafrost Table Depth: 58.4 cm
Annual Thaw Rate: 7.3 cm/year
Min. 10 cm Temperature: -3.12°C
Max. 10 cm Temperature: +3.74°C
Penetration Depth of -0.05°C: 31 cm
Penetration Depth of +3°C: 9 cm

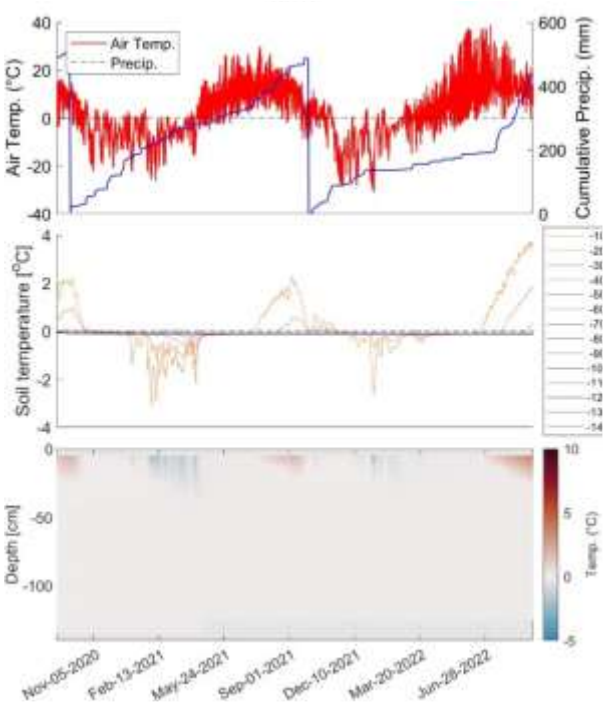

Figure 0.18 Full time series temperature plots and environmental variables for Hummock #5. (Left column) Environmental variables including: microtopographic group, relative-elevation, canopy cover, snow depth, moss thickness, and modeled shortwave radiation. (Right Column) Air temperature (red, left axis) and cumulative precipitation (blue, right axis). Soil temperature at depths from 10 to 140 cm below the soil surface according to colors in the legend. Colormap plot of soil temperature according to color in the legend.

Hummock #6

Environmental Variables:
Location Group: Hollow
Rel. Elevation (5 m): +0.23 m
Canopy Cover: 69%
Snow depth: 20.3 cm
Moss Thickness: 3.1 cm
Model SW Rad.: 3.74 x 10^7 W/m^2

Permafrost and Thermal Metrics
Permafrost Table Depth: 131.9 cm
Annual Thaw Rate: 13.8 cm/year
Min. 10 cm Temperature: -2.06°C
Max. 10 cm Temperature: +3.90°C
Penetration Depth of -0.05°C: 30 cm
Penetration Depth of +3°C: 9 cm

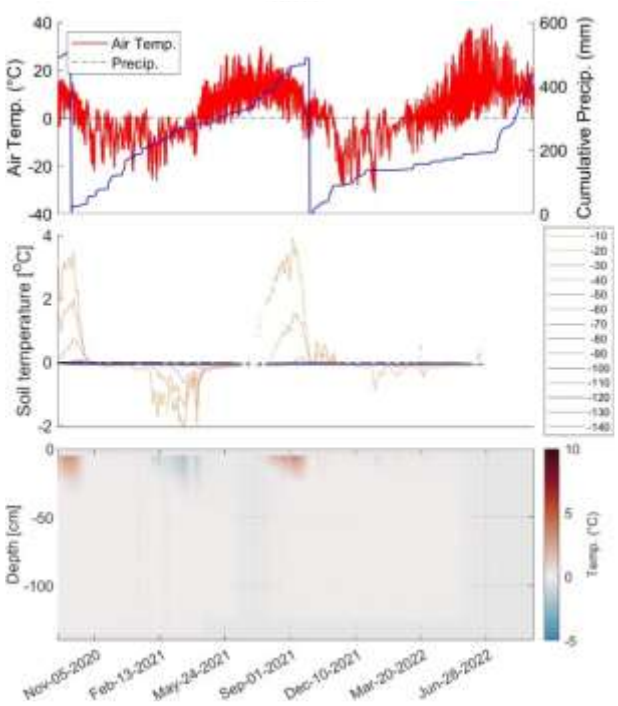

Figure 0.19 Full time series temperature plots and environmental variables for Hummock #6. *(Left column) Environmental variables including: microtopographic group, relative-elevation, canopy cover, snow depth, moss thickness, and modeled shortwave radiation. (Right Column) Air temperature (red, left axis) and cumulative precipitation (blue, right axis). Soil temperature at depths from 10 to 140 cm below the soil surface according to colors in the legend. Colormap plot of soil temperature according to color in the legend.*

SI2. Chapter 3 Supplemental

SI2.1 Modeled Soil Moisture from Local Slope

Soil moisture was measured at seven permafrost locations. Soil moisture at all other locations was modeled based on a statistically significant exponential correlation between observed soil moisture and local slope.

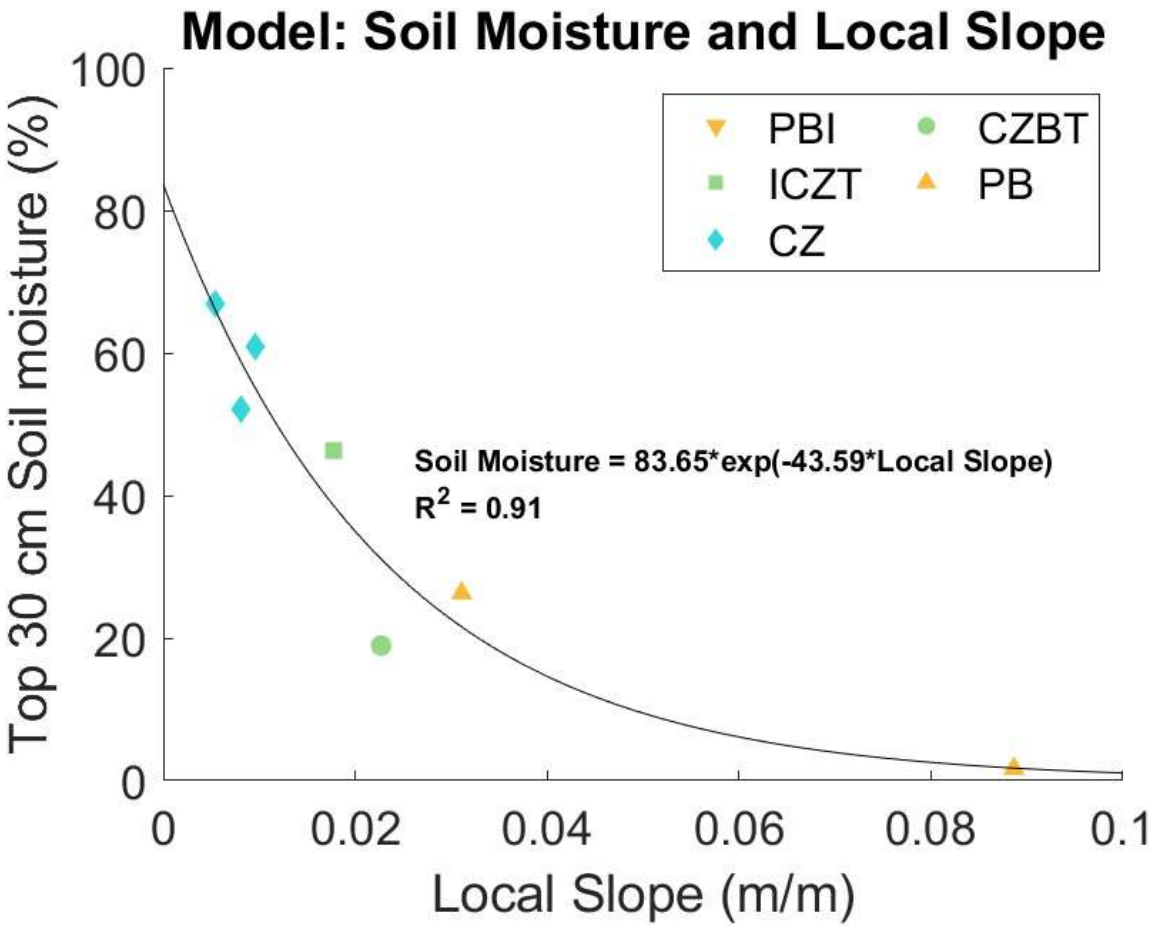

Figure 0.20 Relationship Between Local Slope and Soil Moisture. *A scatter plot matrix showing the exponential relationship between local slopes was calculated from the elevation difference of the immediately upgradient and downgradient locations divided by the distance between them and observed soil moisture.*

SI2.2 Energy Required for Thaw Calculations for Figure 3.2 and Figure 3.5

$$q_{required} = m_{ice\ content} * C_{ice} * (T_{finalsoil} - T_{initialsoil}) + m_{ice\ content} * \Delta H_{ice}$$

$q_{required}$ = heat energy required to cause warming of soils and melting of ground ice

$m_{soil\ ice}$= mass of ice in soil

C_{ice} = 2.1 J/g*C

$T_{initial}$ = Initial average soil temperature at coldest soil temp

T_{final} = 0 °C

$m_{ice\ content}$ = mass of ice in seasonally unfrozen layer = mass of water

ΔH_{ice} = heat of fusion, 333.55 J/g

SI2.3 Chapter 3 Supplementary Figures

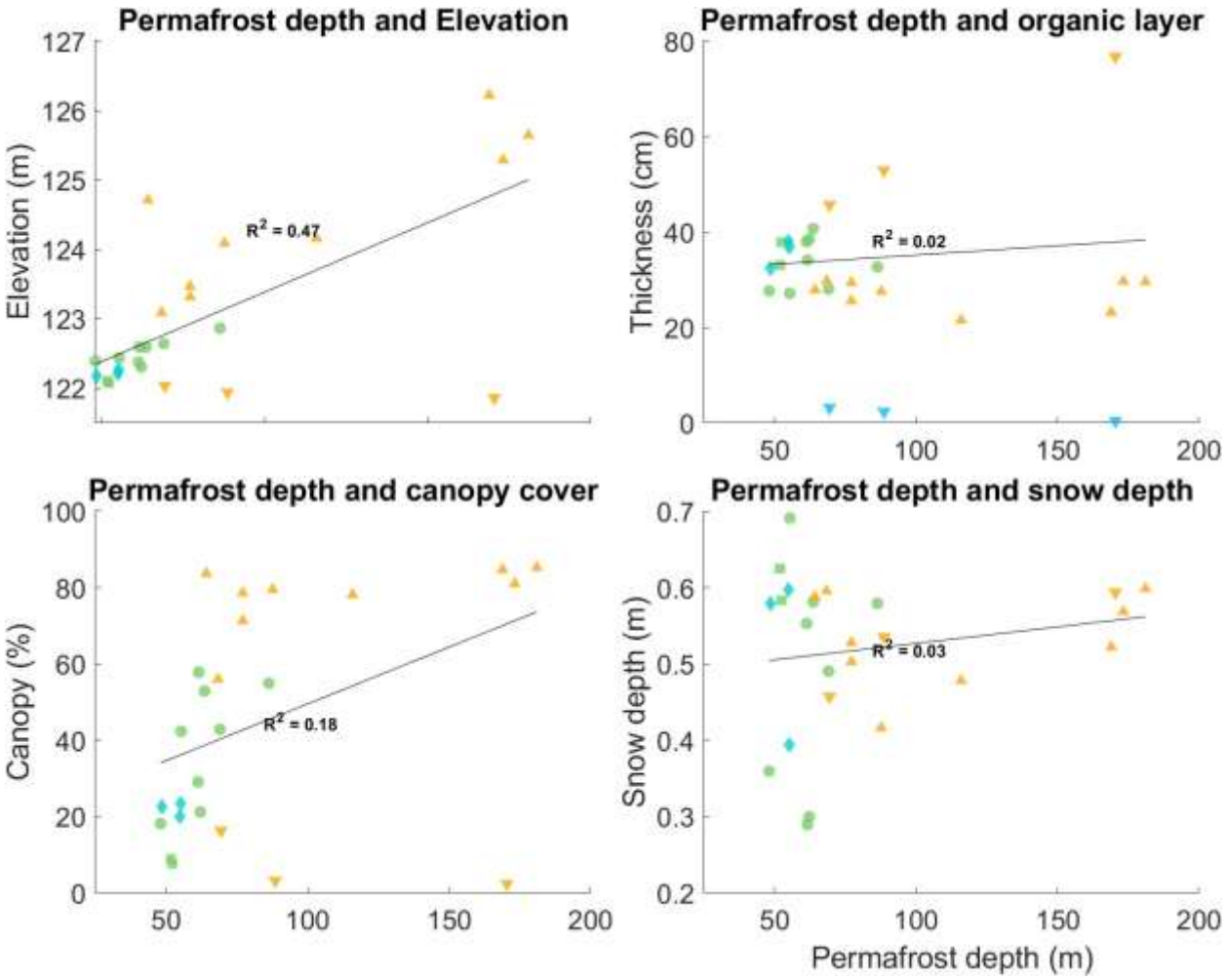

Figure 0.21 Non-Significant Correlations with Depth to Frost Table. *Scatter plots showing depth to permafrost and: elevation, organic layer thickness, canopy cover percentage, and snow depth.*

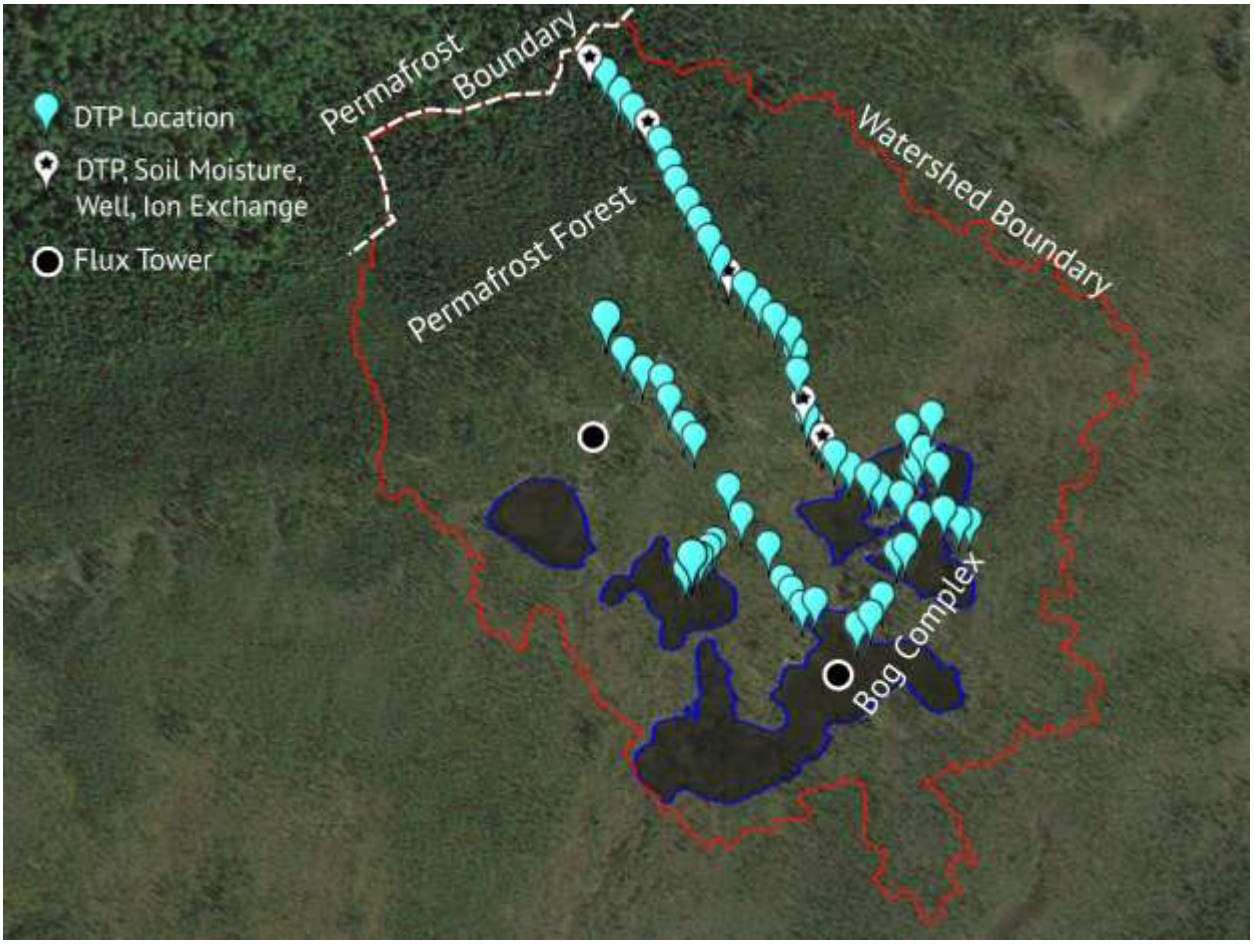

Figure 0.22 Bonanza Creek APEX Site Instrumentation. *A Google Earth image of our study site. All locations with distributed temperature profilers (DTPs) are marked in blue. Core locations, which contain a DTP, well, moisture profiler, and ion exchange resins are shown with a white marker. Flux tower locations are shown with a black circle inside of a white circle.*

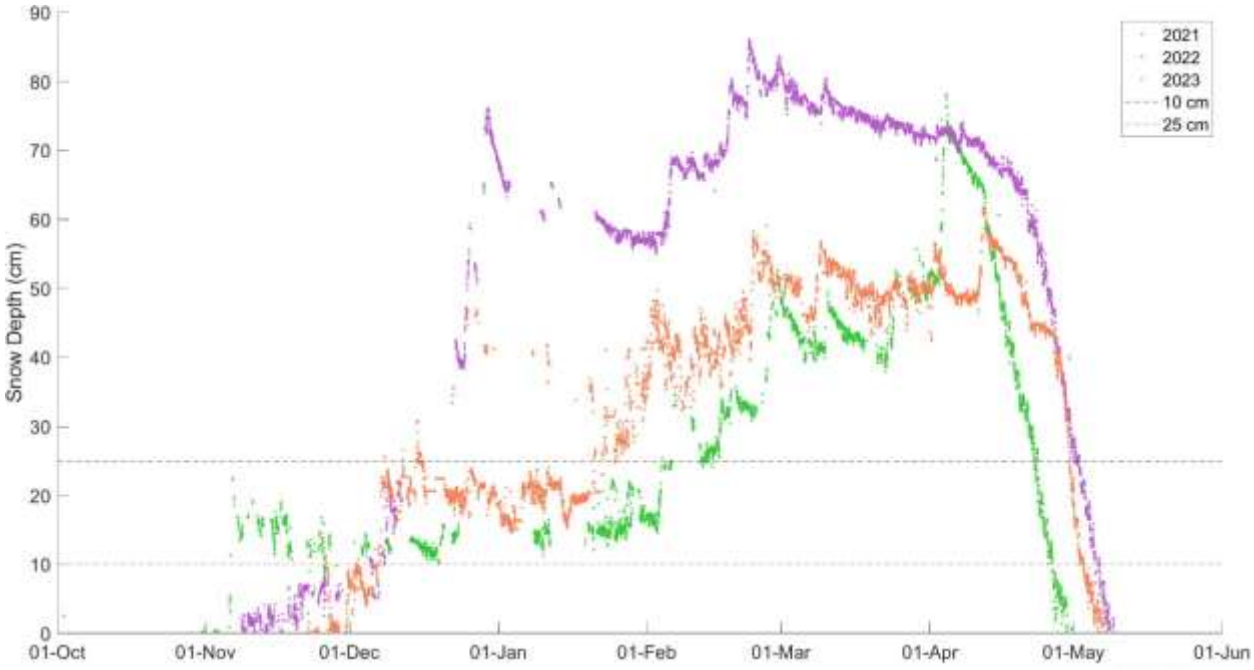

Figure 0.23 Snow Depth During Study Years. *Line plot of tower-based snow depth data from 2021, 2022, and 2023.*

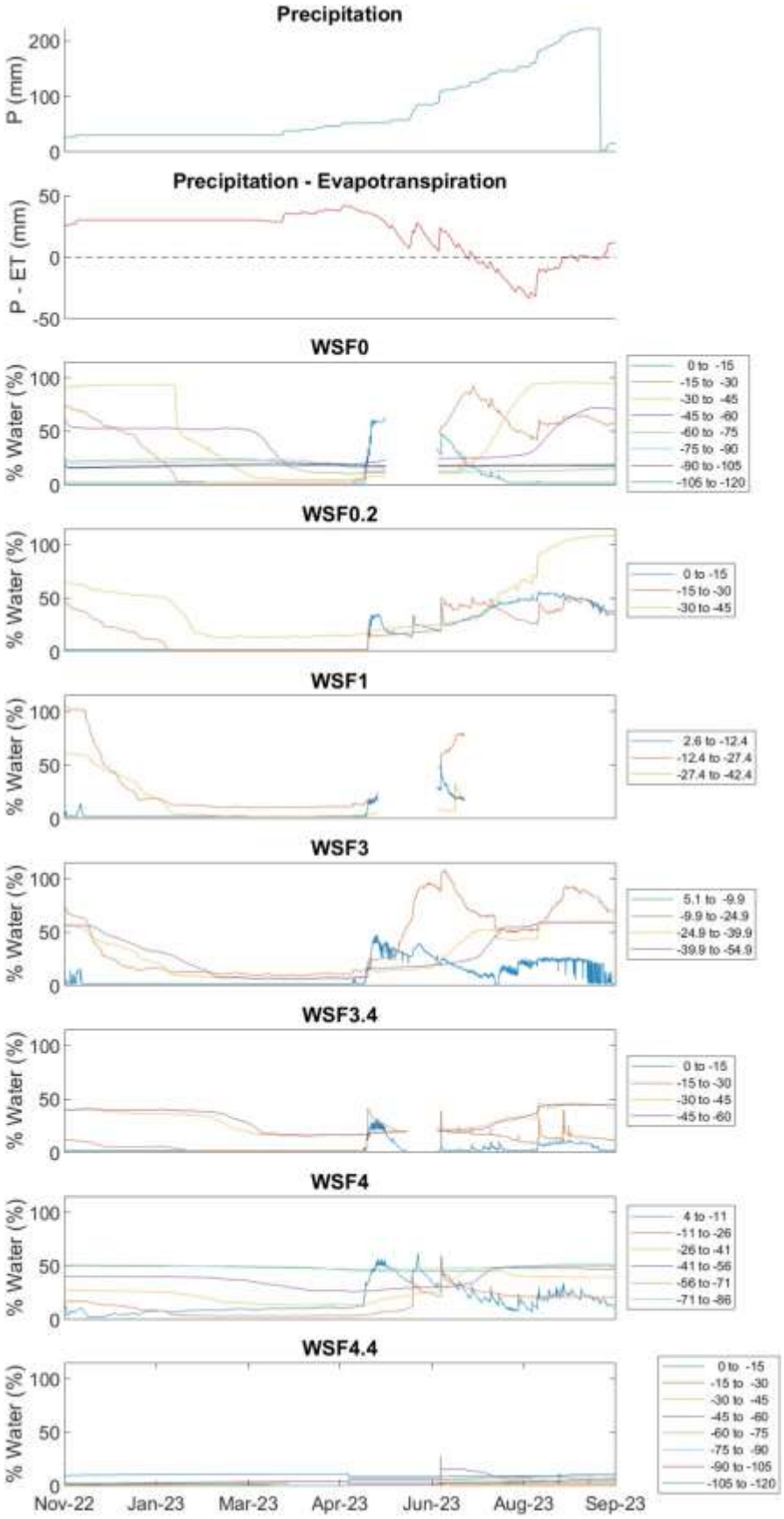

Figure 0.24 Soil Moisture Timeseries All Locations. *Timeseries data showing: precipitation, precipitation minus evapotranspiration, and soil moisture data from WSF0.0, WSF0.2, WSF1, WSF3, WSF3.4, WSF4, and WSF4.4 during the period when all soil moisture probes were installed.*

Zone 1 - BB3

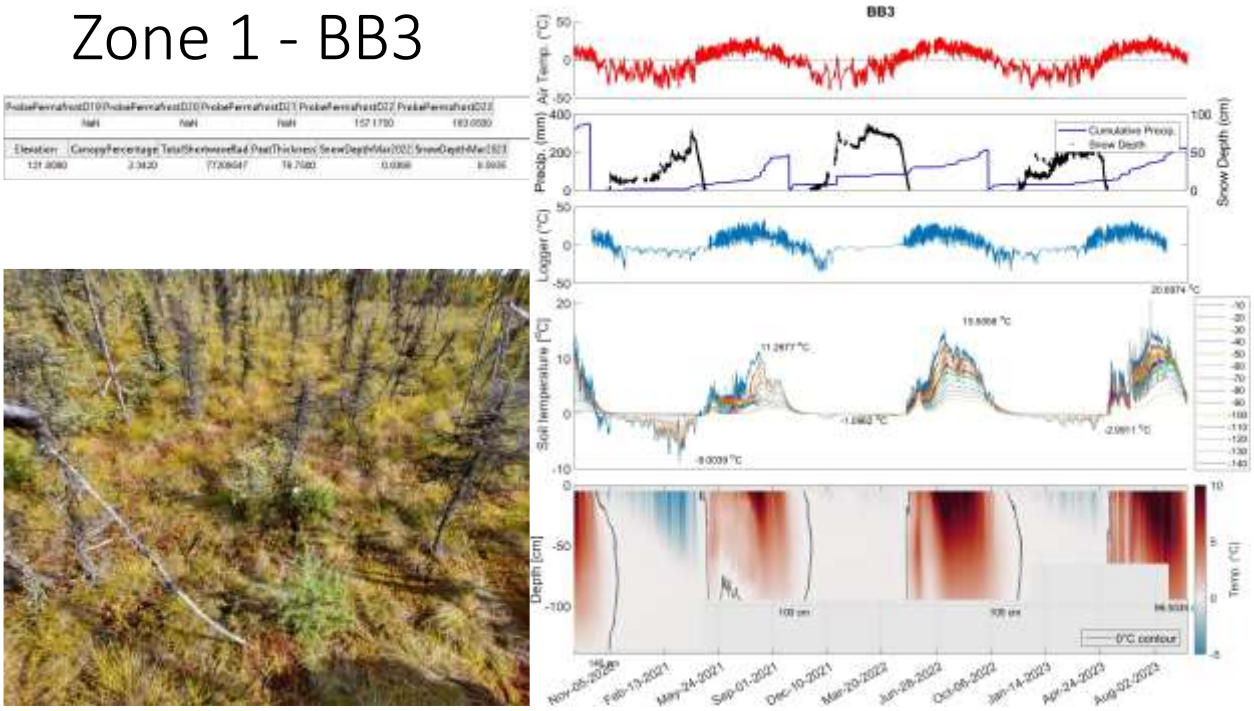

Figure 0.25 Full time series temperature plots and environmental variables for Zone 1 Location 1 *(Left column) Environmental variables including: thermal zone, measured annual depth to permafrost, elevation, canopy cover, snow depth, moss thickness, and modeled shortwave radiation. (Right Column) Air temperature (red, left axis), cumulative precipitation (blue, left axis), snow depth (black, right axis), and temperature inside the logger. Soil temperature at depths from 10 to 140 cm below the soil surface according to colors in the legend. Colormap plot of soil temperature according to color in the legend.*

Zone 2 - WSF0.0

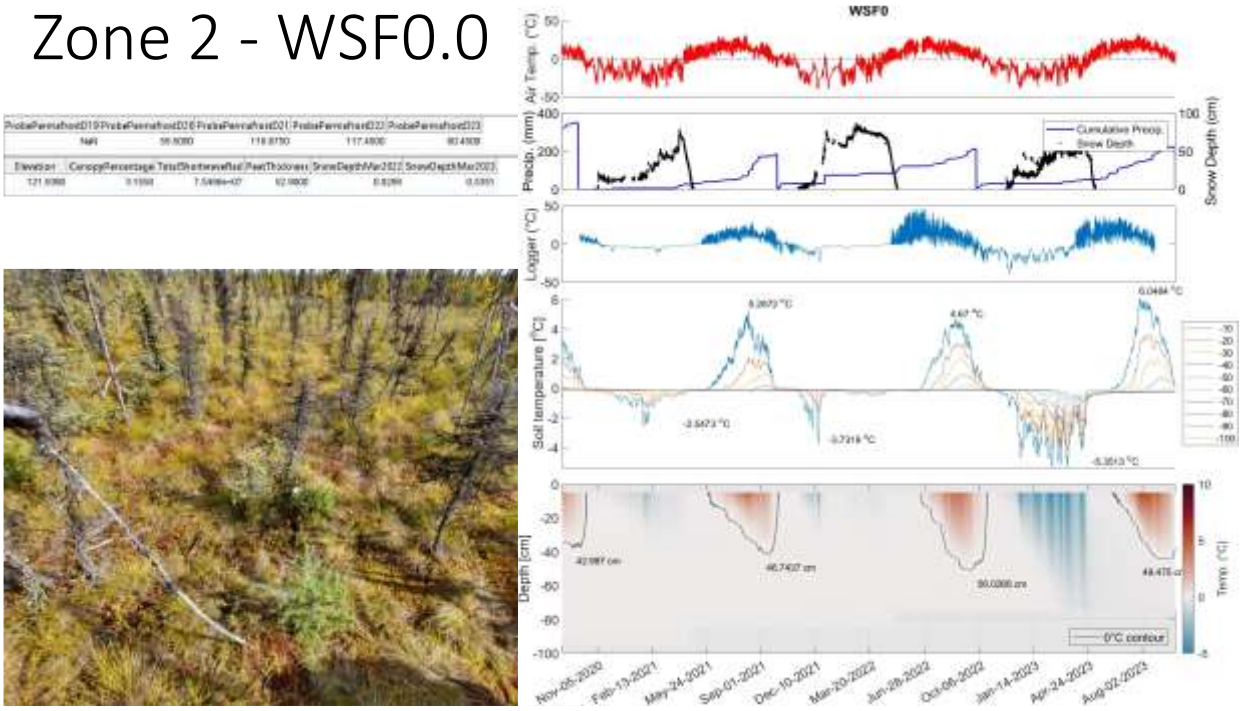

Figure 0.26 Full time series temperature plots and environmental variables for Zone 2 Location 1 *(Left column) Environmental variables including: thermal zone, measured annual depth to permafrost, elevation, canopy cover, snow depth, moss thickness, and modeled shortwave radiation. (Right Column) Air temperature (red, left axis), cumulative precipitation (blue, left axis), snow depth (black, right axis), and temperature inside the logger. Soil temperature at depths from 10 to 140 cm below the soil surface according to colors in the legend. Colormap plot of soil temperature according to color in the legend.*

Zone 2 - WSF0.1

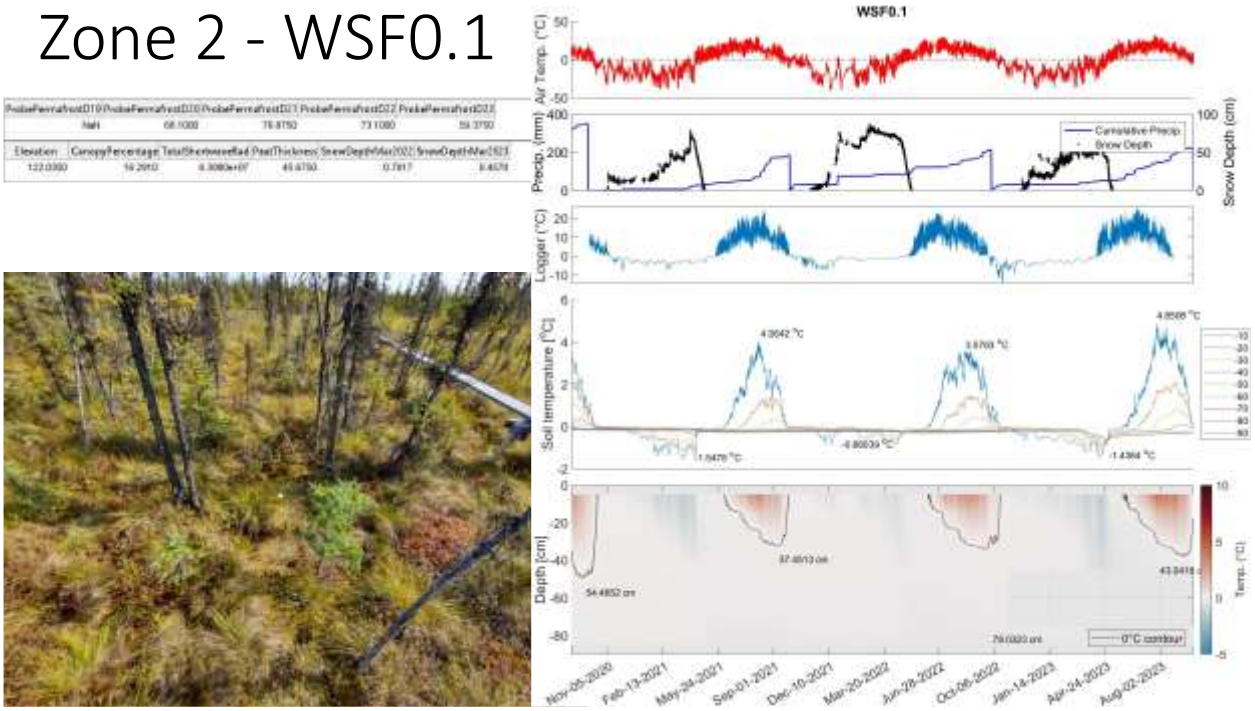

Figure 0.27 Full time series temperature plots and environmental variables for Zone 2 Location 2 *(Left column) Environmental variables including: thermal zone, measured annual depth to permafrost, elevation, canopy cover, snow depth, moss thickness, and modeled shortwave radiation. (Right Column) Air temperature (red, left axis), cumulative precipitation (blue, left axis), snow depth (black, right axis), and temperature inside the logger. Soil temperature at depths from 10 to 140 cm below the soil surface according to colors in the legend. Colormap plot of soil temperature according to color in the legend.*

Zone 3 - WSF0.2

ProbePermafrost019	ProbePermafrost020	ProbePermafrost021	ProbePermafrost022	ProbePermafrost023
NaN	58	48.6500	46.5000	52.3500

Elevation	CanopyPercentage	TotalShortwaveRad	PeatThickness	SnowDepthMar2022	SnowDepthMar2023
122.9970	7.6840	7.1726e+07	37.6500	0.9136	0.5833

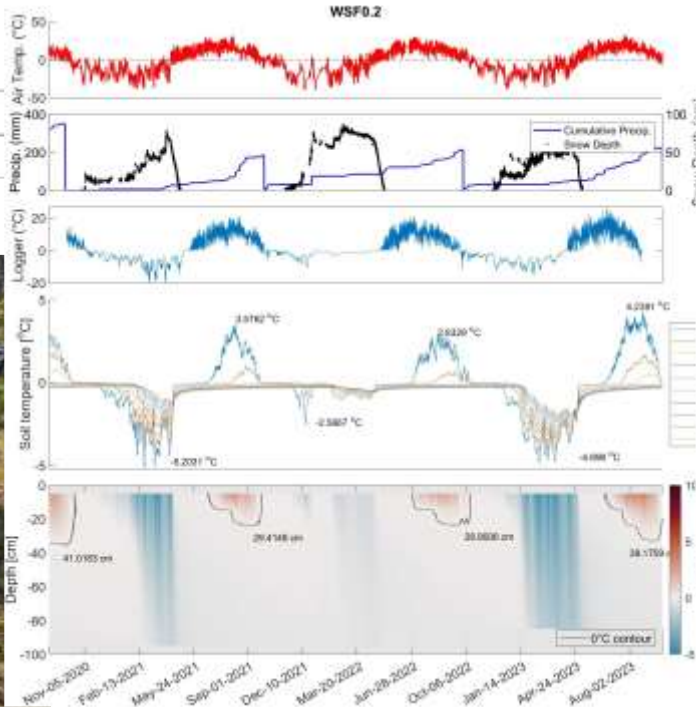

Figure 0.28 Full time series temperature plots and environmental variables for Zone 3 Location 1 *(Left column) Environmental variables including: thermal zone, measured annual depth to permafrost, elevation, canopy cover, snow depth, moss thickness, and modeled shortwave radiation. (Right Column) Air temperature (red, left axis), cumulative precipitation (blue, left axis), snow depth (black, right axis), and temperature inside the logger. Soil temperature at depths from 10 to 140 cm below the soil surface according to colors in the legend. Colormap plot of soil temperature according to color in the legend.*

Zone 3 - WSF0.3

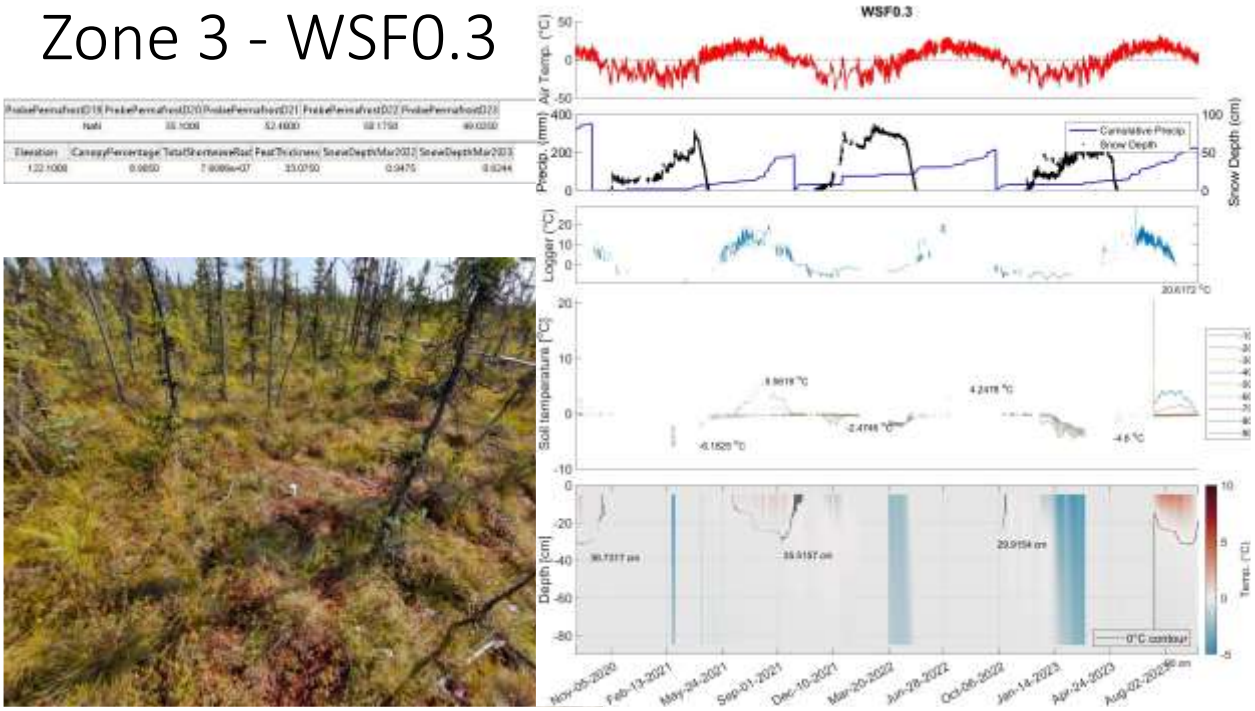

Figure 0.29 Full time series temperature plots and environmental variables for Zone 3 Location 2 *(Left column) Environmental variables including: thermal zone, measured annual depth to permafrost, elevation, canopy cover, snow depth, moss thickness, and modeled shortwave radiation. (Right Column) Air temperature (red, left axis), cumulative precipitation (blue, left axis), snow depth (black, right axis), and temperature inside the logger. Soil temperature at depths from 10 to 140 cm below the soil surface according to colors in the legend. Colormap plot of soil temperature according to color in the legend.*

Zone 3 - WSF1

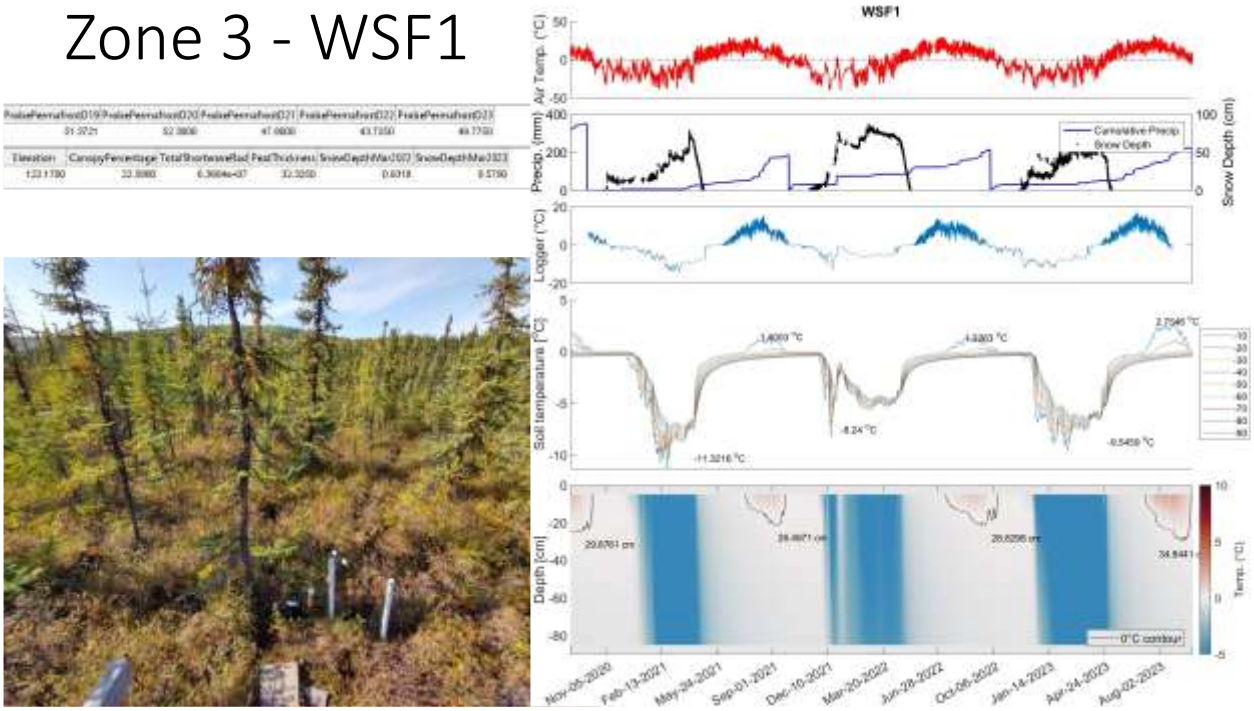

Figure 0.30 Full time series temperature plots and environmental variables for Zone 3 Location 3 *(Left column) Environmental variables including: thermal zone, measured annual depth to permafrost, elevation, canopy cover, snow depth, moss thickness, and modeled shortwave radiation. (Right Column) Air temperature (red, left axis), cumulative precipitation (blue, left axis), snow depth (black, right axis), and temperature inside the logger. Soil temperature at depths from 10 to 140 cm below the soil surface according to colors in the legend. Colormap plot of soil temperature according to color in the legend.*

Zone 3 - WSF1.1

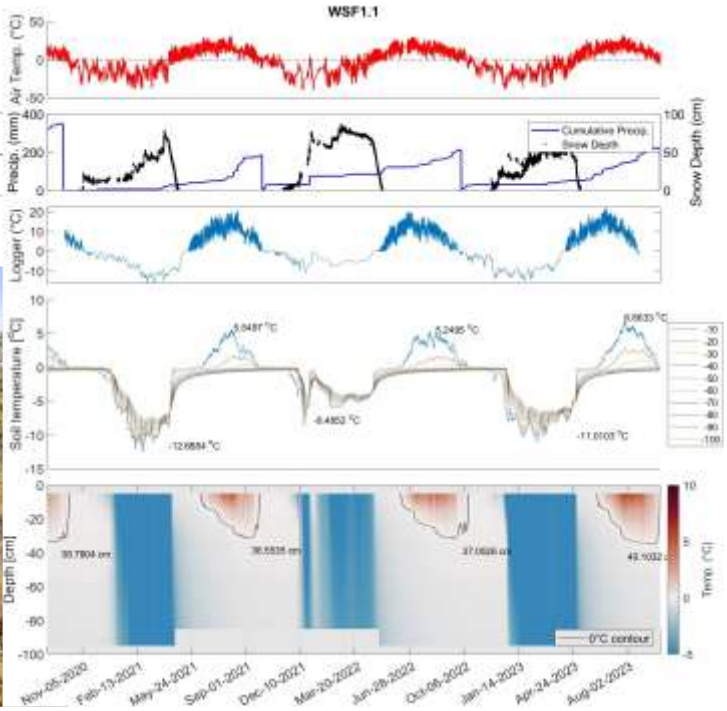

Figure 0.31 Full time series temperature plots and environmental variables for Zone 3 Location 4 *(Left column) Environmental variables including: thermal zone, measured annual depth to permafrost, elevation, canopy cover, snow depth, moss thickness, and modeled shortwave radiation. (Right Column) Air temperature (red, left axis), cumulative precipitation (blue, left axis), snow depth (black, right axis), and temperature inside the logger. Soil temperature at depths from 10 to 140 cm below the soil surface according to colors in the legend. Colormap plot of soil temperature according to color in the legend.*

Zone 3 - WSF1.2

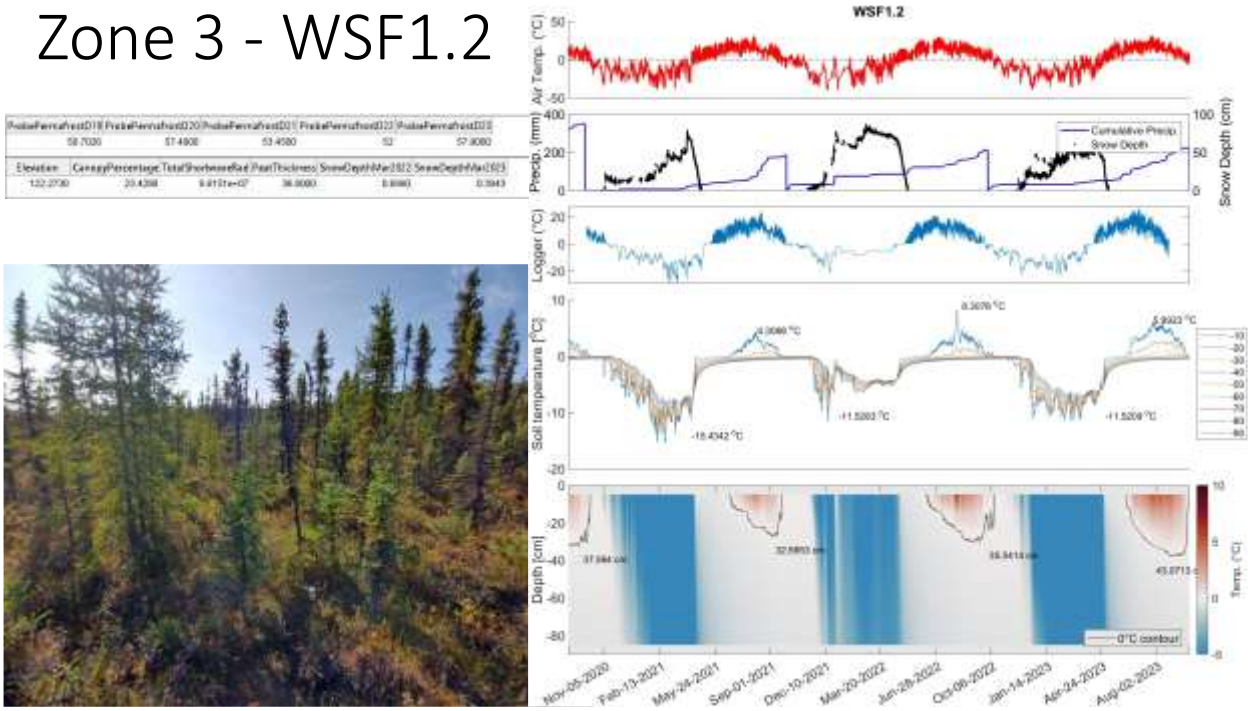

Figure 0.32 Full time series temperature plots and environmental variables for Zone 3 Location 5 *(Left column) Environmental variables including: thermal zone, measured annual depth to permafrost, elevation, canopy cover, snow depth, moss thickness, and modeled shortwave radiation. (Right Column) Air temperature (red, left axis), cumulative precipitation (blue, left axis), snow depth (black, right axis), and temperature inside the logger. Soil temperature at depths from 10 to 140 cm below the soil surface according to colors in the legend. Colormap plot of soil temperature according to color in the legend.*

Zone 3 - WSF2

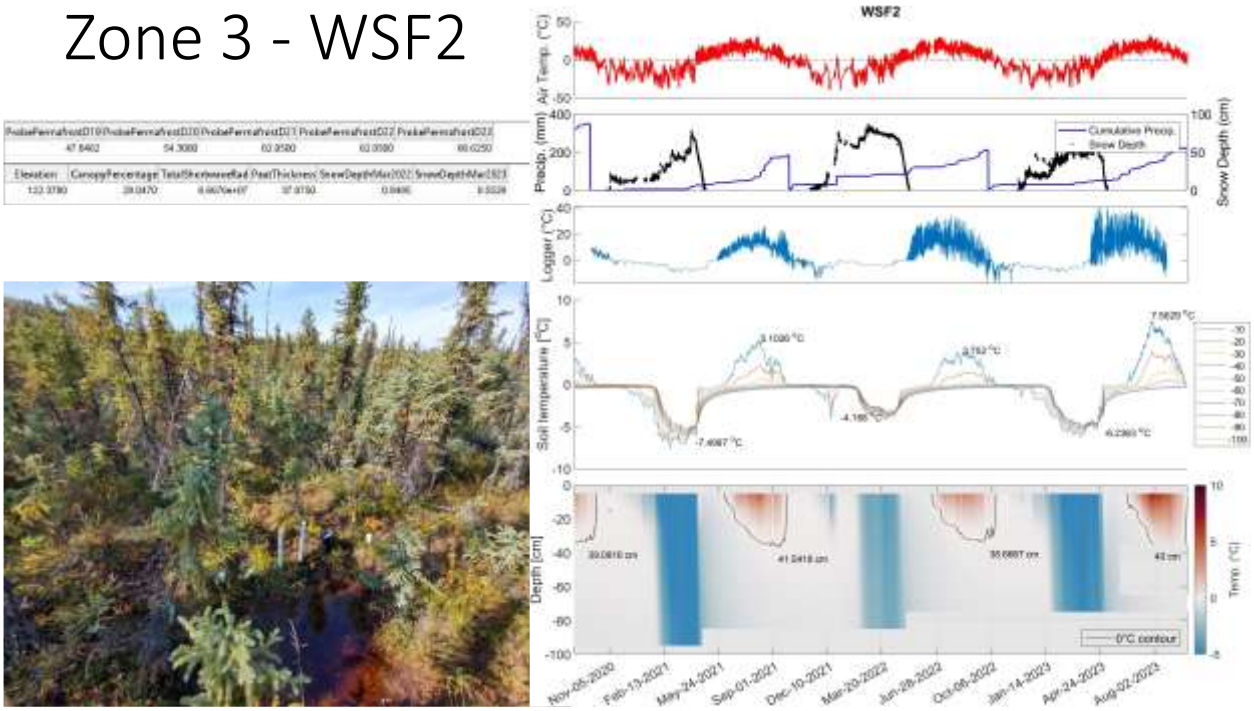

Figure 0.33 Full time series temperature plots and environmental variables for Zone 3 Location 6 *(Left column) Environmental variables including: thermal zone, measured annual depth to permafrost, elevation, canopy cover, snow depth, moss thickness, and modeled shortwave radiation. (Right Column) Air temperature (red, left axis), cumulative precipitation (blue, left axis), snow depth (black, right axis), and temperature inside the logger. Soil temperature at depths from 10 to 140 cm below the soil surface according to colors in the legend. Colormap plot of soil temperature according to color in the legend.*

Zone 3 - WSF2.1

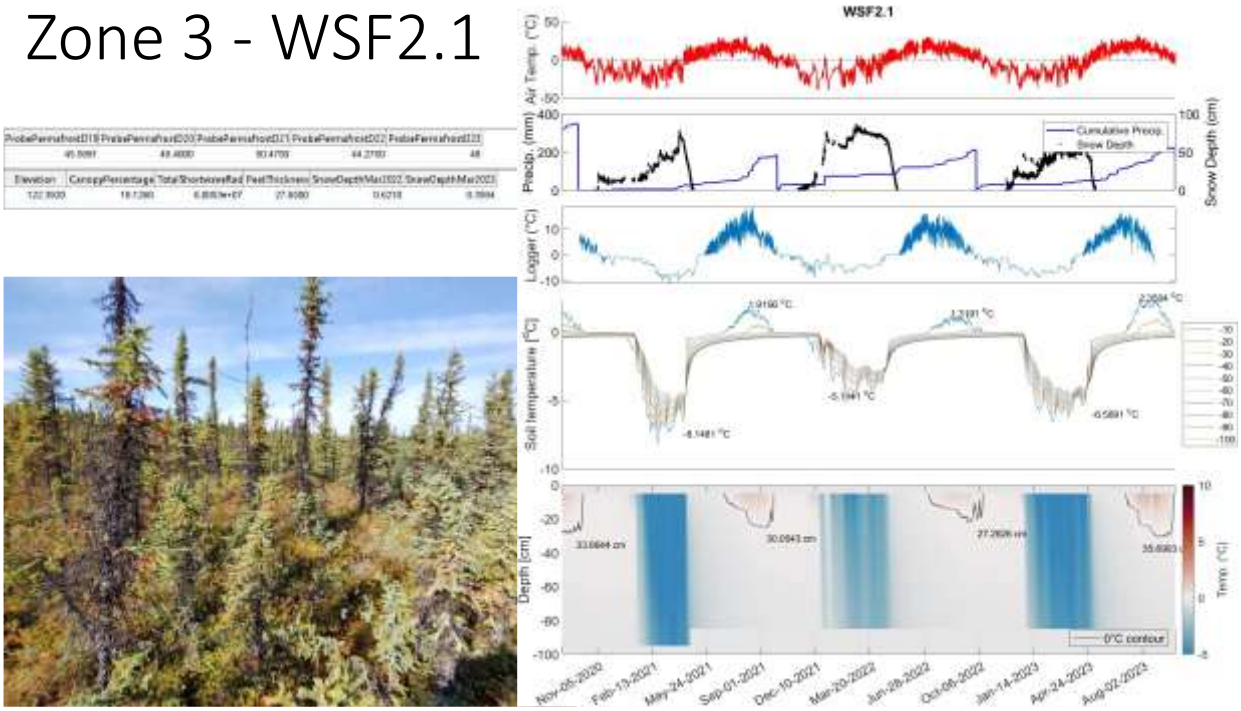

Figure 0.34 Full time series temperature plots and environmental variables for Zone 3 Location 7 *(Left column) Environmental variables including: thermal zone, measured annual depth to permafrost, elevation, canopy cover, snow depth, moss thickness, and modeled shortwave radiation. (Right Column) Air temperature (red, left axis), cumulative precipitation (blue, left axis), snow depth (black, right axis), and temperature inside the logger. Soil temperature at depths from 10 to 140 cm below the soil surface according to colors in the legend. Colormap plot of soil temperature according to color in the legend.*

Zone 3 - WSF2.2

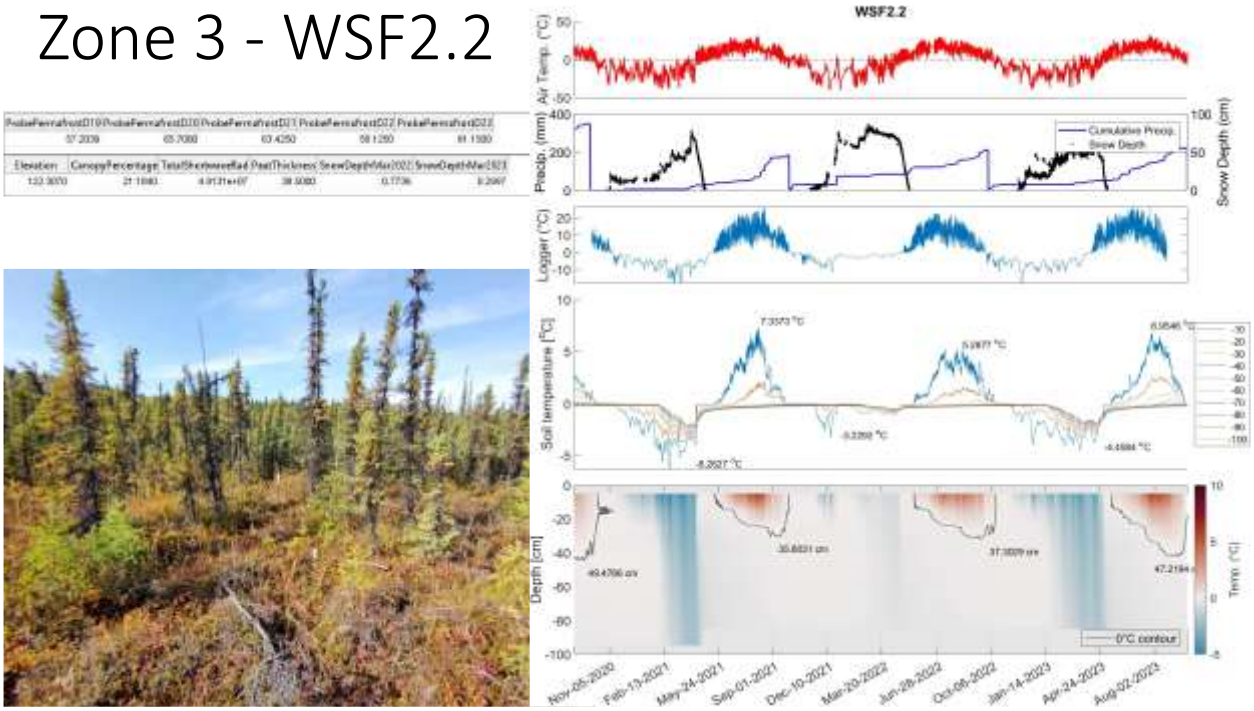

Figure 0.35 Full time series temperature plots and environmental variables for Zone 3 Location 8 *(Left column) Environmental variables including: thermal zone, measured annual depth to permafrost, elevation, canopy cover, snow depth, moss thickness, and modeled shortwave radiation. (Right Column) Air temperature (red, left axis), cumulative precipitation (blue, left axis), snow depth (black, right axis), and temperature inside the logger. Soil temperature at depths from 10 to 140 cm below the soil surface according to colors in the legend. Colormap plot of soil temperature according to color in the legend.*

Zone 3 - WSF2.3

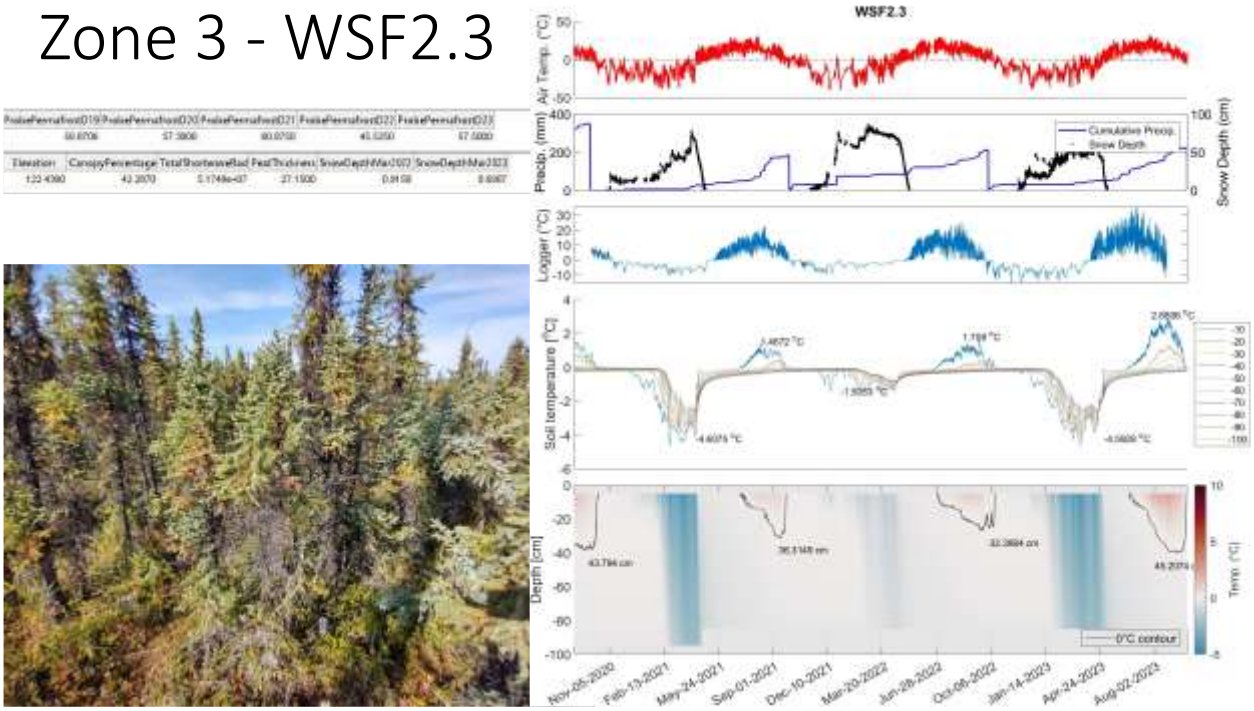

Figure 0.36 Full time series temperature plots and environmental variables for Zone 3 Location 9 *(Left column) Environmental variables including: thermal zone, measured annual depth to permafrost, elevation, canopy cover, snow depth, moss thickness, and modeled shortwave radiation. (Right Column) Air temperature (red, left axis), cumulative precipitation (blue, left axis), snow depth (black, right axis), and temperature inside the logger. Soil temperature at depths from 10 to 140 cm below the soil surface according to colors in the legend. Colormap plot of soil temperature according to color in the legend.*

Zone 3 - WSF3

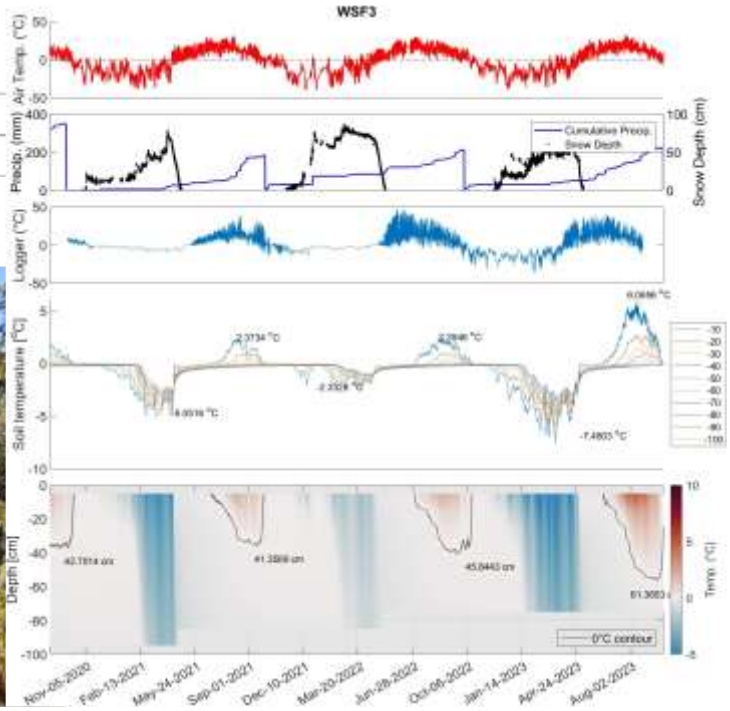

Figure 0.37 Full time series temperature plots and environmental variables for Zone 3 Location 10 *(Left column) Environmental variables including: thermal zone, measured annual depth to permafrost, elevation, canopy cover, snow depth, moss thickness, and modeled shortwave radiation. (Right Column) Air temperature (red, left axis), cumulative precipitation (blue, left axis), snow depth (black, right axis), and temperature inside the logger. Soil temperature at depths from 10 to 140 cm below the soil surface according to colors in the legend. Colormap plot of soil temperature according to color in the legend.*

Zone 3 - WSF3.1

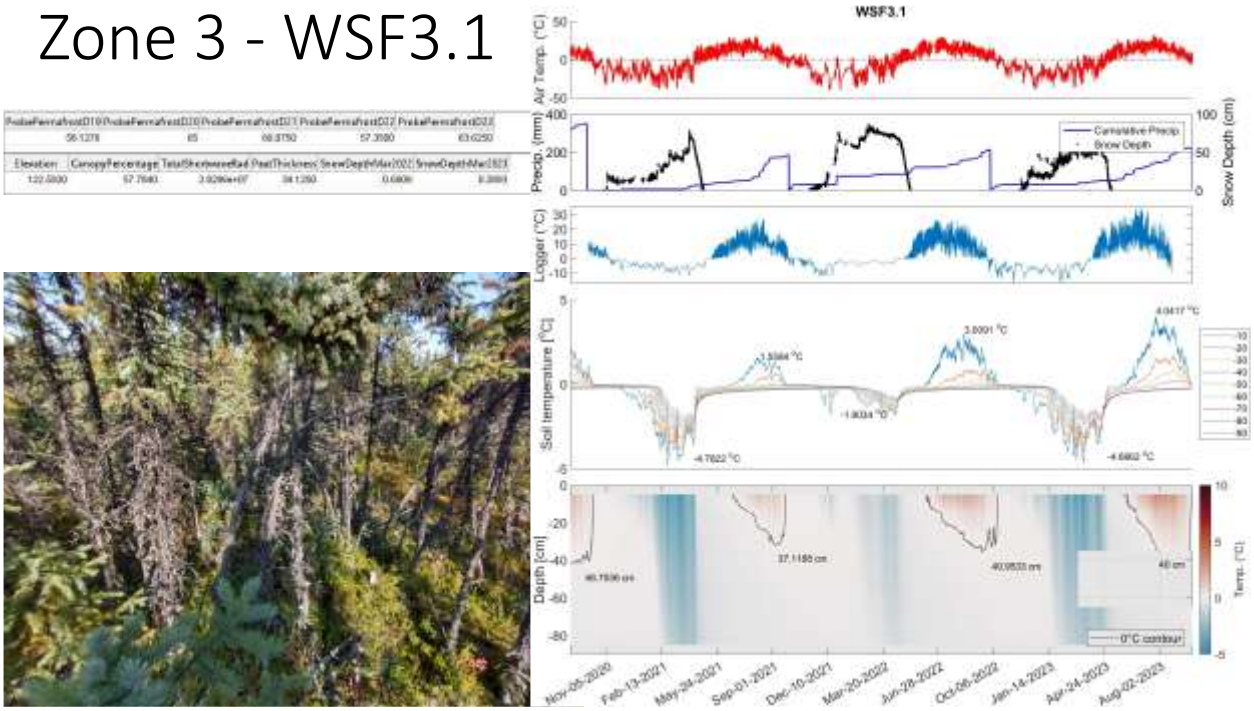

Figure 0.38 Full time series temperature plots and environmental variables for Zone 3 Location 12 *(Left column) Environmental variables including: thermal zone, measured annual depth to permafrost, elevation, canopy cover, snow depth, moss thickness, and modeled shortwave radiation. (Right Column) Air temperature (red, left axis), cumulative precipitation (blue, left axis), snow depth (black, right axis), and temperature inside the logger. Soil temperature at depths from 10 to 140 cm below the soil surface according to colors in the legend. Colormap plot of soil temperature according to color in the legend.*

Zone 3 - WSF3.2

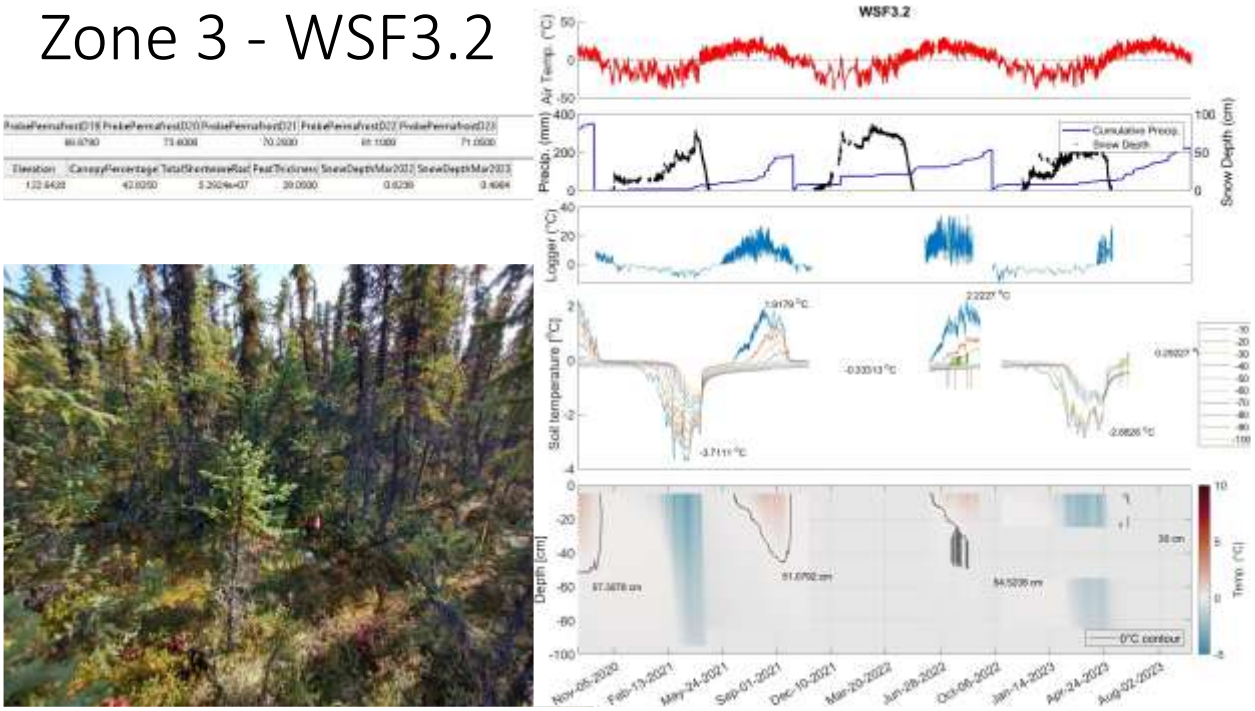

Figure 0.39 Full time series temperature plots and environmental variables for Zone 3 Location 13 *(Left column) Environmental variables including: thermal zone, measured annual depth to permafrost, elevation, canopy cover, snow depth, moss thickness, and modeled shortwave radiation. (Right Column) Air temperature (red, left axis), cumulative precipitation (blue, left axis), snow depth (black, right axis), and temperature inside the logger. Soil temperature at depths from 10 to 140 cm below the soil surface according to colors in the legend. Colormap plot of soil temperature according to color in the legend.*

Zone 4 - WSF3.3

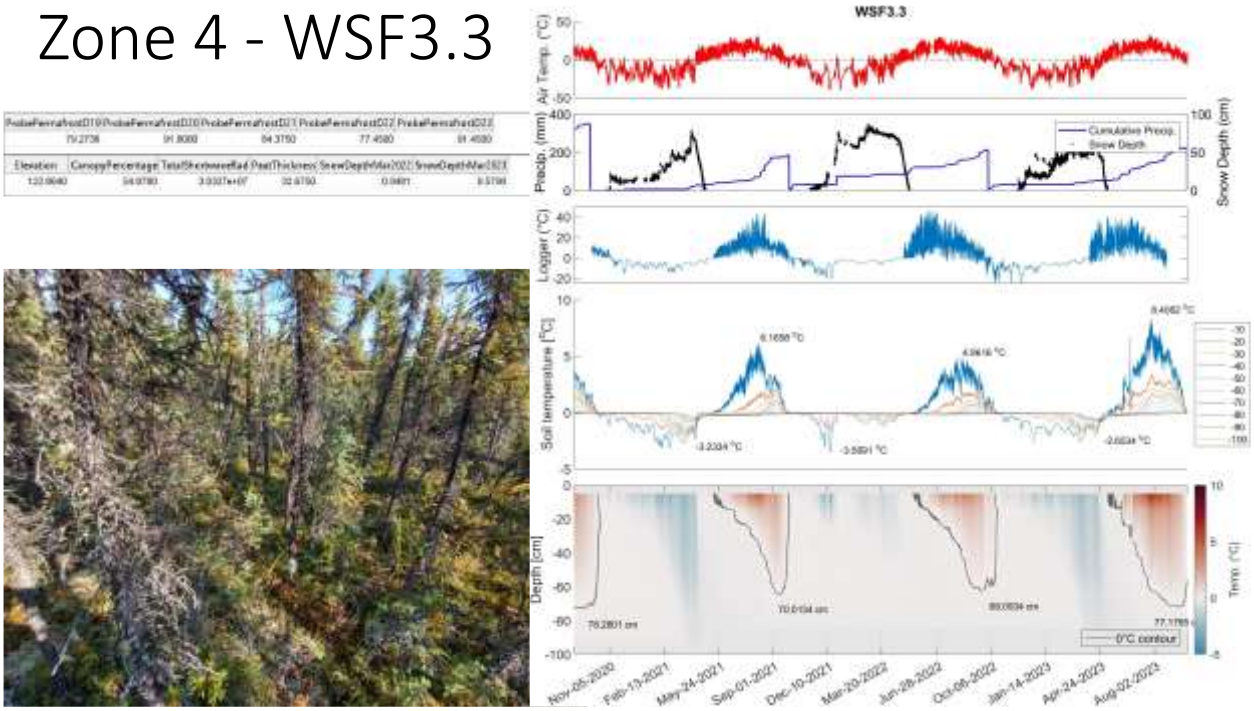

Figure 0.40 Full time series temperature plots and environmental variables for Zone 4 Location 1 *(Left column) Environmental variables including: thermal zone, measured annual depth to permafrost, elevation, canopy cover, snow depth, moss thickness, and modeled shortwave radiation. (Right Column) Air temperature (red, left axis), cumulative precipitation (blue, left axis), snow depth (black, right axis), and temperature inside the logger. Soil temperature at depths from 10 to 140 cm below the soil surface according to colors in the legend. Colormap plot of soil temperature according to color in the legend.*

Zone 4 - WSF3.4

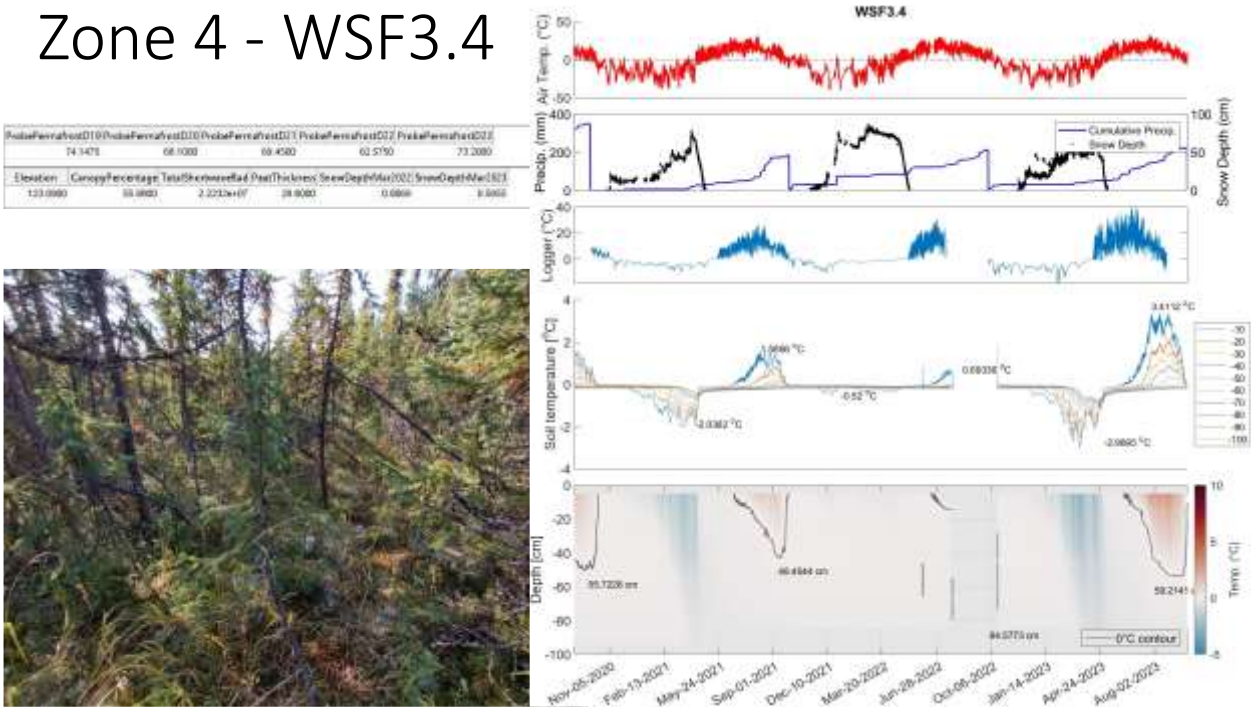

Figure 0.41 Full time series temperature plots and environmental variables for Zone 4 Location 2 *(Left column) Environmental variables including: thermal zone, measured annual depth to permafrost, elevation, canopy cover, snow depth, moss thickness, and modeled shortwave radiation. (Right Column) Air temperature (red, left axis), cumulative precipitation (blue, left axis), snow depth (black, right axis), and temperature inside the logger. Soil temperature at depths from 10 to 140 cm below the soil surface according to colors in the legend. Colormap plot of soil temperature according to color in the legend.*

Zone 4 - WSF3.5

PoldePermafrostD19	PoldePermafrostD20	PoldePermafrostD21	PoldePermafrostD22	PoldePermafrostD23
86.1797	73.1808	72.6750	71.0750	90.0800

Elevation	CanopyPercentage	TotalShortwaveRad	PeatThickness	SnowDepthMar2022	SnowDepthMar2023
123.3180	71.2500	3.0844e+07	35.0750	0.8008	0.5275

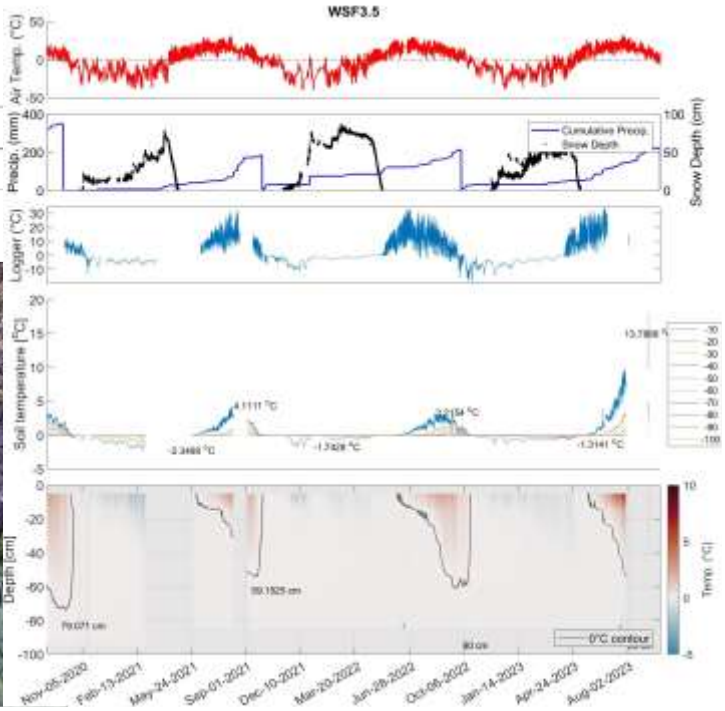

Figure 0.42 Full time series temperature plots and environmental variables for Zone 4 Location 3 *(Left column) Environmental variables including: thermal zone, measured annual depth to permafrost, elevation, canopy cover, snow depth, moss thickness, and modeled shortwave radiation. (Right Column) Air temperature (red, left axis), cumulative precipitation (blue, left axis), snow depth (black, right axis), and temperature inside the logger. Soil temperature at depths from 10 to 140 cm below the soil surface according to colors in the legend. Colormap plot of soil temperature according to color in the legend.*

Zone 5 - WSF3.6

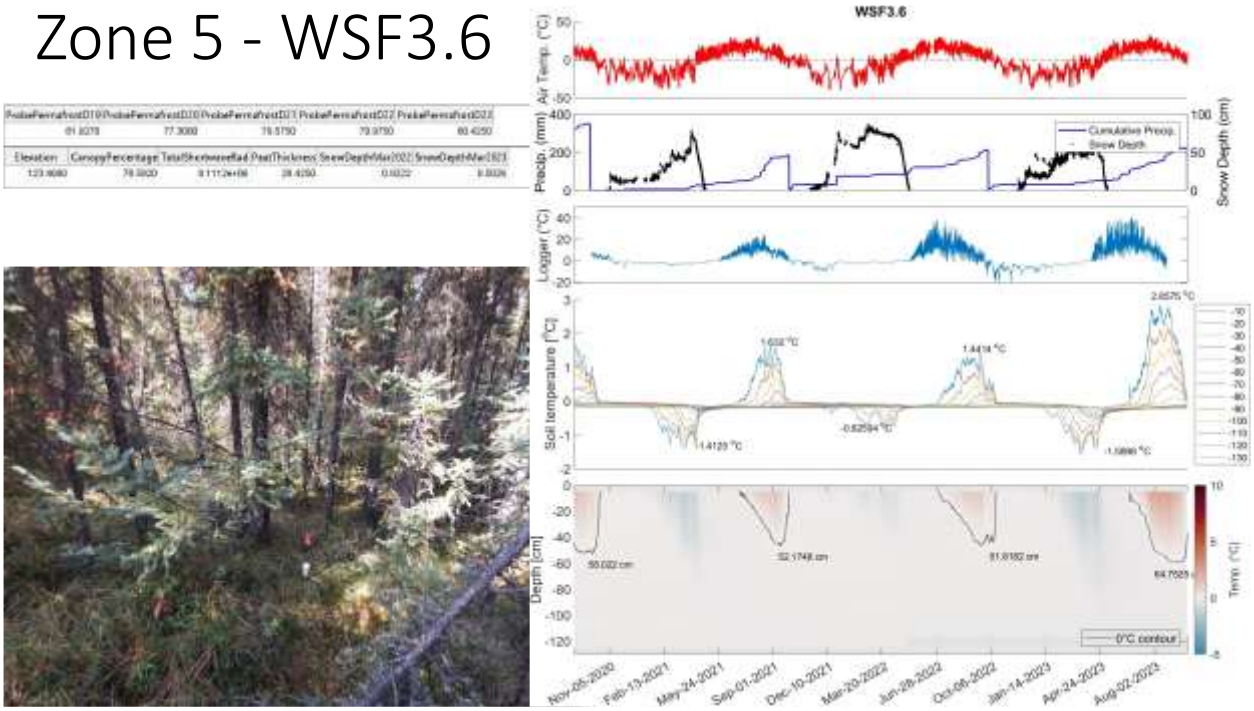

Figure 0.43 Full time series temperature plots and environmental variables for Zone 5 Location 1 *(Left column) Environmental variables including: thermal zone, measured annual depth to permafrost, elevation, canopy cover, snow depth, moss thickness, and modeled shortwave radiation. (Right Column) Air temperature (red, left axis), cumulative precipitation (blue, left axis), snow depth (black, right axis), and temperature inside the logger. Soil temperature at depths from 10 to 140 cm below the soil surface according to colors in the legend. Colormap plot of soil temperature according to color in the legend.*

Zone 5 - WSF3.7

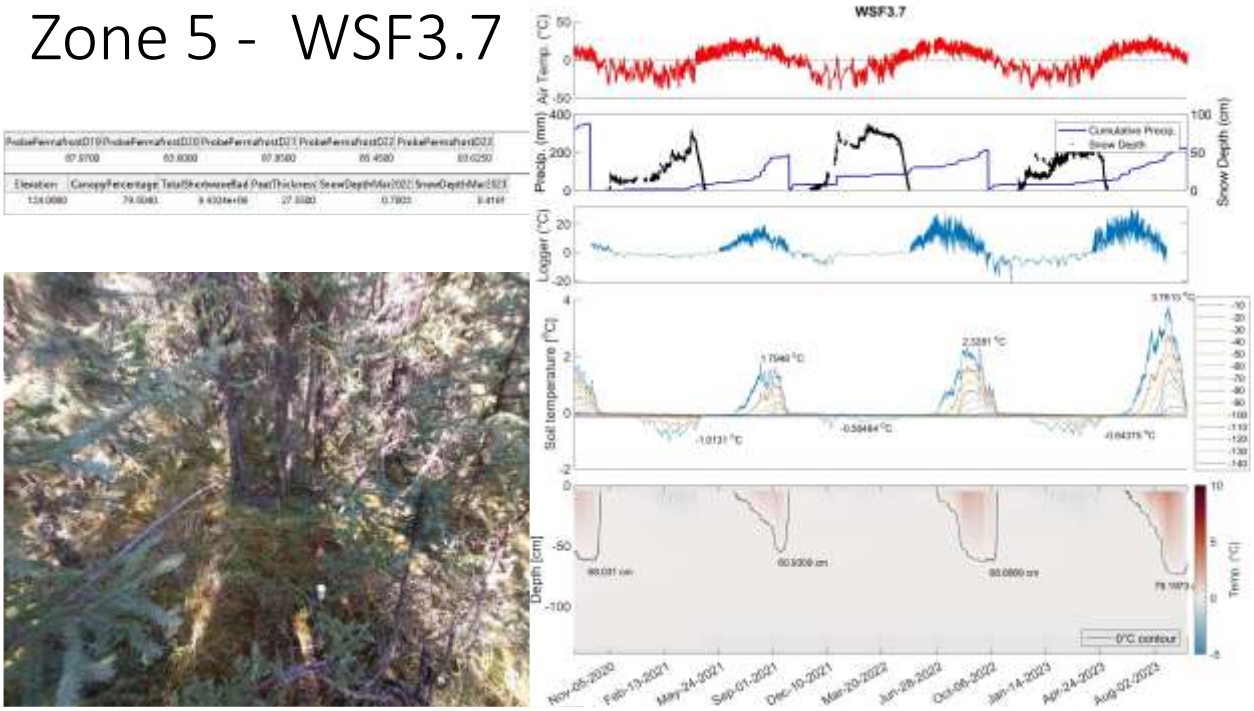

Figure 0.44 Full time series temperature plots and environmental variables for Zone 5 Location 2 *(Left column) Environmental variables including: thermal zone, measured annual depth to permafrost, elevation, canopy cover, snow depth, moss thickness, and modeled shortwave radiation. (Right Column) Air temperature (red, left axis), cumulative precipitation (blue, left axis), snow depth (black, right axis), and temperature inside the logger. Soil temperature at depths from 10 to 140 cm below the soil surface according to colors in the legend. Colormap plot of soil temperature according to color in the legend.*

Zone 5 - WSF4

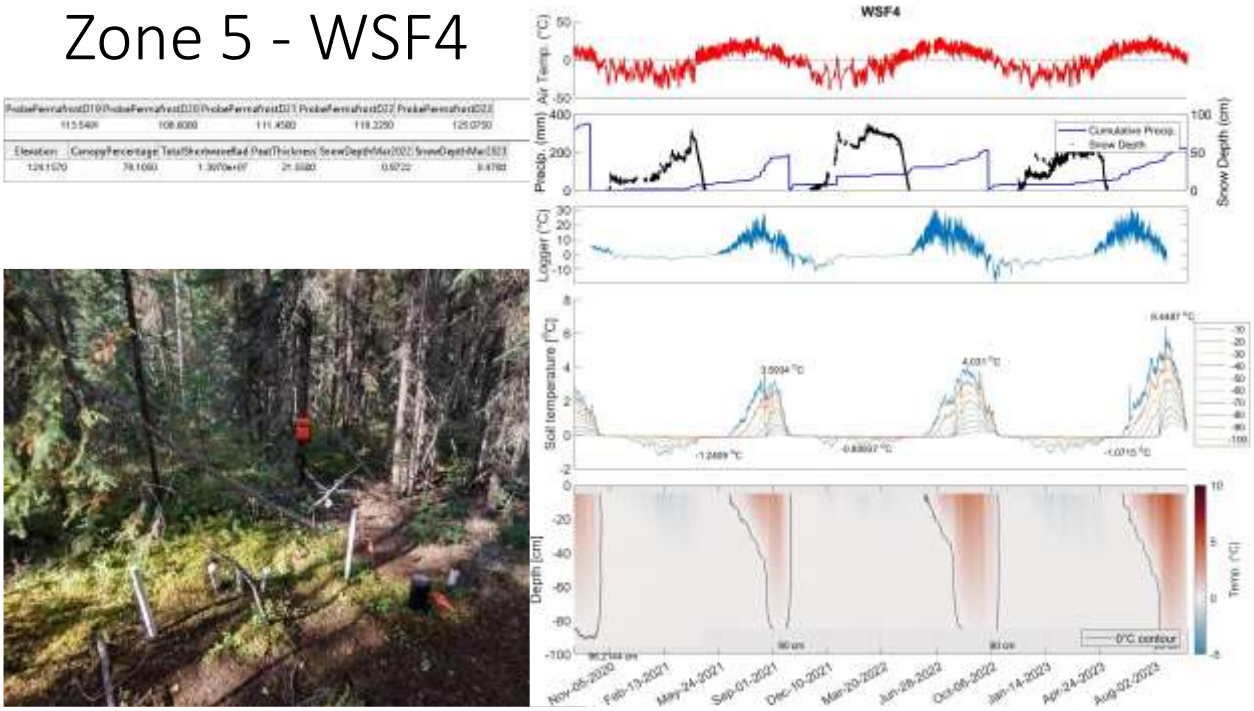

Figure 0.45 Full time series temperature plots and environmental variables for Zone 5 Location 3 *(Left column) Environmental variables including: thermal zone, measured annual depth to permafrost, elevation, canopy cover, snow depth, moss thickness, and modeled shortwave radiation. (Right Column) Air temperature (red, left axis), cumulative precipitation (blue, left axis), snow depth (black, right axis), and temperature inside the logger. Soil temperature at depths from 10 to 140 cm below the soil surface according to colors in the legend. Colormap plot of soil temperature according to color in the legend.*

Zone 5 - WSF4.1

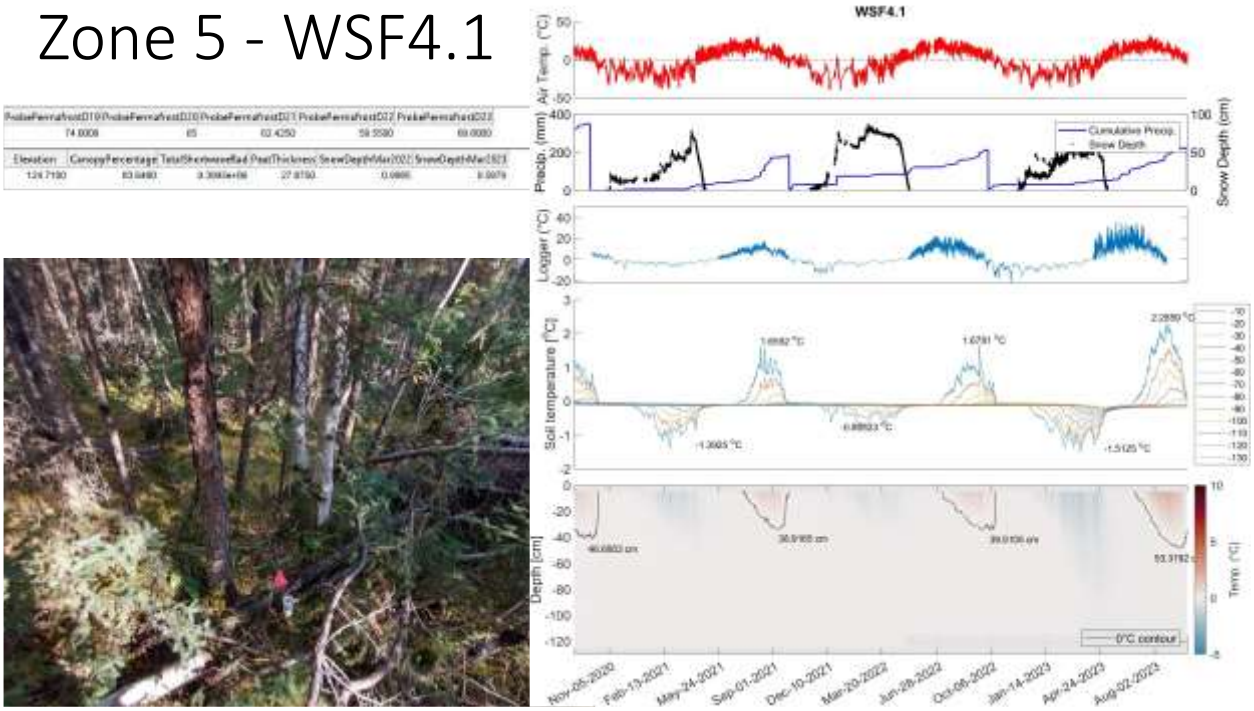

Figure 0.46 Full time series temperature plots and environmental variables for Zone 5 Location 4 *(Left column) Environmental variables including: thermal zone, measured annual depth to permafrost, elevation, canopy cover, snow depth, moss thickness, and modeled shortwave radiation. (Right Column) Air temperature (red, left axis), cumulative precipitation (blue, left axis), snow depth (black, right axis), and temperature inside the logger. Soil temperature at depths from 10 to 140 cm below the soil surface according to colors in the legend. Colormap plot of soil temperature according to color in the legend.*

Zone 5 - WSF4.2

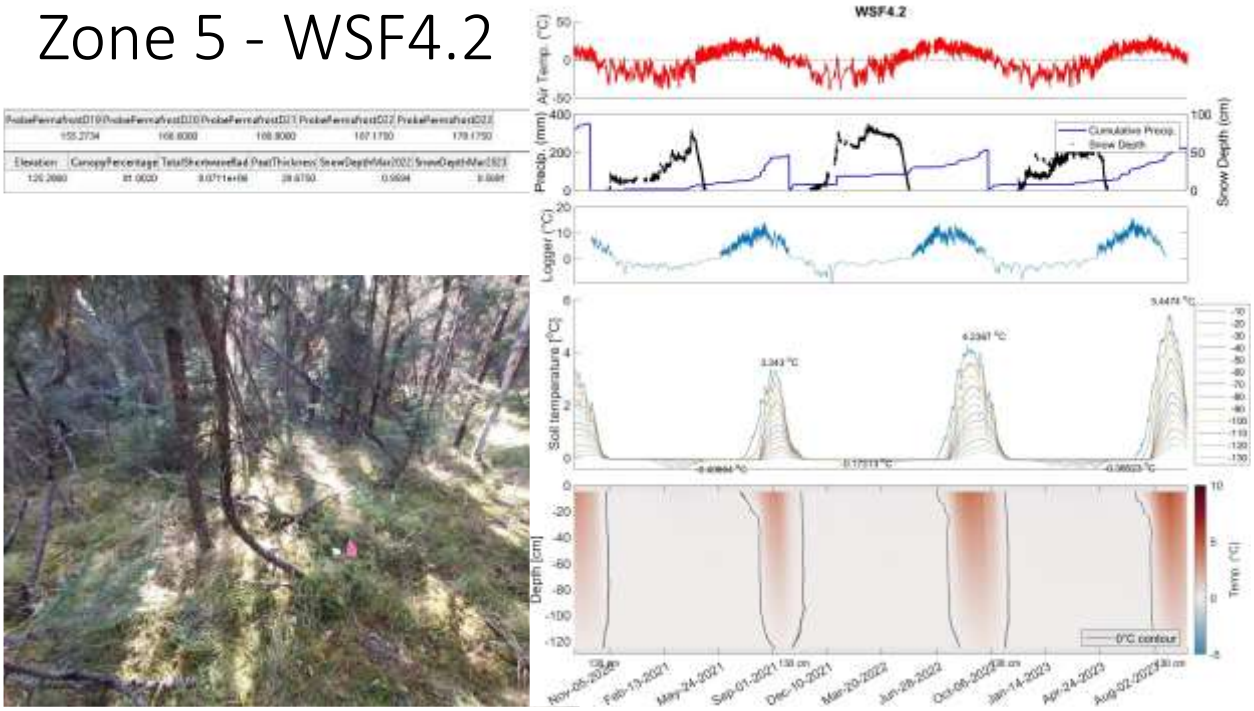

Figure 0.47 Full time series temperature plots and environmental variables for Zone 5 Location 5 *(Left column) Environmental variables including: thermal zone, measured annual depth to permafrost, elevation, canopy cover, snow depth, moss thickness, and modeled shortwave radiation. (Right Column) Air temperature (red, left axis), cumulative precipitation (blue, left axis), snow depth (black, right axis), and temperature inside the logger. Soil temperature at depths from 10 to 140 cm below the soil surface according to colors in the legend. Colormap plot of soil temperature according to color in the legend.*

Zone 5 - WSF4.3

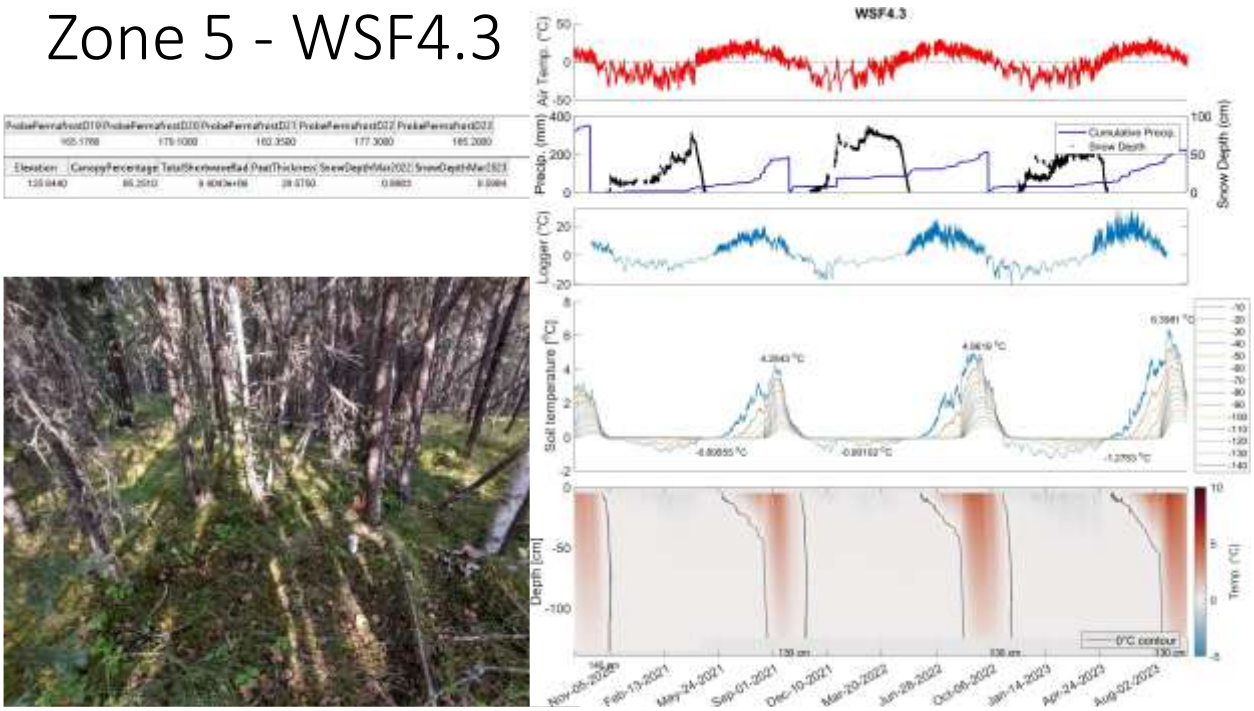

Figure 0.48 Full time series temperature plots and environmental variables for Zone 5 Location 6 *(Left column) Environmental variables including: thermal zone, measured annual depth to permafrost, elevation, canopy cover, snow depth, moss thickness, and modeled shortwave radiation. (Right Column) Air temperature (red, left axis), cumulative precipitation (blue, left axis), snow depth (black, right axis), and temperature inside the logger. Soil temperature at depths from 10 to 140 cm below the soil surface according to colors in the legend. Colormap plot of soil temperature according to color in the legend.*

Zone 5 - WSF4.4

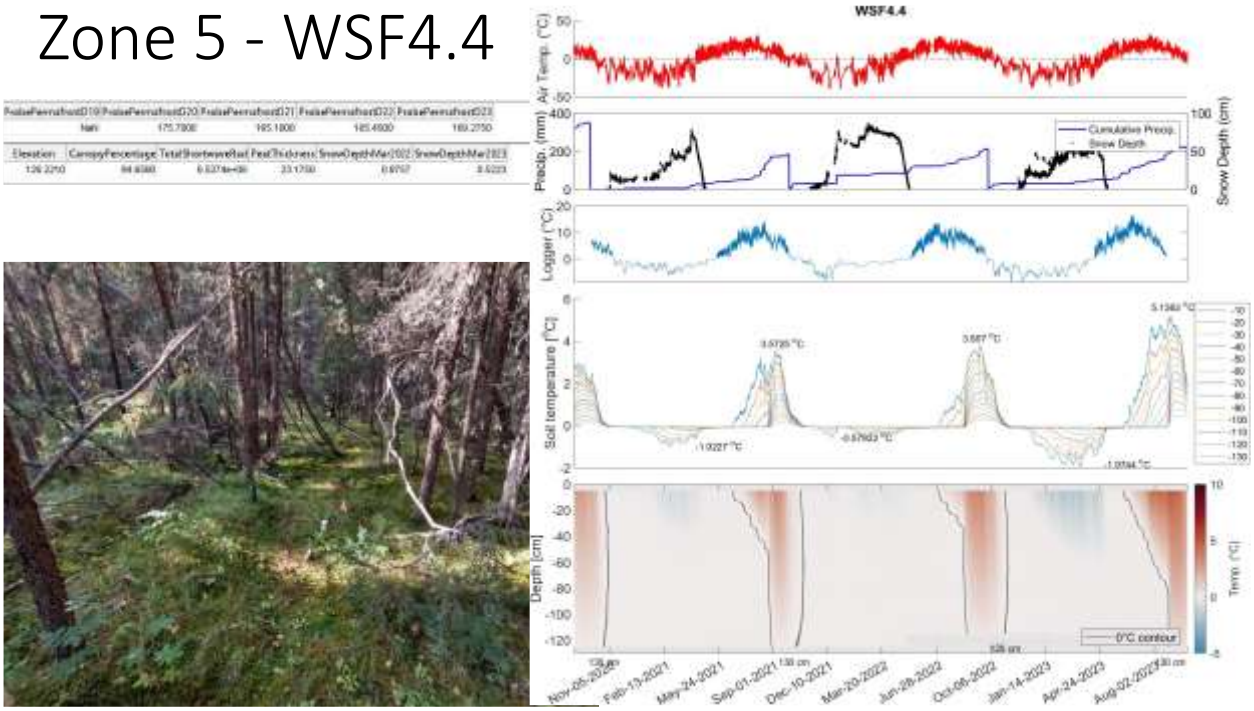

Figure 0.49 Full time series temperature plots and environmental variables for Zone 5 Location 7 *(Left column) Environmental variables including: thermal zone, measured annual depth to permafrost, elevation, canopy cover, snow depth, moss thickness, and modeled shortwave radiation. (Right Column) Air temperature (red, left axis), cumulative precipitation (blue, left axis), snow depth (black, right axis), and temperature inside the logger. Soil temperature at depths from 10 to 140 cm below the soil surface according to colors in the legend. Colormap plot of soil temperature according to color in the legend.*

SI3. Chapter 4 Supplemental

SI3.1 Chapter 4 Supplementary Figures

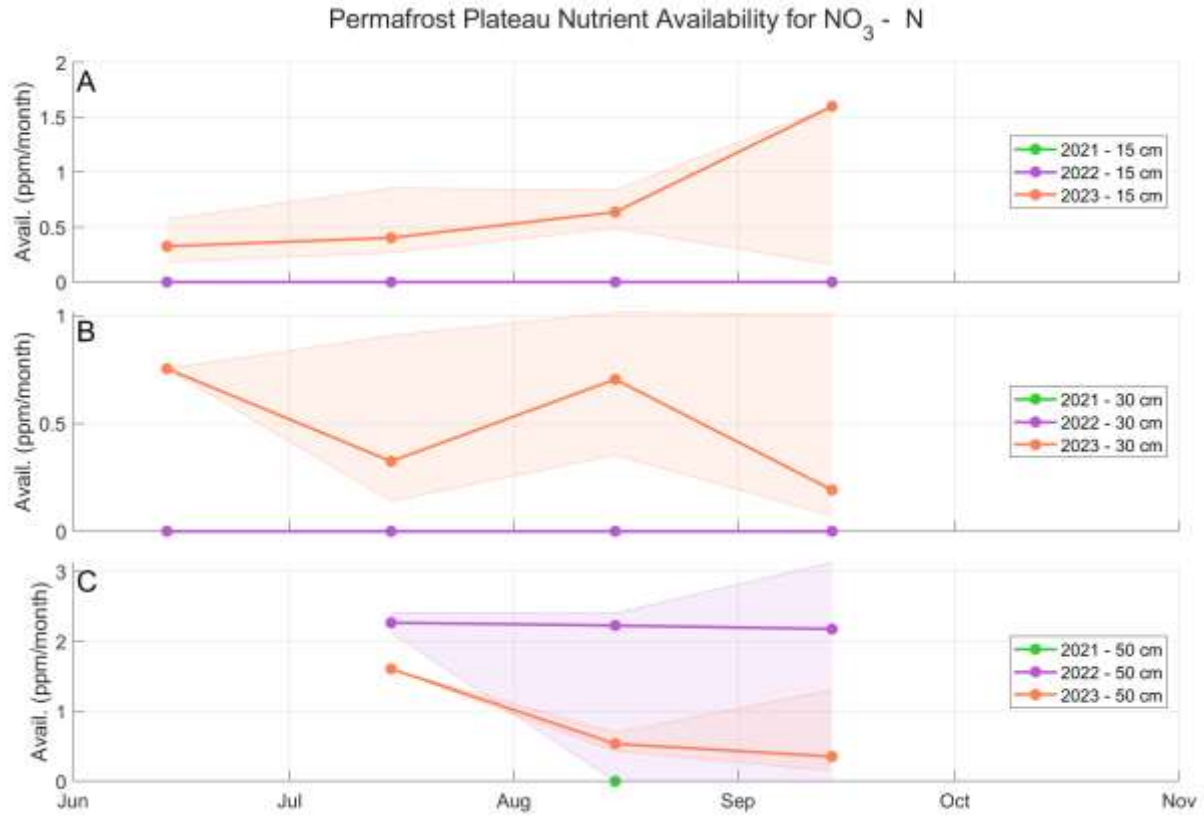

Figure 0.50 Plateau NO_3-N availability time series plots. *Line graphs show stacked time series of availability of NO_3-N at depths of (A) 15 cm, (B) 30 cm, and (C) 50 cm. Data for 2021 is green, 2022 is purple, and 2023 is orange. Shaded areas define the first and third quartiles from the median with color according to the year.*

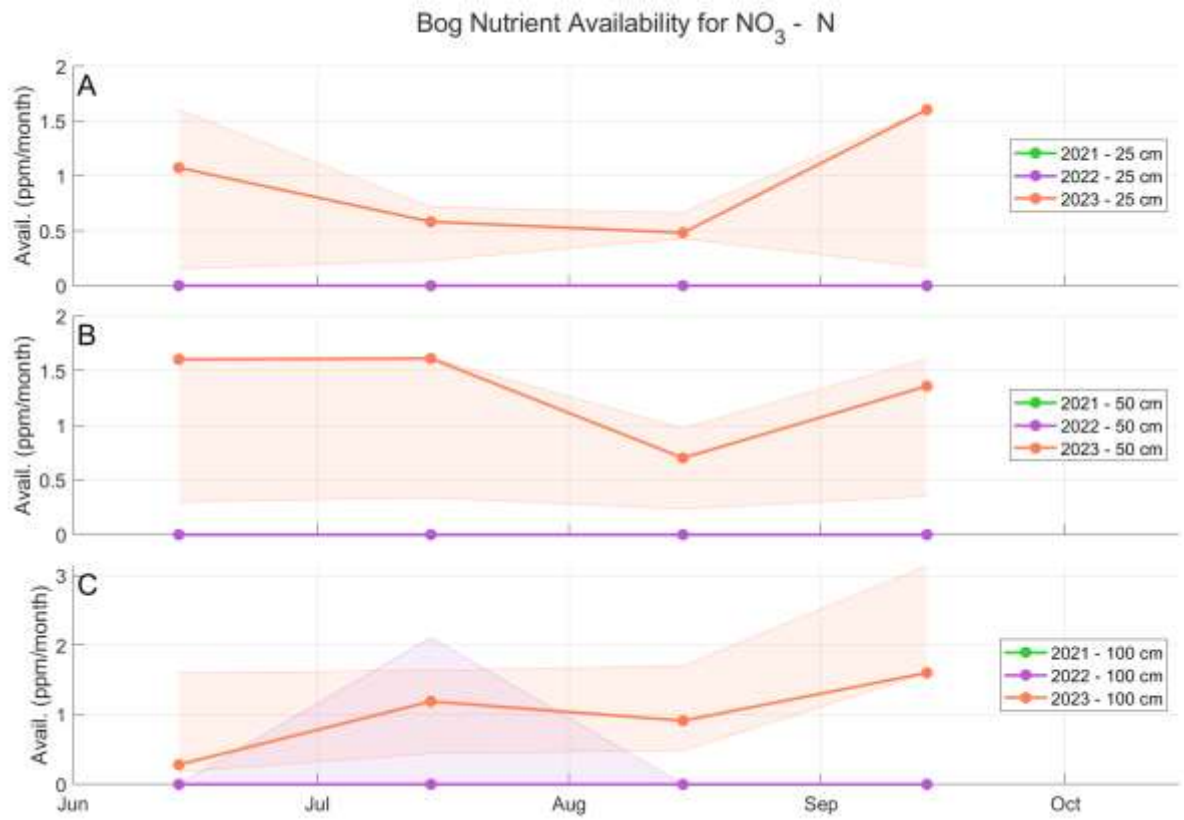

Figure 0.51 Bog NO_3-N availability time series plots. *Line graphs show stacked time series of availability of NO_3- N in piezometers screened at depths of (A) 25 cm, (B) 50 cm, and (C) 100 cm. Data for 2021 is green, 2022 is purple, and 2023 is orange. Shaded areas define the first and third quartiles from the median with color according to the year.*

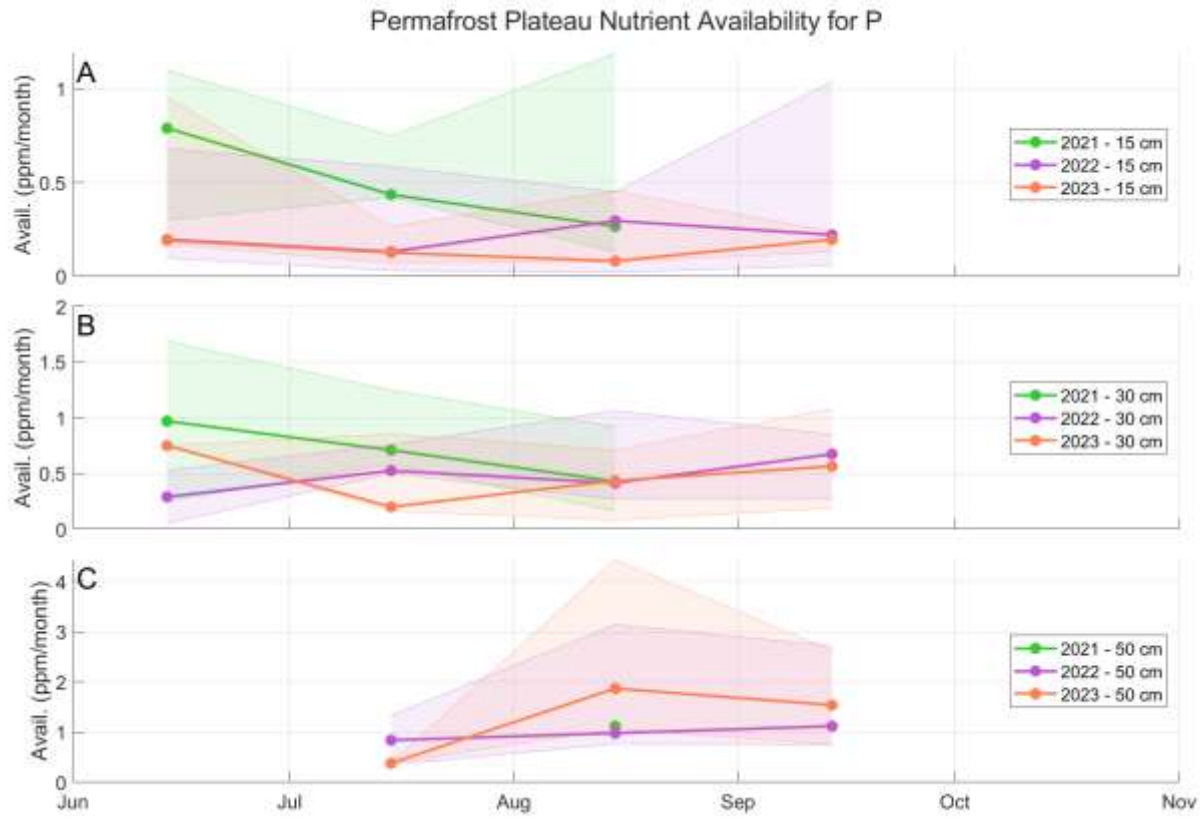

Figure 0.52 Plateau P availability time series plots. *Line graphs show stacked time series of availability of P at depths of (A) 15 cm, (B) 30 cm, and (C) 50 cm. Data for 2021 is green, 2022 is purple, and 2023 is orange. Shaded areas define the first and third quartiles from the median with color according to the year.*

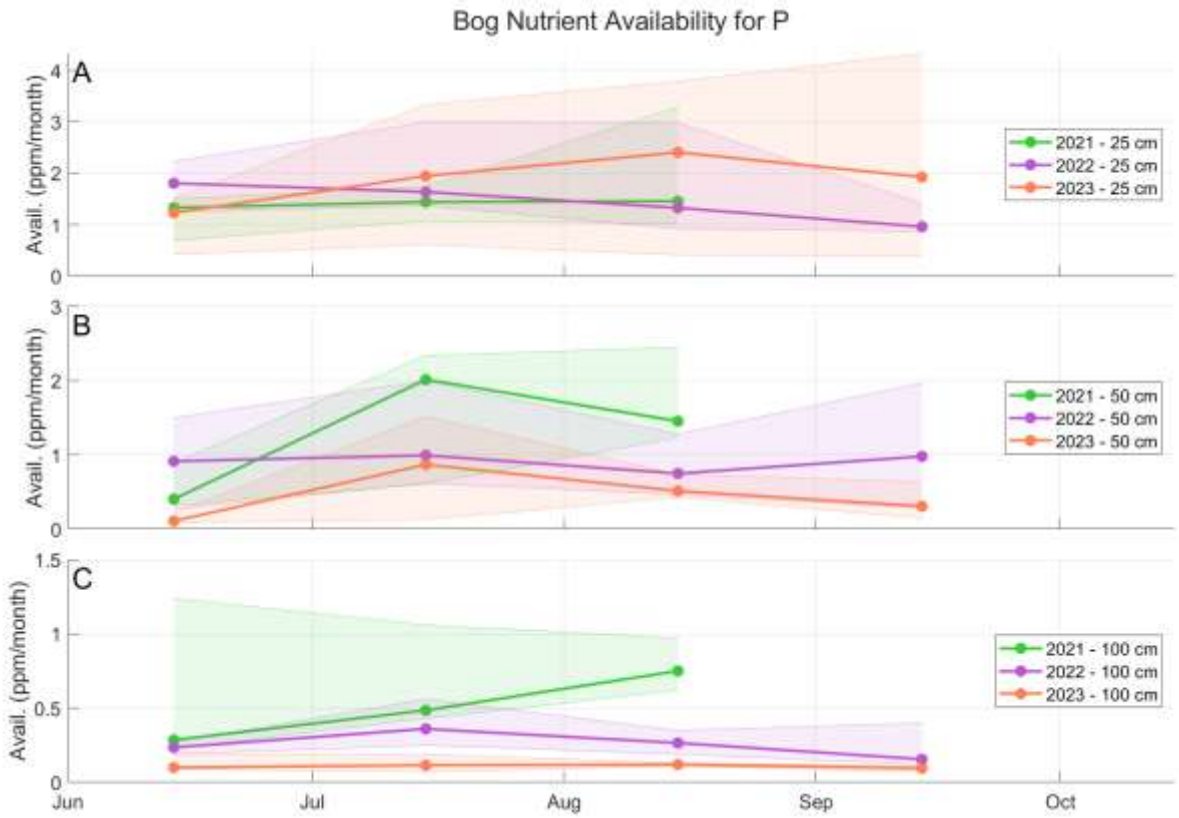

Figure 0.53 Bog P availability time series plots. *Line graphs show stacked time series of availability of P in piezometers screened at depths of (A) 25 cm, (B) 50 cm, and (C) 100 cm. Data for 2021 is green, 2022 is purple, and 2023 is orange. Shaded areas define the first and third quartiles from the median with color according to the year.*

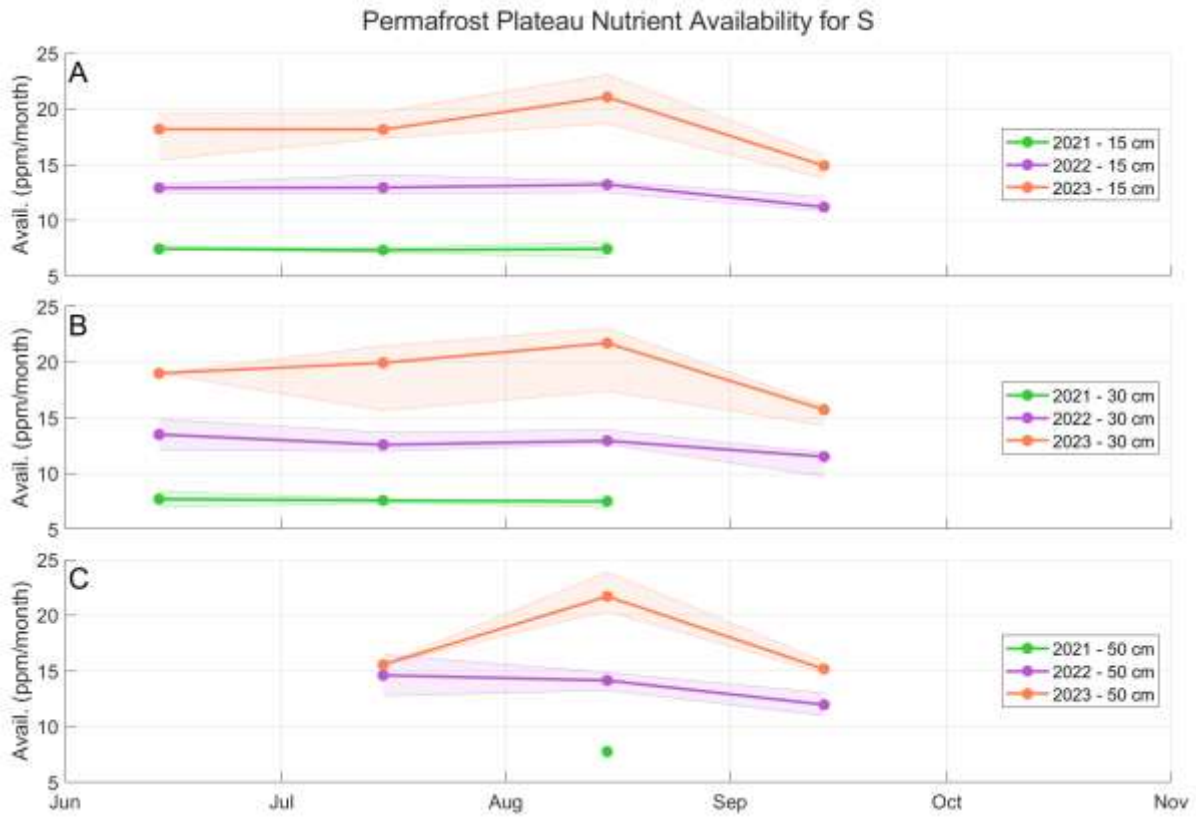

Figure 0.54 Plateau S availability time series plots. *Line graphs show stacked time series of availability of S at depths of (A) 15 cm, (B) 30 cm, and (C) 50 cm. Data for 2021 is green, 2022 is purple, and 2023 is orange. Shaded areas define the first and third quartiles from the median with color according to the year.*

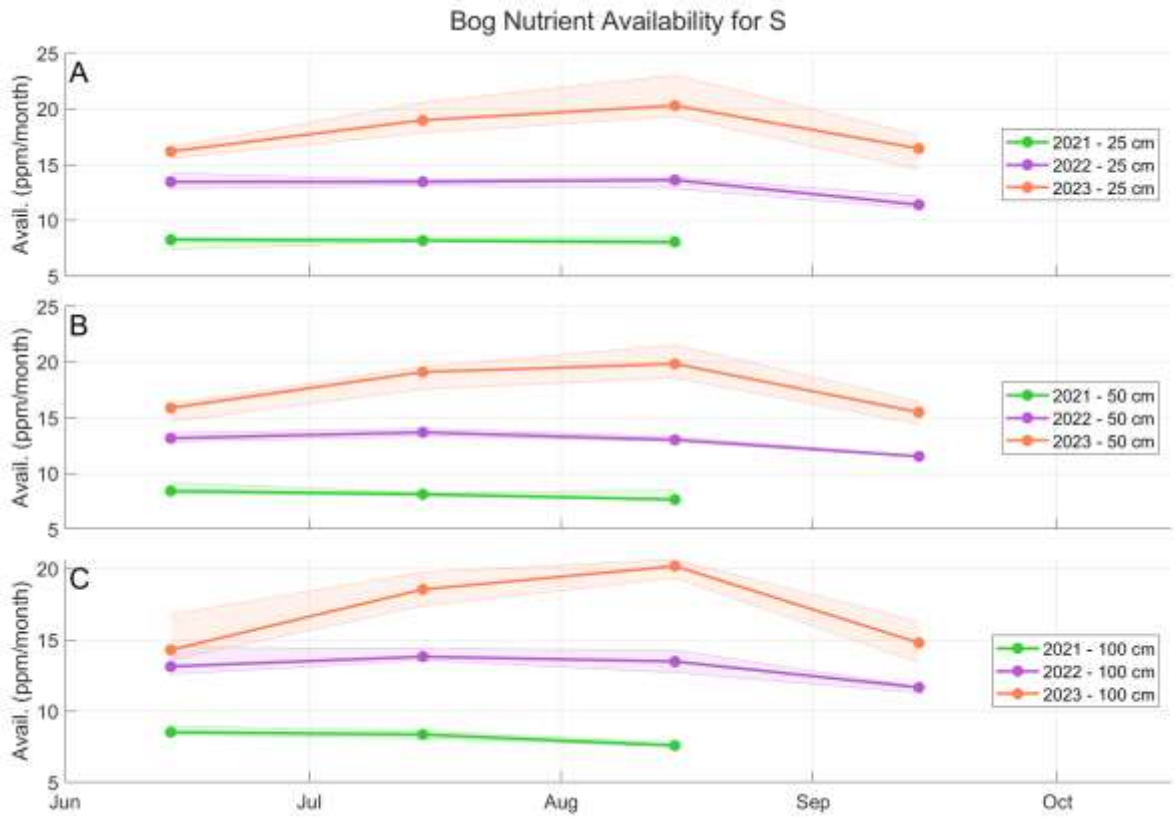

Figure 0.55 Bog S availability time series plots. *Line graphs show stacked time series of availability of S in piezometers screened at depths of (A) 25 cm, (B) 50 cm, and (C) 100 cm. Data for 2021 is green, 2022 is purple, and 2023 is orange. Shaded areas define the first and third quartiles from the median with color according to the year.*

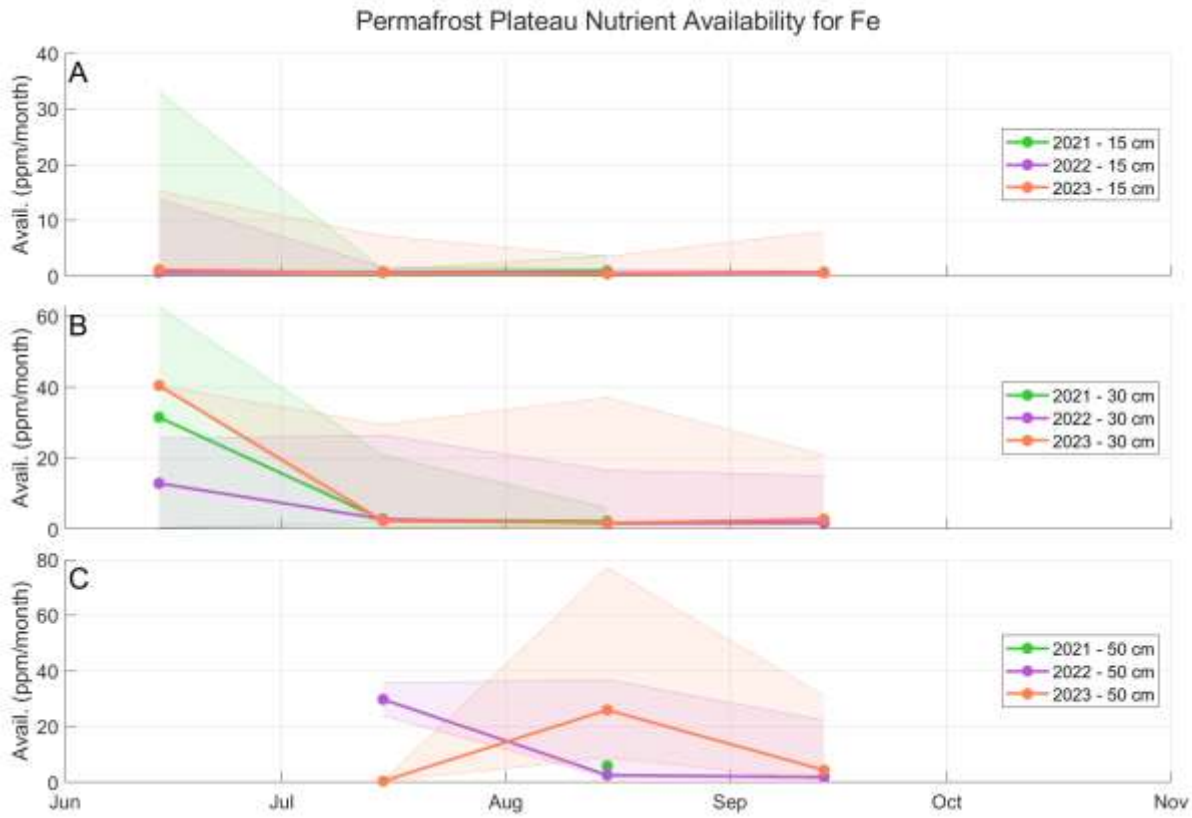

Figure 0.56 Plateau Fe availability time series plots. *Line graphs show stacked time series of availability of Fe at depths of (A) 15 cm, (B) 30 cm, and (C) 50 cm. Data for 2021 is green, 2022 is purple, and 2023 is orange. Shaded areas define the first and third quartiles from the median with color according to the year.*

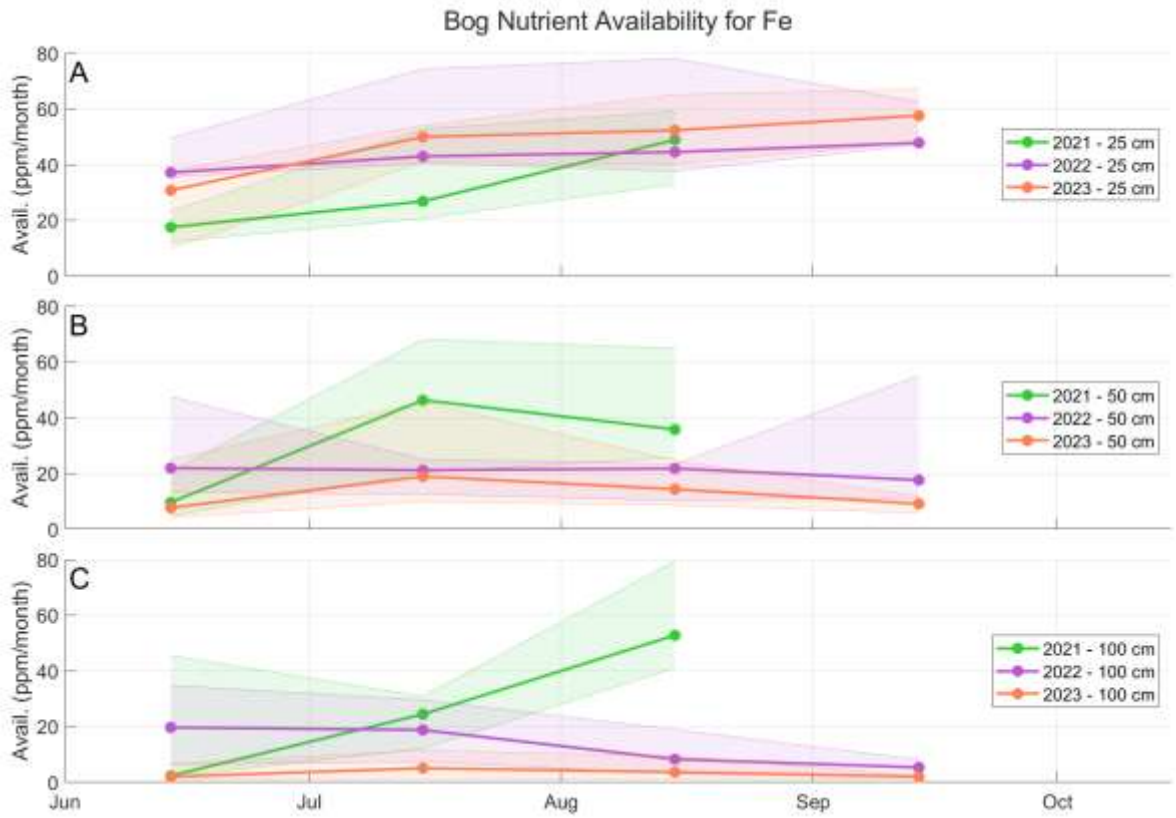

Figure 0.57 Bog Fe availability time series plots. *Line graphs show stacked time series of availability of Fe in piezometers screened at depths of (A) 25 cm, (B) 50 cm, and (C) 100 cm. Data for 2021 is green, 2022 is purple, and 2023 is orange. Shaded areas define the first and third quartiles from the median with color according to the year.*

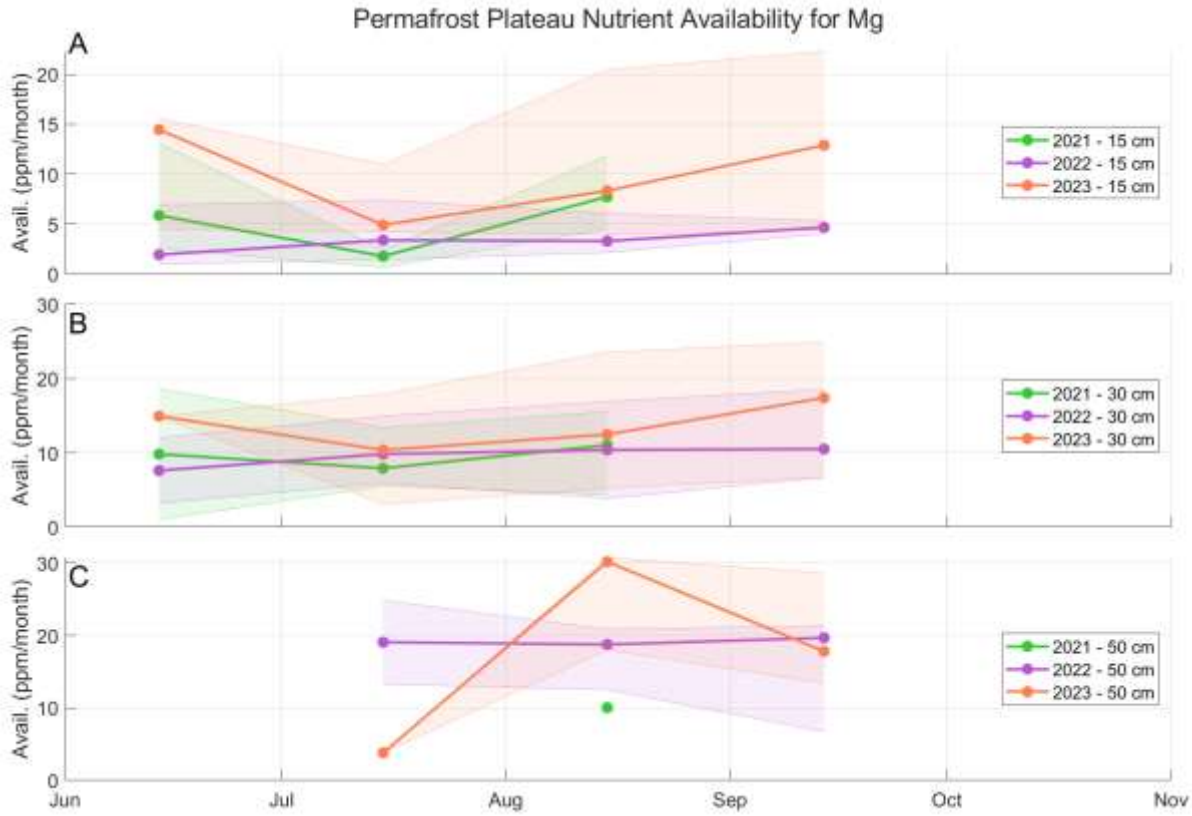

Figure 0.58 ***Plateau Mg availability time series plots.*** *Line graphs show stacked time series of availability of Mg at depths of (A) 15 cm, (B) 30 cm, and (C) 50 cm. Data for 2021 is green, 2022 is purple, and 2023 is orange. Shaded areas define the first and third quartiles from the median with color according to the year.*

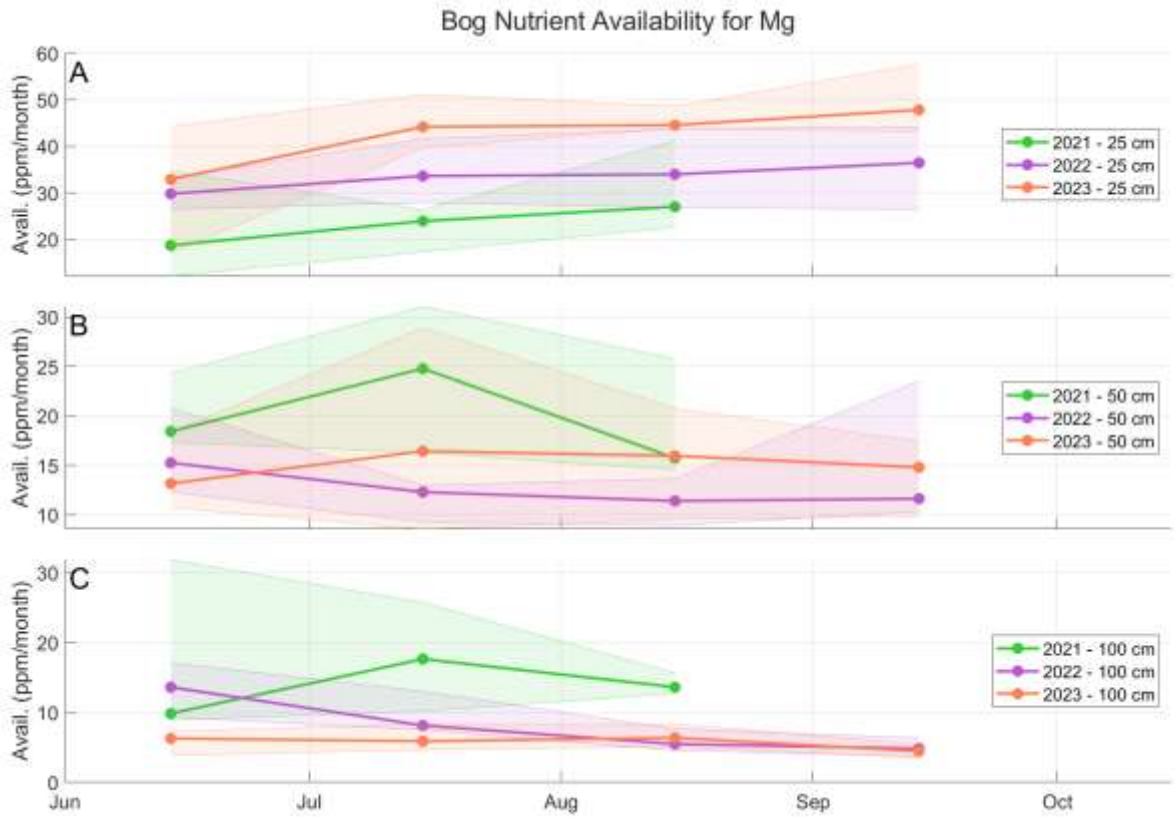

Figure 0.59 Bog Mg availability time series plots. *Line graphs show stacked time series of availability of Mg in piezometers screened at depths of (A) 25 cm, (B) 50 cm, and (C) 100 cm. Data for 2021 is green, 2022 is purple, and 2023 is orange. Shaded areas define the first and third quartiles from the median with color according to the year.*

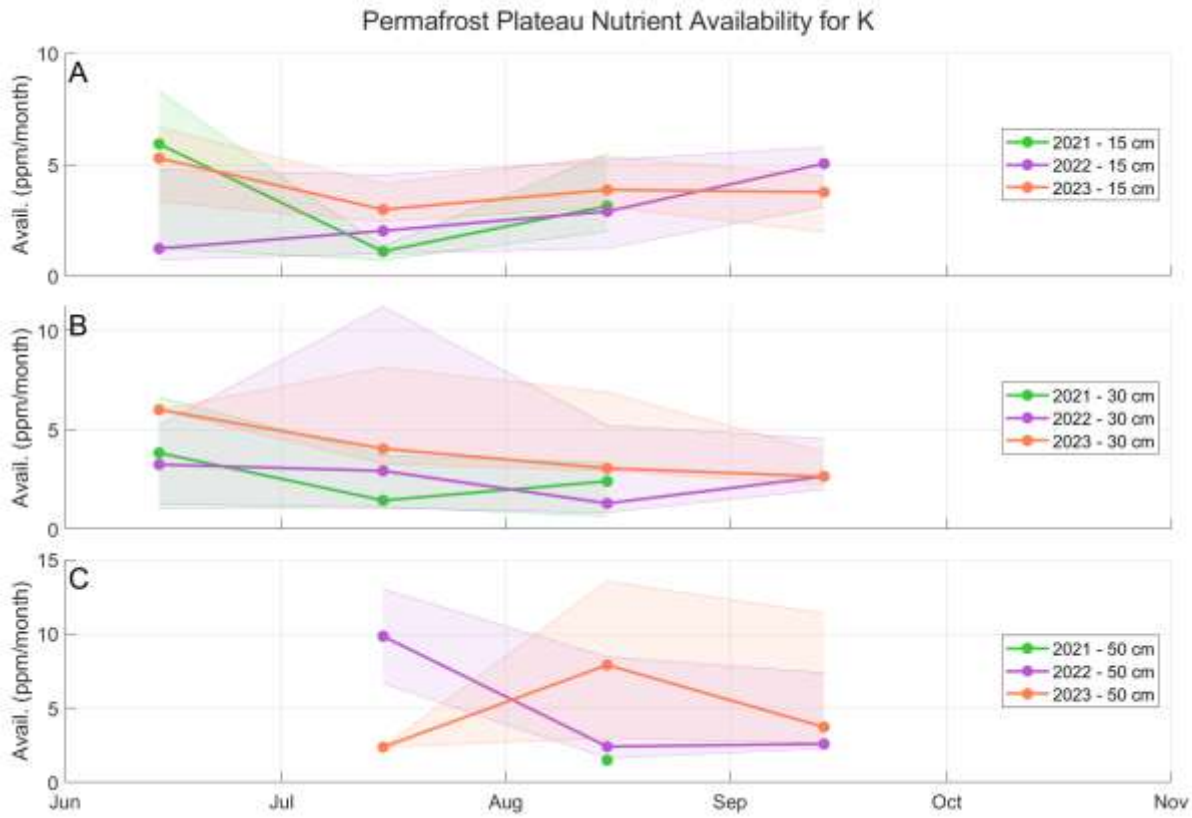

Figure 0.60 Plateau K availability time series plots. *Line graphs show stacked time series of availability of K at depths of (A) 15 cm, (B) 30 cm, and (C) 50 cm. Data for 2021 is green, 2022 is purple, and 2023 is orange. Shaded areas define the first and third quartiles from the median with color according to the year.*

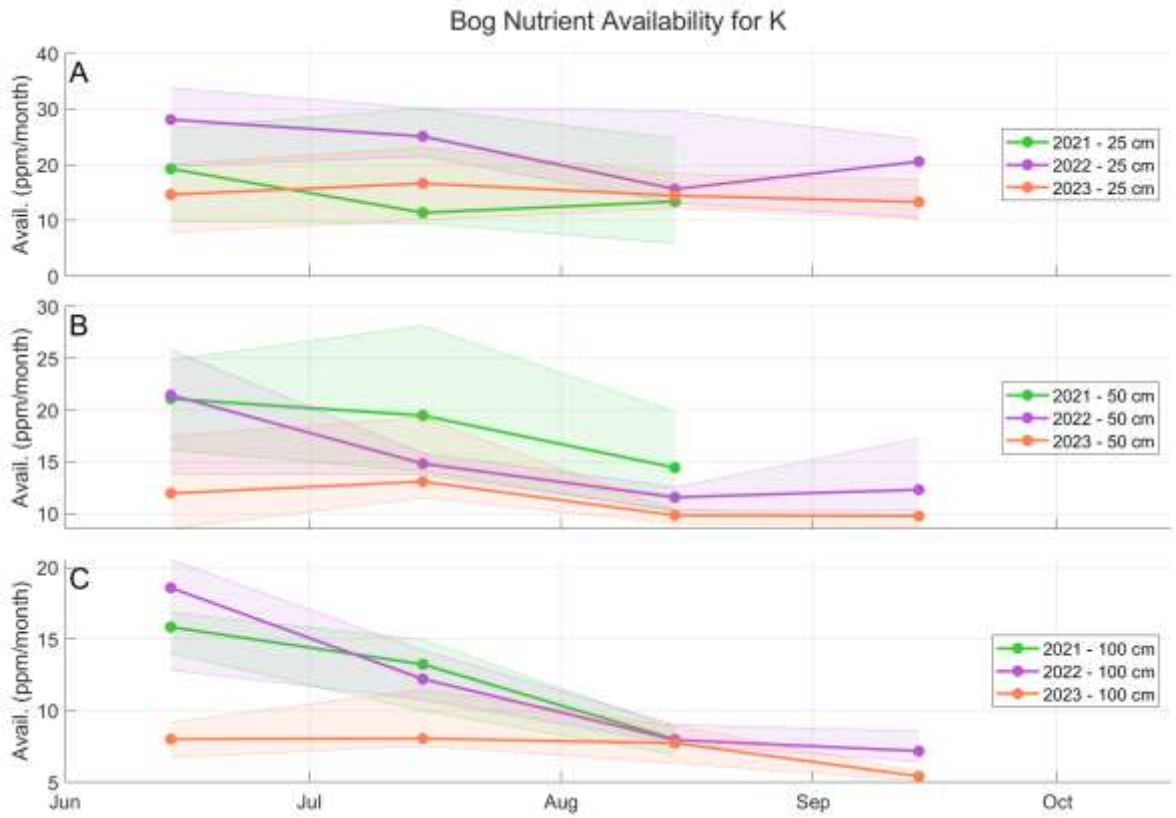

Figure 0.61 Bog K availability time series plots. *Line graphs show stacked time series of availability of K in piezometers screened at depths of (A) 25 cm, (B) 50 cm, and (C) 100 cm. Data for 2021 is green, 2022 is purple, and 2023 is orange. Shaded areas define the first and third quartiles from the median with color according to the year.*

Bog Edge - 1

Canopy Cover	Elevation	Snow Depth
2.7%	121.95 m	95 cm

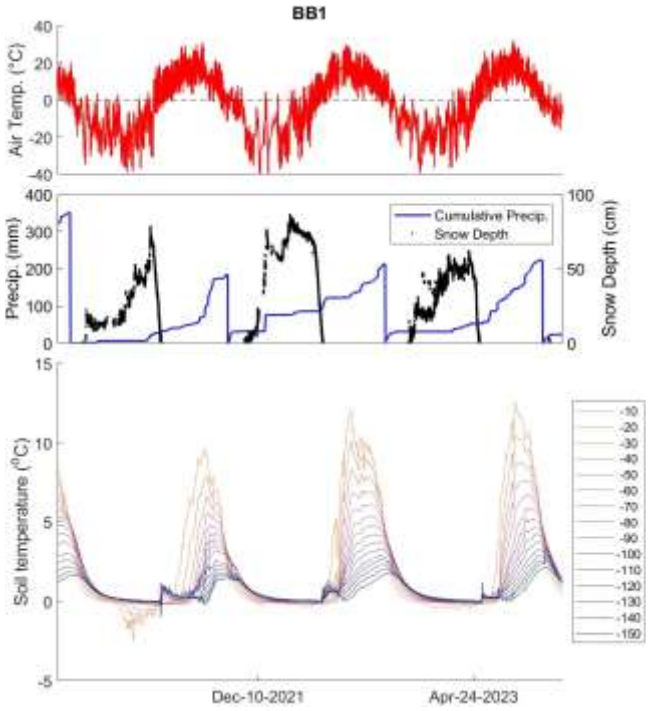

Figure 0.62 Full time series temperature plots and environmental variables for Bog Edge Location 1 *(Left column) Site photo and environmental variables including: canopy cover, elevation, and snow depth. (Right Column) Air temperature (red, left axis), cumulative precipitation (blue, left axis), snow depth (black, right axis). Soil temperature at depths from 10 to 150 cm below the soil surface according to colors in the legend. Colormap plot of soil temperature according to color in the legend.*

Bog Edge - 2

Canopy Cover	Elevation	Snow Depth
2.3%	121.86	94 cm

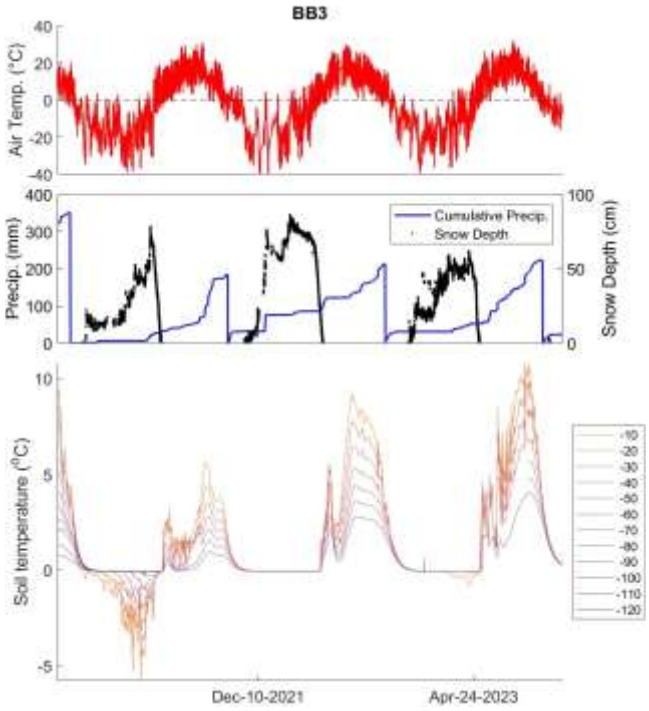

Figure 0.63 Full time series temperature plots and environmental variables for Bog Edge Location 2 *(Left column) Site photo and environmental variables including: canopy cover, elevation, and snow depth. (Right Column) Air temperature (red, left axis), cumulative precipitation (blue, left axis), snow depth (black, right axis). Soil temperature at depths from 10 to 120 cm below the soil surface according to colors in the legend. Colormap plot of soil temperature according to color in the legend.*

Bog Edge - 3

Canopy Cover	Elevation	Snow Depth
5.7%	122.00	98 cm

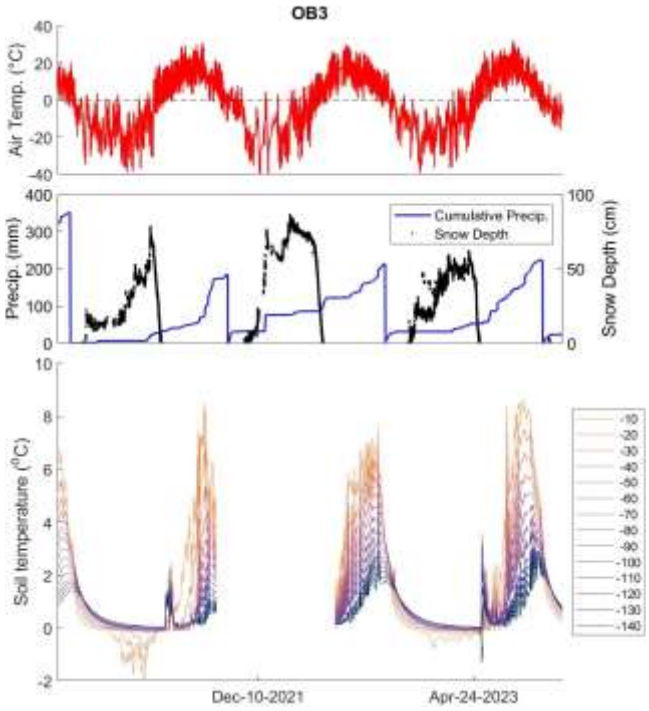

Figure 0.64 Full time series temperature plots and environmental variables for Bog Edge Location 3 *(Left column) Site photo and environmental variables including: canopy cover, elevation, and snow depth. (Right Column) Air temperature (red, left axis), cumulative precipitation (blue, left axis), snow depth (black, right axis). Soil temperature at depths from 10 to 140 cm below the soil surface according to colors in the legend. Colormap plot of soil temperature according to color in the legend.*

Bog Center - 1

Canopy Cover	Elevation	Snow Depth
0.4%	121.99	89 cm

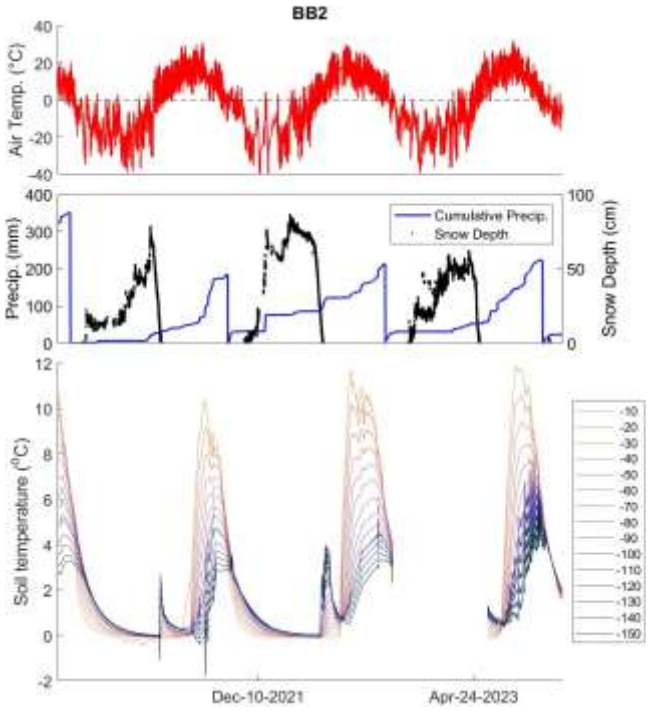

Figure 0.65 Full time series temperature plots and environmental variables for Bog Center Location 1 *(Left column) Site photo and environmental variables including: canopy cover, elevation, and snow depth. (Right Column) Air temperature (red, left axis), cumulative precipitation (blue, left axis), snow depth (black, right axis). Soil temperature at depths from 10 to 150 cm below the soil surface according to colors in the legend. Colormap plot of soil temperature according to color in the legend.*

Bog Center - 2

Canopy Cover	Elevation	Snow Depth
0.6%	121.90	89 cm

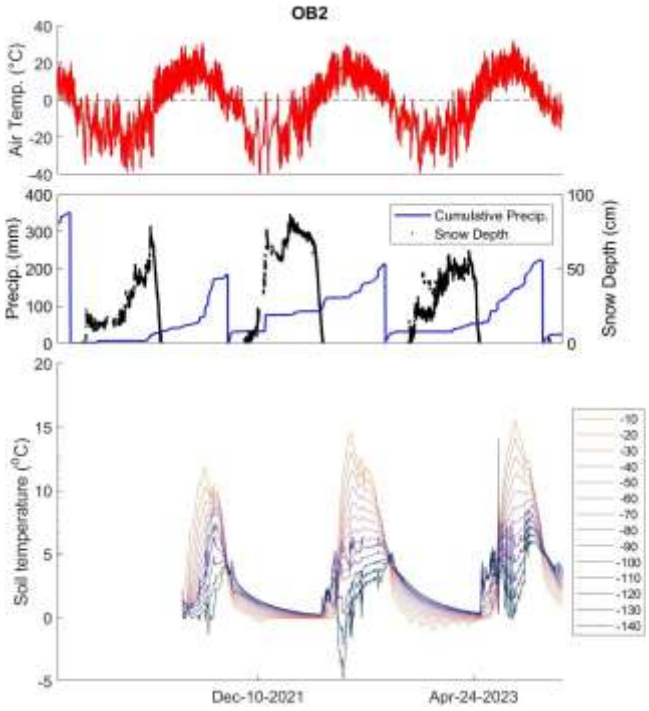

Figure 0.66 ***Full time series temperature plots and environmental variables for Bog Center Location 2*** *(Left column) Site photo and environmental variables including: canopy cover, elevation, and snow depth. (Right Column) Air temperature (red, left axis), cumulative precipitation (blue, left axis), snow depth (black, right axis). Soil temperature at depths from 10 to 140 cm below the soil surface according to colors in the legend. Colormap plot of soil temperature according to color in the legend.*

Bog Center - 3

Canopy Cover	Elevation	Name
1.1%	NaN	99 cm

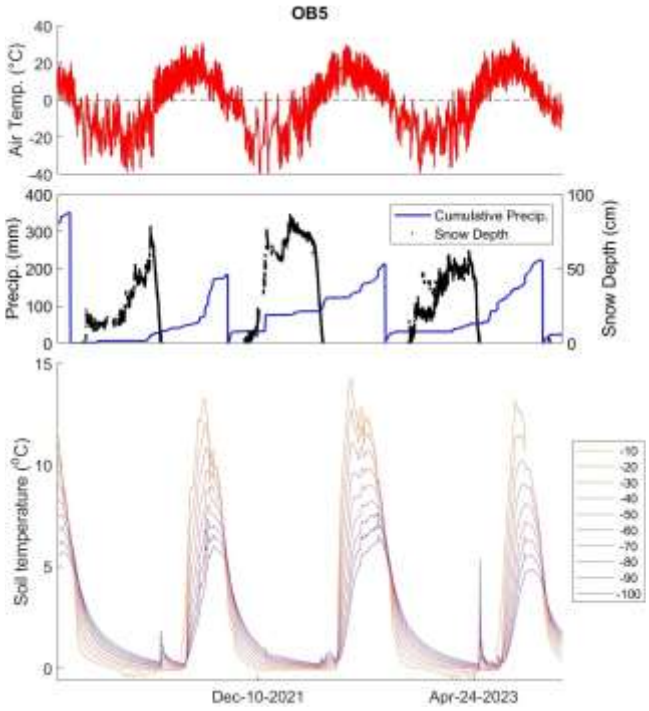

Figure 0.67 Full time series temperature plots and environmental variables for Bog Center Location 3 *(Left column) Site photo and environmental variables including: canopy cover, elevation, and snow depth. (Right Column) Air temperature (red, left axis), cumulative precipitation (blue, left axis), snow depth (black, right axis). Soil temperature at depths from 10 to 100 cm below the soil surface according to colors in the legend. Colormap plot of soil temperature according to color in the legend.*